VERLAG DER TECHNISCHEN UNIVERSITÄT GRAZ

Dominik Pölz

Space-Time Boundary Elements for Retarded Potential Integral Equations

CES 41

MONOGRAPHIC SERIES TU GRAZ
COMPUTATION IN ENGINEERING AND SCIENCE

Dominik Pölz

Space-Time Boundary Elements for Retarded Potential Integral Equations

Monographic Series TU Graz

Computation in Engineering and Science

Monographic Series TU Graz

Computation in Engineering and Science Volume 41

Dominik Pölz

Space-Time Boundary Elements for Retarded Potential Integral Equations

---

This work is based on the dissertation *“Space-Time Boundary Elements for Retarded Potential Integral Equations”*, presented at Graz University of Technology, Institute of Applied Mechanics in 2021.

Supervision / Assessment:

Martin Schanz (Graz University of Technology)
Alessandra Aimi (Università di Parma)

Cover photo	Vier-Spezies-Rechenmaschine by courtesy of the Gottfried Wilhelm Leibniz Bibliothek – Niedersächsische Landesbibliothek Hannover
Cover layout	Verlag der Technischen Universität Graz
Print	DATAFORM Media Ges.m.b.H.

www.tugraz-verlag.at

Print
ISBN 978-3-85125-811-0

E-Book
ISBN 978-3-85125-812-7
DOI 10.3217/978-3-85125-811-0

Von Stund' an sollen Raum für sich und Zeit für sich völlig zu Schatten herabsinken und nur noch eine Art Union der beiden soll Selbstständigkeit bewahren.

H. Minkowski, *Raum und Zeit*, Phys. Z., 10, 104–115 (1909).

Henceforth space by itself, and time by itself, are doomed to fade away into mere shadows, and only a kind of union of the two will preserve an independent reality.

English translation by W. Perrett and G.B. Jeffery (with notes by A. Sommerfeld) in: H.A. Lorentz, A. Einstein, H. Minkowski and H. Weyl, *The Principle of Relativity*, Dover, New York, 1952.

ABSTRACT

This thesis is dedicated towards the development of a novel boundary element method for scattering problems governed by the wave equation. Although these problems are posed on the unbounded exterior of the scatterer, the boundary integral equation method facilitates a reduction to the bounded surface of the scatterer. The strong Huygens principle bestows a special structure upon the integral operators of the wave equation in three spatial dimensions, reverberating through their name "retarded potentials". Space-time discretization methods treat both the continuous as well as the discretized problem as a single operator equation in the 3+1-dimensional space-time cylinder. The proposed scheme is based on unstructured simplex meshes of the lateral boundary of this cylinder. Well-established space-time variational formulations are discretized by means of piecewise polynomial trial spaces defined on these meshes. Integral representations of retarded potentials are derived, which genuinely conform to the space-time setting. Furthermore, this work provides quadrature techniques for pointwise evaluations of retarded potentials as well as the evaluation of energetic bilinear forms. Numerical experiments are exhibited, verifying the implementation and the capacity of the proposed space-time approximation method.

ZUSAMMENFASSUNG

Die vorliegende Dissertation widmet sich der Entwicklung einer neuartigen Randelementmethode für Streuprobleme, die durch die Wellengleichung beschrieben werden. Obgleich diese Probleme auf dem unbeschränkten Außenraum des streuenden Objekts gestellt sind, ermöglicht die Integralgleichungsmethode eine Reduktion auf den beschränkten Rand des streuenden Objekts. Das starke Huygens'sche Prinzip verleiht den Integraloperatoren der Wellengleichung in drei Raumdimensionen eine besondere Struktur, die in deren Namen "retardierte Potentiale" widerhallt. Raumzeit-Methoden behandeln sowohl das kontinuierliche als auch das diskretisierte Problem als eine Operatorgleichung im 3+1-dimensionalen Raumzeit-Zylinder. Das vorgestellte Verfahren basiert auf unstrukturierten simplizialen Vernetzungen des Zylindermantels. Gängige Raumzeit-Variationsformulierungen werden mithilfe von stückweise polynomialen Ansatzräumen, die auf diesen Vernetzungen erklärt sind, diskretisiert. Es werden Integraldarstellungen von retardierten Potentialen hergeleitet, die konform zur Anschauung der Raumzeit sind. Darüber hinaus bespricht diese Abhandlung Quadraturtechniken für punktweise Auswertungen von retardierten Potentialen sowie Auswertungen der verwendeten Bilinearformen. Abschließend werden numerische Experimente vorgestellt, welche die Implementierung verifizieren und die Leistungsfähigkeit der besprochenen Raumzeit-Methode verdeutlichen.

CONTENTS

1 INTRODUCTION

The philosophy of space-time is to treat time as if it were an additional coordinate akin to the spatial ones. In other words, time and space are considered as components of space-time rather than disconnected entities. In modern physics, the concept of space-time is well-established and facilitates deeper understanding of fundamental theories. In 1908, Hermann Minkowski proposed in his famous Cologne lecture that the laws of electrodynamics and the special theory of relativity are thoroughly appreciated only in the context of space-time [77]. Minkowski's revolutionary and controversial view [120] eventually influenced vast branches of physics. A prominent example are Einstein's field equations of the general theory of relativity, which are based on quantities like the metric four-tensor of space-time itself. This grand classical theory of gravity predicts, for instance, the existence of black holes and gravitational waves. The first mathematical derivations of both of these phenomena were published in 1916 [107, 29], however, they are still a highly active field of research even a century after their disclosure. In the second decade of the 21st century spectacular experimental results were acclaimed [1, 8], which support the theoretical predictions.

None of these topics is subject of the present thesis. This thesis is accredited to the field of numerical methods for differential and integral equations. However, above passage demonstrates the sheer capacity inherent to the unification of space and time. Naturally, the question arises of how the space-time philosophy can be exploited to enhance numerical methods for transient problems. In fact, this question motivates the research effort that culminates in this body of work.

1.1 Literature Review

In the present thesis, we develop a space-time approximation scheme for integral equations of the wave equation. The wave equation, which is the prototypical hyperbolic partial differential equation, is a viable model for acoustic as well as electromagnetic waves in various situations. An important class of problems related to these types of waves are scattering problems, in which the wave field in the unbounded exterior of the scatterer is of interest. The boundary integral equation (BIE) method reduces the problem posed on the unbounded exterior to the bounded surface of the scatterer. This inherent advantage of the BIE method facilitates compelling numerical schemes not limited to scattering problems only. The strong Huygens principle, which is valid for the wave equation in three spatial dimensions, bestows an extraordinary structure upon the associated integral operators. This distinguished nature reverberates through their famous name retarded potential boundary integral equations (RPBIEs).

Literature Review of RPBIEs and their Discretization

The inherent advantages of RPBIEs inspired numerous research efforts devoted to their analysis and their discretization. The mathematical analysis of integral equations of hyperbolic problems was sparked by the seminal publications of Bamberger and Ha-Duong [10, 11]. In these articles, the Laplace transform with respect to the time variable is applied to the wave equation and related BIEs, yielding well-posed variational problems. The behavior of the solution of the transformed equations is estimated with respect to the Laplace parameter. These frequency domain estimates are transported to time domain using a Plancherel formula in certain anisotropic Sobolev spaces. In a later paper by Lubich [71], time domain estimates are achieved by means of the inverse Laplace transform. The review articles [51, 21] provide an exhaustive overview of the achievements of this theory. In contrast to this frequency domain approach, the paper of Rynne [97] analyses an RPBIE arising in electrodynamics entirely in time domain using the theory of hyperbolic equations. This technique, however, is restricted to smooth scatterers. The group of Sayas [103, 104] developed a time domain analysis which evolves around the theory of semigroups of operators. This methodology yields better estimates than the ones due to approaches based on the Laplace transform. The analysis was extended and unified in [91, 53]. Further key contributions are due to Aimi and her collaborators [6, 7]. The cited articles investigate so-called energetic bilinear forms of RPBIEs, which are most commonly used in practice. The considerations are restricted to flat boundaries in two spatial dimensions, enabling the application of the Fourier transform with respect to both time and space. For instance, the boundedness property proven in [6] provides a factual justification for the use of discontinuous trial spaces, which is acknowledged in [58]. The paper of Joly and Rodríguez [58] thoroughly investigates the weight function employed in space-time bilinear forms of RPBIEs. Furthermore, this article reviews and expands crucial results of the available literature and features explicit calculations for the wave equation in one spatial dimension.

Discretization methods for RPBIEs can be traced back to Friedman and Shaw [35]. The first boundary element method (BEM) in the modern sense was developed by Mansur [73]. The review article of Costabel and Sayas [21] as well as the preface in the monograph [104] provide an overview of the existing literature. As already indicated, the first BEMs for RPBIEs originate from the work of Mansur [74, 73]. Within these procedures, the unknown surface density is approximated by a product of trial functions in the spatial variables and functions in time. The RPBIE is collocated (interpolated) at a set of points located on the spatial mesh and at fixed time steps, see, e.g., [18]. These methods are plagued by stability issues [17, 95, 98], which is the reason why an array of articles was devoted to the development of stable schemes [96, 23, 22, 24].

Another approach to the numerical solution of RPBIEs are Galerkin methods based on space-time variational formulations. The stability of these schemes is due to coercivity properties of bilinear forms which involve RPBIEs of the first kind, see [51]. Due to their favorable properties, many papers and monographs were dedicated towards the development of Galerkin methods [2, 43, 4, 14, 118, 116, 40, 41, 42]. However, the implementation of these methods is nontrivial due to the occurrence of complicated high-dimensional integrals [85, 5, 101]. This issue is addressed in great detail within this thesis.

While the approaches mentioned yet discretize the BIEs directly in time domain, there exist alternatives that circumvent the intricate implementation of RPBIEs. A renowned discretization scheme is constituted by Lubich's convolution quadrature method (CQM) [69, 70]. The convolutional Volterra type time domain integral operators are approximated via the CQM and the BIE is satisfied at equally sized time steps. This approach is combined with standard spatial boundary element methods, e.g., collocation or Galerkin methods [71, 12, 13, 9]. Decisive advantages of these procedures are their inherent stability properties and the fact that the integral operators have to be computed in Laplace domain only. The latter advantage is particularly acclaimed in the engineering community, see [106]. Further developments of the CQM accommodate variable time step sizes [66, 67, 68].

There exist BEMs for the wave equation which avoid the use of retarded potentials entirely. In Rothe's method [94], the initial-boundary value problem is discretized in time with a suitable implicit time-stepping scheme. The problem at each time step depends only on the spatial variables and can be solved by well-established BEMs for elliptic problems, see [21].

Virtually all of the discussed BEMs have one feature in common: space and time are discretized separately. Disconnected treatment of space and time is inherent to the CQM and Rothe's method, nevertheless even space-time Galerkin methods for RPBIEs unanimously employ trial spaces which are the product of an ansatz in the spatial variables and an ansatz in time, see, e.g., [51, 101, 116]. In the present thesis, we seek to take a step towards genuine space-time discretization schemes for RPBIEs. The following section provides basic concepts and reviews existing literature on space-time discretization methods.

Space-Time Discretization Methods

The basic idea of space-time methods is to treat the time variable as if it were an additional coordinate, quite in the spirit of Minkowski's idea. Inspired by this rationale, the transient problem is considered as a single operator equation in space-time, even within the discretization. Space-time finite elements are based on meshes of the $(n+1)$-dimensional space-time cylinder, where $n \in \mathbb{N}$ the number of spatial dimensions. These meshes do not distinguish between space and time dimensions. Such an unstructured space-time mesh is the key feature of space-time methods, see Figure 1.1, which is adapted from [57, Figures 5, 6, and 7].

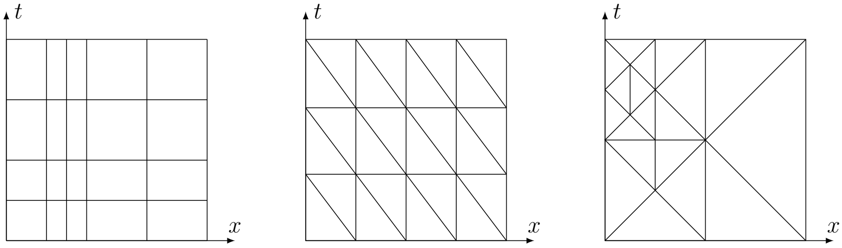

a) tensor product space-time mesh

b) space-time slabs composed of simplices

c) unstructured simplex space-time mesh

Figure 1.1: Types of meshes of the space-time cylinder for $n = 1$ spatial dimension; the tensor product space-time mesh of Figure 1.1a is typically implied by time-stepping schemes. The simplices (triangles) in Figures 1.1b and 1.1c cover space and time dimensions without distinction.

The development of space-time finite element methods has achieved remarkable progress [82, 109, 26, 48, 47, 119]. While the gravest drawback of space-time methods is the necessity of treating $(n+1)$-dimensional domains, they offer several inherent advantages:

- Unstructured space-time meshes can adapt flexibly to special features of the solution [27]. Adaptive space-time BEMs for the wave equation in one spatial dimension are explored in [123, 88].

- Moving or instationary domains can be treated naturally. The deformed configuration at any point in time is captured by the space-time mesh itself [121, 64].

- Considering the discrete problem as a single operator equation facilitates the application and development of parallel solution strategies [82, 38].

- In the context of hyperbolic problems, causality and finite speed propagation can be exploited to construct schemes which are explicit in subregions of space-time. A typical example are tent pitching schemes [46, 87].

On the one hand, one might be inclined to claim that space-time finite element methods have already attained a certain state of maturity. On the other hand, the development of genuine space-time BEMs is in its infancy. An explanation for this research gap is that most existing quadrature techniques for time domain integral operators require that space and time are treated separately [5, 101, 40]. The intricacy of computing retarded potentials in the context of unstructured space-time meshes is the reason why virtually any discretization scheme for RPBIEs features a product structure in space and time.

To the best of our knowledge, the most successful attempt yet at abandoning this product structure is due to Frangi [34]. In the cited article, "causal" shape functions are proposed. They are based on a decomposition of the space-time boundary into space-time slabs, which feature a fixed simplicial substructure. The numerical experiments investigated in the cited reference yield promising results. This approach can be interpreted as a predecessor to trial functions defined on unstructured space-time meshes. We emphasize that BEMs for parabolic problems which feature space-time meshes as well as moving boundaries are actively developed by Tausch and collaborators [72, 111].

1.2 Contribution to the Field and Outline

This thesis aims at the research gap indicated in the previous section, namely the lack of genuine space-time approximation schemes for RPBIEs. Within this monograph the feasibility of the practical realization of such methods is investigated. The considerations are restricted to the wave equation in three spatial dimensions, because it obeys the strong Huygens principle. In the treated case, the lateral boundary of the four-dimensional space-time cylinder is a three-dimensional hypersurface.

This thesis provides two primary contributions. On the one hand, we investigate the use of space-time trial spaces for BEMs from a practical point of view. The proposed method uses tetrahedral meshes, which accommodate space-time trial spaces of piecewise polynomial functions. These boundary element spaces are exposed in Section 3.1 and employed in Section 3.3 to discretize energetic variational formulations of RPBIEs. On the other hand, we propose special integration techniques for retarded potentials in the context of space-time meshes. The integration procedure is based on two aspects:

(i) Alternative integral representations of retarded potentials, which genuinely conform to the space-time setting, are derived in Sections 2.6.1 and 2.6.2. These formulas are not restricted to simplex meshes but hold for sufficiently smooth Lipschitz hypersurfaces. Nevertheless, the integrals are investigated and simplified for the case of simplex meshes in Sections 3.4 and 3.5.

(ii) A numerical integration scheme for the formula developed in Section 3.5 is discussed in Section 3.8.1. This method is a combination of well-established quadrature techniques, which are tailored to the integral at hand. An algorithm for computing the set of panels lit by the light cone is discussed in Section 3.8.3.

As already stated, existing space-time Galerkin methods for RPBIEs discretize space-time variational formulations via product-type trial spaces. The approach examined in the present thesis is based on trial spaces which treat space and time variables uniformly. In the interest of disambiguation, the proposed approach is labeled space-time boundary elements for retarded potential integral equations (which happens to be the title of this monograph).

In a preliminary study, the author of this monograph was involved in a work on BIEs for the wave equation in one spatial dimension [88]. It is duly noted that a significant share of the findings presented in this thesis is published in [89].

Outline

In Chapter 2, the considered initial-boundary value problems are introduced and their reformulation in terms of RPBIEs is addressed. The employed variational formulations are exhibited and we comment on their connection to the energy stored in the wave field. Furthermore, integral representations of retarded potentials are provided and transferred to the chosen space-time setting.

Chapter 3 exhibits the proposed space-time approximation scheme. The employed simplex meshes and piecewise polynomial trial spaces are introduced. The variational problems of Chapter 2 are discretized by means of lowest order space-time boundary element spaces. Numerical integration techniques for retarded potentials as well as their energetic bilinear forms are discussed. An algorithm for computing the intersection of mesh and light cone is proposed at the end of Chapter 3.

In Chapter 4, the methods introduced in Chapter 3 are verified by means of numerical experiments. The conducted studies aim at verifying the space-time trial spaces, the numerical integration techniques, and the proposed space-time BEMs.

Chapter 5 concludes this monograph by summarizing its key findings and discussing topics of further research in this field.

2 WAVE EQUATION AND RETARDED POTENTIALS

In this chapter, we exhibit the wave equation, related initial-boundary value problems, and certain solution operators. The latter are known as retarded potentials and enable a reformulation in terms of BIEs. Sections 2.1 to 2.5 establish the general setting for this thesis and are primarily adapted from existing literature, especially the books [100, 108, 104] and the articles [51, 6, 58]. The scientific novelty of this chapter is encapsulated in Section 2.6, culminating in space-time integral representations of retarded potentials in Sections 2.6.1 and 2.6.2. A part of these results is already published in [89].

2.1 Geometric Setting and Notation

For $n \in \mathbb{N}$ we endow $\mathbb{R}^n$ with the usual Euclidean inner product $\langle \cdot, \cdot \rangle : \mathbb{R}^n \times \mathbb{R}^n \to \mathbb{R}$ with induced norm $\|\cdot\| : x \mapsto \sqrt{\langle x, x \rangle}$. The unit sphere is denoted $\mathbb{S}^{n-1} := \{x \in \mathbb{R}^n : \|x\| = 1\}$. We equip $\mathbb{R}^{n+1}$ with the Cartesian basis $\{\mathfrak{e}_i\}_{i=0}^n$, where $\mathfrak{e}_0$ is the base vector in time direction and $\mathfrak{e}_i, i = 1, \ldots, n$ correspond to the spatial directions. For convenience, the fixed decomposition of points in space-time is introduced

$$\mathbb{R}^{n+1} \ni \mathbf{x} := (t, x), \quad \mathbb{R}^{n+1} \ni \mathbf{y} := (\tau, y),$$

with times $t, \tau \in \mathbb{R}$ and spatial components $x, y \in \mathbb{R}^n$. This enables the expansion

$$\mathbf{x} = t\mathfrak{e}_0 + \sum\nolimits_{i=1}^{n} x_i \mathfrak{e}_i, \quad \mathbf{y} = \tau\mathfrak{e}_0 + \sum\nolimits_{i=1}^{n} y_i \mathfrak{e}_i,$$

with the spatial coordinates $x_i := \langle \mathbf{x}, \mathfrak{e}_i \rangle$ and $y_i := \langle \mathbf{y}, \mathfrak{e}_i \rangle$ for $i = 1, \ldots, n$. All time coordinates are defined as geometrized time, see [78, Section 1.5] or [80, p. 3].

DEFINITION 2.1 (Geometrized time coordinate). *Let the physical dimensions length and time be denoted by* L *and* T*, respectively. Let* $c > 0$ *be a given (wave) velocity with dimension* LT^{-1} *and* t^* *be an ordinary time with dimension* T*. The corresponding geometrized time coordinate is defined by* t^*c *and is of dimension* L*. Conversely, for given geometrized time* t *the corresponding ordinary time is* t/c*.*

Note that in terms of geometrized time coordinates, velocities possess physical dimension one and unit velocity corresponds to wave velocity. We introduce the bilinear form $[\cdot, \cdot] : \mathbb{R}^{n+1} \times \mathbb{R}^{n+1} \to \mathbb{R}$ by

$$[\cdot, \cdot] : (\mathbf{x}, \mathbf{y}) \mapsto \langle x, y \rangle - t\tau.$$

Although $[\cdot,\cdot]$ is known as Lorentzian inner product (or Minkowski inner product), it is not positive definite, but rather a nondegenerate bilinear form of index 1, see [80, Section 1.1]. Define the linear map $M : \mathbb{R}^{n+1} \to \mathbb{R}^{n+1}$ by its action on the basis

$$M : \mathfrak{e}_i \mapsto \begin{cases} -\mathfrak{e}_i & \text{if } i = 0, \\ \mathfrak{e}_i & \text{if } i = 1, \dots, n, \end{cases}$$

and observe that M is a symmetric involution $M = M^\top = M^{-1}$. It is evident that $[\mathfrak{e}_i, \mathfrak{e}_j] = \langle M\mathfrak{e}_i, \mathfrak{e}_j \rangle$ holds for $i, j = 0, \dots, n$ and with respect to the basis M is identified with the metric tensor $\operatorname{diag}(-1, 1, 1, \dots, 1) \in \mathbb{R}^{(n+1)\times(n+1)}$.

Definition 2.2 (Light cone). *Let $n \in \mathbb{N}$ and $\mathbf{x} \in \mathbb{R}^{n+1}$ be given. The set $\{\mathbf{y} \in \mathbb{R}^{n+1} : [\mathbf{x} - \mathbf{y}, \mathbf{x} - \mathbf{y}] = 0\}$ is an n-dimensional conical hypersurface with apex at $\mathbf{x}$, which is denoted double light cone. It is the union of the forward light cone*

$$\Upsilon(\mathbf{x}) := \{\mathbf{y} \in \mathbb{R}^{n+1} : [\mathbf{x} - \mathbf{y}, \mathbf{x} - \mathbf{y}] = 0 \quad \wedge \quad t - \tau \leq 0\}$$

and the backward light cone

$$\Xi(\mathbf{x}) := \{\mathbf{y} \in \mathbb{R}^{n+1} : [\mathbf{x} - \mathbf{y}, \mathbf{x} - \mathbf{y}] = 0 \quad \wedge \quad t - \tau \geq 0\}.$$

Moreover, a vector $v \in \mathbb{R}^{n+1}$ is classified via

$$\begin{aligned} [v,v] < 0 \quad &\Leftrightarrow \quad v \textit{ is timelike}, \\ [v,v] = 0 \quad &\Leftrightarrow \quad v \textit{ is lightlike}, \\ [v,v] > 0 \quad &\Leftrightarrow \quad v \textit{ is spacelike}. \end{aligned}$$

For $n = 2$, i.e., three-dimensional space-time, the light cone is sketched in Figure 2.1 and its significance is elaborated especially in Section 2.6. The backward light cone $\Xi(\mathbf{x})$ can be defined equivalently as the zero level set $\Xi(\mathbf{x}) = \{\mathbf{y} \in \mathbb{R}^4 : \phi_\Xi(\mathbf{x} - \mathbf{y}) = 0\}$ of the (Lipschitz continuous) function $\phi_\Xi : \mathbb{R}^{n+1} \to \mathbb{R}$ given by

$$\phi_\Xi : \mathbf{x} \mapsto \|x\| - t, \quad \nabla\phi_\Xi : \mathbf{x} \mapsto \begin{pmatrix} \partial_t \phi_\Xi(\mathbf{x}) \\ \nabla_x \phi_\Xi(\mathbf{x}) \end{pmatrix} = \begin{pmatrix} -1 \\ x / \|x\| \end{pmatrix}.$$

In the employed notation, ∂_t denotes the time derivative, while ∇_x denotes the gradient with respect to the spatial component.

Let $\Omega^- \subset \mathbb{R}^n$ be a bounded open domain whose complement $\Omega^+ := \mathbb{R}^n \setminus \overline{\Omega^-}$ is the exterior domain. Their union is denoted $\Omega := \Omega^- \cup \Omega^+$. The Lipschitz boundary $\Gamma := \partial\Omega^-$ is equipped with the unit outward normal vector field $\nu_\Gamma : \Gamma \to \mathbb{S}^{n-1}$, which points towards Ω^+. Let $\mathfrak{d} \in \{-,+\}$ and $\operatorname{dist}_\Gamma : \mathbb{R}^n \to \mathbb{R}$ be the signed distance function defined by $\operatorname{dist}_\Gamma : x \mapsto \mathfrak{d} \inf_{y \in \Gamma} \|x - y\|$ for $x \in \Omega^{\mathfrak{d}}$. This configuration is sketched in Figure 2.2. The physical processes are observed in some finite time

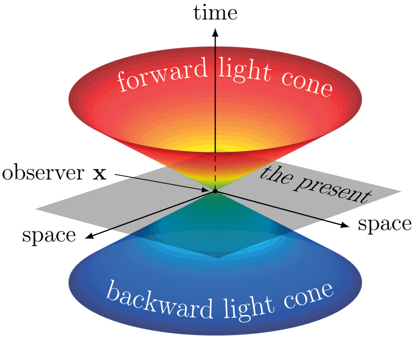

Figure 2.1: Light cone in 2+1 dimensions; the forward light cone $\Upsilon(\mathbf{x})$ is the set of points that perceive a lightlike signal sent out at $\mathbf{x}$. Conversely, the observer at $\mathbf{x}$ perceives lightlike signals only sent out on the backward light cone $\Xi(\mathbf{x})$. This bestows an intuitive interpretation upon the integral formulas of retarded potentials in Section 2.6, which integrate along subsets of $\Xi(\mathbf{x})$.

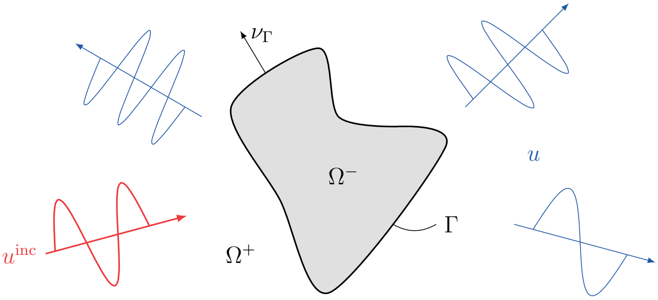

Figure 2.2: Interior and exterior domain with interface Γ, outward normal vector field ν_Γ, and incoming as well as scattered wave fields, see Remark 2.11.

interval $(0, T)$, where $T > 0$ is the simulation end time. Define the space-time cylinders $Q^{\mathfrak{d}} := (0,T) \times \Omega^{\mathfrak{d}}$ and $Q := (0,T) \times \Omega$ with lateral boundary $\Sigma := (0,T) \times \Gamma$. Since Γ is stationary, the signed distance function $\operatorname{dist}_\Sigma : [0,T] \times \mathbb{R}^n \to \mathbb{R}$ simplifies to $\operatorname{dist}_\Sigma : \mathbf{x} \mapsto \operatorname{dist}_\Gamma(x)$. Moreover, the normal vector field $\nu_\Sigma : \Sigma \to \mathbb{S}^n$

$$\nu_\Sigma : \mathbf{x} \mapsto \begin{pmatrix} \nu_{\Sigma,t}(\mathbf{x}) \\ \nu_{\Sigma,x}(\mathbf{x}) \end{pmatrix} = \begin{pmatrix} 0 \\ \nu_\Gamma(x) \end{pmatrix}$$

has vanishing time component. We denote by $C\left(Q^{\mathfrak{d}}\right)$ the space of continuous functions in $Q^{\mathfrak{d}}$ and by $C^k\left(Q^{\mathfrak{d}}\right)$ the space of $k \in \mathbb{N} \cup \{\infty\}$ times continuously differentiable functions in $Q^{\mathfrak{d}}$. Since the focus of this thesis lies on BIEs, we are particularly interested in a thorough description of the hypersurface Σ. We shall impose further assumptions on its smoothness, such that Σ is well apt for the discretization process of Chapter 3. Define the n-dimensional reference simplex

$$\widehat{\sigma}_n := \{\xi \in \mathbb{R}^n : 0 < \xi_1 < 1 \quad \wedge \quad 0 < \xi_i < \xi_{i-1} \ \forall i = 2, \ldots, n\} \subset \mathbb{R}^n. \tag{2.1}$$

For elegance of notation the exposition thus far covered an arbitrary number of spatial dimensions $n \in \mathbb{N}$. However, this thesis solely treats the case $n = 3$, i.e., four-dimensional space-time. In this case, Σ is a three-dimensional hypersurface and we abbreviate the corresponding reference simplex $\widehat{\sigma} := \widehat{\sigma}_3$. The following definitions are adapted from [100, Definitions 2.2.9 and 2.2.10].

DEFINITION 2.3 (Panel). *For $k \in \mathbb{N} \cup \{\infty\}$ an open subset $\sigma \subset \Sigma$ is denoted C^k-panel if there exists a C^k-diffeomorphism $\chi_\sigma : \widehat{\sigma} \to \sigma$ which can be extended to a C^k-diffeomorphism defined in a neighborhood of $\overline{\widehat{\sigma}}$ whose range contains $\overline{\sigma}$.*

Note that $\chi_\sigma : \widehat{\sigma} \to \sigma$ is denoted C^k-diffeomorphism if it is a bijection and χ_σ as well as χ_σ^{-1} are k times continuously differentiable.

DEFINITION 2.4 (Mesh). *The set $\Sigma_N := \{\sigma_i\}_{i=1}^N$ with $|\Sigma_N| = N \in \mathbb{N}$ is*

(i) denoted C^k-mesh if every $\sigma \in \Sigma_N$ is a C^k-panel and $\overline{\Sigma} = \bigcup_{\sigma \in \Sigma_N} \overline{\sigma}$ holds with $\sigma_A \cap \sigma_B = \varnothing$ for nonidentical $\sigma_A, \sigma_B \in \Sigma_N$,

(ii) denoted devoid of hanging nodes if every $\overline{\sigma_A} \cap \overline{\sigma_B}$ of nonidentical $\sigma_A, \sigma_B \in \Sigma_N$ is either empty, a common vertex, a common edge or a common face.

ASSUMPTION 2.5. *Σ is a Lipschitz boundary such that a C^1-mesh Σ_N exists for some $N \in \mathbb{N}$. For any $\sigma \in \Sigma_N$ the map χ_σ coincides with the Lipschitz boundary parametrizations restricted to $\widehat{\sigma}$, see [100, Definition 2.2.10].*

Assumption 2.5 is presumed to hold true throughout the remainder of this thesis. Although the approximation method discussed in Chapter 3 employs C^∞-meshes, the existence of a C^1-mesh suffices for the derivations of this chapter. We introduce the Jacobi matrix as representation of the derivative $\mathrm{D}\,\chi_\sigma$ at $\xi \in \widehat{\sigma}$

$$\mathrm{D}\,\chi_\sigma : \xi \mapsto J_\sigma(\xi) \coloneqq \begin{pmatrix} \partial_1\chi_\sigma(\xi) & \partial_2\chi_\sigma(\xi) & \partial_3\chi_\sigma(\xi) \end{pmatrix} \in \mathbb{R}^{4\times 3}.$$

It holds $\operatorname{rank} J_\sigma(\xi) = 3$ at any $\xi \in \widehat{\sigma}$ because χ_σ is a diffeomorphism. The columns of $J_\sigma(\xi)$ correspond to three linearly independent tangent vectors of Σ at $\chi_\sigma(\xi)$. Therefore, the range of the operator $J_\sigma(\xi) : \mathbb{R}^3 \to \mathbb{R}^4$

$$\operatorname{ran} J_\sigma(\xi) \coloneqq \{J_\sigma(\xi)v : v \in \mathbb{R}^3\}$$

is the three-dimensional tangent space of Σ at $\chi_\sigma(\xi)$. The one-dimensional kernel of $J_\sigma^\top(\xi)$ is spanned by the normal vector

$$\ker J_\sigma^\top(\xi) \coloneqq \{v \in \mathbb{R}^4 : J_\sigma^\top(\xi)v = 0\} = \operatorname{span}\{\nu_\Sigma \circ \chi_\sigma(\xi)\}.$$

Define the Gramian matrix $G_\sigma(\xi) \in \mathbb{R}^{3\times 3}$ at $\xi \in \widehat{\sigma}$ whose entries are the inner products of the tangent vectors

$$\big[G_\sigma(\xi)\big]_{ij} \coloneqq \big\langle \partial_i\chi_\sigma(\xi), \partial_j\chi_\sigma(\xi)\big\rangle\,, \quad i,j = 1,2,3.$$

This matrix contains the covariant components of the first fundamental form of Σ at $\chi_\sigma(\xi)$. From the linear independence of the tangent vectors it follows that $G_\sigma(\xi)$ is symmetric positive definite. The Gramian determinant $\left|\det \mathrm{D}\,\chi_\sigma\right| : \widehat{\sigma} \to (0,\infty)$ given by $\left|\det \mathrm{D}\,\chi_\sigma\right| : \xi \mapsto \sqrt{\det G_\sigma(\xi)}$ facilitates the transformation of differential (surface) elements. The parametrizations of Σ_N enable a natural treatment of integrals along the hypersurface Σ by pulling them back to the simplex $\widehat{\sigma}$. If $f : \Sigma \to \mathbb{R}$ is integrable it holds

$$\int_\Sigma f \,\mathrm{d}S = \sum\nolimits_{\sigma\in\Sigma_N} \int_{\widehat{\sigma}} f \circ \chi_\sigma \left|\det \mathrm{D}\,\chi_\sigma\right| \mathrm{d}\xi \tag{2.2}$$

and we define the surface measure of a panel by $|\sigma| \coloneqq \int_\sigma \mathrm{d}S = \int_{\widehat{\sigma}} \left|\det \mathrm{D}\,\chi_\sigma\right| \mathrm{d}\xi$.

2.2 Wave Equation in 3+1 Dimensions

Consider a (sufficiently smooth) function u defined in $Q^\mathfrak{d}$ subject to the d'Alembertian

$$\Box u \coloneqq \partial_t^2 u - \Delta_x u = -\operatorname{div} M\nabla u,$$

where $\Delta_x \coloneqq \operatorname{div}_x \nabla_x$ denotes the Laplacian with respect to the spatial component.

Remark 2.6. *The d'Alembertian governs a host of physical problems. In linear acoustics, $u : Q^\mathfrak{d} \to \mathbb{R}$ represents the sound pressure field and $\Box u = 0$ describes conservation laws of mass and linear momentum. In electrodynamics, $u : Q^\mathfrak{d} \to \mathbb{R}^4$ describes the electromagnetic four-potential. In this context $\Box u = 0$, applied to the components of u and supplemented by the Lorenz gauge condition* $\operatorname{div} u = 0$, *satisfies Maxwell's equations with vanishing four-current, see, e.g., [50, Section 10.1].*

We employ the notation of Dirichlet and Neumann traces $\gamma_0^{\mathfrak{d}}$ and $\gamma_1^{\mathfrak{d}}$, see [76] and [100, Sections 2.6 and 2.7]. For $w \in C\left((0,T) \times (\Omega^{\mathfrak{d}} \cup \Gamma)\right)$ and $v \in C^1\left((0,T) \times (\Omega^{\mathfrak{d}} \cup \Gamma)\right)$ they coincide with the usual restriction to Σ and normal derivative

$$\gamma_0^{\mathfrak{d}} : w \mapsto w|_{\Sigma}, \quad \gamma_1^{\mathfrak{d}} : v \mapsto \left\langle \nu_\Gamma, \gamma_0^{\mathfrak{d}} \nabla_x v \right\rangle .$$

The following relation between the signed distance function $\operatorname{dist}_\Sigma$ and the normal vector field ν_Σ is discussed in, e.g., [28, Sections 2.1 and 2.2]

$$\gamma_0 \nabla \operatorname{dist}_\Sigma \coloneqq \gamma_0^+ \nabla \operatorname{dist}_\Sigma = \gamma_0^- \nabla \operatorname{dist}_\Sigma = \nu_\Sigma. \tag{2.3}$$

For sufficiently smooth $w, v : Q \to \mathbb{R}$ we introduce the jump and averages across the interface Γ by

$$\begin{aligned} [\![\gamma_0 w]\!]_\Gamma &\coloneqq \gamma_0^+ w - \gamma_0^- w, & \{\!\{\gamma_0 w\}\!\}_\Gamma &\coloneqq \tfrac{1}{2}(\gamma_0^+ w + \gamma_0^- w), \\ [\![\gamma_1 v]\!]_\Gamma &\coloneqq \gamma_1^+ v - \gamma_1^- v, & \{\!\{\gamma_1 v\}\!\}_\Gamma &\coloneqq \tfrac{1}{2}(\gamma_1^+ v + \gamma_1^- v). \end{aligned}$$

Define the energy $\mathbb{E}u : (0,T) \to [0,\infty)$ of wave field $u : Q \to \mathbb{R}$ by

$$\begin{aligned} \mathbb{E}u\,(t) &\coloneqq \frac{1}{2} \int_\Omega \left(|\partial_t u(\mathbf{x})|^2 + \|\nabla_x u(\mathbf{x})\|^2 \right) \mathrm{d}x \\ &= \frac{1}{2} \left(\int_{\Omega^+} \|\nabla u(\mathbf{x})\|^2 \, \mathrm{d}x + \int_{\Omega^-} \|\nabla u(\mathbf{x})\|^2 \, \mathrm{d}x \right), \end{aligned}$$

which can be loosely interpreted as the sum of kinetic and potential energy. If $u : Q \to \mathbb{R}$ is twice differentiable it holds

$$\Box u \partial_t u = \left(\partial_t^2 u - \Delta_x u \right) \partial_t u = \partial_t \frac{1}{2} \left(|\partial_t u|^2 + \|\nabla_x u\|^2 \right) - \operatorname{div}_x \left(\partial_t u \nabla_x u \right). \tag{2.4}$$

Prior to stating the considered problems, we shall explore crucial properties of solutions of the d'Alembertian in a classical mathematical setting.

THEOREM 2.7 (Finite speed propagation). *For $t \in [0,T]$ define $D(t) \subseteq \Omega^-$ by $D(t) \coloneqq \{x \in \Omega^- : t - |\operatorname{dist}_\Gamma(x)| < 0\}$. Let $u \in C^2\left((0,T) \times \Omega^-\right) \cap C^1\left([0,T] \times \overline{\Omega^-}\right)$ satisfy $\Box u = 0$. It holds*

$$\left(u = 0 \quad \wedge \quad \partial_t u = 0 \ \mathit{on}\ \{0\} \times \Omega^- \right) \quad \Rightarrow \quad u = 0 \ \mathit{in}\ \{\mathbf{x} \in \mathbb{R}^4 : t \in [0,T), x \in D(t)\}.$$

Proof. The proof is done analogously to [31, Theorem 6 of Section 2.4]. For $t \in [0,T)$ define the energy in $D(t)$ by $E(t) \coloneqq \frac{1}{2} \int_{D(t)} \|\nabla u(\mathbf{x})\|^2 \, \mathrm{d}x$. The Reynolds transport theorem yields

$$\frac{\mathrm{d}}{\mathrm{d}t} E(t) = \frac{1}{2} \int_{D(t)} \partial_t \|\nabla u(\mathbf{x})\|^2 \, \mathrm{d}x + \frac{1}{2} \int_{\partial D(t)} v_\nu(\mathbf{x}) \|\nabla u(\mathbf{x})\|^2 \, \mathrm{d}S(x),$$

where $v_\nu(\mathbf{x})$ denotes the normal velocity at $x \in \partial D(t)$. With the aid of the level set function $\phi : [0,T] \times \Omega^- \to \mathbb{R}$ defined by $\phi : \mathbf{x} \mapsto t - |\operatorname{dist}_\Gamma(x)|$ we obtain

$$v_\nu(\mathbf{x}) = -\frac{\partial_t \phi(\mathbf{x})}{\|\nabla_x \phi(\mathbf{x})\|} = -\frac{1}{\|\nabla_x \operatorname{dist}_\Gamma(x)\|} = -1$$

for almost any $x \in \partial D(t)$, where the last equality is due to [25, Theorem 5.1.(iii)]. From (2.4) and $\Box u = 0$ it follows that $\partial_t \|\nabla u\|^2 = 2 \operatorname{div}_x (\partial_t u \nabla_x u)$ holds, leading to

$$\begin{aligned}\frac{\mathrm{d}}{\mathrm{d}t} E(t) &= \int_{D(t)} \operatorname{div}_x (\partial_t u(\mathbf{x}) \nabla_x u(\mathbf{x}))\, \mathrm{d}x - \frac{1}{2} \int_{\partial D(t)} \|\nabla u(\mathbf{x})\|^2\, \mathrm{d}S(x) \\ &= \int_{\partial D(t)} \left(\langle \nu_{\partial D(t)}(\mathbf{x}), \nabla_x u(\mathbf{x}) \rangle\, \partial_t u(\mathbf{x}) - \frac{1}{2} \|\nabla u(\mathbf{x})\|^2 \right) \mathrm{d}S(x),\end{aligned}$$

where we used the divergence theorem, see, e.g., [76, Theorem 3.34] and $\nu_{\partial D(t)}$ denotes the unit outward normal vector field of $\partial D(t)$. The Cauchy-Schwarz inequality yields

$$\begin{aligned}\frac{\mathrm{d}}{\mathrm{d}t} E(t) &\leq \int_{\partial D(t)} \left(\|\nabla_x u(\mathbf{x})\|\, |\partial_t u(\mathbf{x})| - \frac{1}{2} \|\nabla u(\mathbf{x})\|^2 \right) \mathrm{d}S(x) \\ &\leq \frac{1}{2} \int_{\partial D(t)} \left(\|\nabla_x u(\mathbf{x})\|^2 + |\partial_t u(\mathbf{x})|^2 - \|\nabla u(\mathbf{x})\|^2 \right) \mathrm{d}S(x) = 0.\end{aligned}$$

This implies $0 \leq E(t) \leq E(0) = 0$ for $t \in (0,T)$ due to the homogeneous initial conditions. From $E(t) = 0$ for any $t \in [0,T)$ it follows that $\nabla u = 0$ holds in $\{\mathbf{x} \in \mathbb{R}^4 : t \in [0,T), x \in D(t)\}$ and the initial conditions yield the assertion. ☐

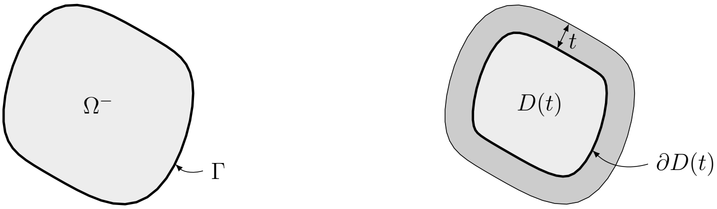

Figure 2.3: Illustration of Theorem 2.7; it is assumed that $u(0,\cdot) = 0$ and $\partial_t u(0,\cdot) = 0$ hold in Ω^-. It follows that $u(t,\cdot)$ vanishes for $t \in [0,T)$ in the domain $D(t)$, whose boundary $\partial D(t)$ is the propagating wave front.

Theorem 2.7 shows that solutions of the d'Alembertian propagate information at finite velocity, which is fixed to 1 due to Definition 2.1. If u is homogeneous on $\{0\} \times \Omega^-$, then points $x \in \Omega^-$ satisfying $|\operatorname{dist}_\Gamma(x)| > t$ have not yet received signals sent out in the exterior domain at $t = 0$. It follows that $u(\mathbf{x}) = 0$ holds for all points sufficiently far away from from the boundary, i.e., $|\operatorname{dist}_\Gamma(x)| > t$, see Figure 2.3.

THEOREM 2.8 (Energy-flux relation). *Let* $u : Q \to \mathbb{R}$ *have bounded support and be such that* $u|_{Q^{\mathfrak{d}}} \in C^2\left(Q^{\mathfrak{d}}\right) \cap C^1\left([0,T] \times (\Omega^{\mathfrak{d}} \cup \Gamma)\right)$ *and* $\Box u|_{Q^{\mathfrak{d}}} = 0$ *hold for* $\mathfrak{d} \in \{+,-\}$. *For* $t \in (0,T)$ *it follows*

$$\frac{\mathrm{d}}{\mathrm{d}t}\mathbb{E}u\,(t) = -\int_\Gamma \left(\{\!\!\{\gamma_1 u(\mathbf{x})\}\!\!\}_\Gamma \llbracket \gamma_0 \partial_t u(\mathbf{x}) \rrbracket_\Gamma + \llbracket \gamma_1 u(\mathbf{x}) \rrbracket_\Gamma \{\!\!\{\gamma_0 \partial_t u(\mathbf{x})\}\!\!\}_\Gamma\right) \mathrm{d}S(x).$$

Proof. Integrating (2.4) over $\{t\} \times \Omega^{\mathfrak{d}}$ in conjunction with $\Box u = 0$ yields

$$0 = \frac{1}{2}\int_{\Omega^{\mathfrak{d}}} \partial_t \left(\left|\partial_t u(\mathbf{x})\right|^2 + \left\|\nabla_x u(\mathbf{x})\right\|^2\right) \mathrm{d}x - \int_{\Omega^{\mathfrak{d}}} \operatorname{div}_x \left(\partial_t u(\mathbf{x}) \nabla_x u(\mathbf{x})\right) \mathrm{d}x.$$

In above formula u should be understood as its restriction to the domain $Q^{\mathfrak{d}}$. By changing the order of integration and differentiation in the first term we obtain

$$\frac{\mathrm{d}}{\mathrm{d}t}\mathbb{E}u|_{Q^{\mathfrak{d}}}\,(t) = \int_{\Omega^{\mathfrak{d}}} \operatorname{div}_x \left(\partial_t u(\mathbf{x}) \nabla_x u(\mathbf{x})\right) \mathrm{d}x = -\mathfrak{d}\int_\Gamma \gamma_1^{\mathfrak{d}} u(\mathbf{x}) \gamma_0^{\mathfrak{d}} \partial_t u(\mathbf{x}) \mathrm{d}S(x),$$

where the last equality is due to the divergence theorem, see, e.g., [76, Theorem 3.34]. Thereby we require that $u(t,\cdot)$ has bounded support in Ω^+ for any $t \in (0,T)$. Summation of the exterior and interior domain leads to

$$\frac{\mathrm{d}}{\mathrm{d}t}\mathbb{E}u\,(t) = -\int_\Gamma \left(\gamma_1^+ u(\mathbf{x}) \gamma_0^+ \partial_t u(\mathbf{x}) - \gamma_1^- u(\mathbf{x}) \gamma_0^- \partial_t u(\mathbf{x})\right) \mathrm{d}S(x)$$

and the assertion is due to the equality

$$\gamma_1^+ v \gamma_0^+ \partial_t w - \gamma_1^- v \gamma_0^- \partial_t w = \{\!\!\{\gamma_1 v\}\!\!\}_\Gamma \llbracket \gamma_0 \partial_t w \rrbracket_\Gamma + \llbracket \gamma_1 v \rrbracket_\Gamma \{\!\!\{\gamma_0 \partial_t w\}\!\!\}_\Gamma\,,$$

where $w, v : Q \to \mathbb{R}$ are as smooth as u, see [58, Proof of Lemma 2.1]. $\Box$

By setting $u = 0$ in either Q^+ or Q^- we can provide one-sided versions of Theorem 2.8 for $u : Q^{\mathfrak{d}} \to \mathbb{R}$

$$\frac{\mathrm{d}}{\mathrm{d}t}\mathbb{E}u\,(t) = -\mathfrak{d}\int_\Gamma \gamma_1^{\mathfrak{d}} u(\mathbf{x}) \gamma_0^{\mathfrak{d}} \partial_t u(\mathbf{x}) \mathrm{d}S(x). \tag{2.5}$$

A well-known result in electrodynamics which corresponds to Theorem 2.8 is Poynting's theorem, see, e.g., [50, Section 8.1.2]. Finally, the key ingredient to boundary integral formulations is the so-called fundamental solution. The fundamental solution $\mathcal{G}$ of the d'Alembertian is the distributional solution of $\Box\mathcal{G} = \delta_0$, where δ_0 is the Dirac delta distribution. Its existence is due to the Malgrange-Ehrenpreis theorem, see, e.g., [84, Section 2.2]. The forward (causal) fundamental solution of the d'Alembertian in three spatial dimensions reads [83, Operator 51]

$$\mathcal{G} : \mathbf{x} \mapsto \frac{\delta_0(t - \|x\|)}{4\pi\,\|x\|} = \frac{\delta_0 \circ \phi_\Xi(\mathbf{x})}{4\pi\,\|x\|}, \tag{2.6}$$

with the level set function ϕ_Ξ as in Section 2.1. Note that the equality in (2.6) holds due to $\delta_0(t) = \delta_0(-t)$ for $t \in \mathbb{R}$.

Remark 2.9 (Huygens principle). *The solution (2.6) is (singularly) supported on the zero level set of ϕ_Ξ, which is the forward light cone $\Upsilon(0)$. In contrast, the forward fundamental solutions of the d'Alembertian in one and two spatial dimensions read*

$$\mathcal{G}_{n=1} : \mathbf{x} \mapsto \frac{1}{2}\theta(t - |x|), \quad \mathcal{G}_{n=2} : \mathbf{x} \mapsto \frac{1}{2\pi}\frac{\theta(t - \|x\|)}{\sqrt{t^2 - \|x\|^2}},$$

where $\theta : \mathbb{R} \to \{0, 1\}$ denotes the Heaviside step function, see [83, Operators 47 and 49]. These solutions are supported in $\{\mathbf{x} \in \mathbb{R}^{n+1} : t \geq \|x\|\}$, which is the interior of $\Upsilon(0)$. We investigate the implications of this disparity via an example. Let $\mathcal{G}_n, n = 1, 2, 3$ be the fundamental solution of the d'Alembertian in n spatial dimensions. For $f \in C(\mathbb{R})$ with $\operatorname{supp} f \subset [0, T]$ let F be defined in $\mathbb{R}^{n+1}$ via $\mathbf{y} \mapsto f(\tau)\delta_0(y)$. Consider the function u_n defined in $\mathbb{R}^{n+1}$ by the formal convolution

$$\begin{aligned} u_n : \mathbf{x} \mapsto & \int_{\mathbb{R}^{n+1}} \mathcal{G}_n(\mathbf{x} - \mathbf{y}) F(\mathbf{y}) \mathrm{d}\mathbf{y} \\ & = \int_{\mathbb{R}^n} \delta_0(y) \int_{\mathbb{R}} \mathcal{G}_n(\mathbf{x} - \mathbf{y}) f(\tau) \mathrm{d}\tau \mathrm{d}y = \int_0^T \mathcal{G}_n\left(\begin{pmatrix} t - \tau \\ x \end{pmatrix}\right) f(\tau) \mathrm{d}\tau, \end{aligned}$$

where we used used the sifting property of δ_0. The function u_n satisfies $\Box u_n(\mathbf{x}) = 0$ for $x \neq 0$ by construction. It describes the wave field due to a point source located at the spatial origin which emits the signal f. The explicit formulas for $\mathcal{G}_n$ lead to

$$\begin{aligned} & u_1 : \mathbf{x} \mapsto \frac{1}{2}\int_0^{t-|x|} f(\tau)\mathrm{d}\tau, \quad u_2 : \mathbf{x} \mapsto \frac{1}{2\pi}\int_0^{t-\|x\|} \frac{f(\tau)}{\sqrt{(t-\tau)^2 - \|x\|^2}}\mathrm{d}\tau, \\ & u_3 : \mathbf{x} \mapsto \frac{f(t - \|x\|)}{4\pi\|x\|}. \end{aligned}$$

While u_1 and u_2 depend on the entire history of f up to $t - \|x\|$, the field u_3 depends only on f at exactly $t - \|x\|$. The retarded time $t - \|x\|$ accounts for the distance the signal has to travel in order to reach x, resulting in delay, see also Remark 2.14. Roughly speaking, for $n \leq 2$ the observer perceives a blend of the information emitted by f up to time $t - \|x\|$. For $n = 3$, however, the observer receives exactly the emitted signal f; it is merely delayed and has weaker amplitude due to the traveled distance $\|x\|$. The fact that u_3 depends only on the retarded time is a manifestation of the strong Huygens principle, which does not hold in the lower-dimensional cases, see [59]. For the d'Alembertian in $n \in \mathbb{N}$ spatial dimensions the Huygens principle holds iff n is odd and $n \geq 3$ holds, see [59] and [84, Equations (1.6.26) and (1.6.27)].

2.3 Initial-Boundary Value Problems

We consider problems in which the excitation, or inhomogeneity, is due to sources on the boundary. The field $u : Q^{\mathfrak{d}} \to \mathbb{R}$ is subject to the homogeneous wave equation

$$\begin{aligned} \Box u &= 0 \quad \text{in } Q^{\mathfrak{d}}, \\ u &= 0 \quad \text{on } \{0\} \times \Omega^{\mathfrak{d}}, \\ \partial_t u &= 0 \quad \text{on } \{0\} \times \Omega^{\mathfrak{d}}. \end{aligned} \tag{2.7}$$

In order to state uniquely solvable problems, (2.7) is to be complemented by suitable boundary conditions. Given Dirichlet and Neumann data $g_D, g_N : \Sigma \to \mathbb{R}$, the solution is either subject to

$$\gamma_0^{\mathfrak{d}} u = g_D \quad \text{on } \Sigma, \tag{2.8}$$

or

$$\gamma_1^{\mathfrak{d}} u = g_N \quad \text{on } \Sigma. \tag{2.9}$$

Conditions (2.7) and (2.8) define the so-called Dirichlet initial-boundary value problem, while (2.7) and (2.9) state the Neumann initial-boundary value problem in $Q^{\mathfrak{d}}$.

Lemma 2.10. *Let* $u \in C^2\left(Q^{\mathfrak{d}}\right) \cap C^1\left([0,T] \times \left(\Omega^{\mathfrak{d}} \cup \Gamma\right)\right)$ *satisfy* (2.7). *From either* $\gamma_0^{\mathfrak{d}} u = 0$ *or* $\gamma_1^{\mathfrak{d}} u = 0$ *it follows* $u = 0$ *in* $Q^{\mathfrak{d}}$.

Proof. From Theorem 2.7 it follows that u has bounded support. Equation (2.5), which is derived from Theorem 2.8, yields in conjunction with either $\gamma_0^{\mathfrak{d}} u = 0$ or $\gamma_1^{\mathfrak{d}} u = 0$

$$\frac{\mathrm{d}}{\mathrm{d}t} \mathbb{E}u\,(t) = -\mathfrak{d} \int_\Gamma \gamma_1^{\mathfrak{d}} u(\mathbf{x}) \partial_t \gamma_0^{\mathfrak{d}} u(\mathbf{x}) \mathrm{d}S(x) = 0,$$

where we recall that time is a tangential derivative on Σ. Moreover, $u = 0$ and $\partial_t u = 0$ on $\{0\} \times \Omega^{\mathfrak{d}}$ imply that

$$\mathbb{E}u\,(0) = \frac{1}{2} \int_{\Omega^{\mathfrak{d}}} \left(|\partial_t u(0,x)|^2 + \|\nabla_x u(0,x)\|^2 \right) \mathrm{d}x = 0$$

because ∇_x is a tangential derivative on $\{0\} \times \Omega^{\mathfrak{d}}$. It follows $\mathbb{E}u\,(t) = \mathbb{E}u\,(0) = 0$ for any $t \in (0,T)$. This implies $\nabla u = 0$ in $Q^{\mathfrak{d}}$ and from $u = 0$ on $\{0\} \times \Omega^{\mathfrak{d}}$ it follows $u = 0$ in $Q^{\mathfrak{d}}$. $\Box$

The linearity of all operators in (2.7)–(2.9) in conjunction with Lemma 2.10 implies that there exists at most one sufficiently smooth solution of the Dirichlet and Neumann initial-boundary value problems.

Remark 2.11 (Scattering problems). *For* $\mathfrak{d} = +$ *the Dirichlet and Neumann boundary value problems of* (2.7) *describe so-called scattering problems. In these problems, the excitation is due to an incoming wave field* $u^{\mathrm{inc}} : Q^+ \to \mathbb{R}$ *such that both* $u^{\mathrm{inc}} = 0$ *and* $\partial_t u^{\mathrm{inc}} = 0$ *hold on* $\{0\} \times \Gamma$. *The scattered wave field* u *satisfies* (2.7). *Assume that the total wave field* $u^{\mathrm{tot}} := u^{\mathrm{inc}} + u$ *satisfies either* $\gamma_0^+ u^{\mathrm{tot}} = 0$ *or* $\gamma_1^+ u^{\mathrm{tot}} = 0$. *By linearity, we obtain either the Dirichlet problem* (2.8) *with* $g_D := -\gamma_0^+ u^{\mathrm{inc}}$ *or the Neumann problem* (2.9) *with* $g_N := -\gamma_1^+ u^{\mathrm{inc}}$. *Since scattering problems are posed on the unbounded exterior domain, their reformulation in terms of BIEs is a particularly elegant approach.*

In Section 2.4, we shall employ potentials which satisfy (2.7) by construction. Consequently, the initial-boundary value problems are reduced to finding a suitable input to the potentials such that either (2.8) or (2.9) is satisfied. These potentials are explained properly via transmission problems of the d'Alembertian. For $u : Q \to \mathbb{R}$ and surface densities $w, v : \Sigma \to \mathbb{R}$ we consider the transmission problems

$$\begin{aligned} \Box u &= 0 && \text{in } Q, \\ u &= 0 && \text{on } \{0\} \times \Omega, \\ \partial_t u &= 0 && \text{on } \{0\} \times \Omega, \\ [\![\gamma_0 u]\!]_\Gamma &= 0 && \text{on } \Sigma, \\ [\![\gamma_1 u]\!]_\Gamma &= -w && \text{on } \Sigma, \end{aligned} \tag{2.10}$$

and

$$\begin{aligned} \Box u &= 0 && \text{in } Q, \\ u &= 0 && \text{on } \{0\} \times \Omega, \\ \partial_t u &= 0 && \text{on } \{0\} \times \Omega, \\ [\![\gamma_0 u]\!]_\Gamma &= v && \text{on } \Sigma, \\ [\![\gamma_1 u]\!]_\Gamma &= 0 && \text{on } \Sigma. \end{aligned} \tag{2.11}$$

Given that u is sufficiently smooth, one can prove that $w = 0$ in (2.10) or $v = 0$ in (2.11) imply that $u = 0$ holds in Q, similar to Lemma 2.10. This implies the uniqueness of sufficiently smooth solutions of (2.10) and (2.11). Investigations regarding the solvability of the wave equation in functional settings that fit the numerical method in Chapter 3 better, can be found in, e.g., [10, 104, 58].

2.4 Retarded Layer Potentials and Integral Equations

This section is dedicated to the introduction of retarded layer potentials and related BIEs. The exposition is adapted immediately from the book of Sayas [104], with the notational difference that our definition of $[\![\cdot]\!]_\Gamma$ features the opposite sign. For admissible $w, v : \Sigma \to \mathbb{R}$ the retarded single layer potential S and retarded double layer potential D are the solution operators

$$\begin{aligned} \mathrm{S} : w &\mapsto u \text{ satisfying (2.10)}, \\ \mathrm{D} : v &\mapsto u \text{ satisfying (2.11)}. \end{aligned}$$

The striking name retarded potential is evident once the integral representations of S and D are discussed, see Section 2.6 and Remark 2.14. Summation of (2.10) and (2.11), in conjunction with the linearity of all involved operators, yields the following observation. If an admissible $u : Q \to \mathbb{R}$ satisfies

$$\begin{aligned} \Box u &= 0 \quad \text{in } Q, \\ u &= 0 \quad \text{on } \{0\} \times \Omega, \\ \partial_t u &= 0 \quad \text{on } \{0\} \times \Omega, \end{aligned} \tag{2.12}$$

then u necessarily obeys Kirchhoff's formula

$$u = \mathrm{D} \llbracket \gamma_0 u \rrbracket_\Gamma - \mathrm{S} \llbracket \gamma_1 u \rrbracket_\Gamma . \tag{2.13}$$

Setting $u = 0$ in either Q^- or Q^+ in (2.13) yields Kirchhoff's formula for $u : Q^{\mathfrak{d}} \to \mathbb{R}$

$$u = \mathfrak{d} \left(\mathrm{D}\, \gamma_0^{\mathfrak{d}} u - \mathrm{S}\, \gamma_1^{\mathfrak{d}} u \right) . \tag{2.14}$$

Furthermore, (2.10) and (2.11) imply the jump properties

$$\begin{aligned} \llbracket \gamma_0 \, \mathrm{S}\, w \rrbracket_\Gamma &= 0, & \llbracket \gamma_0 \, \mathrm{D}\, v \rrbracket_\Gamma &= v, \\ \llbracket \gamma_1 \, \mathrm{S}\, w \rrbracket_\Gamma &= -w, & \llbracket \gamma_1 \, \mathrm{D}\, v \rrbracket_\Gamma &= 0. \end{aligned}$$

In other words, $\mathrm{S}\, w$ is continuous across Σ, while its normal derivative is discontinuous and jumps by $-w$. In contrast, $\mathrm{D}\, v$ is discontinuous across Σ with jump equal to v, however, its normal derivative is continuous. The averages of the potentials induce the four standard boundary integral operators

$$\begin{aligned} \mathrm{V}\, w &:= \{\!\{ \gamma_0 \, \mathrm{S}\, w \}\!\}_\Gamma = \gamma_0^- \, \mathrm{S}\, w = \gamma_0^+ \, \mathrm{S}\, w, \\ \mathrm{K}^{\mathrm{t}}\, w &:= \{\!\{ \gamma_1 \, \mathrm{S}\, w \}\!\}_\Gamma , \\ \mathrm{K}\, v &:= \{\!\{ \gamma_0 \, \mathrm{D}\, v \}\!\}_\Gamma , \\ \mathrm{W}\, v &:= - \{\!\{ \gamma_1 \, \mathrm{D}\, v \}\!\}_\Gamma = -\gamma_1^- \, \mathrm{D}\, v = -\gamma_1^+ \, \mathrm{D}\, v. \end{aligned}$$

REMARK 2.12. *The superscript* t *in* K^{t} *indicates a certain concept of transposition, which is, however, irrelevant for the purposes of this thesis. In fact, the Laplace transform of* K^{t} *is the real-transposed of the Laplace transform of* K. *This transposition refers to the inner product* $(\cdot, \cdot)_{L^2(\Gamma)}$, *which is continuously extended to a bilinear duality pairing between* $H^{-1/2}(\Gamma)$ *and* $H^{1/2}(\Gamma)$, *see [104, Section 3.4].*

The operators V, K, and W are known as single layer, double layer, and hypersingular boundary integral operators respectively. The traces

$$\gamma_1^{\mathfrak{d}}\,\mathrm{S}\,w = -\mathfrak{d}\frac{1}{2}w + \mathrm{K}^{\mathrm{t}}\,w, \quad \gamma_0^{\mathfrak{d}}\,\mathrm{D}\,v = \mathfrak{d}\frac{1}{2}v + \mathrm{K}\,v$$

hold almost everywhere. In particular, they hold for any $\mathbf{x} \in \Sigma$ such that the tangent space of Γ exists at $x \in \Gamma$. Computing the averages of Kirchhoff's formula (2.13) leads to the relation between the jumps and averages of solutions of (2.12)

$$\begin{bmatrix} \{\!\!\{\gamma_0 u\}\!\!\}_\Gamma \\ \{\!\!\{\gamma_1 u\}\!\!\}_\Gamma \end{bmatrix} = \begin{bmatrix} \mathrm{K} & -\mathrm{V} \\ -\mathrm{W} & -\mathrm{K}^{\mathrm{t}} \end{bmatrix} \begin{bmatrix} [\![\gamma_0 u]\!]_\Gamma \\ [\![\gamma_1 u]\!]_\Gamma \end{bmatrix}.$$

Setting $u = 0$ in the complementary domain yields

$$\frac{1}{2}\begin{bmatrix} \gamma_0^{\mathfrak{d}} u \\ \gamma_1^{\mathfrak{d}} u \end{bmatrix} = \mathfrak{d}\begin{bmatrix} \mathrm{K} & -\mathrm{V} \\ -\mathrm{W} & -\mathrm{K}^{\mathrm{t}} \end{bmatrix} \begin{bmatrix} \gamma_0^{\mathfrak{d}} u \\ \gamma_1^{\mathfrak{d}} u \end{bmatrix}.$$

We separate the Dirichlet from the Neumann data and obtain

$$\mathrm{V}\,\gamma_1^{\mathfrak{d}} u = -\mathfrak{d}\frac{1}{2}\gamma_0^{\mathfrak{d}} u + \mathrm{K}\,\gamma_0^{\mathfrak{d}} u \tag{2.15}$$

as well as

$$\mathrm{W}\,\gamma_0^{\mathfrak{d}} u = -\mathfrak{d}\frac{1}{2}\gamma_1^{\mathfrak{d}} u - \mathrm{K}^{\mathrm{t}}\,\gamma_0^{\mathfrak{d}} u. \tag{2.16}$$

Typically (2.15) is called weakly singular BIE, while (2.16) is known as hypersingular BIE. With these relations at our disposal, we are in a position to reformulate the initial-boundary value problems of Section 2.3.

We consider the Dirichlet problem given by (2.7) and (2.8). In this case, Kirchhoff's formula (2.14) reads

$$u = \mathfrak{d}\left(\mathrm{D}\,g_D - \mathrm{S}\,\gamma_1^{\mathfrak{d}} u\right). \tag{2.17}$$

The yet unknown Neumann trace $\gamma_1^{\mathfrak{d}} u$ is determined via the weakly singular BIE

$$\mathrm{V}\,\gamma_1^{\mathfrak{d}} u = -\mathfrak{d}\frac{1}{2}g_D + \mathrm{K}\,g_D. \tag{2.18}$$

Once (2.18) is solved for $\gamma_1^{\mathfrak{d}} u$ we obtain the solution of (2.7) and (2.8) via (2.17). This approach is a direct method because the unknown field (in this case $\gamma_1^{\mathfrak{d}} u$) is part of the Cauchy data. We shall also provide an alternative strategy to solve the Dirichlet problem. This procedure is based on the observation that for any admissible $w : \Sigma \to \mathbb{R}$ the ansatz

$$u := \mathrm{S}\,w \tag{2.19}$$

satisfies (2.7). Consequently, the problem boils down to finding w such that the boundary condition (2.8) holds true. To this end, we apply γ_0 to (2.19), leading to

$$\mathrm{V}\, w = g_D. \tag{2.20}$$

Once (2.20) is solved for w the solution of (2.7) and (2.8) is due to (2.19). This is an indirect approach, since the field w is not part of the Cauchy data. The reformulation of the Neumann problem (2.7) and (2.9) is discussed by means of an indirect approach only. For any admissible $v : \Sigma \to \mathbb{R}$ the ansatz

$$u \coloneqq -\,\mathrm{D}\, v \tag{2.21}$$

satisfies (2.7). Application of γ_1 to (2.21) yields

$$\mathrm{W}\, v = g_N. \tag{2.22}$$

Once (2.22) is solved for v the solution of (2.7) and (2.9) is obtained via (2.21). Altogether three BIEs are exhibited: two for the Dirichlet problem and one for the Neumann problem. They serve as starting point for the development of the discretization method in Chapter 3. There are substantially more BIEs available for the considered problems, each with their individual advantages and drawbacks. We refer the reader to [108, Chapter 7] and [100, Section 3.4] for thorough discussions regarding the choice of BIEs in case of elliptic partial differential equations.

2.5 Variational Boundary Integral Equations

Within the following paragraphs we provide variational formulations of the BIEs (2.18), (2.20), and (2.22). Finding compelling space-time variational formulations of RPBIEs has been the goal of multiple research efforts, see, e.g., [10, 6, 58]. However, computable bilinear forms proven to be coercive in the same (Sobolev space) norm in which they are bounded, are elusive, see [6, Theorems 3.1 and 3.3], [58, Corollary 4.6], and [21, Theorem 3]. In this thesis, we resort to the setting of [21, Theorem 3] with a weight of $\omega_I = 0$, which is similar to [6, Equations (29)–(31)].

Prior to exhibiting the formulations, we demonstrate the rationale behind choosing BIEs in Section 2.4 in which the unknown occurs only under the action of the operators V and W. In the subsequent derivations it is assumed that S and D commute with the time derivative

$$\partial_t\, \mathrm{S}\, w = \mathrm{S}\, \partial_t w, \quad \partial_t\, \mathrm{D}\, v = \mathrm{D}\, \partial_t v.$$

This assumption is justified once the integral representations of S and D are discussed in Section 2.6. Theorem 2.8 indicates the energy-flux relation of solutions of $\Box u = 0$

$$\frac{\mathrm{d}}{\mathrm{d}t}\mathbb{E}u\,(t) = -\int_\Gamma \left(\{\!\{\gamma_1 u(\mathbf{x})\}\!\}_\Gamma\, [\![\gamma_0 \partial_t u(\mathbf{x})]\!]_\Gamma + [\![\gamma_1 u(\mathbf{x})]\!]_\Gamma\, \{\!\{\gamma_0 \partial_t u(\mathbf{x})\}\!\}_\Gamma \right) \mathrm{d}S(x).$$

For given $w : \Sigma \to \mathbb{R}$ let $u_{\mathrm{S}} \coloneqq \mathrm{S}\, w$ and exploiting the jump properties of S yields

$$\frac{\mathrm{d}}{\mathrm{d}t} \mathbb{E} u_{\mathrm{S}}\left(t\right) = \int_{\Gamma} w(\mathbf{x})\, \mathrm{V}\, \partial_t w(\mathbf{x}) \mathrm{d}S(x).$$

Similarly, for given $v : \Sigma \to \mathbb{R}$ let $u_{\mathrm{D}} \coloneqq \mathrm{D}\, v$ and observe

$$\frac{\mathrm{d}}{\mathrm{d}t} \mathbb{E} u_{\mathrm{D}}\left(t\right) = \int_{\Gamma} \partial_t v(\mathbf{x})\, \mathrm{W}\, v(\mathbf{x}) \mathrm{d}S(x).$$

Integrating these relations with respect to time yields

$$\mathbb{E} u_{\mathrm{S}}\left(T\right) = \int_{\Sigma} w(\mathbf{x})\, \mathrm{V}\, \partial_t w(\mathbf{x}) \mathrm{d}S(\mathbf{x}), \quad \mathbb{E} u_{\mathrm{D}}\left(T\right) = \int_{\Sigma} \partial_t v(\mathbf{x})\, \mathrm{W}\, v(\mathbf{x}) \mathrm{d}S(\mathbf{x}), \tag{2.23}$$

where we used that $\mathrm{S}\, w$ and $\mathrm{D}\, v$ satisfy (2.12) and, therefore, $\mathbb{E} u_{\mathrm{S}}\left(0\right) = \mathbb{E} u_{\mathrm{D}}\left(0\right) = 0$ holds. Integration by parts in the relation involving V yields, see [6, Equation (31)]

$$\mathbb{E} u_{\mathrm{S}}\left(T\right) = \int_{\{T\}\times\Gamma} w(\mathbf{x})\, \mathrm{V}\, w(\mathbf{x}) \mathrm{d}S(\mathbf{x}) - \int_{\Sigma} \partial_t w(\mathbf{x})\, \mathrm{V}\, w(\mathbf{x}) \mathrm{d}S(\mathbf{x}). \tag{2.24}$$

In [43, Remark 4.1], the first term in (2.24) is omitted because w is assumed to vanish at $\{T\} \times \Gamma$. For $\mathrm{T} \in \{\mathrm{V}, \mathrm{K}, \mathrm{K}^{\mathrm{t}}, \mathrm{W}\}$ define the abstract bilinear form b_{T} by

$$b_{\mathrm{T}} : (w, v) \mapsto \int_{\Sigma} \partial_t v(\mathbf{x})\, \mathrm{T}\, w(\mathbf{x}) \mathrm{d}S(\mathbf{x})$$

and note the identities of energy at simulation end time implied by (2.23) and (2.24)

$$\begin{aligned} b_{\mathrm{V}}(w, w) &= \int_{\{T\}\times\Gamma} w(\mathbf{x})\, \mathrm{V}\, w(\mathbf{x}) \mathrm{d}S(\mathbf{x}) - \mathbb{E}\left[\mathrm{S}\, w\right]\left(T\right), \\ b_{\mathrm{W}}(v, v) &= \mathbb{E}\left[\mathrm{D}\, v\right]\left(T\right). \end{aligned} \tag{2.25}$$

The nonnegativity of energy implies that the quadratic form of b_{W} is positive semidefinite, while the quadratic form of b_{V} is negative semidefinite for input densities vanishing at $\{T\} \times \Gamma$. In [58], the bilinear forms $b_T^{\mathcal{Z}}$ and $b_T^{\mathcal{Y}}$ are considered, satisfying

$$b_T^{\mathcal{Z}}(w, v) = -b_{\mathrm{V}}(w, v), \quad b_T^{\mathcal{Y}}(\partial_t w, \partial_t v) = b_{\mathrm{W}}(w, v). \tag{2.26}$$

The derivation of the relation between $b_T^{\mathcal{Z}}$ and b_{V} in (2.26) is based on the assumption that w and v are such that the integral along $\{T\} \times \Gamma$ in (2.25) vanishes. It is shown [58, Proposition 3.4] that the condition $T < 2T_\Omega$ with

$$T_\Omega \coloneqq \sup \left\{ t > 0 : \{x \in \Omega^- : |\operatorname{dist}_\Gamma(x)| \geq t\} \neq \varnothing \right\}$$

is sufficient for positive definiteness of $b_T^{\mathcal{Z}}$ and $b_T^{\mathcal{Y}}$

$$b_T^{\mathcal{Z}}(w, w) = 0 \quad \Rightarrow \quad w = 0, \quad b_T^{\mathcal{Y}}(v, v) = 0 \quad \Rightarrow \quad v = 0.$$

From (2.26) we deduce that b_{V} and b_{W} are negative/positive definite for $T < 2T_\Omega$

$$b_{\mathrm{V}}(w,w) = 0 \quad \Rightarrow \quad w = 0, \quad b_{\mathrm{W}}(v,v) = 0 \quad \Rightarrow \quad \partial_t v = 0 \quad \Rightarrow \quad v = 0,$$

where we use homogeneous initial conditions to infer that $\partial_t v = 0$ implies $v = 0$. Note that for the wave equation in one spatial dimension [58, Proposition 4.1] states stronger short-time coercivity properties similar to the ones observed in [3, 88].

Even for $T < 2T_\Omega$ the norm induced by $b_T^{\mathcal{Z}}$ is rather weak (for more than one spatial dimension). In particular, it is not equivalent to the $H^s(\Sigma)$-norm for any $s \in \mathbb{R}$, see [6, Theorem 3.1]. We are inclined to conjecture that a similar result holds true for b_{W} as well. As already indicated in Chapter 1, the mathematical analysis of RPBIEs and associated variational formulations is delicate. This topic is not addressed in this monograph, with the sole exception of Remark 2.13. It is merely assumed that there are appropriate Sobolev spaces $\mathcal{H}_0$ and $\mathcal{H}_1$ such that the bilinear forms

$$b_{\mathrm{V}} : \mathcal{H}_0 \times \mathcal{H}_0 \to \mathbb{R}, \quad b_{\mathrm{K}} : \mathcal{H}_1 \times \mathcal{H}_0 \to \mathbb{R}, \quad b_{\mathrm{W}} : \mathcal{H}_1 \times \mathcal{H}_1 \to \mathbb{R}$$

are well-defined. The spaces $\mathcal{H}_0$ and $\mathcal{H}_1$ simply serve as devices to distinguish qualitative properties of certain fields, in particular Dirichlet and Neumann traces, in the discretization process of Chapter 3. The observations of (2.23) and (2.25) suggest to multiply (2.18), (2.20), and (2.22) by the time derivative of a test function and integrate along Σ. This yields the variational problems exhibited in the following paragraph. For a given surface density $g : \Sigma \to \mathbb{R}$ define the functional ℓ_g via

$$\ell_g : v \mapsto \int_\Sigma \partial_t v(\mathbf{x}) g(\mathbf{x}) \mathrm{d}S(\mathbf{x}).$$

It is assumed that $\ell_{g_1} : \mathcal{H}_0 \to \mathbb{R}$ is well-defined for $g_1 \in \mathcal{H}_1$ and $\ell_{g_0} : \mathcal{H}_1 \to \mathbb{R}$ is well-defined for $g_0 \in \mathcal{H}_0$.

For given $g_D \in \mathcal{H}_1$ we consider the variational formulation of (2.18) with $w := \gamma_0^{\mathfrak{d}} u$:

$$\text{Find } w \in \mathcal{H}_0 : \; b_{\mathrm{V}}(w,z) = -\mathfrak{d}\frac{1}{2}\ell_{g_D}(z) + b_{\mathrm{K}}(g_D, z) \;\; \forall z \in \mathcal{H}_0. \tag{2.27}$$

Analogously, given $g_D \in \mathcal{H}_1$ we replace (2.20) by the problem:

$$\text{Find } w \in \mathcal{H}_0 : \; b_{\mathrm{V}}(w,z) = \ell_{g_D}(z) \;\; \forall z \in \mathcal{H}_0. \tag{2.28}$$

Given $g_N \in \mathcal{H}_0$ the same procedure leads to the variational formulation of (2.22):

$$\text{Find } v \in \mathcal{H}_1 : \; b_{\mathrm{W}}(v,z) = \ell_{g_N}(z) \;\; \forall z \in \mathcal{H}_1. \tag{2.29}$$

The space-time discretization of these problems is discussed in Chapter 3.

REMARK 2.13. *The analysis of RPBIEs sparked by Bamberger and Ha-Duong [10] involves weighted bilinear forms of the form*

$$(w, v) \mapsto \int_{\Sigma} \exp(-2\eta t)\, v(\mathbf{x})\, \mathrm{V}\, \partial_t w(\mathbf{x}) \mathrm{d}S(\mathbf{x})$$

for some $\eta > 0$. Joly and Rodríguez [58] consider the bilinear form (among others)

$$b_\omega : (w, v) \mapsto \int_{\Sigma} \omega(t) v(\mathbf{x})\, \mathrm{V}\, \partial_t w(\mathbf{x}) \mathrm{d}S(\mathbf{x}),$$

with the general weighting function $\omega \in C^1(0, T)$ such that $\omega(t) > 0$ holds for all $t \in [0, T]$ and $\omega(0) = 1$. In [58, Proposition 3.8] it is shown that for $u := \mathrm{S}\, w$ it holds

$$b_\omega(w, w) = \frac{1}{2} \omega(T)\, \mathbb{E}u\,(T) - \frac{1}{2} \int_0^T \omega'(t)\, \mathbb{E}u\,(t)\, \mathrm{d}t.$$

For $\omega : t \mapsto \exp(-2\eta t)$ one recovers the bilinear form originally studied by Bamberger and Ha-Doung. If $\eta > 0$ and Γ is a plane, e.g., $\Gamma = \mathbb{R}^2 \times \{0\}$, it is shown [58, Corollary 4.6, Remark 4.7] that there exist positive constants $c_1 \leq c_2$ such that

$$c_1 \|w\|^2_{L^2\left(0,T;H^{-1/2}(\Gamma)\right)} \leq b_\omega(w, w) \leq c_2 \|w\|^2_{L^2\left(0,T;H^{1/4}(\Gamma)\right)}$$

holds. Although the norms in the lower and upper bound feature the same L^2-regularity in time, their regularity in space differs. The authors of the cited reference state that there is a coercivity-regularity gap of 0 in time and 3/4 in space. Such gaps plague the mathematical analysis of RPBIEs, because numerical experiments yield better results than the theoretical predictions, see [43, Remark 3.49, Section 5.5]. For $\eta = 0$ (in this case b_ω coincides with $b_T^{\mathcal{Z}}$) the boundedness of b_ω in $L^2\left(0, T; H^{1/4}(\Gamma)\right)$ is due to Aimi and collaborators [6, Proposition 3.2] in the case of two spatial dimensions and flat Γ. This result provides a factual justification for the use of discontinuous trial functions to discretize the arguments of $b_T^{\mathcal{Z}}$ and b_{V}. Finally, the question is addressed briefly why coercivity and boundedness in the same Sobolev space norm is such a valuable property, especially in the field of numerical analysis. If the bilinear form $b : \mathcal{H} \times \mathcal{H} \to \mathbb{R}$ is bounded and coercive in the same Hilbert space norm $\|\cdot\|_{\mathcal{H}}$, the Lax-Milgram lemma [122, Section III.7] ensures that the operator $\mathcal{H} \to \mathcal{H}'$, $u \mapsto b(u, \cdot)$ is an isomorphism. This implies well-posedness (existence of a unique solution which depends continuously on the data) of the problem:

$$\text{Given } \ell \in \mathcal{H}', \text{ find } w \in \mathcal{H} : \; b(w, v) = \ell(v) \quad \forall v \in \mathcal{H}.$$

If b is restricted to the Hilbert space $\mathcal{H}_h \subset \mathcal{H}$ it is bounded and coercive on $\mathcal{H}_h$ (with the original constants) and we deduce the well-posedness of:

$$\text{Given } \ell \in \mathcal{H}', \text{ find } w_h \in \mathcal{H}_h : \; b(w_h, v_h) = \ell(v_h) \quad \forall v_h \in \mathcal{H}_h.$$

In other words, the well-posedness of the continuous problem is inherited by any conforming discretization, see [19, Remark 1.5.1]. Such discretization schemes are unconditionally stable and, therefore, well-suited for the hyperbolic problem at hand.

2.6 Integral Representations of Retarded Potentials

In this section, explicit integral representations of the operators of Section 2.4 are provided. The fundamental solution (2.6) and partial derivatives of it act as integral kernels. In the following formulas, the surface densities $w, v : \Sigma \to \mathbb{R}$ are assumed to be sufficiently smooth. For $\mathbf{x} \in Q$ the retarded single layer potential reads

$$\mathrm{S}\, w(\mathbf{x}) = \int_\Sigma \mathcal{G}(\mathbf{x}-\mathbf{y}) w(\mathbf{y}) \mathrm{d}S(\mathbf{y}) = \int_\Sigma k_1(x,y) \delta_0 \circ \phi_\Xi(\mathbf{x}-\mathbf{y}) w(\mathbf{y}) \mathrm{d}S(\mathbf{y}), \tag{2.30}$$

while the retarded double layer potential is given by

$$\begin{aligned} \mathrm{D}\, v(\mathbf{x}) &= \int_\Sigma \gamma_{1,y} \mathcal{G}(\mathbf{x}-\mathbf{y}) v(\mathbf{y}) \mathrm{d}S(\mathbf{y}) \\ &= \int_\Sigma \left(k_3(x,y) v(\mathbf{y}) + k_2(x,y) \partial_\tau v(\mathbf{y}) \right) \delta_0 \circ \phi_\Xi(\mathbf{x}-\mathbf{y}) \mathrm{d}S(\mathbf{y}), \end{aligned} \tag{2.31}$$

with the kernel functions $k_i : \mathbb{R}^3 \times \mathbb{R}^3 \to \mathbb{R}, i = 1,2,3$ defined by

$$k_1 : (x,y) \mapsto \frac{1}{4\pi \|x-y\|}, \quad k_j : (x,y) \mapsto \frac{\langle \nu_\Gamma(y), x-y \rangle}{4\pi \|x-y\|^j}, \ j = 2,3, \tag{2.32}$$

see, e.g., [104]. Their traces have similar integral representations. In particular, for $\mathbf{x} \in \Sigma$ it holds

$$\begin{aligned} \mathrm{V}\, w(\mathbf{x}) &= \int_\Sigma k_1(x,y) \delta_0 \circ \phi_\Xi(\mathbf{x}-\mathbf{y}) w(\mathbf{y}) \mathrm{d}S(\mathbf{y}), \\ \mathrm{K}\, v(\mathbf{x}) &= \int_\Sigma \left(k_3(x,y) v(\mathbf{y}) + k_2(x,y) \partial_\tau v(\mathbf{y}) \right) \delta_0 \circ \phi_\Xi(\mathbf{x}-\mathbf{y}) \mathrm{d}S(\mathbf{y}), \\ \mathrm{K}^{\mathrm{t}}\, w(\mathbf{x}) &= \int_\Sigma \left(k_3^*(x,y) w(\mathbf{y}) + k_2^*(x,y) \partial_\tau w(\mathbf{y}) \right) \delta_0 \circ \phi_\Xi(\mathbf{x}-\mathbf{y}) \mathrm{d}S(\mathbf{y}), \end{aligned} \tag{2.33}$$

with the kernel functions $k_j^* : \mathbb{R}^3 \times \mathbb{R}^3 \to \mathbb{R}, j = 2,3$ given by

$$k_j^* : (x,y) \mapsto \frac{\langle \nu_\Gamma(x), x-y \rangle}{4\pi \|x-y\|^j}. \tag{2.34}$$

The integral formula of the hypersingular operator W is more involved, see [4, Equations (2.16) and (2.20)] or [81, Theorem 3.4.2]. For our purposes, we only require an explicit representation of the bilinear form b_{W}. The employed formula

$$\begin{aligned} b_{\mathrm{W}}(w,v) = &\int_\Sigma \langle \mathrm{curl}_\Gamma\, \partial_t v(\mathbf{x}), \mathrm{V}\, \mathrm{curl}_\Gamma\, w(\mathbf{x}) \rangle \, \mathrm{d}S(\mathbf{x}) \\ &+ \int_\Sigma \left\langle \nu_\Gamma(x) \partial_t^2 v(\mathbf{x}), \mathrm{V} \left(\nu_\Gamma \partial_t w \right) (\mathbf{x}) \right\rangle \mathrm{d}S(\mathbf{x}) \end{aligned} \tag{2.35}$$

is due to integration by parts, see [11, Equation (2.17)] or [51, Equation (13)]. The operator V is applied component-wise in (2.35) and the tangential curl operator on Γ is defined by

$$\operatorname{curl}_\Gamma v : \mathbf{x} \mapsto \nu_\Gamma(x) \times \nabla_\Gamma v(\mathbf{x}).$$

Note that ∇_Γ is the spatial component of the surface gradient ∇_Σ

$$\nabla_\Sigma v : \mathbf{x} \mapsto \begin{pmatrix} \partial_t v(\mathbf{x}) \\ \nabla_\Gamma v(\mathbf{x}) \end{pmatrix}$$

for some $v \in H^1(\Sigma)$ in the considered stationary case. By virtue of (2.35) the evaluation of the bilinear form of the hypersingular operator W is enabled via evaluations of the single layer operator V.

Remark 2.14 (Etymology of retarded potential). *The name retarded potential is due to classical integral representations of these operators. Consider the operator* S, *for which we have (tacitly assuming that all integrals are interchangeable)*

$$\begin{aligned} \mathrm{S}\, w(\mathbf{x}) &= \int_0^T \int_\Gamma k_1(x,y)\delta_0 \circ \phi_\Xi(\mathbf{x}-\mathbf{y}) w(\mathbf{y}) \mathrm{d}S(y) \mathrm{d}\tau \\ &= \int_\Gamma k_1(x,y) \int_0^T \delta_0\big(\|x-y\| - (t-\tau)\big) w(\tau,y) \mathrm{d}\tau \, \mathrm{d}S(y). \end{aligned}$$

The sifting property of δ_0 *and insertion of* k_1 *from* (2.32) *yield the classical expression*

$$\mathrm{S}\, w(t,x) = \int_\Gamma \frac{w(t-\|x-y\|,y)}{4\pi \|x-y\|} \mathrm{d}S(y),$$

where w *is evaluated at the retarded time* $t - \|x-y\|$ *and extended by* $w(t,\cdot) = 0$ *for* $t < 0$. *Solutions of the d'Alembertian propagate information at finite speed, see Theorem 2.7, which is fixed to unit velocity due to Definition 2.1. Consequently, the field* $\mathrm{S}\, w$ *at time* t *cannot depend on the density at time greater than* $t - \|x-y\|$, *where* $\|x-y\|$ *is the delay due to the spatial separation of the observer and the source. As already mentioned in Remark 2.9, the strong Huygens principle causes these potentials to depend only on the retarded time itself, rather than smaller times as well.*

In total, we are confronted with six operators, namely two potentials S and D as well as four boundary integral operators $\mathrm{V}, \mathrm{K}, \mathrm{K}^{\mathrm{t}}$, and W. The remainder of this chapter is devoted to studying their integral formulas (2.30), (2.31), and (2.33) in greater detail. The goal is to abolish the Dirac delta functions in the integral kernels. We derive formulas apt for implementation which also enhance the understanding of these operators. The key ingredient is the coarea formula, whose proof can be found in [32, Theorem 3.2.12].

THEOREM 2.15 (Coarea formula). *Let* $m, n \in \mathbb{N}$ *with* $m > n$, $f : \mathbb{R}^m \to \mathbb{R}^n$ *be Lipschitz continuous and* $g : \mathbb{R}^m \to \mathbb{R}$ *be integrable. It holds*

$$\int_{\mathbb{R}^m} g(x) \left|\det \mathrm{D} f(x)\right| \mathrm{d}x = \int_{\mathbb{R}^n} \int_{f^{-1}\{y\}} g(x) \mathrm{d}S(x) \mathrm{d}y,$$

where $|\det \mathrm{D} f(x)|$ *is the* n*-dimensional Jacobian of* f *at* $x \in \mathbb{R}^m$.

Let f and g be as in Theorem 2.15 with the addition that $x \mapsto g(x)/|\det \mathrm{D} f(x)|$ is integrable. In this case, Theorem 2.15 leads to

$$\begin{aligned}\int_{\mathbb{R}^m} g(x)\delta_0 \circ f(x)\mathrm{d}x &= \int_{\mathbb{R}^n} \int_{f^{-1}\{y\}} \frac{g(x)\delta_0 \circ f(x)}{|\det \mathrm{D} f(x)|} \mathrm{d}S(x)\mathrm{d}y \\ &= \int_{\mathbb{R}^n} \delta_0(y) \int_{f^{-1}\{y\}} \frac{g(x)}{|\det \mathrm{D} f(x)|} \mathrm{d}S(x)\mathrm{d}y.\end{aligned}$$

With the sifting property of the Dirac delta function δ_0 we obtain

$$\int_{\mathbb{R}^m} g(x)\delta_0 \circ f(x)\mathrm{d}x = \int_{f^{-1}\{0\}} \frac{g(x)}{|\det \mathrm{D} f(x)|} \mathrm{d}S(x), \tag{2.36}$$

if the integral on the right hand side exists. A formula similar to (2.36) for $n = 1$ can be found in [55, Theorem 6.1.5]. Moreover, (2.36) for $f = \mathrm{dist}_\Sigma$ and $g : Q \to \mathbb{R}$ with $\gamma_0 g := \gamma_0^+ g = \gamma_0^- g$ as well as (2.3) yield

$$\int_{\mathbb{R}^4} g(\mathbf{x})\delta_0 \circ \mathrm{dist}_\Sigma(\mathbf{x})\mathrm{d}\mathbf{x} = \int_{\mathrm{dist}_\Sigma^{-1}\{0\}} \frac{\gamma_0 g(\mathbf{x})}{\|\nabla \gamma_0 \,\mathrm{dist}_\Sigma(\mathbf{x})\|} \mathrm{d}S(\mathbf{x}) = \int_\Sigma \gamma_0 g(\mathbf{x})\mathrm{d}S(\mathbf{x}). \tag{2.37}$$

We introduce an operator that unifies the integrals in (2.30), (2.31), and (2.33).

DEFINITION 2.16. *Let* $\mathbf{x} \in \mathbb{R}^4$ *be an arbitrary evaluation point and* $k : \mathbb{R}^3 \times \mathbb{R}^3 \to \mathbb{R}$ *be the integral kernel. For sufficiently smooth* $f : \mathbb{R}^4 \to \mathbb{R}$ *with bounded support define the abstract retarded Newtonian potential*

$$\mathrm{N}_k f(\mathbf{x}) := \int_{\mathbb{R}^4} k(x, y) f(\mathbf{y})\delta_0 \circ \phi_\Xi(\mathbf{x} - \mathbf{y})\mathrm{d}\mathbf{y}. \tag{2.38}$$

For sufficiently smooth $w : \Sigma \to \mathbb{R}$ *define analogously the abstract retarded layer potential*

$$\mathrm{T}_k w(\mathbf{x}) := \int_\Sigma k(x, y) w(\mathbf{y})\delta_0 \circ \phi_\Xi(\mathbf{x} - \mathbf{y})\mathrm{d}S(\mathbf{y}). \tag{2.39}$$

By inserting $f = \widetilde{w}\delta_0 \circ \mathrm{dist}_\Sigma$ in (2.38) with $\widetilde{w} : Q \to \mathbb{R}$ satisfying $w = \gamma_0^+ \widetilde{w} = \gamma_0^- \widetilde{w}$, we obtain from (2.37)

$$\mathrm{N}_k \left(\widetilde{w}\delta_0 \circ \mathrm{dist}_\Sigma\right) = \mathrm{T}_k w. \tag{2.40}$$

As an example, we recover single and double layer potentials via

$$\mathrm{S} = \mathrm{T}_{k_1}, \quad \mathrm{D} = \mathrm{T}_{k_3} + \mathrm{T}_{k_2}\,\partial_t,$$

with the kernel functions of (2.32). In Sections 2.6.1 and 2.6.2, we recast the abstract operator T_k of Definition 2.16, based on two different perspectives. We investigate T_k not just for stationary boundaries $\Sigma = (0,T) \times \Gamma$ as in Section 2.1, but for more general hypersurfaces $\Sigma = \{\mathbf{x} \in \mathbb{R}^4 : t \in (0,T), x \in \Gamma(t)\}$, where $\Gamma(t)$ is a Lipschitz boundary. The lateral boundary Σ is assumed to adhere to Assumption 2.5 and the treatment of instationary boundaries will effectively only be visible in the normal vector field. In the general case $\nu_\Sigma : \Sigma \to \mathbb{S}^3$ has nontrivial time component

$$\nu_\Sigma : \mathbf{x} \mapsto \begin{pmatrix} \nu_{\Sigma,t}(\mathbf{x}) \\ \nu_{\Sigma,x}(\mathbf{x}) \end{pmatrix} = \begin{pmatrix} -v_\nu(\mathbf{x}) \\ \nu_\Gamma(\mathbf{x}) \end{pmatrix} \Big/ \sqrt{1 + v_\nu^2(\mathbf{x})},$$

where $\nu_\Gamma : \Sigma \to \mathbb{S}^2$ is the unit outward normal vector field of $\Gamma(t)$ and $v_\nu : \Sigma \to \mathbb{R}$ is the normal velocity field. It holds $v_\nu(\mathbf{x}) = -\nu_{\Sigma,t}(\mathbf{x}) / \|\nu_{\Sigma,x}(\mathbf{x})\|$ for any $\mathbf{x} \in \Sigma$ such that $\nu_\Sigma(\mathbf{x})$ exists. The normalization $1 = \|\nu_\Sigma(\mathbf{x})\|^2 = |\nu_{\Sigma,t}(\mathbf{x})|^2 + \|\nu_{\Sigma,x}(\mathbf{x})\|^2$ yields

$$|\nu_{\Sigma,t}(\mathbf{x})|^2 = \frac{|v_\nu(\mathbf{x})|^2}{1 + |v_\nu(\mathbf{x})|^2}, \quad [\nu_\Sigma(\mathbf{x}), \nu_\Sigma(\mathbf{x})] = \frac{1 - |v_\nu(\mathbf{x})|^2}{1 + |v_\nu(\mathbf{x})|^2}. \tag{2.41}$$

Concerning actual solutions of the d'Alembertian we are only interested in the case

$$[\nu_\Sigma(\mathbf{x}), \nu_\Sigma(\mathbf{x})] > 0 \quad \Leftrightarrow \quad |v_\nu(\mathbf{x})| < 1$$

for any $\mathbf{x} \in \Sigma$ such that $\nu_\Sigma(\mathbf{x})$ exists. The case $[\nu_\Sigma(\mathbf{x}), \nu_\Sigma(\mathbf{x})] \leq 0$ is solely motivated by curiosity, because it implies that the boundary travels at or beyond wave velocity, which is 1 due to Definition 2.1. While the instationary setting reveals intriguing results for T_k, we emphasize that they are of limited applicability to the solution operators of the d'Alembertian. The key difference to the stationary case is that the notion of normal derivative γ_1 is altered, see, e.g., [111]. Consequently, the integral representations that involve γ_1 are potentially invalid in the moving case. Still, T_k is a valid model for (at least) two out of the six operators in case of moving boundaries, namely S in (2.30) and V in (2.33). This justifies its treatment in the general case.

2.6.1 Representation in Terms of the Space-Time Boundary

The results of this section are already published in [89] for the case of stationary boundaries. The contribution of this section lies in the treatment of moving surfaces.

For $\mathbf{x} \in \mathbb{R}^4$ let $\phi_\Xi^{\mathbf{x}} : \mathbb{R}^4 \to \mathbb{R}$ be defined by $\phi_\Xi^{\mathbf{x}} : \mathbf{y} \mapsto \phi_\Xi(\mathbf{x} - \mathbf{y})$. Our starting point is T_k as in (2.39) and the parametrizations of the mesh Σ_N as in Section 2.1 yield

$$\begin{aligned}\mathrm{T}_k\, w(\mathbf{x}) &= \int_\Sigma k(x,y) w(\mathbf{y}) \delta_0 \circ \phi_\Xi(\mathbf{x}-\mathbf{y}) \mathrm{d}S(\mathbf{y}) = \int_\Sigma k(x,y) w(\mathbf{y}) \delta_0 \circ \phi_\Xi^{\mathbf{x}}(\mathbf{y}) \mathrm{d}S(\mathbf{y}) \\ &= \sum_{\sigma \in \Sigma_N} \int_{\widehat{\sigma}} k(x,\cdot) \circ |_x \chi_\sigma(\xi) w \circ \chi_\sigma(\xi) \delta_0 \circ \phi_\Xi^{\mathbf{x}} \circ \chi_\sigma(\xi) \left|\det \mathrm{D}\, \chi_\sigma\,(\xi)\right| \mathrm{d}\xi,\end{aligned}$$

where $|_x \chi_\sigma(\xi)$ denotes the restriction of the vector $\chi_\sigma(\xi)$ to its spatial component. Applying (2.36) with $f = \phi_\Xi^{\mathbf{x}} \circ \chi_\sigma$ yields

$$\begin{aligned}&\int_{\widehat{\sigma}} k(x,\cdot) \circ |_x \chi_\sigma(\xi) w \circ \chi_\sigma(\xi) \delta_0 \circ \phi_\Xi^{\mathbf{x}} \circ \chi_\sigma(\xi) \left|\det \mathrm{D}\, \chi_\sigma\,(\xi)\right| \mathrm{d}\xi \\ &\qquad = \int_{\xi \in \widehat{\sigma} :\, \phi_\Xi^{\mathbf{x}} \circ \chi_\sigma(\xi) = 0} k(x,\cdot) \circ |_x \chi_\sigma(\xi) w \circ \chi_\sigma(\xi) \frac{\left|\det \mathrm{D}\, \chi_\sigma\,(\xi)\right|}{\left\|\nabla\left(\phi_\Xi^{\mathbf{x}} \circ \chi_\sigma(\xi)\right)\right\|} \mathrm{d}S(\xi),\end{aligned}$$

which integrates along the intersection of the backward light cone $\Xi(\mathbf{x})$ and σ

$$\chi_\sigma^{-1}\left(\Xi(\mathbf{x}) \cap \sigma\right) = \{\xi \in \widehat{\sigma} : \phi_\Xi^{\mathbf{x}} \circ \chi_\sigma(\xi) = \phi_\Xi\left(\mathbf{x} - \chi_\sigma(\xi)\right) = 0\}.$$

This leads to

$$\mathrm{T}_k\, w(\mathbf{x}) = \sum_{\sigma \in \Sigma_N} \int_{\chi_\sigma^{-1}(\Xi(\mathbf{x}) \cap \sigma)} k(x,\cdot) \circ |_x \chi_\sigma(\xi) w \circ \chi_\sigma(\xi) \frac{\left|\det \mathrm{D}\, \chi_\sigma\,(\xi)\right|}{\left\|\nabla\left(\phi_\Xi^{\mathbf{x}} \circ \chi_\sigma(\xi)\right)\right\|} \mathrm{d}S(\xi), \quad (2.42)$$

where the chain rule implies $\nabla\left(\phi_\Xi^{\mathbf{x}} \circ \chi_\sigma\right) = J_\sigma^\top \left(\nabla \phi_\Xi^{\mathbf{x}} \circ \chi_\sigma\right)$, wherever $\phi_\Xi^{\mathbf{x}}$ is differentiable. Equation (2.42) shows that retarded layer potentials integrate along the intersection of the backward light cone and the hypersurface Σ. An intriguing observation, unveiled due to the treatment of instationary boundaries, is yet hidden in the term $\xi \mapsto \nabla\left(\phi_\Xi^{\mathbf{x}} \circ \chi_\sigma(\xi)\right)$ due to the coarea formula.

LEMMA 2.17. *Let σ be a C^1-panel and $\xi \in \widehat{\sigma}$ satisfy $|_x \chi_\sigma(\xi) \neq x$. Then it holds*

$$\lambda_2 \frac{\left(1 - |v_\nu \circ \chi_\sigma(\xi)|\right)^2}{1 + |v_\nu \circ \chi_\sigma(\xi)|^2} \leq \left\|\nabla\left(\phi_\Xi^{\mathbf{x}} \circ \chi_\sigma(\xi)\right)\right\|^2 \leq 2\lambda_4,$$

where $0 = \lambda_1 < \lambda_2 \leq \lambda_3 \leq \lambda_4$ are the eigenvalues of $J_\sigma(\xi) J_\sigma^\top(\xi) \in \mathbb{R}^{4\times 4}$.

Proof. For $\xi \in \widehat{\sigma}$ and $\mathbf{y} := \chi_\sigma(\xi)$ it holds

$$\nabla \phi_\Xi^{\mathbf{x}}(\mathbf{y}) = \begin{pmatrix} 1 \\ -\frac{x-y}{\|x-y\|} \end{pmatrix}, \quad \left\|\nabla \phi_\Xi^{\mathbf{x}}(\mathbf{y})\right\|^2 = 2$$

if $x \neq y$. Since σ is a C^1-panel, $J_\sigma(\xi)$ exists for every $\xi \in \widehat{\sigma}$ and we get by the chain rule $\nabla \left(\phi_\Xi^{\mathbf{x}} \circ \chi_\sigma(\xi)\right) = J_\sigma^\top \left(\nabla \phi_\Xi^{\mathbf{x}} \circ \chi_\sigma(\xi)\right)$ when $x \neq y$. For simplicity of notation set

$$q := \nabla \phi_\Xi^{\mathbf{x}}(\mathbf{y}), \quad \nu := \nu_\Sigma \circ \chi_\sigma(\xi), \quad v := v_\nu \circ \chi_\sigma(\xi)$$

and we omit all argument lists and the subscript σ from here on. We have

$$\left\|\nabla \left(\phi_\Xi^{\mathbf{x}} \circ \chi_\sigma(\xi)\right)\right\|^2 = \left\|J^\top q\right\|^2 = \left\langle JJ^\top q, q\right\rangle.$$

Let $z := q - \langle q, \nu\rangle \nu$, where $\operatorname{span}\{\nu\} = \ker J^\top$ holds. From $\|\nu\| = 1$ it follows $\|z\|^2 = \|q\|^2 - \langle q,\nu\rangle^2 = 2 - \langle q,\nu\rangle^2$ and the Cauchy-Schwarz inequality yields

$$|\langle q,\nu\rangle| = \left|\nu_t - \left\langle \frac{x-y}{\|x-y\|}, \nu_x \right\rangle\right| \leq |\nu_t| + \|\nu_x\| = (1+|v|)\|\nu_x\|,$$

where we used $\nu_t = -v\,\|\nu_x\|$. The normalization $\|\nu\| = 1$ leads to

$$\|\nu_x\|^2 = 1 - \nu_t^2 = 1 - v^2\|\nu_x\|^2 \quad \Leftrightarrow \quad \|\nu_x\|^2 = \frac{1}{1+v^2} \quad \Rightarrow \quad \langle q,\nu\rangle^2 \leq \frac{(1+|v|)^2}{1+v^2}$$

and we conclude

$$\|z\|^2 = 2 - \langle q,\nu\rangle^2 \geq 2 - \frac{(1+|v|)^2}{1+v^2} = \frac{1-2|v|+v^2}{1+v^2} = \frac{(1-|v|)^2}{1+v^2}. \tag{2.43}$$

We denote by $\lambda_1 \leq \lambda_2 \leq \lambda_3 \leq \lambda_4$ the eigenvalues and by $e_i \in \mathbb{R}^4, i = 1,\dots,4$ the eigenvectors of the matrix $JJ^\top$. Since $JJ^\top$ is symmetric positive-semidefinite, $\{e_i\}_{i=1}^4$ is an orthonormal basis and $\lambda_1 \geq 0$ holds. From $\operatorname{span}\{\nu\} = \ker J^\top$ it follows $\lambda_2 > \lambda_1 = 0$ and $e_1 = \nu$. This enables the decomposition $JJ^\top = EDE^\top$ with $D := \operatorname{diag}(\lambda_i)_{i=1}^4$ and the columns of E are the basis $\{\nu, e_2, e_3, e_4\}$. The orthonormality implies $E^\top = E^{-1}$. From $q - z = \langle q,\nu\rangle \nu \in \ker J^\top$ it follows $DE^\top(q-z) = 0$ and

$$\left\langle JJ^\top q, q\right\rangle = \left\langle DE^\top q, E^\top q\right\rangle = \left\langle DE^\top z, E^\top q\right\rangle = \left\langle E^\top z, DE^\top q\right\rangle = \left\langle DE^\top z, E^\top z\right\rangle.$$

Parseval's identity $\|z\|^2 = \sum_{i=2}^4 \langle z, e_i\rangle^2 + \langle z,\nu\rangle^2$ and $\langle z,\nu\rangle = 0$ lead to

$$\left\langle DE^\top z, E^\top z\right\rangle = \sum\nolimits_{i=2}^4 \lambda_i \langle z, e_i\rangle^2 \geq \lambda_2 \sum\nolimits_{i=2}^4 \langle z, e_i\rangle^2 = \lambda_2 \|z\|^2. \tag{2.44}$$

Combination of (2.44) with (2.43) yields the desired lower bound

$$\left\|\nabla \left(\phi_\Xi^{\mathbf{x}} \circ \chi_\sigma(\xi)\right)\right\|^2 = \left\langle JJ^\top q, q\right\rangle = \left\langle DE^\top z, E^\top z\right\rangle \geq \lambda_2 \|z\|^2 \geq \lambda_2 \frac{(1-|v|)^2}{1+v^2}.$$

The upper bound is a direct consequence of $\left\langle JJ^\top q, q\right\rangle \leq \left\|JJ^\top\right\| \|q\|^2 = 2\lambda_4$. $\square$

From Lemma 2.17 it follows for any $\xi \in \widehat{\sigma}$ satisfying $|_x \chi_\sigma(\xi) \neq x$

$$\left\|\nabla\left(\phi_\Xi^{\mathbf{x}} \circ \chi_\sigma(\xi)\right)\right\| = 0 \quad \Rightarrow \quad v_\nu \circ \chi_\sigma(\xi) = \pm 1 \quad \Leftrightarrow \quad \left[\nu_\Sigma \circ \chi_\sigma(\xi), \nu_\Sigma \circ \chi_\sigma(\xi)\right] = 0,$$

where the last implication is due to (2.41). Consequently, the term due to the coarea formula $\xi \mapsto 1/\left\|\nabla\left(\phi_\Xi^{\mathbf{x}} \circ \chi_\sigma(\xi)\right)\right\|$ in (2.42) is bounded if the absolute value of the normal velocity is bounded away from 1. Equivalently, the normal vector ν_Σ may not be a lightlike vector. In other words, the integral in (2.42) is well-defined if the boundary does not travel (locally) at the speed of wave propagation.

REMARK 2.18. *There is a clear parallel between Lemma 2.17 and well-established results of electromagnetism. Liénard-Wiechert potentials, see, e.g., [50, Section 10.3], describe solutions of the inhomogeneous wave equation due to moving point sources (charges). Let $y : [0, T] \to \mathbb{R}^3$ be the position of the charged particle and y' be its velocity. Let $x \in \mathbb{R}^3$ be the spatial position of the observer. In these potentials, there is an amplification factor of the form*

$$t \mapsto \frac{1}{1 - \langle y'(t), x - y(t)\rangle / \|x - y(t)\|},$$

which is bounded if $\|y'(t)\| < 1$ holds. Moreover, if $\|y'(t)\| < 1$ does not hold, one cannot guarantee the uniqueness of the retarded time t_r solving

$$\|x - y(t_r)\| - (t - t_r) = 0.$$

In other words, the observer might see the particle in several places at the same time. Lemma 2.17 indicates that in (2.42) *the role of the amplification factor is played by the term due to the coarea formula $\xi \mapsto 1/\left\|\nabla\left(\phi_\Xi^{\mathbf{x}} \circ \chi_\sigma(\xi)\right)\right\|$.*

2.6.2 Representation in Terms of the Light Cone

Equation (2.42) clearly shows that retarded potentials integrate along the intersection of the backward light cone and the space-time boundary $\Xi(\mathbf{x}) \cap \Sigma$. While Section 2.6.1 advocates a point of view based on parametrizations of Σ, we develop in this section an alternative that is based on a parametrization of $\Xi(\mathbf{x})$. The representation of N_k as in (2.38) serves as starting point and application of (2.36) yields

$$\begin{aligned}
\mathrm{N}_k\, f(\mathbf{x}) &= \int_{\mathbb{R}^4} k(x, y) f(\mathbf{y}) \delta_0 \circ \phi_\Xi(\mathbf{x} - \mathbf{y}) \mathrm{d}\mathbf{y} \\
&= \int_{\mathbf{y} \in \mathbb{R}^4 \colon \phi_\Xi(\mathbf{x} - \mathbf{y}) = 0} \frac{k(x, y) f(\mathbf{y})}{\|\nabla_{\mathbf{y}} \phi_\Xi(\mathbf{x} - \mathbf{y})\|} \mathrm{d}S(\mathbf{y}) = \frac{1}{\sqrt{2}} \int_{\Xi(\mathbf{x})} k(x, y) f(\mathbf{y}) \mathrm{d}S(\mathbf{y}).
\end{aligned}$$

The behavior of the layer potential T_k is reconstructed by means of (2.40), yielding

$$\mathrm{T}_k\, w(\mathbf{x}) = \mathrm{N}_k\left(\widetilde{w} \delta_0 \circ \mathrm{dist}_\Sigma\right)(\mathbf{x}) = \frac{1}{\sqrt{2}} \int_{\Xi(\mathbf{x})} k(x, y) \widetilde{w}(\mathbf{y}) \delta_0 \circ \mathrm{dist}_\Sigma(\mathbf{y}) \mathrm{d}S(\mathbf{y}).$$

Assume we have access to a differentiable bijection $\psi_{\mathbf{x}} : \mathcal{P} \to \Xi(\mathbf{x})$ with parameter domain $\mathcal{P} \subset \mathbb{R}^3$. Such a mapping is specified in Definition 2.20 and it follows

$$\int_{\Xi(\mathbf{x})} k(x, y)\widetilde{w}(\mathbf{y})\delta_0 \circ \operatorname{dist}_\Sigma(\mathbf{y}) \mathrm{d}S(\mathbf{y}) \\ = \int_{\mathcal{P}} k(x, \cdot) \circ |_x \psi_{\mathbf{x}}(\zeta)\widetilde{w} \circ \psi_{\mathbf{x}}(\zeta)\delta_0 \circ \operatorname{dist}_\Sigma \circ\psi_{\mathbf{x}}(\zeta) \left|\det \mathrm{D}\, \psi_{\mathbf{x}}(\zeta)\right| \mathrm{d}\zeta.$$

Another application of (2.36) leads to

$$\int_{\Xi(\mathbf{x})} k(x, y)\widetilde{w}(\mathbf{y})\delta_0 \circ \operatorname{dist}_\Sigma(\mathbf{y}) \mathrm{d}S(\mathbf{y}) \\ = \int_{\zeta\in\mathcal{P}:\, \operatorname{dist}_\Sigma \circ\psi_{\mathbf{x}}(\zeta)=0} k(x, \cdot) \circ |_x \psi_{\mathbf{x}}(\zeta) w \circ \psi_{\mathbf{x}}(\zeta) \frac{\left|\det \mathrm{D}\, \psi_{\mathbf{x}}(\zeta)\right|}{\left\|\nabla\left(\operatorname{dist}_\Sigma \circ\psi_{\mathbf{x}}(\zeta)\right)\right\|} \mathrm{d}S(\zeta),$$

which integrates along the intersection of $\Xi(\mathbf{x})$ and the lateral boundary Σ

$$\psi_{\mathbf{x}}^{-1}\left(\Xi(\mathbf{x}) \cap \Sigma\right) = \{\zeta \in \mathcal{P} : \operatorname{dist}_\Sigma \circ\psi_{\mathbf{x}}(\zeta) = 0\}.$$

These considerations yield the intermediate result

$$\mathrm{T}_k\, w(\mathbf{x}) = \int_{\psi_{\mathbf{x}}^{-1}(\Xi(\mathbf{x})\cap\Sigma)} k(x, \cdot)\circ|_x \psi_{\mathbf{x}}(\zeta) w\circ\psi_{\mathbf{x}}(\zeta) \frac{\left|\det \mathrm{D}\, \psi_{\mathbf{x}}(\zeta)\right|}{\sqrt{2}\left\|\nabla\left(\operatorname{dist}_\Sigma \circ\psi_{\mathbf{x}}(\zeta)\right)\right\|} \mathrm{d}S(\zeta). \quad (2.45)$$

Prior to elaborating (2.45), we discuss a suitable parametrization of the light cone.

Definition 2.19 (Lorentz transformation). *For $n \in \mathbb{N}$ the linear operator $\Lambda : \mathbb{R}^{n+1} \to \mathbb{R}^{n+1}$ is a Lorentz transformation if it preserves the Lorentzian inner product*

$$[\Lambda\mathbf{x}, \Lambda\mathbf{y}] = [\mathbf{x}, \mathbf{y}] \quad \forall\mathbf{x}, \mathbf{y} \in \mathbb{R}^{n+1}$$

or equivalently $M = \Lambda^\top M\Lambda$ holds. Moreover, a Lorentz transformation is denoted proper if $\det\Lambda = 1$ *holds and orthochronous if $\Lambda_{11} := \langle\Lambda\mathfrak{e}_0, \mathfrak{e}_0\rangle > 0$ holds, see [80, Sections 1.2 and 1.3].*

Lorentz transformations form a group under usual matrix multiplication; proper orthochronous Lorentz transformations form a subgroup of it [80, Section 1.3]. For any Lorentz transformation Λ Definition 2.19 implies the convenient formula

$$\Lambda^{-1} = M\Lambda^\top M \quad (2.46)$$

and applying Λ from the left and M from the right to (2.46) yields

$$M = \Lambda M\Lambda^\top,$$

implying that $\Lambda^\top$ is also a Lorentz transformation.

DEFINITION 2.20 (Light cone parametrization). *Define the parameter domain* $\mathcal{P} := [0,\infty) \times [0,2\pi) \times [0,\pi]$, *the dense subset* $\mathcal{P}_0 := (0,\infty) \times [0,2\pi) \times (0,\pi)$, *and the parameters* $\zeta := (\rho,\varphi,\theta) \in \mathcal{P}$. *Let* $\mathbf{x} \in \mathbb{R}^4$, $r_0 > 0$, *and the proper orthochronous Lorentz transformation* $\Lambda \in \mathbb{R}^{4\times 4}$ *be given. Define* $\psi_{\mathbf{x}} : \mathcal{P} \to \mathbb{R}^4$ *by*

$$\psi_{\mathbf{x}} : \zeta \mapsto \mathbf{x} - r_0\rho\Lambda \begin{pmatrix} 1 \\ e_{\mathbb{S}}(\varphi,\theta) \end{pmatrix},$$

where $e_{\mathbb{S}} : [0,2\pi) \times [0,\pi] \to \mathbb{S}^2$ *is the parametrization of the unit sphere*

$$e_{\mathbb{S}} : (\varphi,\theta) \mapsto \begin{pmatrix} \cos\varphi\sin\theta \\ \sin\varphi\sin\theta \\ \cos\theta \end{pmatrix}.$$

Convenient choices for r_0 and Λ in Definition 2.20 are discussed in Section 3.5.

LEMMA 2.21. *Let* $\psi_{\mathbf{x}}$ *be as in Definition 2.20. It holds* $\operatorname{ran}\psi_{\mathbf{x}} = \Xi(\mathbf{x})$ *and for any* $\mathbf{y} \in \Xi(\mathbf{x})$ *the solution* $\zeta \in \mathcal{P}$ *of* $\psi_{\mathbf{x}}(\zeta) = \mathbf{y}$ *is unique iff* $\zeta \in \mathcal{P}_0$ *holds.*

Proof. Definitions 2.19 and 2.20 yield for any $\zeta \in \mathcal{P}$

$$[\mathbf{x} - \psi_{\mathbf{x}}(\zeta), \mathbf{x} - \psi_{\mathbf{x}}(\zeta)] = r_0^2\rho^2 \left[\Lambda\begin{pmatrix} 1 \\ e_{\mathbb{S}} \end{pmatrix}, \Lambda\begin{pmatrix} 1 \\ e_{\mathbb{S}} \end{pmatrix}\right] = r_0^2\rho^2 \left[\begin{pmatrix} 1 \\ e_{\mathbb{S}} \end{pmatrix}, \begin{pmatrix} 1 \\ e_{\mathbb{S}} \end{pmatrix}\right] = 0 \quad (2.47)$$

because $\begin{pmatrix} 1 & e_{\mathbb{S}}^\top \end{pmatrix}^\top$ is lightlike. Note that we omit the arguments (φ,θ) of $e_{\mathbb{S}}$ for the sake of brevity. Furthermore, let $|_t\psi_{\mathbf{x}}(\zeta)$ be the time component of $\psi_{\mathbf{x}}(\zeta)$ and observe

$$t - |_t\psi_{\mathbf{x}}(\zeta) = r_0\rho\ |_t\Lambda\begin{pmatrix} 1 \\ e_{\mathbb{S}} \end{pmatrix}. \quad (2.48)$$

In (2.48), the orthochronous Lorentz transformation Λ acts on a lightlike vector and [80, Theorem 1.3.3] yields the implication

$$\operatorname{sgn}|_t\Lambda\begin{pmatrix} 1 \\ e_{\mathbb{S}} \end{pmatrix} = \operatorname{sgn}|_t\begin{pmatrix} 1 \\ e_{\mathbb{S}} \end{pmatrix} = 1.$$

The properties $r_0 > 0$ and $\rho \geq 0$ for $\zeta \in \mathcal{P}$, see Definition 2.20, lead to

$$\operatorname{sgn}(t - |_t\psi_{\mathbf{x}}(\zeta)) = \operatorname{sgn} r_0\rho \geq 0. \quad (2.49)$$

Definition 2.2 states that (2.47) and (2.49) are equivalent to $\psi_{\mathbf{x}}(\zeta) \in \Xi(\mathbf{x})$ for any $\zeta \in \mathcal{P}$, yielding $\operatorname{ran}\psi_{\mathbf{x}} \subseteq \Xi(\mathbf{x})$. Next, we show that the equation $\psi_{\mathbf{x}}(\zeta) = \mathbf{y}$ has a solution $\zeta \in \mathcal{P}$ for every $\mathbf{y} \in \Xi(\mathbf{x})$, which is equivalent to $\Xi(\mathbf{x}) \subseteq \operatorname{ran}\psi_{\mathbf{x}}$. Consider an arbitrary $\mathbf{y} \in \Xi(\mathbf{x})$ and observe that $\psi_{\mathbf{x}}(\zeta) = \mathbf{y}$ holds iff

$$\mathbf{x} - \mathbf{y} = r_0\rho\Lambda\begin{pmatrix} 1 \\ e_{\mathbb{S}}(\varphi,\theta) \end{pmatrix} \quad\Leftrightarrow\quad r_0\rho\begin{pmatrix} 1 \\ e_{\mathbb{S}}(\varphi,\theta) \end{pmatrix} = \Lambda^{-1}(\mathbf{x} - \mathbf{y}).$$

We define $\mathbf{z} := \Lambda^{-1}(\mathbf{x}-\mathbf{y})$ and use the decomposition $\mathbf{z} := (s, z)$ with $s \in \mathbb{R}$ and $z \in \mathbb{R}^3$. From $\mathbf{y} \in \Xi\,(\mathbf{x})$ it follows $[\mathbf{x}-\mathbf{y}, \mathbf{x}-\mathbf{y}] = 0$ and

$$\|z\|^2 - s^2 = [\mathbf{z}, \mathbf{z}] = \left[\Lambda^{-1}(\mathbf{x}-\mathbf{y}), \Lambda^{-1}(\mathbf{x}-\mathbf{y})\right] = [\mathbf{x}-\mathbf{y}, \mathbf{x}-\mathbf{y}] = 0,$$

implying $|s| = \|z\|$ and $s = 0$ iff $z = 0$. It follows that $\psi_{\mathbf{x}}(\zeta) = \mathbf{y}$ holds iff

$$r_0\rho = s \quad \wedge \quad r_0\rho e_{\mathbb{S}}(\varphi, \theta) = z. \tag{2.50}$$

From the first condition in (2.50) we deduce $\rho = s/r_0$, implying $\rho = 0$ iff $s = 0$ iff $z = 0$ iff $\mathbf{y} = \mathbf{x}$. For $\mathbf{y} \in \Xi\,(\mathbf{x}) \setminus \{\mathbf{x}\}$ we have $t - \tau > 0$ and since Λ^{-1} is orthochronous [80, Theorem 1.3.3] implies $s > 0$ and consequently $\rho > 0$. In this case, (2.50) holds true iff $e_{\mathbb{S}}(\varphi, \theta) = z/s$. The right hand side satisfies $\|z/s\| = 1$, i.e., it is in the range of $e_{\mathbb{S}}$. We conclude that $\Xi\,(\mathbf{x}) \subseteq \operatorname{ran}\psi_{\mathbf{x}}$ and eventually $\operatorname{ran}\psi_{\mathbf{x}} = \Xi\,(\mathbf{x})$ hold true. Concerning the uniqueness result recall that for $\rho = 0$ we have $z = 0$ and the second condition in (2.50) holds for any (φ, θ). For $\rho > 0$ the pair $(\varphi, \theta) \in [0, 2\pi) \times [0, \pi]$ such that $e_{\mathbb{S}}(\varphi, \theta) = z/s$ holds is unique iff $\sin\theta \neq 0$, i.e., $\theta \notin \{0, \pi\}$. □

Lemma 2.21 indicates that only the restriction of $\psi_{\mathbf{x}}$ to $\mathcal{P}_0$ is injective. Therefore, we expect $|\det \mathrm{D}\,\psi_{\mathbf{x}}\,(\zeta)| = 0$ for $\zeta \in \mathcal{P} \setminus \mathcal{P}_0$. As we shall see in Proposition 3.15 and Lemma 3.16 this behavior helps in lifting the singularities of the kernel functions in (2.32). We introduce the matrix representation J_ψ of the derivative $\mathrm{D}\,\psi_{\mathbf{x}}$

$$\mathrm{D}\,\psi_{\mathbf{x}} : \zeta \mapsto J_\psi(\zeta) := \begin{pmatrix}\partial_\rho\psi_{\mathbf{x}}(\zeta) & \partial_\varphi\psi_{\mathbf{x}}(\zeta) & \partial_\theta\psi_{\mathbf{x}}(\zeta)\end{pmatrix} \in \mathbb{R}^{4\times 3}.$$

Define the matrix of partial derivatives of the map $\zeta \mapsto \rho\begin{pmatrix}1 & e_{\mathbb{S}}^\top(\varphi, \theta)\end{pmatrix}^\top$ by

$$T_\psi(\zeta) := \begin{pmatrix} 1 & 0 & 0 \\ \cos\varphi\sin\theta & -\rho\sin\varphi\sin\theta & \rho\cos\varphi\cos\theta \\ \sin\varphi\sin\theta & \rho\cos\varphi\sin\theta & \rho\sin\varphi\cos\theta \\ \cos\theta & 0 & -\rho\sin\theta \end{pmatrix} \in \mathbb{R}^{4\times 3}, \tag{2.51}$$

whose columns are denoted $e_i^\psi(\zeta)$, $i = 1, 2, 3$. We have $\left\langle e_i^\psi(\zeta), e_j^\psi(\zeta)\right\rangle = 0$ for any $\zeta \in \mathcal{P}$ and $i \neq j$. Moreover, for any $\zeta \in \mathcal{P}$ we observe

$$\left\|e_1^\psi(\zeta)\right\| = \sqrt{2}, \quad \left\|e_2^\psi(\zeta)\right\| = \rho\sin\theta, \quad \left\|e_3^\psi(\zeta)\right\| = \rho,$$

and $J_\psi(\zeta) = -r_0\Lambda T_\psi(\zeta)$. For any $\zeta \in \mathcal{P}_0$ it holds $\operatorname{rank} T_\psi(\zeta) = 3$ and

$$\ker T_\psi^\top(\zeta) = \operatorname{span}\{M e_1^\psi(\zeta)\} = \operatorname{span}\left\{\begin{pmatrix}-1 & \cos\varphi\sin\theta & \sin\varphi\sin\theta & \cos\theta\end{pmatrix}^\top\right\}. \tag{2.52}$$

The product rule and (2.3) yield

$$\nabla\left(\operatorname{dist}_\Sigma \circ\psi_{\mathbf{x}}(\zeta)\right) = J_\psi^\top\left(\nu_\Sigma \circ \psi_{\mathbf{x}}(\zeta)\right)$$

for $\zeta \in \psi_{\mathbf{x}}^{-1}(\Xi(\mathbf{x}) \cap \Sigma)$. The following representation is obtained from (2.45)

$$\mathrm{T}_k\, w(\mathbf{x}) = \int_{\psi_{\mathbf{x}}^{-1}(\Xi(\mathbf{x})\cap\Sigma)} k(x,\cdot) \circ |_x \psi_{\mathbf{x}}(\zeta) w \circ \psi_{\mathbf{x}}(\zeta) \frac{|\det \mathrm{D}\, \psi_{\mathbf{x}}(\zeta)|}{\sqrt{2}\left\| J_\psi^\top (\nu_\Sigma \circ \psi_{\mathbf{x}}(\zeta))\right\|} \mathrm{d}S(\zeta). \quad (2.53)$$

Similar to Section 2.6.1, the behavior of the denominator $\zeta \mapsto J_\psi^\top(\nu_\Sigma \circ \psi_{\mathbf{x}}(\zeta))$ is of particular interest. For the sake of brevity, we shall not derive an analogue to Lemma 2.17, however, we provide a slightly weaker property in the following proposition. Nevertheless, Section 3.5 establishes a choice of Λ in Definition 3.11 which leads to a bound comparable to Lemma 2.17, see Proposition 3.15.

PROPOSITION 2.22. *Let $\zeta \in \mathcal{P}_0$ and $v \in \ker J_\psi^\top(\zeta)$. It follows $[v,v] = 0$, or in other words, v is lightlike.*

Proof. From $J_\psi^\top(\zeta)v = -r_0 T_\psi^\top(\zeta)\Lambda^\top v$ and $r_0 > 0$ it follows $v \in \ker J_\psi^\top(\zeta)$ iff $\Lambda^\top v \in \ker T_\psi^\top(\zeta)$. For $\zeta \in \mathcal{P}_0$ we have $\ker T_\psi^\top(\zeta) = \operatorname{span}\{M e_1^\psi(\zeta)\}$ by (2.52). Consequently, there exists an $\alpha \in \mathbb{R}$ such that $\Lambda^\top v = \alpha M e_1^\psi(\zeta)$ holds and

$$\left[\Lambda^\top v, \Lambda^\top v\right] = \alpha^2 \left[M e_1^\psi(\zeta), M e_1^\psi(\zeta)\right] = \alpha^2 \left[e_1^\psi(\zeta), e_1^\psi(\zeta)\right] = 0.$$

It follows $0 = \left[\Lambda^\top v, \Lambda^\top v\right] = [v,v]$ since $\Lambda^\top$ is a Lorentz transformation. ☐

Proposition 2.22 predicts that the denominator in (2.53) is zero only if $\nu_\Sigma \circ \psi_{\mathbf{x}}(\zeta)$ is lightlike at $\zeta \in \mathcal{P}_0$ such that $\psi_{\mathbf{x}}(\zeta) \in \Sigma$ holds. Recall that (2.41) implies that the normal vector is lightlike iff the absolute value of the normal velocity is 1.

3 SPACE-TIME BOUNDARY ELEMENT METHOD

This chapter discusses a novel discretization scheme for the variational problems exhibited in Section 2.5. In Section 3.1, the employed boundary element spaces are introduced. These trial spaces treat time and space variables uniformly. Section 3.4 investigates the geometric interpretation of the discretized integral in (2.42). The discretized variational problems considered in this thesis are discussed in Sections 3.2 and 3.3. Section 3.5 is dedicated towards the evaluation of the retarded potential integrals derived in Section 2.6.2. In Sections 3.6 and 3.7, we provide a quadrature technique for the bilinear forms of Section 2.5. Finally, Section 3.8 glimpses at implementational aspects. Several of these results are already published in [89].

3.1 Simplex Meshes and Space-Time Boundary Elements

The proposed space-time boundary element method is based on simplex decompositions of the hypersurface Σ. As in Definition 2.4, we employ a mesh $\Sigma_N = \{\sigma_i\}_{i=1}^N$ of $N \in \mathbb{N}$ panels. Each panel $\sigma \in \Sigma_N$ is a tetrahedron, which is the image of the reference simplex $\widehat{\sigma}$ under the affine transformation $\chi_\sigma : \widehat{\sigma} \to \sigma$

$$\chi_\sigma : \xi \mapsto \mathbf{x}_\sigma + J_\sigma \xi, \tag{3.1}$$

with the vertex $\mathbf{x}_\sigma \in \partial\sigma$ and the Jacobi matrix $J_\sigma \in \mathbb{R}^{4\times 3}$. We denote by $\operatorname{ran} J_\sigma$ the range of the mapping $\mathbb{R}^3 \to \mathbb{R}^4$ induced by $\xi \mapsto J_\sigma \xi$. The tangent hyperplane is denoted $\mathcal{T}_\sigma := \{\mathbf{x}_\sigma\} + \operatorname{ran} J_\sigma$ and $\operatorname{rank} J_\sigma = 3$ implies that $\operatorname{ran} J_\sigma$ is the three-dimensional tangent space of the panel. The normal vector of the panel $\nu_\sigma \in \mathbb{S}^3$ is orthogonal to the tangent space

$$\big(\operatorname{ran} J_\sigma\big)^\perp := \{v \in \mathbb{R}^4 : \langle v, z\rangle = 0 \ \ \forall z \in \operatorname{ran} J_\sigma\} = \ker J_\sigma^\top = \operatorname{span}\{\nu_\sigma\},$$

where $(\cdot)^\perp$ denotes the orthogonal complement. From the first-order parametrization (3.1) it follows that the Gramian matrix $G_\sigma = J_\sigma^\top J_\sigma$ and its determinant $\big|\det \mathrm{D}\,\chi_\sigma\big| = \sqrt{\det G_\sigma} = |\sigma|/|\widehat{\sigma}|$ are constant for each panel. A tentative visualization of such a space-time hypersurface panel is exhibited in Figure 3.1. Furthermore, define the local and global mesh sizes by

$$h_\sigma := \operatorname{diam}\sigma = \sup_{\mathbf{x},\mathbf{y}\in\sigma} \|\mathbf{x}-\mathbf{y}\|, \quad h := \max_{\sigma\in\Sigma_N} h_\sigma, \quad h_{\min} := \min_{\sigma\in\Sigma_N} h_\sigma.$$

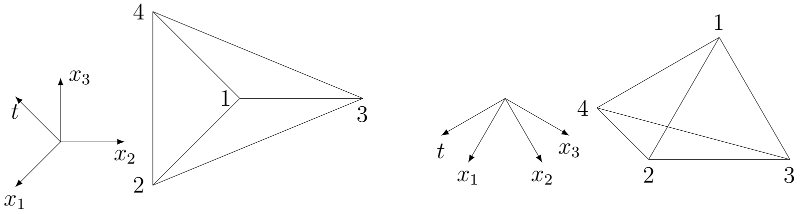

Figure 3.1: Two wireframe depictions of the tetrahedron defined by the four corners $\mathbf{x}_1 := 0\mathfrak{e}_0$, $\mathbf{x}_2 := 1\mathfrak{e}_1$, $\mathbf{x}_3 := 1\mathfrak{e}_2$, and $\mathbf{x}_4 := 1\mathfrak{e}_0$. Here, $\{\mathfrak{e}_i\}_{i=0}^3$ denotes the Cartesian basis introduced in Section 2.1 and t indicates the $\mathfrak{e}_0$ direction, while x_i represents the $\mathfrak{e}_i$ direction for $i = 1, 2, 3$. The projections of the base vectors are displayed shifted away from the origin. To provide a better sense of orientation, the number at each corner indicates its index.

Let $r_\sigma > 0$ be the radius of the inscribed sphere of the simplex $\sigma \in \Sigma_N$. Note that the inscribed sphere of an n-simplex, which is tangent to all faces, exists and is unique [112, Proposition 4.1].

DEFINITION 3.1 (Shape regularity, quasiuniformity). *A sequence of meshes* $(\Sigma_N)_{N\in\mathbb{N}}$ *is called shape regular if there exists a* $c_S > 0$ *such that*

$$\sup_{N\in\mathbb{N}} \max_{\sigma\in\Sigma_N} \frac{h_\sigma}{r_\sigma} \le c_S$$

holds and quasiuniform if there exists a $c_U > 0$ *satisfying the following inequality*

$$\sup_{N\in\mathbb{N}} \frac{h}{h_{\min}} = \sup_{N\in\mathbb{N}} \frac{\max_{\sigma\in\Sigma_N} h_\sigma}{\min_{\sigma\in\Sigma_N} h_\sigma} \le c_U.$$

In the tests conducted in Chapter 4, all employed families of meshes are devoid of hanging nodes, shape regular, and quasiuniform. The meshes are generated by the algorithm proposed in [60]. In the considered case, the algorithm requires a decomposition of Γ into triangles, which is obtained by standard meshing techniques. Each triangle is extruded to a space-time prism which is decomposed into three tetrahedrons. Other strategies for the meshing of space-time domains are exhibited in [16, 33]. Alternatively, certain meshing schemes respect locally the causal structure of the underlying hyperbolic problem, known as tent-pitching schemes [114].

DEFINITION 3.2 (Space-time boundary element spaces). *Let $\mathbb{P}_p(\widehat{\sigma})$ be the space of polynomials in the reference simplex of degree up to $p \in \mathbb{N}_0$. Define for $p \in \mathbb{N}_0$ the discontinuous boundary element space*

$$S_p^{\mathrm{d}}(\Sigma_N) \coloneqq \{w : \Sigma \to \mathbb{R} \mid w \circ \chi_\sigma \in \mathbb{P}_p(\widehat{\sigma}) \ \ \forall \sigma \in \Sigma_N\},$$

with $\dim S_p^{\mathrm{d}}(\Sigma_N) = \frac{1}{6}(p+1)(p+2)(p+3)N$. *For $p \in \mathbb{N}$ define the continuous space*

$$S_p^{\mathrm{c}}(\Sigma_N) \coloneqq S_p^{\mathrm{d}}(\Sigma_N) \cap C(\Sigma).$$

We use standard Lagrange functions as a basis for these spaces, see [20, Sections 2.2 and 2.3] or [19, Section 2.2]. In order to construct such a basis for $S_p^{\mathrm{c}}(\Sigma_N)$ in the usual way, we require that Σ_N is devoid of hanging nodes. The space $S_p^{\mathrm{d}}(\Sigma_N)$ is intended to discretize $\mathcal{H}_0$ of Section 2.5, while $S_p^{\mathrm{c}}(\Sigma_N)$ is used to approximate $\mathcal{H}_1$.

REMARK 3.3. *Although Definition 3.2 appears inconspicuous, it marks a cornerstone of this work. The trial spaces stem from unstructured meshes of the space-time boundary Σ. There is no inherent distinction between space and time variables.*

In the remainder of this section, we discuss orthogonal projections involving the trial spaces of Definition 3.2. While these projections are well-studied, their discretization in Section 3.2 serves as a convenient tool for code verification in Section 4.1. We denote by $L^2(\Sigma)$ the usual Lebesgue space of square integrable functions on Σ. It is a Hilbert space equipped with the inner product $(\cdot,\cdot)_{L^2(\Sigma)} : L^2(\Sigma) \times L^2(\Sigma) \to \mathbb{R}$, $(w, v) \mapsto \int_\Sigma wv \,\mathrm{d}S$. Let $W \subset L^2(\Sigma)$ be a closed subspace and $w \in L^2(\Sigma)$; consider the problem:

$$\text{Find } w_h \in W: \ (w_h, z)_{L^2(\Sigma)} = (w, z)_{L^2(\Sigma)} \quad \forall z \in W. \tag{3.2}$$

Furthermore, we employ the Sobolev space $H^1(\Sigma) \coloneqq \{v \in L^2(\Sigma) : \nabla_\Sigma v \in L^2(\Sigma)\}$, where ∇_Σ denotes the weak surface gradient. Let $H^1_{0,\cdot}(\Sigma) \coloneqq \{v \in H^1(\Sigma) : v|_{\{0\}\times\Gamma} = 0\}$ be the subspace with homogeneous initial values. The notation $v|_{\{0\}\times\Gamma}$ should be understood as follows: the trace of $v \in H^1(\Sigma)$ to $\partial\Sigma = \{0, T\} \times \Gamma$ is performed, which is then restricted to the subset $\{0\} \times \Gamma$. The quadratic form $v \mapsto (\nabla_\Sigma v, \nabla_\Sigma v)_{L^2(\Sigma)}$ defines the square of a norm in $H^1_{0,\cdot}(\Sigma)$ due to the Poincaré inequality, see, e.g., [100, Theorem 2.5.7, Corollary 2.5.8]. Consequently, we may define a projection onto $H^1_{0,\cdot}(\Sigma)$ based on the scalar product $(\nabla_\Sigma \cdot, \nabla_\Sigma \cdot)_{L^2(\Sigma)}$. Let $V \subset H^1_{0,\cdot}(\Sigma)$ be a closed subspace and $v \in H^1_{0,\cdot}(\Sigma)$; consider the problem:

$$\text{Find } v_h \in V: \ (\nabla_\Sigma v_h, \nabla_\Sigma z)_{L^2(\Sigma)} = (\nabla_\Sigma v, \nabla_\Sigma z)_{L^2(\Sigma)} \quad \forall z \in V. \tag{3.3}$$

By the Hilbert projection theorem, see, e.g., [122, Theorem 1 of Section III.1], both (3.2) and (3.3) are uniquely solvable. Since the error is orthogonal to the solution space, i.e., $w - w_h \in W^\perp$ in (3.2) and $v - v_h \in V^\perp$ in (3.3) hold, its norm is minimal

$$\|w - w_h\|_{L^2(\Sigma)} = \inf_{z_h \in W} \|w - z_h\|_{L^2(\Sigma)}, \quad \|v - v_h\|_{H^1_{0,\cdot}(\Sigma)} = \inf_{z_h \in V} \|v - z_h\|_{H^1_{0,\cdot}(\Sigma)}.$$

We close this section by stating a posteriori error estimates, which will be of significance in Section 4.1. They are proven in [100, Section 4.3] for boundary element spaces defined on the two-dimensional surface Γ. However, most of the proofs can be translated word by word to n-simplex meshes of n-dimensional hypersurfaces, provided that the families of meshes obey Definition 3.1. Precise assumptions on the smoothness of the solutions are omitted in favor of simplicity. For sufficiently smooth $w \in L^2(\Sigma)$ [100, Theorem 4.3.19] suggests

$$\min_{w_h \in S_p^{\mathrm{d}}(\Sigma_N)} \|w - w_h\|_{L^2(\Sigma)} = \mathcal{O}\left(h^{p+1}\right) \tag{3.4}$$

as $h \to 0$. For sufficiently smooth $w \in L^2(\Sigma)$ and $v \in H^1(\Sigma)$ [100, Theorem 4.3.22] predicts the behavior

$$\min_{v_h \in S_p^{\mathrm{c}}(\Sigma_N)} \|w - v_h\|_{L^2(\Sigma)} = \mathcal{O}\left(h^{p+1}\right), \qquad \min_{v_h \in S_p^{\mathrm{c}}(\Sigma_N)} \|v - v_h\|_{H^1(\Sigma)} = \mathcal{O}\left(h^{p}\right). \tag{3.5}$$

3.2 Orthogonal Projections onto Boundary Element Spaces

This section investigates the discretization of (3.2) and (3.3). It serves as a preparatory step for the discretization of the variational problems of Section 2.5, which is discussed in Section 3.3. Let S be a finite-dimensional vector space over the field $\mathbb{R}$ with the fixed basis $\{e_i\}_{i=1}^{\dim S}$. The space S is a placeholder for the trial spaces of Definition 3.2. For $w \in S$ let $\mathsf{w} \in \mathbb{R}^{\dim S}$ be the coefficient vector such that

$$w = \sum\nolimits_{i=1}^{\dim S} \mathsf{w}_i e_i \tag{3.6}$$

holds, where $\mathsf{w}_i \in \mathbb{R}$ denotes the ith entry of w.

Proposition 3.4. *The linear map* $\mathrm{R}_S : S \to \mathbb{R}^{\dim S}$, $w \mapsto \mathsf{w}$ *satisfying* (3.6) *is well-defined iff the vectors* $\{e_i\}_{i=1}^{\dim S}$ *are linearly independent. In this case* R_S *is a bijection.*

Proof. For an arbitrary $w \in S$ assume that there exist $\mathsf{w}, \mathsf{v} \in \mathbb{R}^{\dim S}$ such that $\mathrm{R}_S w = \mathsf{w}$ and $\mathrm{R}_S w = \mathsf{v}$ hold. Application of (3.6) yields

$$w = \sum\nolimits_{i=1}^{\dim S} \mathsf{w}_i e_i = \sum\nolimits_{i=1}^{\dim S} \mathsf{v}_i e_i \quad \Leftrightarrow \quad \sum\nolimits_{i=1}^{\dim S} (\mathsf{w}_i - \mathsf{v}_i)\, e_i = 0.$$

It follows $\mathsf{w}_i = \mathsf{v}_i$ for $i = 1, \ldots, \dim S$ and, therefore, $\mathsf{w} = \mathsf{v}$ iff the vectors $\{e_i\}_{i=1}^{\dim S}$ are linearly independent. For $w, v \in S$ and $\alpha \in \mathbb{R}$ the linearity of R_S is an immediate consequence of

$$\alpha w + \alpha v = \alpha \sum\nolimits_{i=1}^{\dim S} \mathsf{w}_i e_i + \alpha \sum\nolimits_{i=1}^{\dim S} \mathsf{v}_i e_i = \sum\nolimits_{i=1}^{\dim S} \alpha\, (\mathsf{w}_i + \mathsf{v}_i)\, e_i$$

for $\mathrm{R}_S w = \mathsf{w}$ and $\mathrm{R}_S v = \mathsf{v}$. From $\mathsf{w} = \mathsf{0}$ it follows $w = 0$ and, therefore, injectivity of R_S by $\ker \mathrm{R}_S = \{0\}$. Since $\dim S$ is finite, R_S is injective iff it is surjective. ☐

The map R_S is typically known as Ritz isomorphism, see [86, Section 1.2.3].

PROPOSITION 3.5. *Let V be a vector space over the field $\mathbb{R}$, $S \subset V$ be finite-dimensional, and $b : V \times V \to \mathbb{R}$ be a bilinear form. Define $\mathsf{B} \in \mathbb{R}^{\dim S \times \dim S}$ by its coefficients $\mathsf{B}_{ij} := b(e_j, e_i)$ for $i, j = 1, \dots, \dim S$. It holds*

(i) $b(w,v) = b(v,w) \quad \forall w, v \in V \quad \Rightarrow \quad \mathsf{B} = \mathsf{B}^\top$,

(ii) $\big(b(w,w) = 0 \Leftrightarrow w = 0\big) \quad \Rightarrow \quad \big(\mathsf{w}^\top \mathsf{B} \mathsf{w} \Leftrightarrow \mathsf{w} = \mathsf{0}\big)$.

Proof. For any $w, v \in S \subset V$ it holds $b(w,v) = \mathsf{v}^\top \mathsf{B} \mathsf{w}$ with $\mathsf{w} = \mathrm{R}_S\, w$ and $\mathsf{v} = \mathrm{R}_S\, v$. In order to show (i) assume that $b(w,v) = b(v,w)$ holds and observe

$$\mathsf{B}_{ij} = b(e_j, e_i) = b(e_i, e_j) = \mathsf{B}_{ji} \quad \forall i, j = 1 \dots, \dim S.$$

To show (ii) note that $w = 0$ yields $\mathsf{w} = \mathsf{0}$ due to Proposition 3.4. Therefore, if $\mathsf{w}^\top \mathsf{B} \mathsf{w} = b(w,w) = 0$ implies $w = 0$ then $\mathsf{w} = \mathsf{0}$ follows and the proof is complete. ☐

Let S be either $S_p^{\mathrm{d}}(\Sigma_N)$ or $S_p^{\mathrm{c}}(\Sigma_N)$ from Definition 3.2. For $f \in L^2(\Sigma)$ its $L^2(\Sigma)$-orthogonal projection onto S (3.2) is equivalent to the linear system

$$\mathsf{M}\mathsf{w} = \mathsf{r}, \tag{3.7}$$

with the mass matrix $\mathsf{M} \in \mathbb{R}^{\dim S \times \dim S}$ and $\mathsf{r} \in \mathbb{R}^{\dim S}$ defined by

$$\mathsf{M}_{ij} := (e_j, e_i)_{L^2(\Sigma)}, \quad \mathsf{r}_i := (f, e_i)_{L^2(\Sigma)}.$$

The solution $\mathsf{w} \in \mathbb{R}^{\dim S}$ is identified with $w_h \in S$ solving (3.2) for $W = S$ and right hand side f via $\mathsf{w} = \mathrm{R}_S\, w_h$. Application of (2.2) for $w, v \in L^2(\Sigma)$ yields

$$(w,v)_{L^2(\Sigma)} = \int_\Sigma wv \mathrm{d}S = \sum\nolimits_{\sigma \in \Sigma_N} \int_{\widehat{\sigma}} w \circ \chi_\sigma v \circ \chi_\sigma \left|\det \mathrm{D}\, \chi_\sigma\right| \mathrm{d}\xi$$

and the use of affine parametrizations (3.1) enables the simplification

$$\mathsf{M}_{ij} = \sum\nolimits_{\sigma \in \Sigma_N} \frac{|\sigma|}{|\widehat{\sigma}|} \int_{\widehat{\sigma}} e_j \circ \chi_\sigma e_i \circ \chi_\sigma \mathrm{d}\xi, \quad \mathsf{r}_i = \sum\nolimits_{\sigma \in \Sigma_N} \frac{|\sigma|}{|\widehat{\sigma}|} \int_{\widehat{\sigma}} f \circ \chi_\sigma e_i \circ \chi_\sigma \mathrm{d}\xi.$$

We switch our attention to (3.3). Let $S := S_p^{\mathrm{c}}(\Sigma_N) \cap H^1_{0,\cdot}(\Sigma)$ and for $f \in H^1_{0,\cdot}(\Sigma)$ its $H^1_{0,\cdot}(\Sigma)$-orthogonal projection onto S leads to

$$\mathsf{H}\mathsf{v} = \mathsf{r}, \tag{3.8}$$

with the stiffness matrix $\mathsf{H} \in \mathbb{R}^{\dim S \times \dim S}$ and $\mathsf{r} \in \mathbb{R}^{\dim S}$ defined by

$$\mathsf{H}_{ij} := (\nabla_\Sigma e_j, \nabla_\Sigma e_i)_{L^2(\Sigma)}, \quad \mathsf{r}_i := (\nabla_\Sigma f, \nabla_\Sigma e_i)_{L^2(\Sigma)}.$$

The coefficient vector $\mathsf{v} \in \mathbb{R}^{\dim S}$ is identified with the solution v_h of (3.3) for $V = S$ and right hand side f via $\mathsf{v} = \mathrm{R}_S\, v_h$. For $w, v \in H^1(\Sigma)$ we observe

$$(\nabla_\Sigma w, \nabla_\Sigma v)_{L^2(\Sigma)} = \int_\Sigma \langle \nabla_\Sigma w, \nabla_\Sigma v \rangle \,\mathrm{d}S$$

$$= \sum\nolimits_{\sigma \in \Sigma_N} \int_{\widehat{\sigma}} \big\langle (\nabla_\Sigma w) \circ \chi_\sigma, (\nabla_\Sigma v) \circ \chi_\sigma \big\rangle \left|\det \mathrm{D}\, \chi_\sigma\right| \mathrm{d}\xi$$

and $(\nabla_\Sigma w) \circ \chi_\sigma = J_\sigma G_\sigma^{-1} \nabla(w \circ \chi_\sigma)$, see [100, Equation (3.79)], as well as (3.1) yield

$$\mathsf{H}_{ij} = \sum\nolimits_{\sigma \in \Sigma_N} \frac{|\sigma|}{|\widehat{\sigma}|} \int_{\widehat{\sigma}} \big\langle G_\sigma^{-1} \nabla(e_j \circ \chi_\sigma), \nabla(e_i \circ \chi_\sigma) \big\rangle \,\mathrm{d}\xi.$$

Note that $G_\sigma \in \mathbb{R}^{3\times 3}$ is constant for each panel. The right hand side is given by

$$\mathsf{r}_i = \sum\nolimits_{\sigma \in \Sigma_N} \frac{|\sigma|}{|\widehat{\sigma}|} \int_{\widehat{\sigma}} \big\langle G_\sigma^{-1} J_\sigma^\top (\nabla_\Sigma f) \circ \chi_\sigma, \nabla(e_i \circ \chi_\sigma) \big\rangle \,\mathrm{d}\xi.$$

The computation of $\nabla_\Sigma f$ is particularly convenient if $f \in H^1(\Sigma)$ can be extended to a neighborhood around Σ. For our purposes in Section 4.1 such an extension f^* is readily available. If f^* is sufficiently smooth and $\gamma_0 f^* = f$ holds, then it follows

$$\nabla_\Sigma f = \mathrm{P}_\sigma\, \nabla f^* := \nabla f^* - \langle \nabla f^*, \nu_\sigma \rangle\, \nu_\sigma,$$

where $\mathrm{P}_\sigma : \mathbb{R}^4 \to \operatorname{ran} J_\sigma$ denotes the projector to the tangent space. From $\ker J_\sigma^\top = \operatorname{span}\{\nu_\sigma\}$ it follows $J_\sigma^\top \nabla_\Sigma f = J_\sigma^\top \nabla f^*$.

The matrices M and H are symmetric and positive definite due to Proposition 3.5. However, for w in either $S_p^{\mathrm{d}}(\Sigma_N)$ or $S_p^{\mathrm{c}}(\Sigma_N)$ as in Definition 3.2, the norm equivalence of $\|\mathsf{w}\|_2$ and $\|w\|_{L^2(\Sigma)}$ depends on the mesh. Here, $\|\cdot\|_2$ denotes the usual vector 2-norm. For $v \in S_p^{\mathrm{c}}(\Sigma_N) \cap H^1_{0,\cdot}(\Sigma)$ we shall see that the equivalence of $\|\mathsf{v}\|_2$ and $\|\nabla_\Sigma v\|_{L^2(\Sigma)}$ depends even more critically on the mesh. In order to keep the exposition simple, the sequence of meshes is assumed to adhere to Definition 3.1. In [100, Section 4.4], such norm equivalences are proven for trial spaces on the two-dimensional surface Γ. Nevertheless, most arguments used in the proofs of the cited reference can be transferred to n-simplex meshes of n-dimensional hypersurfaces, if the families of meshes obey Definition 3.1. The major quantitative deviation for different values of $n \in \mathbb{N}$ is

$$|\sigma| \sim h_\sigma^n,$$

which is naturally fixed to $n = 2$ in the cited source. In the n-dimensional setting [100, Theorem 4.4.7] suggests the existence of $0 < c_1 \leq c_2$ such that

$$c_1 h^{n/2} \|\mathsf{w}\|_2 \leq \|w\|_{L^2(\Sigma)} \leq c_2 h^{n/2} \|\mathsf{w}\|_2$$

holds for w in a Lagrange-type piecewise polynomial space. In our context

$$c_1 h^{3/2} \left\| \mathsf{w} \right\|_2 \leq \left\| w \right\|_{L^2(\Sigma)} \leq c_2 h^{3/2} \left\| \mathsf{w} \right\|_2$$

would hold for w in either $S_p^{\mathrm{d}}(\Sigma_N)$ or $S_p^{\mathrm{c}}(\Sigma_N)$. Moreover, for $v \in S_p^{\mathrm{c}}(\Sigma_N)$ [100, Theorem 4.4.3] hints that the inverse inequality

$$\left\| v \right\|_{H^1(\Sigma)} \leq C h^{-1} \left\| v \right\|_{L^2(\Sigma)}$$

holds for some $C > 0$. These estimates would imply

$$h^3 \left\| \mathsf{w} \right\|_2^2 \lesssim \mathsf{w}^\top \mathsf{M} \mathsf{w} \lesssim h^3 \left\| \mathsf{w} \right\|_2^2, \quad h^3 \left\| \mathsf{w} \right\|_2^2 \lesssim \mathsf{w}^\top \mathsf{H} \mathsf{w} \lesssim h \left\| \mathsf{w} \right\|_2^2,$$

where the constants are suppressed. The Rayleigh quotient yields the estimates for the extremal eigenvalues

$$h^3 \lesssim \lambda_{\min}(\mathsf{M}) \leq \lambda_{\max}(\mathsf{M}) \lesssim h^3, \quad h^3 \lesssim \lambda_{\min}(\mathsf{H}) \leq \lambda_{\max}(\mathsf{H}) \lesssim h^1.$$

Since M and H are symmetric and have full rank, their spectral condition numbers can be computed from $\lambda_{\max}/\lambda_{\min}$. This leads to

$$\mathrm{cond}_2(\mathsf{M}) \lesssim 1, \quad \mathrm{cond}_2(\mathsf{H}) \lesssim h^{-2}.$$

In our implementation, (3.7) and (3.8) are solved via the conjugate gradient method, see [54] or [99, Section 6.7]. The number of iterations necessary to achieve a fixed level of accuracy behaves like $\mathcal{O}\left(\sqrt{\mathrm{cond}_2}\right)$. In particular, for (3.8) this suggests that the behavior of number of iterations is $\mathcal{O}\left(h^{-1}\right)$. A possible remedy is constituted by preconditioning techniques. We merely employ a simple Jacobi preconditioner; more intricate procedures exceed the purposes of this thesis.

3.3 Discretized Variational Boundary Integral Equations

This section exhibits discretizations of the variational problems discussed in Section 2.5. The trial spaces are chosen according to Definition 3.2, leading to genuine space-time discretizations of RPBIEs. We restrict our considerations to boundary element spaces of lowest order. On the one hand, a curved boundary Σ is approximated by the simplex panels introduced in Section 3.1 only in a first-order fashion. On the other hand, this choice simplifies the integrals in Section 3.6. With the aid of the spaces introduced in Definition 3.2 we define the trial spaces

$$U_h \coloneqq S_0^{\mathrm{d}}(\Sigma_N), \quad V_h \coloneqq S_1^{\mathrm{c}}(\Sigma_N) \cap H_{0,\cdot}^1(\Sigma),$$

where U_h is intended to discretize $\mathcal{H}_0$, while V_h should approximate $\mathcal{H}_1$ of Section 2.5. It holds $\dim U_h = N$ and $\dim V_h$ equals the number of vertices of Σ_N minus the number of vertices located at initial time. These spaces are equipped with the bases

$$U_h = \operatorname{span}\left\{e_i^0\right\}_{i=1}^{N}, \quad V_h = \operatorname{span}\left\{e_i^1\right\}_{i=1}^{\dim V_h}.$$

The basis functions of U_h are the indicator functions for $i = 1, \dots, N$

$$e_i^0 : \mathbf{x} \mapsto \begin{cases} 1 & \text{if } \mathbf{x} \in \sigma_i, \\ 0 & \text{otherwise,} \end{cases}$$

where each panel in Σ_N possesses a unique label in $\{1, \dots, N\}$. We choose the usual hat functions as basis functions for V_h.

In (2.27) the Dirichlet data g_D appear under the action of the integral operator K. In such cases it is common practice in BEMs for elliptic problems to approximate the data, see [108, Chapter 12]. Assuming that $g_D \in L^2(\Sigma)$ holds, the $L^2(\Sigma)$-orthogonal projection (3.2) of g_D onto V_h is denoted by g_h. It is the unique solution of:

$$\text{Find } g_h \in V_h : \ (g_h, z_h)_{L^2(\Sigma)} = (g_D, z_h)_{L^2(\Sigma)} \quad \forall z_h \in V_h. \tag{3.9}$$

This intermediate approximation leads to the discretization of (2.27) based on U_h:

$$\text{Find } w_h \in U_h : \ b_{\mathrm{V}}(w_h, z_h) = -\mathfrak{d}\frac{1}{2}\ell_{g_h}(z_h) + b_{\mathrm{K}}(g_h, z_h) \ \ \forall z_h \in U_h. \tag{3.10}$$

Once (3.10) is solved for the approximate Neumann unknown $w_h \approx \gamma_1^{\mathfrak{d}} u$, the corresponding wave field is due to Kirchhoff's formula (2.17)

$$u_h := \mathfrak{d}\left(\mathrm{D}\, g_h - \mathrm{S}\, w_h\right). \tag{3.11}$$

Similarly, the discretization of (2.28) via U_h is given by:

$$\text{Find } w_h \in U_h : \ b_{\mathrm{V}}(w_h, z_h) = \ell_{g_D}(z_h) \ \ \forall z_h \in U_h. \tag{3.12}$$

Note that the right hand side in (3.10) features the approximate data g_h, however, (3.12) involves the exact data g_D. Solving (3.12) for the proxy density w_h yields the related wave field by means of the single layer potential ansatz (2.19)

$$u_h := \mathrm{S}\, w_h. \tag{3.13}$$

Analogously, we consider the discretization of (2.29) based on V_h:

$$\text{Find } v_h \in V_h : \ b_{\mathrm{W}}(v_h, z_h) = \ell_{g_N}(z_h) \ \ \forall z_h \in V_h. \tag{3.14}$$

Once (3.14) is solved for the proxy density v_h, the corresponding wave field is given by the double layer potential ansatz (2.21)

$$u_h := -\,\mathrm{D}\, v_h. \tag{3.15}$$

Remark 3.6. *The solutions u_h in* (3.11), (3.13), *and* (3.15) *are defined exclusively via actions of the potentials* S *and* D, *or more succinctly*

$$u_h \in \operatorname{span}\{\operatorname{ran}\mathrm{S}, \operatorname{ran}\mathrm{D}\}.$$

This notation, however, should be understood formally because we never defined the domains of S *and* D *clearly. Retarded layer potentials are solution operators of the transmission problems* (2.10) *and* (2.11), *see Section 2.4. As a result, any element of* $\operatorname{ran}\mathrm{S}$ *or* $\operatorname{ran}\mathrm{D}$ *satisfies* (2.12), *implying that u_h satisfies* (2.12) *by construction. It follows that u_h enjoys the properties predicted by Theorems 2.7 and 2.8 (we tacitly disregard the classical regularity assumptions in these theorems). The approximation u_h inherits all key properties of exact solutions of the d'Alembertian, like energy conservation and propagation of information at unit velocity. The linearity of all involved operators compels the error $u-u_h$ to satisfy* (2.12) *as well. This intriguing property proves to be of great use in its mathematical analysis [104, Chapter 5]. We conclude that the sole source of the error $u-u_h$ is the inexact enforcement of the boundary condition.*

In the remainder of this chapter we discuss linear systems equivalent to the exhibited variational problems. First, the computation of the approximate data g_h in (3.9) is examined. To this end, define the mass matrix $\mathsf{M} \in \mathbb{R}^{\dim V_h \times \dim V_h}$ and the right hand side $\mathsf{r}^P \in \mathbb{R}^{\dim V_h}$ by

$$\mathsf{M}_{ij} := \left(e_j^1, e_i^1\right)_{L^2(\Sigma)}, \quad \mathsf{r}_i^P := \left(g_D, e_i^1\right)_{L^2(\Sigma)}.$$

By virtue of the Ritz isomorphism $\mathrm{R}_{V_h} : V_h \to \mathbb{R}^{\dim V_h}$ (3.9) is equivalent to

$$\mathsf{M}\mathsf{g} = \mathsf{r}^P$$

for $\mathsf{g} = \mathrm{R}_{V_h} g_h$. Next, we introduce the matrices of the bilinear forms in (3.10), (3.12), and (3.14). Let $\mathsf{V} \in \mathbb{R}^{N\times N}$, $\mathsf{K} \in \mathbb{R}^{N\times \dim V_h}$, and $\mathsf{W} \in \mathbb{R}^{\dim V_h \times \dim V_h}$ be defined by

$$\mathsf{V}_{ij} := b_{\mathrm{V}}\left(e_j^0, e_i^0\right), \quad \mathsf{K}_{ij} := b_{\mathrm{K}}\left(e_j^1, e_i^0\right), \quad \mathsf{W}_{ij} := b_{\mathrm{W}}\left(e_j^1, e_i^1\right).$$

The entries of the first two matrices read in a more explicit fashion

$$\mathsf{V}_{ij} = \int_\Sigma \partial_t e_i^0(\mathbf{x})\, \mathrm{V}\, e_j^0(\mathbf{x}) \mathrm{d}S(\mathbf{x}), \quad \mathsf{K}_{ij} = \int_\Sigma \partial_t e_i^0(\mathbf{x})\, \mathrm{K}\, e_j^1(\mathbf{x}) \mathrm{d}S(\mathbf{x}).$$

Moreover, define the auxiliary matrix $\mathsf{A} \in \mathbb{R}^{N\times \dim V_h}$ by

$$\mathsf{A}_{ij} := \int_\Sigma \partial_t e_i^0(\mathbf{x}) e_i^1(\mathbf{x}) \mathrm{d}S(\mathbf{x})$$

such that it holds $[\mathsf{Ag}]_i = \ell_{g_h}(e_i^0)$. With these matrices (3.10) is equivalent to

$$\mathsf{Vw} = -\mathfrak{d}\frac{1}{2}\mathsf{Ag} + \mathsf{Kg}$$

for $\mathsf{w} = \mathrm{R}_{U_h}\, w_h$. Furthermore, (3.12) is equivalent to

$$\mathsf{Vw} = \mathsf{r}^D,$$

with the right hand side $\mathsf{r}^D \in \mathbb{R}^N$ defined by $\mathsf{r}_i^D \coloneqq \ell_{g_D}(e_i^0)$. Finally, with the aid of the identification $\mathsf{v} = \mathrm{R}_{V_h}\, v_h$ (3.14) is equivalent to

$$\mathsf{Wv} = \mathsf{r}^N,$$

where $\mathsf{r}^N \in \mathbb{R}^{\dim V_h}$ is defined by $\mathsf{r}_i^N \coloneqq \ell_{g_N}(e_i^1)$.

REMARK 3.7. *The strong Huygens principle endows the matrices* V, K, *and* W *with a special sparsity pattern. In classical schemes based on semi-discretization they are block lower triangular (if indexed correctly), see [4, 102]. If a constant time step size is chosen these matrices feature a block lower triangular Toeplitz structure, reducing the computational complexity of their assembly, see [102, Remark 2]. This property hinges on the fact that the involved operators depend only on the time separation* $t-\tau$, *a property which would be surrendered if the weighted bilinear forms of Remark 2.13 were used. This, in conjunction with a deterioration of the condition number [3, Section 6], is the reason why nonweighted bilinear forms are preferred. In the context of unstructured space-time discretizations, the rationale outlined in Section 3.8.3 encourages the conjecture that each row of* V, K, *and* W *has at most* $\mathcal{O}\left(N^{2/3}\right)$ *nonzero entries as* $N \to \infty$ *for meshes obeying Definition 3.1. These matrices have* $\mathcal{O}(N)$ *rows and columns, yielding an* $\mathcal{O}\left(N^{5/3}\right)$ *behavior of the total number of nonzero entries. The relative density (number of nonzero entries divided by entries) satisfies*

$$\lim_{N\to\infty} \frac{\#\,\text{nonzero entries}}{\#\,\text{entries}} \lesssim \lim_{N\to\infty} \frac{N^{5/3}}{N^2} = 0,$$

supporting the claimed sparsity. The behavior $N \sim h^{-3}$ *implies a computational complexity of* $\mathcal{O}\left(N^{5/3}\right) \sim \mathcal{O}\left(h^{-5}\right)$ *for the assembly of* V, K, *and* W. *To alleviate the order of complexity, we employ meshes* Σ_N *constructed by stacking the simplex mesh of a space-time slab repeatedly on top of itself, see Figure 1.1b. The resulting block lower triangular Toeplitz structure of the involved matrices reduces the (speculated) complexity from* $\mathcal{O}\left(h^{-5}\right)$ *to* $\mathcal{O}\left(h^{-4}\right)$ *for meshes as in Definition 3.1. This order of complexity is optimal in the sense that it matches the (negative) number of space-time dimensions. The design of fast methods capable of approximating RPBIEs on unstructured space-meshes, as in Figure 1.1c, in nigh* $\mathcal{O}\left(h^{-4}\right)$ *complexity is well beyond the scope of this work. Nevertheless, many key results of this thesis, like the integral formulas in Sections 2.6.1 and 2.6.2 and the quadrature procedures in Sections 3.5, 3.6 and 3.8.1 are valid for unstructured space-time meshes.*

We conclude this segment about linear systems related to RPBIEs by providing a formula for the matrix W. It exploits (2.35), which relates the bilinear form b_{W} to b_{V} via tangential differential operators. The following notation is introduced for the sake of clarity. Consider a given vector $z \in \mathbb{R}^3$ and denote its ith component by $|_i z$. Using the Cartesian basis $\{\mathfrak{e}_i\}_{i=0}^{3}$ of Section 2.1 we have

$$|_i z = \left\langle \begin{pmatrix} 0 \\ z \end{pmatrix}, \mathfrak{e}_i \right\rangle$$

for $i = 1, 2, 3$. With this notation (2.35) can be rewritten as

$$b_{\mathrm{W}}(w, v) = \sum\nolimits_{k=1}^{3} b_{\mathrm{V}}\left(|_k \mathrm{curl}_\Gamma\, w, |_k \mathrm{curl}_\Gamma\, v\right) + \sum\nolimits_{k=1}^{3} b_{\mathrm{V}}\left(|_k \nu_\Gamma \partial_t w, |_k \nu_\Gamma \partial_t v\right). \tag{3.16}$$

Let $v_h \in V_h$ and $\sigma \in \Sigma_N$, consider the formula for ∇_Σ already used in Section 3.2

$$(\nabla_\Sigma v_h) \circ \chi_\sigma = J_\sigma G_\sigma^{-1} \nabla (v_h \circ \chi_\sigma).$$

For $v_h \in V_h \subset S_1^{\mathrm{c}}(\Sigma_N)$ we have $v_h \circ \chi_\sigma \in \mathbb{P}_1(\widehat{\sigma})$, consequently $\nabla(v_h \circ \chi_\sigma) \in \left(\mathbb{P}_0(\widehat{\sigma})\right)^3$ holds. The matrices J_σ and G_σ are constant due to the affine parametrization introduced in Section 3.1. It follows that $(\nabla_\Sigma v_h) \circ \chi_\sigma \in \left(\mathbb{P}_0(\widehat{\sigma})\right)^4$ holds and, therefore, the weak surface gradient maps $\nabla_\Sigma : V_h \to (U_h)^4$. This leads to

$$\mathrm{curl}_\Gamma\, v_h \in (U_h)^3, \quad \nu_{\sigma,x} \partial_t v_h \in (U_h)^3$$

because the normal vector $\nu_\sigma \in \mathbb{S}^3$ is constant. For $k = 1, 2, 3$ define the matrix $\mathsf{C}^k \in \mathbb{R}^{\dim V_h \times N}$ for the surface curl of the basis of V_h

$$\mathsf{C}^k_{ij} := |_k \mathrm{curl}_\Gamma\, e^1_i(\mathbf{y}_j) = \left\langle \begin{pmatrix} 0 \\ \mathrm{curl}_\Gamma\, e^1_i(\mathbf{y}_j) \end{pmatrix}, \mathfrak{e}_k \right\rangle$$

and $\mathsf{N}^k \in \mathbb{R}^{\dim V_h \times N}$ for the product of normal vector and time derivative of V_h

$$\mathsf{N}^k_{ij} := |_k \nu_\Gamma \partial_t e^1_i(\mathbf{y}_j) = \left\langle \nu_{\sigma_j}, \mathfrak{e}_k \right\rangle \partial_t e^1_i(\mathbf{y}_j),$$

where $\mathbf{y}_j \in \sigma_j, j = 1, \dots, N$ is an arbitrary point in the panel. These matrices are sparse because the support of $e^1_i, i = 1, \dots, \dim V_h$ is the closure of the union of all panels that share the vertex associated to the ith degree of freedom. The relations

$$|_k \mathrm{curl}_\Gamma\, e^1_i(\mathbf{x}) = \sum\nolimits_{m=1}^{N} \mathsf{C}^k_{im} e^0_m(\mathbf{x}), \quad |_k \nu_\Gamma \partial_t e^1_i(\mathbf{x}) = \sum\nolimits_{m=1}^{N} \mathsf{N}^k_{im} e^0_m(\mathbf{x})$$

hold true for $\mathbf{x} \in \Sigma$. We observe for the first term in (3.16)

$$\begin{aligned} b_{\mathrm{V}}\left(|_k \mathrm{curl}_\Gamma\, e^1_j, |_k \mathrm{curl}_\Gamma\, e^1_i\right) &= b_{\mathrm{V}}\left(\sum_m \mathsf{C}^k_{jm} e^0_m, \sum_n \mathsf{C}^k_{in} e^0_n\right) \\ &= \sum_n \sum_m \mathsf{C}^k_{in} b_{\mathrm{V}}\left(e^0_m, e^0_n\right) \mathsf{C}^k_{jm} = \sum_n \sum_m \mathsf{C}^k_{in} \mathsf{V}_{nm} \mathsf{C}^k_{jm}, \end{aligned}$$

where we identify the matrix of the single layer potential operator $\mathsf{V}_{nm} = b_{\mathrm{V}}\left(e^0_m, e^0_n\right)$ for $m, n = 1, \ldots, N$. Treating the second term in (3.16) in the same fashion yields

$$\mathsf{W} = \sum\nolimits_{k=1}^{3} \mathsf{C}^k\, \mathsf{V}\left(\mathsf{C}^k\right)^\top + \sum\nolimits_{k=1}^{3} \mathsf{N}^k\, \mathsf{V}\left(\mathsf{N}^k\right)^\top .$$

This identity enables the computation of W directly from V. The derivation is based on similar investigations for Laplace's equation, see, e.g., [93, Section 2.3.2].

Unlike the case of elliptic self-adjoint operators, neither b_{V} nor b_{W} are symmetric, leading to nonsymmetric matrices V and W. Estimates for their condition number are not obvious, due to the intricacy of the correct functional setting of variational formulations of RPBIEs. If the experience from BIEs of elliptic self-adjoint operators [108, Lemmas 12.6 and 12.9] indeed carried over to hyperbolic RPBIEs, the spectral condition numbers of both V and W were expected to behave like $\mathcal{O}\left(h^{-1}\right)$ as $h \to 0$.

3.4 Intersection of Simplex Panel and Light Cone

A crucial result of Section 2.6.1 displayed in (2.42) is that the retarded potential T_k integrates along the intersection $\Xi\left(\mathbf{x}\right) \cap \sigma$. In the following paragraphs, we thoroughly investigate the geometric meaning of $\Xi\left(\mathbf{x}\right) \cap \sigma$ for tetrahedral panels σ as introduced in Section 3.1. As in Section 2.6, we shall assume that the boundary moves, i.e., the panel σ describes a motion at constant normal velocity $v_\sigma := -\nu_{\sigma,t} / \left\|\nu_{\sigma,x}\right\|$.

Throughout this section we consider an arbitrary but fixed evaluation point $\mathbf{x} \in \mathbb{R}^4$ and a tetrahedral panel $\sigma \in \Sigma_N$ as discussed in Section 3.1. Rather than treating $\Xi\left(\mathbf{x}\right) \cap \sigma$ directly, we deal with the superset

$$\left(\Upsilon\left(\mathbf{x}\right) \cup \Xi\left(\mathbf{x}\right)\right) \cap \mathcal{T}_\sigma = \left\{\mathbf{y} \in \mathbb{R}^4 : \left[\mathbf{x} - \mathbf{y}, \mathbf{x} - \mathbf{y}\right] = 0\right\} \cap \mathcal{T}_\sigma, \tag{3.17}$$

which is the intersection of the double light cone and the hyperplane induced by the panel, see Definition 2.2. In this context, note that the affine map χ_σ of (3.1) can be defined in entire $\mathbb{R}^3$. In a slight abuse of notation, the domain of the affine transformation χ_σ is extended to $\mathbb{R}^3$ and we observe $\chi_\sigma\left(\mathbb{R}^3\right) = \mathcal{T}_\sigma$. With the aid of this extended parametrization we have

$$\chi_\sigma^{-1}\left(\left\{\mathbf{y} \in \mathbb{R}^4 : \left[\mathbf{x} - \mathbf{y}, \mathbf{x} - \mathbf{y}\right] = 0\right\} \cap \mathcal{T}_\sigma\right) = \left\{\xi \in \mathbb{R}^3 : Q^{\mathbf{x}}_\sigma(\xi) = 0\right\},$$

with the quadratic function $Q^{\mathbf{x}}_\sigma : \mathbb{R}^3 \to \mathbb{R}$ defined by $Q^{\mathbf{x}}_\sigma : \xi \mapsto \left[\mathbf{x} - \chi_\sigma(\xi), \mathbf{x} - \chi_\sigma(\xi)\right]$. It remains to investigate the quadric $\left\{\xi \in \mathbb{R}^3 : Q^{\mathbf{x}}_\sigma(\xi) = 0\right\}$. Insertion of (3.1) yields

$$Q^{\mathbf{x}}_\sigma : \xi \mapsto \left\langle A_\sigma \xi, \xi\right\rangle + 2\left\langle b^{\mathbf{x}}_\sigma, \xi\right\rangle + \left[\mathbf{x} - \mathbf{x}_\sigma, \mathbf{x} - \mathbf{x}_\sigma\right],$$

where $A_\sigma \in \mathbb{R}^{3\times 3}$ and $b_\sigma^{\mathbf{x}} \in \mathbb{R}^3$ are defined by

$$A_\sigma := J_\sigma^\top M J_\sigma, \quad b_\sigma^{\mathbf{x}} := -J_\sigma^\top M\left(\mathbf{x} - \mathbf{x}_\sigma\right).$$

Here, $M \in \mathbb{R}^{4\times 4}$ denotes the metric tensor introduced in Section 2.1. Let $\lambda_1^\sigma \leq \lambda_2^\sigma \leq \lambda_3^\sigma$ be the eigenvalues of the symmetric matrix A_σ. The symmetry of A_σ implies the existence of the diagonalization $A_\sigma = E_\sigma D_\sigma E_\sigma^\top$, where $D_\sigma := \operatorname{diag}\{\lambda_i^\sigma\}_{i=1}^3$ is diagonal and $E_\sigma \in \mathbb{R}^{3\times 3}$ is orthogonal, i.e., $E_\sigma^{-1} = E_\sigma^\top$ holds.

LEMMA 3.8. *It holds* $\operatorname{sgn} \lambda_1^\sigma = -\operatorname{sgn}\left[\nu_\sigma, \nu_\sigma\right]$ *and* $0 < \lambda_2^\sigma \leq \lambda_3^\sigma$.

Proof. In favor of brevity we omit all sub- and superscripts related to σ in this proof. The normalization of ν, i.e., $1 = \|\nu\|^2 = \nu_t^2 + \|\nu_x\|^2$ yields

$$[\nu, \nu] = \|\nu_x\|^2 - \nu_t^2 = 2\|\nu_x\|^2 - 1 = 1 - 2\nu_t^2. \tag{3.18}$$

It holds $A = J^\top M J = J^\top J - 2 j_t j_t^\top$, where $j_t \in \mathbb{R}^3$ is the first column of $J^\top$. From $\operatorname{rank} J = 3$ it follows that $J^\top J$ is symmetric positive definite and, therefore, A has at most one nonpositive eigenvalue [44, p. 325], yielding $0 < \lambda_2 \leq \lambda_3$. It follows

$$\lambda_1 < 0 \quad \Leftrightarrow \quad \exists x \in \mathbb{R}^3 \setminus \{0\} : \langle Ax, x\rangle < 0 \quad \Leftrightarrow \quad \exists \mathbf{y} \in \operatorname{ran} J \setminus \{0\} : [\mathbf{y}, \mathbf{y}] < 0,$$

where we used $\langle Ax, x\rangle = [Jx, Jx]$. It holds $\mathbf{y} \in \operatorname{ran} J$ iff $\mathbf{y} \perp \ker J^\top$ and since ν spans $\ker J^\top$ it has to hold $0 = \langle \mathbf{y}, \nu\rangle = \tau\nu_t + \langle y, \nu_x\rangle$, leading to

$$\lambda_1 < 0 \quad \Leftrightarrow \quad \exists \mathbf{y} \in \mathbb{R}^4 \setminus \{0\} : \langle y, \nu_x\rangle = -\tau\nu_t \quad \wedge \quad \|y\|^2 - \tau^2 < 0.$$

If $\nu_t = 0$ holds we may choose $\tau \in \mathbb{R} \setminus \{0\}$ and $y = 0$ to confirm that above condition is satisfied and, therefore, $\lambda_1 < 0$ holds. From (3.18) it follows that $\nu_t = 0$ implies $[\nu, \nu] > 0$, conforming to the assertion. For $\nu_t \neq 0$ we have

$$\langle y, \nu_x\rangle = -\tau\nu_t \quad \Leftrightarrow \quad \tau = -\frac{\langle y, \nu_x\rangle}{\nu_t} \quad \Rightarrow \quad \tau^2 = \frac{\langle y, \nu_x\rangle^2}{1 - \|\nu_x\|^2},$$

where we used the normalization of ν. It follows

$$\lambda_1 < 0 \quad \Leftrightarrow \quad \exists y \in \mathbb{R}^3 \setminus \{0\} : \|y\|^2 < \frac{\langle y, \nu_x\rangle^2}{1 - \|\nu_x\|^2} \quad \Leftrightarrow \quad \max_{y \in \mathbb{R}^3 \setminus \{0\}} \frac{\langle y, \nu_x\rangle^2}{\|y\|^2} > 1 - \|\nu_x\|^2$$

and we note that the maximum is attained by $y = \nu_x$, which can be confirmed by the Cauchy-Schwarz inequality. Finally, we obtain

$$\lambda_1 < 0 \quad \Leftrightarrow \quad \|\nu_x\|^2 > 1/2 \quad \Leftrightarrow \quad [\nu, \nu] > 0,$$

where the latter implication is due to (3.18). Combining above results for $\nu_t = 0$ and $\nu_t \neq 0$ yields $\lambda_1 < 0 \Leftrightarrow [\nu, \nu] > 0$. Since all eigenvalues but λ_1 are certainly positive, $\lambda_1 = 0$ holds iff the kernel of $A = J^\top M J$ is nontrivial

$$\lambda_1 = 0 \quad \Leftrightarrow \quad \exists x \in \mathbb{R}^3 \setminus \{0\} : J^\top M J x = 0 \quad \Leftrightarrow \quad \exists x \in \mathbb{R}^3 \setminus \{0\} : M J x \in \ker J^\top.$$

We obtain by virtue of $\ker J^\top = \operatorname{span}\{\nu\}$ and $M = M^{-1}$

$$\lambda_1 = 0 \quad \Leftrightarrow \quad \exists x \in \mathbb{R}^3 \setminus \{0\}, \alpha \in \mathbb{R} \setminus \{0\} : Jx = \alpha M \nu.$$

A solution to $Jx = \alpha M\nu$ exists iff the right hand side is orthogonal to $\ker J^\top$

$$\exists x \in \mathbb{R}^3 : Jx = \alpha M \nu \quad \Leftrightarrow \quad 0 = \langle \alpha M \nu, \nu \rangle = \alpha \, [\nu, \nu]$$

and the equivalence $\lambda_1 = 0 \Leftrightarrow [\nu, \nu] = 0$ follows. We conclude $\lambda_1 > 0 \Leftrightarrow [\nu, \nu] < 0$ by exclusion. □

The matrix A_σ is regular iff $\big[v_\sigma, v_\sigma\big] \neq 0$ holds due to Lemma 3.8. In this case, we define the origin $\xi_\sigma^{\mathbf{x}} := -A_\sigma^{-1} b_\sigma^{\mathbf{x}}$ and the principal axes transform $\kappa_\sigma^{\mathbf{x}} : \mathbb{R}^3 \to \mathbb{R}^3$ by

$$\kappa_\sigma^{\mathbf{x}} : \eta \mapsto \xi_\sigma^{\mathbf{x}} + E_\sigma \eta. \tag{3.19}$$

This leads to the quadratic function in principal coordinates

$$Q_\sigma^{\mathbf{x}} \circ \kappa_\sigma^{\mathbf{x}} : \eta \mapsto \big\langle D_\sigma \eta, \eta \big\rangle + c_\sigma^{\mathbf{x}},$$

with $c_\sigma^{\mathbf{x}} := \big\langle \xi_\sigma^{\mathbf{x}}, b_\sigma^{\mathbf{x}} \big\rangle + \big[\mathbf{x} - \mathbf{x}_\sigma, \mathbf{x} - \mathbf{x}_\sigma\big]$.

LEMMA 3.9. *If* $[\nu_\sigma, \nu_\sigma] \neq 0$ *holds it follows* $c_\sigma^{\mathbf{x}} = \big\langle \mathbf{x} - \mathbf{x}_\sigma, \nu_\sigma \big\rangle^2 / [\nu_\sigma, \nu_\sigma]$.

Proof. The assumption $[\nu_\sigma, \nu_\sigma] \neq 0$ implies the invertibility of A_σ by Lemma 3.8. Consequently, the solution $\xi_\sigma^{\mathbf{x}}$ of $A_\sigma \xi_\sigma^{\mathbf{x}} = -b_\sigma^{\mathbf{x}}$ is unique. Insertion of the definitions of A_σ and $b_\sigma^{\mathbf{x}}$ yields

$$A_\sigma \xi_\sigma^{\mathbf{x}} = -b_\sigma^{\mathbf{x}} \quad \Leftrightarrow \quad J_\sigma^\top M J_\sigma \xi_\sigma^{\mathbf{x}} = J_\sigma^\top M (\mathbf{x} - \mathbf{x}_\sigma) \quad \Leftrightarrow \quad J_\sigma^\top M \big(J_\sigma \xi_\sigma^{\mathbf{x}} - (\mathbf{x} - \mathbf{x}_\sigma) \big) = 0,$$

which is equivalent to $M \big(J_\sigma \xi_\sigma^{\mathbf{x}} - (\mathbf{x} - \mathbf{x}_\sigma) \big) \in \ker J_\sigma^\top$ or

$$\exists \beta \in \mathbb{R} : J_\sigma \xi_\sigma^{\mathbf{x}} = \mathbf{x} - \mathbf{x}_\sigma + \beta M \nu_\sigma,$$

where we used $M = M^{-1}$ and $\ker J_\sigma^\top = \operatorname{span}\{\nu_\sigma\}$. The right hand side $\mathbf{x} - \mathbf{x}_\sigma + \beta M \nu_\sigma$ is in $\operatorname{ran} J_\sigma$ iff it is orthogonal to $\ker J_\sigma^\top$. Therefore, $\big\langle \mathbf{x} - \mathbf{x}_\sigma + \beta M \nu_\sigma, \nu_\sigma \big\rangle = 0$ must hold and $\beta = -\big\langle \mathbf{x} - \mathbf{x}_\sigma, \nu_\sigma \big\rangle / [\nu_\sigma, \nu_\sigma]$ follows. Insertion into $c_\sigma^{\mathbf{x}}$ leads to

$$\begin{aligned} c_\sigma^{\mathbf{x}} &= \big\langle \xi_\sigma^{\mathbf{x}}, b_\sigma^{\mathbf{x}} \big\rangle + \big[\mathbf{x} - \mathbf{x}_\sigma, \mathbf{x} - \mathbf{x}_\sigma\big] = -\big\langle J_\sigma^\top M (\mathbf{x} - \mathbf{x}_\sigma), \xi_\sigma^{\mathbf{x}} \big\rangle + \big\langle M(\mathbf{x} - \mathbf{x}_\sigma), \mathbf{x} - \mathbf{x}_\sigma \big\rangle \\ &= \big\langle M(\mathbf{x} - \mathbf{x}_\sigma), \mathbf{x} - \mathbf{x}_\sigma - J_\sigma \xi_\sigma^{\mathbf{x}} \big\rangle = -\beta \big\langle M(\mathbf{x} - \mathbf{x}_\sigma), M \nu_\sigma \big\rangle \\ &= \big\langle \mathbf{x} - \mathbf{x}_\sigma, \nu_\sigma \big\rangle^2 / [\nu_\sigma, \nu_\sigma]. \end{aligned}$$

□

Assuming that $\left[v_\sigma, v_\sigma\right] \neq 0$ holds the principal axes transform (3.19) and Lemma 3.9 lead to the diagonalized quadratic function

$$Q_\sigma^{\mathbf{x}} \circ \kappa_\sigma^{\mathbf{x}} : \eta \mapsto c_\sigma^{\mathbf{x}} + \sum\nolimits_{i=1}^{3} \lambda_i^\sigma \eta_i, \tag{3.20}$$

with $c_\sigma^{\mathbf{x}} = \left\langle \mathbf{x} - \mathbf{x}_\sigma, \nu_\sigma \right\rangle^2 / \left[\nu_\sigma, \nu_\sigma\right]$. Clearly, $c_\sigma^{\mathbf{x}} = 0$ holds iff $\left\langle \mathbf{x} - \mathbf{x}_\sigma, \nu_\sigma \right\rangle = 0$, or equivalently $\mathbf{x} \in \mathcal{T}_\sigma$. We summarize the following conclusions about the zero level set of (3.20):

- $[\nu_\sigma, \nu_\sigma] > 0$: Lemmas 3.8 and 3.9 imply that $\lambda_1^\sigma < 0$ and $c_\sigma^{\mathbf{x}} \geq 0$ hold. The zero level set of (3.20) is an elliptic double cone if $\mathbf{x} \in \mathcal{T}_\sigma$ or an elliptic hyperboloid of two sheets if $\mathbf{x} \notin \mathcal{T}_\sigma$. One cone of the double cone or one sheet of the hyperboloid corresponds to the forward light cone $\Upsilon(\mathbf{x})$, while the other one is associated to the backward light cone $\Xi(\mathbf{x})$.
- $[\nu_\sigma, \nu_\sigma] < 0$: It holds $\lambda_1^\sigma > 0$ and $c_\sigma^{\mathbf{x}} \leq 0$ by Lemmas 3.8 and 3.9. The zero level set of (3.20) is an ellipsoid if $\mathbf{x} \notin \mathcal{T}_\sigma$ or degenerates to a point if $\mathbf{x} \in \mathcal{T}_\sigma$.
- The case $[\nu_\sigma, \nu_\sigma] = 0$ would require a different definition of the origin $\xi_\sigma^{\mathbf{x}}$ because A_σ is irregular. One might be inclined to conclude that the zero level set is an elliptic paraboloid in this case. We emphasize that $[\nu_\sigma, \nu_\sigma] = 0$ implies $|v_\sigma| = 1$ and, therefore, Lemma 2.17 does not yield an upper bound for the term due to the coarea formula in (2.42).

The set (3.17) is the image of the zero level set of (3.20) under affine transformation

$$\{\mathbf{y} \in \mathbb{R}^4 : [\mathbf{x} - \mathbf{y}, \mathbf{x} - \mathbf{y}] = 0\} \cap \mathcal{T}_\sigma = \chi_\sigma \circ \kappa_\sigma^{\mathbf{x}} \left(\left\{\eta \in \mathbb{R}^3 : Q_\sigma^{\mathbf{x}} \circ \kappa_\sigma^{\mathbf{x}}(\eta) = 0\right\}\right).$$

Therefore, above conclusions about the shape of the zero level set of (3.20) can be transferred directly to (3.17). Recall from Section 2.6 and Remark 2.18 that the case $[\nu_\sigma, \nu_\sigma] \leq 0$ is not deemed valuable for solutions of the d'Alembertian and is motivated by mere curiosity. In the relevant case $[\nu_\sigma, \nu_\sigma] > 0$, the set $\Xi(\mathbf{x}) \cap \mathcal{T}_\sigma$ is a two-dimensional cone if $\mathbf{x} \in \mathcal{T}_\sigma$ or one sheet of a two-sheeted (two-dimensional) hyperboloid for $\mathbf{x} \notin \mathcal{T}_\sigma$. Finally, $\Xi(\mathbf{x}) \cap \sigma$ is a proper subset of $\Xi(\mathbf{x}) \cap \mathcal{T}_\sigma$.

3.5 Pointwise Evaluation of Retarded Layer Potentials

In this section, we introduce an integration scheme for evaluations of the retarded potential T_k of Definition 2.16. The approach is tailored to piecewise flat decompositions of Σ into tetrahedrons, as discussed in Section 3.1. In principle, either (2.42) or (2.53) could be used as a starting point for deriving such procedures. In [89], we propose a quadrature method based on (2.42). In this thesis, we discuss a procedure for evaluating T_k via (2.53). From our point of view, the approach developed in this section can be seen as a competitive alternative to the technique exhibited in [89].

Inserting the simplex decomposition Σ_N of Section 3.1 into (2.53) yields

$$\mathrm{T}_k\, w(\mathbf{x}) = \sum_{\sigma\in\Sigma_N} \int_{\psi_{\mathbf{x}}^{-1}(\Xi(\mathbf{x})\cap\sigma)} k(x,\cdot)\circ|_x\psi_{\mathbf{x}}(\zeta) w\circ\psi_{\mathbf{x}}(\zeta) \frac{|\det \mathrm{D}\,\psi_{\mathbf{x}}(\zeta)|}{\sqrt{2}\left\|J_\psi^\top(\zeta)\nu_\sigma\right\|} \mathrm{d}S(\zeta). \quad (3.21)$$

In order to implement the retarded potential T_k, we require a numerical integration scheme capable of evaluating above formula for any combination of $\mathbf{x}\in\mathbb{R}^4$ and $\sigma\in\Sigma_N$. To this end, the following integral is examined throughout this section.

Definition 3.10 (Inner integral). *Consider the integral in* (3.21)*. Let* $\mathbf{x}\in\mathbb{R}^4$ *be arbitrary but fixed and* σ *be a tetrahedron embedded in* $\mathbb{R}^4$ *with normal vector* $\nu\in\mathbb{S}^3$*. The unit outward conormal vectors of the triangular faces of the tetrahedron* $\nu_i\in\mathbb{S}^3, i=1,\dots,4$ *satisfy* $\langle\nu,\nu_i\rangle=0$*. Let* $k:\mathbb{R}^3\times\mathbb{R}^3\to\mathbb{R}$ *be as in* (2.32) *or* (2.34)*,* $w:\sigma\to\mathbb{R}$ *be analytic, and* $\psi_{\mathbf{x}}:\mathcal{P}\to\Xi(\mathbf{x})$ *be as in Definition 2.20. Define the integral kernel* $k_\psi:\mathcal{P}\to\mathbb{R}$ *and the integral* $\mathcal{I}$ *by*

$$k_\psi:\zeta\mapsto\frac{k(x,\cdot)\circ|_x\psi_{\mathbf{x}}(\zeta)\,|\det\mathrm{D}\,\psi_{\mathbf{x}}(\zeta)|}{\sqrt{2}\left\|J_\psi^\top(\zeta)\nu\right\|},\qquad \mathcal{I}:=\int_{\psi_{\mathbf{x}}^{-1}(\Xi(\mathbf{x})\cap\sigma)} k_\psi(\zeta)w\circ\psi_{\mathbf{x}}(\zeta)\mathrm{d}S(\zeta).$$

The notation of Definition 3.10 is employed from here on. Let $v_\sigma := -\nu_t/\left\|\nu_x\right\|$ be the constant normal velocity of σ, see Section 3.4. Recall the tangent hyperplane of the panel $\mathcal{T}_\sigma=\{\mathbf{y}\in\mathbb{R}^4:\langle\mathbf{y}-\mathbf{x}_\sigma,\nu\rangle=0\}$ for an arbitrary point $\mathbf{x}_\sigma\in\overline{\sigma}$. Each triangular face of σ induces the half-space $\{\mathbf{y}\in\mathbb{R}^4:\langle\mathbf{y}-\mathbf{x}_i,\nu_i\rangle<0\}$ for some vertex $\mathbf{x}_i$ in the ith face, $i=1,\dots,4$. The panel σ is the intersection of $\mathcal{T}_\sigma$ and the four half-spaces

$$\sigma=\{\mathbf{y}\in\mathcal{T}_\sigma:\langle\mathbf{y}-\mathbf{x}_i,\nu_i\rangle<0\quad\forall\, i=1,\dots,4\}. \quad (3.22)$$

For $\zeta\in\mathcal{P}$ the condition $\psi_{\mathbf{x}}(\zeta)\in\mathcal{T}_\sigma$, with $\psi_{\mathbf{x}}$ as in Definition 2.20, is equivalent to

$$0=\left\langle\mathbf{x}-r_0\rho\Lambda\begin{pmatrix}1\\ e_{\mathbb{S}}(\varphi,\theta)\end{pmatrix}-\mathbf{x}_\sigma,\nu\right\rangle=\langle\mathbf{x}-\mathbf{x}_\sigma,\nu\rangle-r_0\rho\left\langle\begin{pmatrix}1\\ e_{\mathbb{S}}(\varphi,\theta)\end{pmatrix},\Lambda^\top\nu\right\rangle$$

and

$$\psi_{\mathbf{x}}(\zeta)\in\mathcal{T}_\sigma\quad\Leftrightarrow\quad\langle\mathbf{x}-\mathbf{x}_\sigma,\nu\rangle=r_0\rho\left\langle\begin{pmatrix}1\\ \cos\varphi\sin\theta\\ \sin\varphi\sin\theta\\ \cos\theta\end{pmatrix},\Lambda^\top\nu\right\rangle. \quad (3.23)$$

In general, the set of parameters $\zeta=(\rho,\varphi,\theta)$ solving (3.23) features a convoluted behavior with respect to all three components. However, the Lorentz transformation Λ can be chosen such that (3.23) is simplified immensely, see Figure 3.2. That is

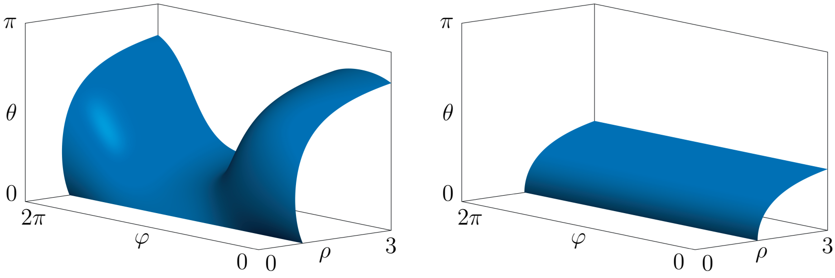

a) basic choice $\Lambda := I$ b) Λ chosen as in Definition 3.11

Figure 3.2: In the illustrated example, the hyperplane $\mathcal{T}_\sigma$ is given by $\mathbf{x}_\sigma := (2\ 1\ 1\ 1)^\top$ and $\nu := \frac{1}{2}(1\ 1\ 1\ 1)^\top$. The shaded surface is the solution of (3.23), i.e., $\psi_{\mathbf{x}}^{-1}\left(\Xi(\mathbf{x}) \cap \mathcal{T}_\sigma\right)$, for $\mathbf{x} := \mathbf{x}_\sigma + 1\nu$ and $r_0 := 1$. In Figure 3.2b, Λ is chosen according to Definition 3.11, thereby reducing (3.23) to (3.25).

why Λ is introduced in Definition 2.20 in the first place. Two auxiliary matrices are established in order to construct Λ. For $R \in SO(3)$, the special orthogonal group of rotation matrices, define $\Lambda_R \in \mathbb{R}^{4\times 4}$ by

$$\Lambda_R := \begin{pmatrix} 1 & \\ & R \end{pmatrix}.$$

For $\beta \in (-1,1)$ define the Lorentz boost in x_3-direction $\Lambda_3(\beta) \in \mathbb{R}^{4\times 4}$ by

$$\Lambda_3(\beta) := \begin{pmatrix} \gamma(\beta) & & & -\beta\gamma(\beta) \\ & 1 & & \\ & & 1 & \\ -\beta\gamma(\beta) & & & \gamma(\beta) \end{pmatrix},$$

where $\gamma(\beta) := 1/\sqrt{1-\beta^2}$ is the Lorentz factor. It is obvious that $\Lambda_R \in SO(4)$ holds and one can easily verify that both Λ_R and $\Lambda_3(\beta)$ are proper orthochronous Lorentz transformations in the sense of Definition 2.19. Therefore, their product also obeys Definition 2.19 and the proposed transformation can be stated.

Definition 3.11. *Let $\mathcal{T}_\sigma$ be equipped with the normal vector $\nu \in \mathbb{S}^3$ with spatial component $\nu_x \in \mathbb{R}^3$ and normal velocity $v_\sigma \in (-1,1)$. Set $R \in SO(3)$ such that*

$$R^\top \nu_x = \begin{pmatrix} 0 & 0 & \|\nu_x\| \end{pmatrix}^\top$$

holds and define the proper orthochronous Lorentz transformation by

$$\Lambda := \Lambda_R \Lambda_3(-v_\sigma).$$

Remark 3.12. *Using the notation of Definition 3.11, let* $n_i \in \mathbb{R}, i = 1,2,3$ *be the coefficients of* $\nu_x \in \mathbb{R}^3$ *such that we have* $\nu_x = \begin{pmatrix} n_1 & n_2 & n_3 \end{pmatrix}^\top$ *and* $\|\nu_x\|^2 = \sum_{i=1}^3 n_i^2$. *For* $n_1^2 + n_2^2 > 0$ *a matrix* $R \in SO(3)$ *that obeys Definition 3.11 is given by*

$$R := \frac{1}{n_1^2 + n_2^2} \begin{pmatrix} n_1^2 \frac{n_3}{\|\nu_x\|} + n_2^2 & n_1 n_2 \frac{n_3}{\|\nu_x\|} - n_1 n_2 & 0 \\ n_1 n_2 \frac{n_3}{\|\nu_x\|} - n_1 n_2 & n_1^2 + n_2^2 \frac{n_3}{\|\nu_x\|} & 0 \\ 0 & 0 & 0 \end{pmatrix} + \frac{1}{\|\nu_x\|} \begin{pmatrix} 0 & 0 & n_1 \\ 0 & 0 & n_2 \\ -n_1 & -n_2 & n_3 \end{pmatrix}.$$

The condition $|v_\sigma| < 1$ in Definition 3.11 poses no handicap since this is the relevant case for actual solutions of the d'Alembertian. For Λ_R as in Definition 3.11 it holds

$$\Lambda_R^\top \nu = \begin{pmatrix} \nu_t \\ R^\top \nu_x \end{pmatrix} = \begin{pmatrix} \nu_t & 0 & 0 & \|\nu_x\| \end{pmatrix}^\top = \begin{pmatrix} -v_\sigma & 0 & 0 & 1 \end{pmatrix}^\top / \sqrt{1 + v_\sigma^2},$$

where the last equality is due to $\|\nu_x\|^2 = 1 - |\nu_t|^2$ and (2.41). Choosing Λ according to Definition 3.11 leads to

$$\Lambda^\top \nu = \Lambda_3(-v_\sigma) \Lambda_R^\top \nu = \frac{\gamma(-v_\sigma)}{\sqrt{1 + v_\sigma^2}} \begin{pmatrix} 0 \\ 0 \\ 0 \\ 1 - v_\sigma^2 \end{pmatrix} = \sqrt{\frac{1 - v_\sigma^2}{1 + v_\sigma^2}} \begin{pmatrix} 0 \\ 0 \\ 0 \\ 1 \end{pmatrix} \tag{3.24}$$

and (3.23) is reduced to

$$\psi_{\mathbf{x}}(\zeta) \in \mathcal{T}_\sigma \quad \Leftrightarrow \quad \langle \mathbf{x} - \mathbf{x}_\sigma, \nu \rangle = r_0 \rho \sqrt{\frac{1 - v_\sigma^2}{1 + v_\sigma^2}} \cos\theta.$$

Define the coefficient

$$\rho_0 := \frac{\langle \mathbf{x} - \mathbf{x}_\sigma, \nu \rangle}{r_0} \sqrt{\frac{1 + v_\sigma^2}{1 - v_\sigma^2}}$$

and observe

$$\psi_{\mathbf{x}}(\zeta) \in \mathcal{T}_\sigma \quad \Leftrightarrow \quad \rho_0 = \rho \cos\theta \tag{3.25}$$

if Λ is chosen as in Definition 3.11. This nimble choice of the Lorentz transformation simplifies (3.23) to (3.25). The criterion (3.25) depends in a clear-cut fashion on the two parameters ρ and θ. Note that from $|\cos\theta| \leq 1$ it follows that $\rho \geq |\rho_0|$ is necessary for solutions of (3.25). A few solutions of (3.25), for several different values of ρ_0, are illustrated in Figure 3.3a.

Remark 3.13. *The transformation in Definition 3.11 is designed to sift out the last component of the lightlike vector* $\begin{pmatrix} 1 & e_{\mathbb{S}}^\top \end{pmatrix}$ *in* (3.23), *namely* $\cos\theta$. *An equation even simpler than* (3.25) *would be obtained if* Λ *were chosen such that the first component, namely* 1, *were sifted out. For* $\Lambda^\top \nu = \alpha \mathfrak{e}_0 = (\alpha \; 0 \; 0 \; 0)^\top$, $\alpha \in \mathbb{R} \setminus \{0\}$ (3.23) *reads*

$$\psi_{\mathbf{x}}(\zeta) \in \mathcal{T}_\sigma \quad \Leftrightarrow \quad \langle \mathbf{x} - \mathbf{x}_\sigma, \nu \rangle = \alpha r_0 \rho.$$

By virtue of the next proposition such a transformation does not exist for $|v_\sigma| \leq 1$.

Proposition 3.14. *Let $\nu \in \mathbb{S}^3$ be such that $[\nu, \nu] \geq 0$ holds. There exists no Lorentz transformation Λ such that $\Lambda^\top \nu \in \operatorname{span}\{\mathfrak{e}_0\}$ holds true.*

Proof. The proof is done by contradiction. Assume there exists a Lorentz transformation Λ with $\Lambda^\top \nu = \alpha \mathfrak{e}_0$ for some $\alpha \in \mathbb{R} \setminus \{0\}$. It holds

$$0 \leq [\nu, \nu] = \left[\Lambda^\top \nu, \Lambda^\top \nu\right] = [\alpha \mathfrak{e}_0, \alpha \mathfrak{e}_0] = \alpha^2 [\mathfrak{e}_0, \mathfrak{e}_0] = -\alpha^2$$

because $\Lambda^\top$ is a Lorentz transformation, implying the contradiction $-\alpha^2 \geq 0$. □

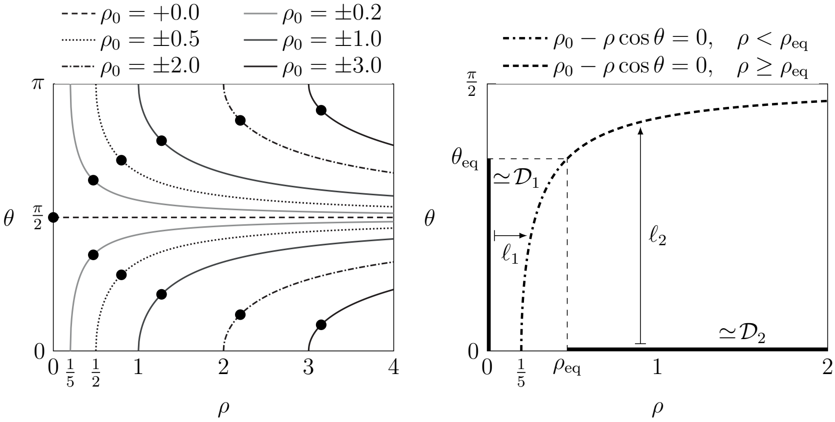

a) solutions of (3.25) for varying ρ_0 b) piecewise parametrization via ℓ_1 and ℓ_2

Figure 3.3: In Figure 3.3a curves below $\theta = \pi/2$ are solutions of (3.25) for $\rho_0 > 0$, while those above $\pi/2$ correspond to $\rho_0 < 0$. The massive dots indicate the points $(\rho_{\mathrm{eq}}, \theta_{\mathrm{eq}})$, where the tangent to the curve has unit slope. Figure 3.3b shows the solution for $\rho_0 = 1/5$ and the piecewise parametrization of $\psi_{\mathbf{x}}^{-1}\left(\Xi(\mathbf{x}) \cap \mathcal{T}_\sigma\right)$ via ℓ_1 and ℓ_2. Depiction of the φ-component is omitted, since the curve is simply extruded into the third direction.

Our next goal is to find a suitable parametrization of the solution of (3.25). Solving (3.25) for either ρ or θ yields the corresponding height functions

$$h_\rho : \theta \mapsto \rho_0 / \cos\theta, \quad h_\theta : \rho \mapsto \arccos(\rho_0/\rho).$$

Furthermore, define the level set function $\phi : (\rho, \theta) \mapsto \rho_0 - \rho\cos\theta$ and compute

$$\partial_\rho \phi : (\rho, \theta) \mapsto -\cos\theta, \quad \partial_\theta \phi : (\rho, \theta) \mapsto \rho\sin\theta.$$

We restrict these two functions to the parameters (ρ, θ) that solve (3.25). For $\rho \geq \rho_0$ this leads to $\phi_\rho := \partial_\rho \phi|_{\cos\theta=\rho_0/\rho}$ and $\phi_\theta := \partial_\theta \phi|_{\cos\theta=\rho_0/\rho}$ given by

$$\phi_\rho : \rho \mapsto -\rho_0/\rho, \quad \phi_\theta : \rho \mapsto \sqrt{\rho^2 - \rho_0^2}.$$

The absolute value of ϕ_ρ is monotonically decreasing, while the absolute value of ϕ_θ is increasing. Consequently, for sufficiently small ρ the map $\theta \mapsto h_\rho(\theta)$ is suitable for parametrizing (3.25). For larger values of ρ the map $\rho \mapsto h_\theta(\rho)$ becomes the better choice. We determine the point ρ_{eq} where the magnitudes of ϕ_ρ and ϕ_θ match

$$|\phi_\rho(\rho_{\text{eq}})|^2 = |\phi_\theta(\rho_{\text{eq}})|^2 \quad \Leftrightarrow \quad \rho_0^2/\rho_{\text{eq}}^2 = \rho_{\text{eq}}^2 - \rho_0^2 \quad \Leftrightarrow \quad \rho_0^2 = \rho_{\text{eq}}^2\left(\rho_{\text{eq}}^2 - \rho_0^2\right)$$

and obtain the nonnegative solution

$$\rho_{\text{eq}} = \frac{1}{\sqrt{2}}\sqrt{\rho_0^2 + \sqrt{\rho_0^4 + 4\rho_0^2}}.$$

The corresponding angle θ_{eq} such that $(\rho_{\text{eq}}, \theta_{\text{eq}})$ solves (3.25) is given by

$$\theta_{\text{eq}} := h_\theta\left(\rho_{\text{eq}}\right) = \arccos\left(\operatorname{sgn}(\rho_0)\sqrt{\frac{2|\rho_0|}{|\rho_0| + \sqrt{\rho_0^2 + 4}}}\right).$$

Above expression is handy for implementation: it avoids division by zero if $\rho_0 = 0$, hence $\rho_{\text{eq}} = 0$, and yields the correct value $\theta_{\text{eq}} = \pi/2$. Define the domains

$$\mathcal{D}_1 := \begin{cases} [0, \theta_{\text{eq}}) \times [0, 2\pi) & \text{if } \rho_0 > 0, \\ (\theta_{\text{eq}}, \pi] \times [0, 2\pi) & \text{if } \rho_0 < 0, \\ \varnothing & \text{if } \rho_0 = 0, \end{cases} \quad \mathcal{D}_2 := [\rho_{\text{eq}}, \infty) \times [0, 2\pi)$$

and the parametrizations $\ell_i : \mathcal{D}_i \to \mathbb{R}^3, i = 1, 2$ by

$$\ell_1 : (\theta, \varphi) \mapsto \begin{pmatrix} h_\rho(\theta) \\ \varphi \\ \theta \end{pmatrix}, \quad \ell_2 : (\rho, \varphi) \mapsto \begin{pmatrix} \rho \\ \varphi \\ h_\theta(\rho) \end{pmatrix}.$$

By virtue of this careful construction, the union of their disjoint ranges satisfies

$$\operatorname{ran} \ell_{1\wedge 2} := \operatorname{ran} \ell_1 \cup \operatorname{ran} \ell_2 = \psi_{\mathbf{x}}^{-1}\left(\Xi\left(\mathbf{x}\right) \cap \mathcal{T}_\sigma\right)$$

and, therefore, $\psi_{\mathbf{x}}\left(\operatorname{ran} \ell_{1\wedge 2}\right) = \Xi\left(\mathbf{x}\right) \cap \mathcal{T}_\sigma$ holds. This piecewise parametrization of the intersection of light cone and tangent hyperplane is depicted in Figure 3.3b. The stated property of $\operatorname{ran} \ell_{1\wedge 2}$ in conjunction with (3.22) leads to

$$\psi_{\mathbf{x}}(\zeta) \in \sigma \quad \Leftrightarrow \quad \zeta \in \operatorname{ran} \ell_{1\wedge 2} \ \wedge \ \langle \psi_{\mathbf{x}}(\zeta) - \mathbf{x}_i, \nu_i \rangle < 0 \quad \forall\, i = 1, \ldots, 4.$$

Define $\phi_i : \mathcal{P} \to \mathbb{R}, i = 1, \dots, 4$ by

$$\phi_i : \zeta \mapsto \langle \psi_{\mathbf{x}}(\zeta) - \mathbf{x}_i, \nu_i \rangle \tag{3.26}$$

and $\phi_\sigma : \mathcal{P} \to \mathbb{R}$ by

$$\phi_\sigma : \zeta \mapsto \max_{i=1,\dots,4} \phi_i(\zeta). \tag{3.27}$$

This leads to the parametrized version of the integral of Definition 3.10

$$\mathcal{I} = \sum\nolimits_{i=1,2} \int_{\eta \in \mathcal{D}_i : \phi_\sigma \circ \ell_i(\eta) < 0} k_\psi \circ \ell_i(\eta) w \circ \psi_{\mathbf{x}} \circ \ell_i(\eta) \left| \det \mathrm{D}\, \ell_i\, (\eta) \right| \mathrm{d}\eta, \tag{3.28}$$

where the parameter η is defined by $\eta := (\theta, \varphi)$ if $i = 1$ or $\eta := (\rho, \varphi)$ if $i = 2$ and

$$\left| \det \mathrm{D}\, \ell_i \right| : \eta \mapsto \begin{cases} \sqrt{1 + \left(h'_\rho(\eta_1) \right)^2} & \text{if } i = 1, \\ \sqrt{1 + \left(h'_\theta(\eta_1) \right)^2} & \text{if } i = 2, \end{cases}$$

holds. In (3.28) the integral $\mathcal{I}$ is transformed to integrals involving implicitly defined subsets of the rectangular patches $\mathcal{D}_1$ and $\mathcal{D}_2$. A few useful properties concerning this integral are collected in the following proposition for convenience.

PROPOSITION 3.15. *Let Λ be as in Definition 3.11, then for any $\zeta \in \mathcal{P}$ it holds*

- *(i)* $\| x - |_x \psi_{\mathbf{x}}(\zeta) \| = r_0 \rho (1 + v_\sigma \cos\theta) \gamma(v_\sigma)$,
- *(ii)* $\left\| J_\psi^\top(\zeta) \nu \right\| = r_0 \sqrt{(1 - v_\sigma^2)/(1 + v_\sigma^2)} \sqrt{(\cos\theta)^2 + (\rho \sin\theta)^2}$.

If in addition $v_\sigma = 0$ holds, then for any $\zeta \in \mathcal{P}$ it follows

- *(iii)* $\left| \det \mathrm{D}\, \psi_{\mathbf{x}}\, (\zeta) \right| = \sqrt{2}\, r_0^3 \rho^2 \sin\theta$.

Proof. The assertions are verified via direct computation. To show (i) let $\mathbf{y} := \psi_{\mathbf{x}}(\zeta)$ for some $\zeta \in \mathcal{P}$. From $\psi_{\mathbf{x}}(\zeta) \in \Xi\,(\mathbf{x})$ it follows that $\|x - y\| = t - \tau$ holds. Using $\psi_{\mathbf{x}}$ as in Definition 2.20 we observe

$$\mathbf{x} - \mathbf{y} = \begin{pmatrix} t - \tau \\ x - y \end{pmatrix} = r_0 \rho \Lambda \begin{pmatrix} 1 \\ e_{\mathbb{S}}(\varphi, \theta) \end{pmatrix} = r_0 \rho\, \Lambda_R \Lambda_3(-v_\sigma) \begin{pmatrix} 1 \\ e_{\mathbb{S}}(\varphi, \theta) \end{pmatrix}.$$

Inserting the definitions of Λ_R, $\Lambda_3(-v_\sigma)$, and $e_{\mathbb{S}}(\varphi, \theta)$ confirms

$$t - \tau = r_0 \rho (1 + v_\sigma \cos\theta) \gamma(v_\sigma).$$

For (ii) we use (2.51) of Section 2.6.2 to write $J_\psi(\zeta) = -r_0 \Lambda T_\psi(\zeta)$ and

$$J_\psi^\top(\zeta) \nu = -r_0 T_\psi^\top(\zeta) \Lambda^\top \nu.$$

Using (3.24) and the definition of T_ψ yields

$$J_\psi^\top(\zeta)\nu = -r_0\sqrt{\frac{1-v_\sigma^2}{1+v_\sigma^2}}\begin{pmatrix}1 & \cos\varphi\sin\theta & \sin\varphi\sin\theta & \cos\theta\\ 0 & -\rho\sin\varphi\sin\theta & \rho\cos\varphi\sin\theta & 0\\ 0 & \rho\cos\varphi\cos\theta & \rho\sin\varphi\cos\theta & -\rho\sin\theta\end{pmatrix}\begin{pmatrix}0\\0\\0\\1\end{pmatrix}$$

and (ii) follows. We turn our attention to (iii) and set $v_\sigma = 0$, yielding $\Lambda_3(0) = I$ and $\Lambda = \Lambda_R$. We observe for this very case

$$J_\psi^\top(\zeta)J_\psi(\zeta) = r_0^2\,T_\psi^\top(\zeta)\Lambda_R^\top\Lambda_R T_\psi(\zeta) = r_0^2\,T_\psi^\top(\zeta)T_\psi(\zeta)$$

since $\Lambda_R^\top = \Lambda_R^{-1}$ holds. As already discussed in Section 2.6.2, the column vectors of of T_ψ are orthogonal, leading to

$$J_\psi^\top(\zeta)J_\psi(\zeta) = r_0^2\operatorname{diag}\left(2,\ (\rho\sin\theta)^2,\ \rho^2\right)$$

and the assertion follows from $|\det \mathrm{D}\,\psi_{\mathbf{x}}(\zeta)| = \sqrt{\det J_\psi^\top(\zeta)J_\psi(\zeta)}$. □

With the aid of Proposition 3.15 the following observation about the kernel function in (3.28) can be stated.

LEMMA 3.16. *Let Λ be as in Definition 3.11 with $v_\sigma = 0$. Moreover, let k_ψ be as in Definition 3.10 with the kernel functions $k_j, j = 1,2,3$ from* (2.32). *It follows that the integral kernel $k_\psi \circ \ell_i, i = 1,2$ in* (3.28) *is smooth, i.e., $k_\psi \circ \ell_i \in C^\infty(\mathcal{D}_i)$ holds.*

Proof. Define $k_j^* : \operatorname{ran}\ell_{1\wedge 2} \to \mathbb{R}$ by $\zeta \mapsto k_j(x,\cdot) \circ |_x\psi_{\mathbf{x}}(\zeta)$ with $k_j, j = 1,2,3$ as in (2.32) apart from the factor 4π. Definition 3.11 with $v_\sigma = 0$ yields $\Lambda = \Lambda_R$. For any $\zeta \in \mathcal{P}$ we observe

$$\langle \nu_x, x - |_x\psi_{\mathbf{x}}(\zeta)\rangle = \langle \nu_x, r_0\rho R e_{\mathbb{S}}(\varphi,\theta)\rangle = r_0\rho\left\langle R^\top\nu_x, e_{\mathbb{S}}(\varphi,\theta)\right\rangle = r_0\rho\cos\theta,$$

where we used that $\|\nu_x\| = 1$ holds for $v_\sigma = 0$, see (2.41). Furthermore, for any $\zeta \in \operatorname{ran}\ell_{1\wedge 2}$ (3.25) holds true, yielding $\langle \nu_x, x - |_x\psi_{\mathbf{x}}(\zeta)\rangle = r_0\rho_0$. This, in conjunction with Proposition 3.15, leads to

$$k_1^* : \zeta \mapsto (r_0\rho)^{-1}, \quad k_j^* : \zeta \mapsto r_0\rho_0(r_0\rho)^{-j}, j = 2,3, \tag{3.29}$$

which are smooth apart from $\rho = 0$. Define $k_{\psi,j} : \operatorname{ran}\ell_{1\wedge 2} \to \mathbb{R}$ for $j = 1,2,3$ by

$$k_{\psi,j} : \zeta \mapsto \frac{k_j^*(\zeta)\,|\det \mathrm{D}\,\psi_{\mathbf{x}}(\zeta)|}{\sqrt{2}\left\|J_\psi^\top(\zeta)\nu\right\|} = k_j^*(\zeta)\frac{r_0^2\rho^2\sin\theta}{\sqrt{(\cos\theta)^2 + (\rho\sin\theta)^2}},$$

where the latter identity is due to Proposition 3.15. Insertion of (3.29) yields

$$\begin{aligned} k_{\psi,1} &: \zeta \mapsto \frac{r_0 \rho \sin\theta}{\sqrt{(\cos\theta)^2 + (\rho\sin\theta)^2}}, \\ k_{\psi,j} &: \zeta \mapsto \rho_0 r_0^{3-j} \rho^{2-j} \frac{\sin\theta}{\sqrt{(\cos\theta)^2 + (\rho\sin\theta)^2}}, j = 2, 3. \end{aligned}$$

For $\rho_0 = 0$ (3.25) yields $\theta = \pi/2$ (for $\rho \neq 0$) and, therefore, $k_{\psi,1}(\zeta) = r_0$ as well as $k_{\psi,j}(\zeta) = 0$, $j = 2, 3$ hold. For $\rho_0 \neq 0$ the singularity of (3.29) is of importance only for ℓ_1, since ℓ_2 maps to $\rho \geq \rho_{\mathrm{eq}} > 0$. For $\rho_0 \neq 0$ using $\rho := h_\rho(\theta) = \rho_0 / \cos\theta$ leads to

$$k_{\psi,1} \circ \ell_1 : (\theta, \varphi) \mapsto \rho_0 r_0 \frac{\tan\theta}{\sqrt{(\cos\theta)^2 + (\rho_0 \tan\theta)^2}}$$

and

$$k_{\psi,j} \circ \ell_1 : (\theta, \varphi) \mapsto \rho_0^{3-j} r_0^{3-j} (\cos\theta)^{j-1} \frac{\tan\theta}{\sqrt{(\cos\theta)^2 + (\rho_0 \tan\theta)^2}}$$

for $j = 2, 3$. These functions are smooth for $\theta \neq \pi/2$. The assertion follows because θ_{eq} is bounded away from $\pi/2$ for $\rho_0 \neq 0$. ☐

Finally, we provide a choice of r_0 that enables the use of a finite patch $\mathcal{D}_2$ in (3.28).

DEFINITION 3.17. *For given* $\mathbf{x} \in \mathbb{R}^4$*, Lorentz transformation* Λ*, and simplex* σ *define* $\sigma_\Lambda^{\mathbf{x}} := \{\Lambda^{-1}(\mathbf{x} - \mathbf{y}) : \mathbf{y} \in \sigma\}$. *Set* $r_0 := \sup\{\tau : \mathbf{y} \in \sigma_\Lambda^{\mathbf{x}}\}$ *to the largest time coordinate in* $\sigma_\Lambda^{\mathbf{x}}$.

The following comments clarify the implications of Definition 3.17:

- From $r_0 \leq 0$ in Definition 3.17 it follows that $\Xi(\mathbf{x}) \cap \sigma \in \{\varnothing, \{\mathbf{x}\}\}$ holds, implying $\mathcal{I} = 0$. Consequently, the disagreement with the assumption $r_0 > 0$ in Definition 2.20 is of no practical significance.
- The set $\sigma_\Lambda^{\mathbf{x}}$ is a simplex, since it is the image of the simplex σ under the affine transformation $\mathbf{y} \mapsto \Lambda^{-1}\mathbf{x} - \Lambda^{-1}\mathbf{y}$. Let $\{\mathbf{y}_i\}_{i=1}^4$ be the vertices of $\sigma_\Lambda^{\mathbf{x}}$ and observe

  $$\overline{\sigma_\Lambda^{\mathbf{x}}} = \left\{ \sum\nolimits_{i=1}^4 \alpha_i \mathbf{y}_i : \alpha_i \geq 0 \ \ \forall i = 1, \dots, 4 \ \ \wedge \ \ \sum\nolimits_{i=1}^4 \alpha_i = 1 \right\},$$

  where $\alpha_i, i = 1, \dots, 4$ are the barycentric coordinates. For any $\mathbf{y} \in \overline{\sigma_\Lambda^{\mathbf{x}}}$ it holds

  $$\tau = \langle \mathbf{y}, \mathfrak{e}_0 \rangle = \sum\nolimits_{i=1}^4 \alpha_i \langle \mathbf{y}_i, \mathfrak{e}_0 \rangle \leq \max_{i=1,\dots,4} \langle \mathbf{y}_i, \mathfrak{e}_0 \rangle \sum\nolimits_{i=1}^4 \alpha_i = \max_{i=1,\dots,4} \tau_i.$$

  This confirms that the largest time coordinate in $\sigma_\Lambda^{\mathbf{x}}$ is attained at a vertex.

- If r_0 is chosen according to Definition 3.17 $\psi_{\mathbf{x}}$ maps every argument with $\rho > 1$ to a point with smaller time coordinate than anywhere in σ. As a result, it suffices to consider the domain $\mathcal{D}_2$ in (3.28) defined by

$$\mathcal{D}_2 := \begin{cases} [\rho_{\mathrm{eq}}, 1] \times [0, 2\pi) & \text{if } \rho_{\mathrm{eq}} < 1, \\ \varnothing & \text{if } \rho_{\mathrm{eq}} \geq 1. \end{cases}$$

We propose to compute (3.28) via numerical integration in order to evaluate $\mathcal{I}$ and eventually $\mathrm{T}_k\, w(\mathbf{x})$. Although Lemma 3.16 shows that the integrand is smooth, the numerical evaluation of (3.28) is not straightforward. The integral involves the implicitly defined sets $\{\eta \in \mathcal{D}_i : \phi_\sigma \circ \ell_i(\eta) < 0\}, i = 1, 2$, where ϕ_σ is continuous but not differentiable in the classical sense. Handling such level set functions in a robust and efficient manner is a delicate task.

There exist several quadrature methods for integrals like (3.28), provided its integrand is smooth. Prominent procedures are based on (high-order) approximations of the implicitly defined set [63, 37, 36, 56], while others avoid such reconstructions [79, 56]. In [39], piecewise parametrizations of the exact zero level set, denoted ideal transformations in [65], are constructed. Alternatively, the technique proposed in [105] is based on local parametrizations, whose existence is due to the implicit function theorem. For a detailed review of the available literature the reader is referred to the introductions of [105, 56]. In this thesis, we suggest to tackle (3.28) by an algorithm tailored to ϕ_σ. It is a blend of the methodology proposed in [37] and the ideal transformation of [65]. Details on the implementation are provided in Section 3.8.1.

We conclude the discussion on techniques for evaluating T_k by comparing the method introduced in this section to the one we proposed in [89]. Both approaches have in common that the integrals are posed on implicitly defined subsets of $\mathbb{R}^2$ (see (3.28) and [89, Equations (3.10) and (3.11)]) and that they involve smooth integrands (see Lemma 3.16 and [89, Theorem 3.5]). Therefore, both approaches can be treated by the same quadrature procedures listed in the previous paragraph. From this point of view their differences are rather subtle.

On the one hand, the method of this work is based on the parametrization of the space-time light cone $\psi_{\mathbf{x}}$ introduced in Definition 2.20. Auxiliary mappings $\ell_i, i = 1, 2$ restrict the range to the tangent hyperplane $\psi_{\mathbf{x}} \circ \ell_i : \mathcal{D}_i \to \Xi(\mathbf{x}) \cap \mathcal{T}_\sigma$. On the other hand, the approach of [89] is based on the parametrization in reference space $\widehat{\psi} : [0, 2\pi) \times [0, \infty) \to \chi_\sigma^{-1}\left(\Xi(\mathbf{x}) \cap \mathcal{T}_\sigma\right)$, which is denoted ψ in [89, p. A3869]. It is a composition of the principal axes transform $\kappa_\sigma^{\mathbf{x}}$ defined in (3.19) and suitable parametrizations of a two-dimensional cone or a (two-dimensional) two-sheeted hyperboloid, respectively. While the construction of $\psi_{\mathbf{x}}$ requires computation of Λ as in Definition 3.11 and r_0 as in Definition 3.17, the construction of $\kappa_\sigma^{\mathbf{x}}$ involves the eigendecomposition of the symmetric matrix A_σ discussed in Section 3.4. Finally, the basis functions of the spaces of Definition 3.2 are typically defined in the three-dimensional reference space of $\widehat{\sigma}$. While $\widehat{\psi}$ maps to this reference space, $\psi_{\mathbf{x}}$ maps to four-dimensional space-time. In order to evaluate basis functions, the inverse of χ_σ defined in (3.1) has to be applied to $\mathbf{y} := \psi_{\mathbf{x}} \circ \ell_i(\eta)$ for $\eta \in \mathcal{D}_i$. This can be accomplished via $\chi_\sigma^{-1} : \mathbf{y} \mapsto G_\sigma^{-1} J_\sigma^\top (\mathbf{y} - \mathbf{x}_\sigma)$, which involves inversion of the symmetric positive definite Gramian matrix G_σ.

3.6 Evaluation of Energetic Bilinear Forms

The goal of this segment is to devise a quadrature approach for the discretized bilinear forms of Section 3.3. For the retarded potential T_k discussed in Section 2.6 the bilinear form b_{T_k} introduced in Section 2.5 reads

$$b_{\mathrm{T}_k} : (w, v) \mapsto \int_\Sigma \partial_t v(\mathbf{x})\, \mathrm{T}_k\, w(\mathbf{x}) \mathrm{d}S(\mathbf{x}).$$

Insertion of Definition 2.16 yields

$$b_{\mathrm{T}_k} : (w, v) \mapsto \int_\Sigma \int_\Sigma k(x, y) \partial_t v(\mathbf{x}) w(\mathbf{y}) \delta_0 \circ \phi_\Xi\, (\mathbf{x} - \mathbf{y})\, \mathrm{d}S(\mathbf{y}) \mathrm{d}S(\mathbf{x}). \tag{3.30}$$

The two integrals in above formula are denoted by outer integral (Galerkin testing with respect to $\mathbf{x}$) and inner integral (integral operator T_k with respect to $\mathbf{y}$), respectively. In the context of BIEs for elliptic problems, the most successful quadrature techniques for bilinear forms analogous to (3.30) are based on treating the outer and inner integral together as one high-dimensional integral, see [30] or [100, Chapter 5]. This approach has compelling advantages, which can be exploited for parabolic problems as well [72]. In the context of RPBIEs, the design such a scheme is considerably more intricate. Although we pursue a simpler method in this thesis, we glimpse at such high-dimensional approaches in the following paragraph.

Let $f : \Sigma \times \Sigma \to \mathbb{R}$ be given by $f : (\mathbf{x}, \mathbf{y}) \mapsto k(x, y) \partial_t v(\mathbf{x}) w(\mathbf{y})$. With the aid of the mesh Σ_N introduced in Section 2.1 the integral in (3.30) is rewritten

$$\begin{aligned} &\int_\Sigma \int_\Sigma f(\mathbf{x}, \mathbf{y}) \delta_0 \circ \phi_\Xi\, (\mathbf{x} - \mathbf{y})\, \mathrm{d}S(\mathbf{y}) \mathrm{d}S(\mathbf{x}) \\ &\quad = \sum_{\sigma_{\mathbf{x}} \in \Sigma_N} \sum_{\sigma_{\mathbf{y}} \in \Sigma_N} \int_{\sigma_{\mathbf{x}}} \int_{\sigma_{\mathbf{y}}} f(\mathbf{x}, \mathbf{y}) \delta_0 \circ \phi_\Xi\, (\mathbf{x} - \mathbf{y})\, \mathrm{d}S(\mathbf{y}) \mathrm{d}S(\mathbf{x}). \end{aligned} \tag{3.31}$$

In (3.31) we tacitly assume that f is such that the integral over Σ coincides with the sum of the integrals over all panels. This assumption is revisited in Remark 3.20. The parametrizations $\chi_{\sigma_{\mathbf{x}}} : \widehat{\sigma} \to \sigma_{\mathbf{x}}$ and $\chi_{\sigma_{\mathbf{y}}} : \widehat{\sigma} \to \sigma_{\mathbf{y}}$ yield

$$\int_{\sigma_{\mathbf{x}}} \int_{\sigma_{\mathbf{y}}} f(\mathbf{x}, \mathbf{y}) \delta_0 \circ \phi_\Xi\, (\mathbf{x} - \mathbf{y})\, \mathrm{d}S(\mathbf{y}) \mathrm{d}S(\mathbf{x}) = \int_{\widehat{\sigma}} \int_{\widehat{\sigma}} \widehat{f}(\xi, \zeta) \delta_0 \circ \widehat{\phi_\Xi}(\xi, \zeta) \mathrm{d}\zeta \mathrm{d}\xi,$$

where $\widehat{f} : \widehat{\sigma} \times \widehat{\sigma} \to \mathbb{R}$ is defined by

$$\widehat{f} : (\xi, \zeta) \mapsto f\left(\chi_{\sigma_{\mathbf{x}}}(\xi), \chi_{\sigma_{\mathbf{y}}}(\zeta)\right) \left|\det \mathrm{D}\, \chi_{\sigma_{\mathbf{y}}}(\zeta)\right| \left|\det \mathrm{D}\, \chi_{\sigma_{\mathbf{x}}}(\xi)\right|$$

and $\widehat{\phi_\Xi} : \widehat{\sigma} \times \widehat{\sigma} \to \mathbb{R}$ by

$$\widehat{\phi_\Xi} : (\xi, \zeta) \mapsto \phi_\Xi\left(\chi_{\sigma_{\mathbf{x}}}(\xi) - \chi_{\sigma_{\mathbf{y}}}(\zeta)\right).$$

Note that the parameter $\zeta \in \widehat{\sigma}$ is not to be confused with the parameter coordinate of Definition 2.20. Application of Theorem 2.15 in the form of (2.36) yields

$$\int_{\widehat{\sigma}} \int_{\widehat{\sigma}} \widehat{f}(\xi, \zeta) \delta_0 \circ \widehat{\phi_\Xi}(\xi, \zeta) \mathrm{d}\zeta \mathrm{d}\xi = \int_{(\xi,\zeta) \,\in\, \widehat{\sigma} \times \widehat{\sigma} :\, \widehat{\phi_\Xi}(\xi,\zeta) = 0} \frac{\widehat{f}(\xi, \zeta)}{\left\|\nabla \widehat{\phi_\Xi}(\xi, \zeta)\right\|} \mathrm{d}S(\xi, \zeta), \tag{3.32}$$

where ∇ differentiates with respect to the group variable (ξ, ζ). The integral in (3.32) is posed on

$$\left\{(\xi, \zeta) \in \widehat{\sigma} \times \widehat{\sigma} : \phi_\Xi\left(\chi_{\sigma_{\mathbf{x}}}(\xi) - \chi_{\sigma_{\mathbf{y}}}(\zeta)\right) = 0\right\},$$

which is, in general, a five-dimensional hypersurface embedded in the six-dimensional parameter domain $\widehat{\sigma} \times \widehat{\sigma}$. With the affine parametrizations of Section 3.1 and the rationale of Section 3.4 it is evident that this hypersurface is a subset of

$$\begin{aligned} (\xi, \zeta) \in \mathbb{R}^3 \times \mathbb{R}^3 : \qquad & \left[\chi_{\sigma_{\mathbf{x}}}(\xi) - \chi_{\sigma_{\mathbf{y}}}(\zeta), \chi_{\sigma_{\mathbf{x}}}(\xi) - \chi_{\sigma_{\mathbf{y}}}(\zeta)\right] = 0 \\ \Leftrightarrow \quad & \left[\mathbf{x}_\sigma + J_{\mathbf{x}}\xi - \mathbf{y}_\sigma - J_{\mathbf{y}}\zeta, \mathbf{x}_\sigma + J_{\mathbf{x}}\xi - \mathbf{y}_\sigma - J_{\mathbf{y}}\zeta\right] = 0, \end{aligned} \tag{3.33}$$

where $\mathbf{x}_\sigma \in \partial\sigma_{\mathbf{x}}$ and $\mathbf{y}_\sigma \in \partial\sigma_{\mathbf{y}}$ are vertices, while $J_{\mathbf{x}}, J_{\mathbf{y}} \in \mathbb{R}^{4\times 3}$ are the Jacobi matrices of $\chi_{\sigma_{\mathbf{x}}}$ and $\chi_{\sigma_{\mathbf{y}}}$, respectively. In more concise notation (3.33) is the zero level set

$$\mathcal{Q}_{\mathbf{x},\mathbf{y}}^{-1}\{0\} = \left\{(\xi, \zeta) \in \mathbb{R}^3 \times \mathbb{R}^3 : \mathcal{Q}_{\mathbf{x},\mathbf{y}}(\xi, \zeta) = 0\right\}$$

of the quadratic function in six-dimensional reference space $\mathcal{Q}_{\mathbf{x},\mathbf{y}} : \mathbb{R}^3 \times \mathbb{R}^3 \to \mathbb{R}$

$$\mathcal{Q}_{\mathbf{x},\mathbf{y}} : (\xi, \zeta) \mapsto \left\langle A_{\mathbf{x},\mathbf{y}} \begin{pmatrix} \xi \\ \zeta \end{pmatrix}, \begin{pmatrix} \xi \\ \zeta \end{pmatrix} \right\rangle + 2 \left\langle b_{\mathbf{x},\mathbf{y}}, \begin{pmatrix} \xi \\ \zeta \end{pmatrix} \right\rangle + \left[\mathbf{x}_\sigma - \mathbf{y}_\sigma, \mathbf{x}_\sigma - \mathbf{y}_\sigma\right],$$

where $A_{\mathbf{x},\mathbf{y}} \in \mathbb{R}^{6\times 6}$ and $b_{\mathbf{x},\mathbf{y}} \in \mathbb{R}^6$ are defined by

$$\begin{aligned} A_{\mathbf{x},\mathbf{y}} &:= \begin{pmatrix} J_{\mathbf{x}}^\top \\ -J_{\mathbf{y}}^\top \end{pmatrix} M \begin{pmatrix} J_{\mathbf{x}} & -J_{\mathbf{y}} \end{pmatrix} = \begin{pmatrix} J_{\mathbf{x}}^\top M J_{\mathbf{x}} & -J_{\mathbf{x}}^\top M J_{\mathbf{y}} \\ -J_{\mathbf{y}}^\top M J_{\mathbf{x}} & J_{\mathbf{y}}^\top M J_{\mathbf{y}} \end{pmatrix}, \\ b_{\mathbf{x},\mathbf{y}} &:= \begin{pmatrix} J_{\mathbf{x}}^\top \\ -J_{\mathbf{y}}^\top \end{pmatrix} M(\mathbf{x}_\sigma - \mathbf{y}_\sigma) = \begin{pmatrix} J_{\mathbf{x}}^\top M(\mathbf{x}_\sigma - \mathbf{y}_\sigma) \\ -J_{\mathbf{y}}^\top M(\mathbf{x}_\sigma - \mathbf{y}_\sigma) \end{pmatrix}. \end{aligned}$$

In order to characterize the quadric $\mathcal{Q}_{\mathbf{x},\mathbf{y}}^{-1}\{0\}$, the following observation about the spectrum of the symmetric matrix $A_{\mathbf{x},\mathbf{y}}$ might be useful.

PROPOSITION 3.18. *Let* $\nu_{\mathbf{x}}, \nu_{\mathbf{y}} \in \mathbb{S}^3$ *be the normal vectors of the simplex panels* $\sigma_{\mathbf{x}}, \sigma_{\mathbf{y}}$ *and* $\{\lambda_i\}_{i=1}^6$ *be the eigenvalues of* $A_{\mathbf{x},\mathbf{y}}$ *sorted in ascending order:* $\lambda_i \le \lambda_j$ *for all* $j \ge i$. *It holds* $\lambda_2 = \lambda_3 = 0 < \lambda_5 \le \lambda_6$. *Furthermore, assuming* $\nu_{\mathbf{x}} \in \operatorname{span}\{\nu_{\mathbf{y}}\}$ *it follows*

$$\lambda_1 \begin{cases} < 0 & \text{if } [\nu_{\mathbf{x}}, \nu_{\mathbf{x}}] > 0, \\ = 0 & \text{if } [\nu_{\mathbf{x}}, \nu_{\mathbf{x}}] \le 0, \end{cases} \qquad \lambda_4 \begin{cases} = 0 & \text{if } [\nu_{\mathbf{x}}, \nu_{\mathbf{x}}] \ge 0, \\ > 0 & \text{if } [\nu_{\mathbf{x}}, \nu_{\mathbf{x}}] < 0, \end{cases}$$

while for $\nu_{\mathbf{x}} \notin \operatorname{span}\{\nu_{\mathbf{y}}\}$ *it follows* $\lambda_1 < 0 < \lambda_4$.

Proof. The proof is similar to the proof of Lemma 3.8. We write $\nu_{\mathbf{x}} \parallel \nu_{\mathbf{y}}$ iff $\nu_{\mathbf{x}} \in \operatorname{span}\{\nu_{\mathbf{y}}\}$ holds and $\nu_{\mathbf{x}} \nparallel \nu_{\mathbf{y}}$ iff $\nu_{\mathbf{x}} \notin \operatorname{span}\{\nu_{\mathbf{y}}\}$ holds. Define $J := \begin{pmatrix} J_{\mathbf{x}} & -J_{\mathbf{y}} \end{pmatrix} \in \mathbb{R}^{4\times 6}$ and observe $A_{\mathbf{x},\mathbf{y}} = J^\top M J$. The kernel of $J^\top$ is given by

$$\ker J^\top = \left\{ v \in \mathbb{R}^4 : J^\top v = \begin{pmatrix} J_{\mathbf{x}}^\top v \\ -J_{\mathbf{y}}^\top v \end{pmatrix} = 0 \right\},$$

which shows that $\ker J^\top = \ker J_{\mathbf{x}}^\top \cap \ker J_{\mathbf{y}}^\top$ holds. Since the one-dimensional kernels of $J_{\mathbf{x}}^\top$ and $J_{\mathbf{y}}^\top$ are spanned by $\nu_{\mathbf{x}}$ and $\nu_{\mathbf{y}}$, respectively, we observe

$$\ker J^\top = \begin{cases} \{0\} & \text{if } \nu_{\mathbf{x}} \nparallel \nu_{\mathbf{y}}, \\ \operatorname{span}\{\nu_{\mathbf{x}}\} & \text{if } \nu_{\mathbf{x}} \parallel \nu_{\mathbf{y}}, \end{cases} \quad \Rightarrow \quad \dim \ker J = \begin{cases} 2 & \text{if } \nu_{\mathbf{x}} \nparallel \nu_{\mathbf{y}}, \\ 3 & \text{if } \nu_{\mathbf{x}} \parallel \nu_{\mathbf{y}}, \end{cases} \tag{3.34}$$

where we used $\dim \ker J = 2 + \dim \ker J^\top$ due to the rank-nullity theorem. A direct calculation confirms that $A_{\mathbf{x},\mathbf{y}} = J^\top J - 2 j_t j_t^\top$ holds, where $j_t \in \mathbb{R}^6$ is the first column of $J^\top$. Since $J^\top J$ is symmetric positive semidefinite it follows that $A_{\mathbf{x},\mathbf{y}}$ can have at most one negative eigenvalue [44, p. 325]. Similar to the argument used in the proof of Lemma 3.8 we observe that $\langle A_{\mathbf{x},\mathbf{y}} v, v\rangle = [Jv, Jv]$ for any $v \in \mathbb{R}^6$ leads to

$$\lambda_1 < 0 \quad \Leftrightarrow \quad \exists \mathbf{y} \in \operatorname{ran} J : [\mathbf{y}, \mathbf{y}] < 0 \quad \Leftrightarrow \quad \exists \mathbf{y} \in \left(\ker J^\top\right)^\perp : [\mathbf{y}, \mathbf{y}] < 0. \tag{3.35}$$

For $\nu_{\mathbf{x}} \nparallel \nu_{\mathbf{y}}$ (3.34) yields $\left(\ker J^\top\right)^\perp = \mathbb{R}^4$ and (3.35) implies $\lambda_1 < 0$, because the existence of timelike vectors in entire $\mathbb{R}^4$ is trivial. For $\nu_{\mathbf{x}} \parallel \nu_{\mathbf{y}}$ (3.34) and (3.35) yield

$$\lambda_1 < 0 \quad \Leftrightarrow \quad \exists \mathbf{y} \in \mathbb{R}^4 : \langle \mathbf{y}, \nu_{\mathbf{x}} \rangle = 0 \quad \wedge \quad [\mathbf{y}, \mathbf{y}] < 0 \quad \Leftrightarrow \quad [\nu_{\mathbf{x}}, \nu_{\mathbf{x}}] > 0,$$

where the last implication is shown in the proof of Lemma 3.8. It remains to determine $\dim \ker A_{\mathbf{x},\mathbf{y}}$. The orthogonal decomposition $\mathbb{R}^6 = \ker J \oplus (\ker J)^\perp$ yields

$$\begin{aligned} \ker A_{\mathbf{x},\mathbf{y}} &= \left\{ v \in \ker J \oplus (\ker J)^\perp : J^\top M J v = 0 \right\} \\ &= \left\{ v_1 + v_2 : v_1 \in \ker J, v_2 \in (\ker J)^\perp, J^\top M J v_1 + J^\top M J v_2 = 0 \right\} \\ &= \left\{ v_1 + v_2 : v_1 \in \ker J, v_2 \in (\ker J)^\perp, J^\top M J v_2 = 0 \right\} \\ &= \ker J \oplus \left\{ v \in (\ker J)^\perp : J^\top M J v = 0 \right\} \end{aligned}$$

and

$$\dim\ker A_{\mathbf{x},\mathbf{y}} = \dim\ker J + \dim\left\{v \in (\ker J)^\perp : J^\top M J v = 0\right\}. \tag{3.36}$$

Any $v \in \mathbb{R}^6$ satisfies $J^\top M J v = 0$ iff $Jv \in \ker J^\top M$. By virtue of $M = M^{-1}$ it follows

$$\left\{v \in (\ker J)^\perp : J^\top M J v = 0\right\} = \left\{v \in (\ker J)^\perp : Jv \in M\left(\ker J^\top\right)\right\}.$$

For $\nu_\mathbf{x} \nparallel \nu_\mathbf{y}$ (3.34) implies $\ker J^\top = \{0\}$, which leads to

$$\left\{v \in (\ker J)^\perp : J^\top M J v = 0\right\} = \left\{v \in (\ker J)^\perp : Jv = 0\right\} = (\ker J)^\perp \cap \ker J = \{0\}.$$

Consequently, (3.36) yields $\dim\ker A_{\mathbf{x},\mathbf{y}} = 2$ for $\nu_\mathbf{x} \nparallel \nu_\mathbf{y}$. In the remainder of this proof we assume that $\nu_\mathbf{x} \parallel \nu_\mathbf{y}$ holds. In this case (3.34) yields

$$\left\{v \in (\ker J)^\perp : J^\top M J v = 0\right\} = \left\{v \in (\ker J)^\perp : Jv \in \operatorname{span}\{M\nu_\mathbf{x}\}\right\}.$$

For any $r \in \mathbb{R}^4$ there is at most one $v \in (\ker J)^\perp$ such that $Jv = r$ holds, implying

$$\dim\left\{v \in (\ker J)^\perp : Jv \in \operatorname{span}\{M\nu_\mathbf{x}\}\right\} \le 1.$$

The solution $v \in (\ker J)^\perp$ to $Jv = r$ exists iff r is orthogonal to $\ker J^\top = \operatorname{span}\{\nu_\mathbf{x}\}$. Therefore, $0 = \langle M\nu_\mathbf{x}, \nu_\mathbf{x}\rangle = [\nu_\mathbf{x}, \nu_\mathbf{x}]$ is equivalent to the existence of a unique $v \in (\ker J)^\perp$ solving $Jv = r$ for any $r \in \operatorname{span}\{M\nu_\mathbf{x}\}$. We have for $\nu_\mathbf{x} \parallel \nu_\mathbf{y}$

$$\dim\left\{v \in (\ker J)^\perp : Jv \in \operatorname{span}\{M\nu_\mathbf{x}\}\right\} = \begin{cases} 0 & \text{if } [\nu_\mathbf{x}, \nu_\mathbf{x}] \neq 0, \\ 1 & \text{if } [\nu_\mathbf{x}, \nu_\mathbf{x}] = 0. \end{cases}$$

and (3.36) as well as (3.34) yield for $\nu_\mathbf{x} \parallel \nu_\mathbf{y}$

$$\dim\ker A_{\mathbf{x},\mathbf{y}} = \begin{cases} 3 & \text{if } [\nu_\mathbf{x}, \nu_\mathbf{x}] \neq 0, \\ 4 & \text{if } [\nu_\mathbf{x}, \nu_\mathbf{x}] = 0. \end{cases}$$

Collecting all results leads to the assertion. □

The next statement recaps the spectrum in case of spacelike normal vectors, which is the physically relevant scenario.

Corollary 3.19. *Using the notation and assumptions of Proposition 3.18 let* $\nu_\mathbf{x}$ *be such that* $[\nu_\mathbf{x}, \nu_\mathbf{x}] > 0$ *holds. It holds* $\lambda_1 < 0 = \lambda_2 = \lambda_3 < \lambda_5 \le \lambda_6$ *as well as* $\lambda_4 = 0$ *if* $\nu_\mathbf{x} \in \operatorname{span}\{\nu_\mathbf{y}\}$ *and* $\lambda_4 > 0$ *if* $\nu_\mathbf{x} \notin \operatorname{span}\{\nu_\mathbf{y}\}$.

A quadrature scheme for (3.32) could be based on a suitable parametrization of the intersection of the quadric $\mathcal{Q}_{\mathbf{x},\mathbf{y}}^{-1}\{0\}$ and the Cartesian product of both reference tetrahedra $\widehat{\sigma} \times \widehat{\sigma}$. The design of such a technique is, at least from our point of view, worthy of an independent research effort. In this thesis, we resort to an approach well-established in BEMs for RPBIEs based on semi-discretization, see [52, 5, 42]. The idea is to approximate the outer integral by a suitable quadrature formula

$$\int_{\sigma_{\mathbf{x}}} \partial_t v(\mathbf{x}) \, \mathrm{T}_k \, w(\mathbf{x}) \mathrm{d}S(\mathbf{x}) \approx \sum\nolimits_{i=1}^{m_Q} \partial_t v(\mathbf{x}_i) \, \mathrm{T}_k \, w(\mathbf{x}_i) \omega_i, \tag{3.37}$$

where $\{\mathbf{x}_i\}_{i=1}^{m_Q}$ and $\{\omega_i\}_{i=1}^{m_Q}$ are the $m_Q \in \mathbb{N}$ quadrature points and weights, respectively. The evaluation of $\mathrm{T}_k \, w$ at the quadrature points is performed via the procedure discussed in Sections 3.5 and 3.8.1.

Quadrature formulas like (3.37) are well-defined only if pointwise evaluations of $\mathrm{T}_k \, w$ along Σ are well-defined. To this end, we impose the continuity assumptions $\mathrm{V} \, w_h \in C(\Sigma)$ for any $w_h \in S_p^{\mathrm{d}}(\Sigma_N), p \in \mathbb{N}_0$ and $\mathrm{K} \, v_h \in C(\Sigma)$ for any $v_h \in S_p^{\mathrm{c}}(\Sigma_N) \cap H_{0,\cdot}^1(\Sigma), p \in \mathbb{N}$, respectively. The entries of the matrices V, K, and A of Section 3.3 involve integrals of the form

$$\int_{\Sigma} \partial_t v_h(\mathbf{x}) w(\mathbf{x}) \mathrm{d}S(\mathbf{x}), \tag{3.38}$$

where v_h is in the discontinuous space $S_p^{\mathrm{d}}(\Sigma_N)$ for $p \in \mathbb{N}_0$ and $w : \Sigma \to \mathbb{R}$ is either in the continuous space $S_p^{\mathrm{c}}(\Sigma_N), p \in \mathbb{N}$ or defined via action of the operators V or K, respectively. In order to tackle (3.38), an interpretation of the time derivative of a discontinuous function is necessary. To this end, let $\sigma \in \Sigma_N$ be a panel with unit outward conormal vector field $\nu_{\partial\sigma} : \partial\sigma \to \mathbb{S}^3$. For the piecewise flat boundary decomposition of Section 3.1 the conormal vector satisfies $\langle \nu_{\partial\sigma}(\mathbf{x}), \nu_\sigma \rangle = 0$ for any $\mathbf{x} \in \partial\sigma$ for which it exists. Consider $v \in C^1(\Sigma)$ and define $v_0 : \Sigma \to \mathbb{R}$ by

$$v_0 : \mathbf{x} \mapsto \begin{cases} v(\mathbf{x}) & \text{if } \mathbf{x} \in \sigma, \\ 0 & \text{otherwise.} \end{cases}$$

For $w \in C(\Sigma)$ application of [55, Theorem 3.1.9] yields

$$\int_{\Sigma} w \partial_t v_0 \mathrm{d}S = \int_{\sigma} w \partial_t v \mathrm{d}S - \int_{\partial\sigma} \nu_{\partial\sigma,t} v w \mathrm{d}S,$$

where $\nu_{\partial\sigma,t}$ denotes the time component of the conormal vector. Note that the application of the cited theorem is justified because time is a tangential coordinate on Σ. It is evident that the time derivative of a function that jumps across $\partial\sigma$ features a Dirac delta function supported on $\partial\sigma$, weighted by the jump and the time component of the outward conormal vector. This leads to the formula for $v \in \prod_{\sigma \in \Sigma_N} C^1(\sigma)$

$$\int_{\Sigma} w \partial_t v \mathrm{d}S = \sum\nolimits_{\sigma \in \Sigma_N} \int_{\sigma} w \partial_t v|_{\sigma} \mathrm{d}S - \sum\nolimits_{\sigma \in \Sigma_N} \int_{\partial\sigma} \nu_{\partial\sigma,t} v|_{\partial\sigma} w \mathrm{d}S,$$

where $v|_{\partial\sigma}$ denotes the trace of the restriction $v|_\sigma$ to $\partial\sigma$. If $w : \Sigma \to \mathbb{R}$ is such that $\mathrm{T}_k\, w \in C(\Sigma)$ holds we deduce the expression for the bilinear form b_{T_k} for test functions $v \in \prod_{\sigma\in\Sigma_N} C^1(\sigma)$

$$b_{\mathrm{T}_k} : (w, v) \mapsto \sum\nolimits_{\sigma\in\Sigma_N} \int_\sigma \mathrm{T}_k\, w\, \partial_t v|_\sigma \mathrm{d}S - \sum\nolimits_{\sigma\in\Sigma_N} \int_{\partial\sigma} \nu_{\partial\sigma,t} v|_{\partial\sigma}\, \mathrm{T}_k\, w \mathrm{d}S. \tag{3.39}$$

We simplify (3.39) for the lowest order boundary element spaces employed in Section 3.3. The bilinear forms b_{V} and b_{K} are tested with functions in $U_h = S_0^{\mathrm{d}}(\Sigma_N)$. For any $v_h \in S_0^{\mathrm{d}}(\Sigma_N)$ it holds $\partial_t v_h|_\sigma = 0$ for all $\sigma \in \Sigma_N$ and we obtain

$$b_{\mathrm{T}_k} : (w, v_h) \mapsto -\sum\nolimits_{\sigma\in\Sigma_N} \int_{\partial\sigma} \nu_{\partial\sigma,t} v_h|_{\partial\sigma}\, \mathrm{T}_k\, w \mathrm{d}S$$

or for the basis $U_h = \operatorname{span}\{e_i^0\}_{i=1}^N$ of Section 3.3 with $i = 1, \ldots, N$

$$b_{\mathrm{T}_k} : \left(w, e_i^0\right) \mapsto -\int_{\partial\sigma_i} \nu_{\partial\sigma_i,t}\, \mathrm{T}_k\, w \mathrm{d}S. \tag{3.40}$$

Due to the use of lowest order trial functions, only integrals along the boundary of the panels have to be computed. The restriction to lowest order spaces is justified because this thesis aims at exploring the feasibility of space-time methods for RPBIEs. The design of sophisticated high-order convergent schemes for RPBIEs exceeds the scope of this work and constitutes, at least form our point of view, an independent research endeavor.

In order to evaluate (3.40), numerical integration has to be carried out over the boundaries of all panels in Σ_N. Let $\mathcal{F}_N$ be the set of triangular faces of the tetrahedral mesh Σ_N. Using (3.40) we obtain for $i = 1, \ldots, N$

$$b_{\mathrm{T}_k} : \left(w, e_i^0\right) \mapsto - \sum_{\mathfrak{f}\in\mathcal{F}_N : \mathfrak{f}\cap\partial\sigma_i \neq \varnothing} \int_{\mathfrak{f}} \nu_{\partial\sigma_i,t}\, \mathrm{T}_k\, w \mathrm{d}S.$$

Clearly, a quadrature approach for triangular faces is required. For $\mathfrak{f} \in \mathcal{F}_N$ consider the functions $v, w : \Sigma \to \mathbb{R}$ and the model integral

$$\int_{\mathfrak{f}} v(\mathbf{x})\, \mathrm{T}_k\, w(\mathbf{x}) \mathrm{d}S(\mathbf{x}) = \int_{\widehat{\sigma}_2} v \circ \chi_{\mathfrak{f}}(\xi)\, (\mathrm{T}_k\, w) \circ \chi_{\mathfrak{f}}(\xi)\, |\det \mathrm{D}\, \chi_{\mathfrak{f}}(\xi)|\, \mathrm{d}\xi, \tag{3.41}$$

with the affine parametrization $\chi_{\mathfrak{f}} : \widehat{\sigma}_2 \to \mathfrak{f}$ and the reference triangle $\widehat{\sigma}_2$ (2-simplex) of Section 2.1. We suggest to evaluate (3.41) by means of composite midpoint rules, see Figure 3.4. In order to achieve optimal convergence of Gaussian quadrature, the integrand has to be analytic. However, the function $\mathbf{x} \mapsto \mathrm{T}_k\, w(\mathbf{x})$ is of quite low regularity, which is elaborated in Section 3.7 for an illustrative example. In this sense, the approximation of (3.41) by means of composite low-order quadrature rules is a blunt alternative. Nevertheless, the design of tailored quadrature schemes is an extensive undertaking, see the discussion in Section 3.7.

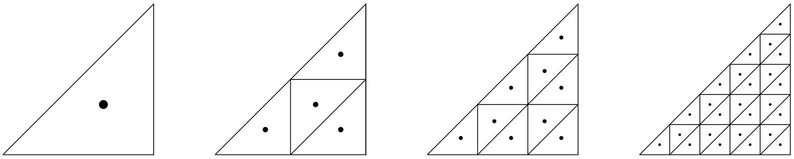

Figure 3.4: Illustration of quadrature rules employed for (3.41); for $m_Q \in \mathbb{N}$ the reference triangle $\widehat{\sigma}_2$ is subdivided into m_Q^2 congruent triangles. Due to the lack of smoothness of the integrand, the midpoint rule is applied in each triangle. The triangles and midpoints, indicated by black dots, are displayed for $m_Q = 1, 2, 3, 5$ (from left to right).

Remark 3.20. *It is clear that* (3.31) *is only applicable to the first term in* (3.39). *In order to design the high-dimensional quadrature schemes mentioned at the outset of this section, it does not suffice to consider* (3.32). *The second term in* (3.39) *is supported on the boundaries of the panels. By virtue of appropriate parametrizations, this yields an integral posed on the intersection of* $\widehat{\sigma}_2 \times \widehat{\sigma}_3$ *and a quadric, which is a four-dimensional hypersurface in the five-dimensional parameter space of* $\widehat{\sigma}_2 \times \widehat{\sigma}_3$ *(excluding any degeneracy).*

3.7 Regularity of Retarded Potentials: An Example

In Section 3.6, it is claimed that the function $\mathbf{x} \mapsto \mathrm{T}_k\, w_h(\mathbf{x})$ is not smooth for typical boundary element functions w_h. The following paragraphs supply this hypothesis with an example. The integral $\mathrm{T}_k\, w_h(\mathbf{x})$ is computed for a simple combination of evaluation point $\mathbf{x}$ and density function w_h. We investigate its partial derivatives in order to reveal certain singularities. This approach is directly adapted from [110]. In the cited publication, the smoothness of retarded potentials is studied in the context of classical methods which separate time and space discretization. The thesis of Ostermann [85] expands this work and provides substantial insight into the regularity of retarded potentials. Moreover, the encountered singularities drive the design of graded quadrature schemes. A similar survey is conducted in the thesis of Gläfke [43] for the wave equation in two spatial dimensions.

In this section, the function $\mathbf{x} \mapsto \mathrm{T}_k\, w_h(\mathbf{x})$ is studied for the following case:

- T_k is set to the single layer potential S. In other words, the kernel function

  $$k : (x, y) \mapsto \|x - y\|^{-1}$$

  is employed, where the factor 4π of k_1 in (2.32) is omitted.

- The density function $w_h : \Sigma \to \mathbb{R}$ is defined as the indicator function

$$w_h : \mathbf{y} \mapsto \begin{cases} 1 & \text{if } \mathbf{y} \in \sigma, \\ 0 & \text{otherwise,} \end{cases}$$

  of a tetrahedral panel σ. For some $h > 0$ this panel is the convex hull

$$\sigma := \operatorname{conv}\{h\mathfrak{e}_0,\, h\mathfrak{e}_1,\, h\mathfrak{e}_2,\, 0\mathfrak{e}_3\},$$

  where $\{\mathfrak{e}_i\}_{i=0}^3$ is the Cartesian basis of Section 2.1. In a slight abuse of notation h is not equal to the diameter of σ, but $\operatorname{diam}\sigma = \sqrt{2}h$ holds.

- The evaluation point $\mathbf{x}$ is confined to the tangent hyperplane $\mathcal{T}_\sigma$. We only investigate the two particular sets of locations studied in [110]. This simple combination of σ, w_h, and $\mathbf{x}$ facilitates the expression of $\mathbf{x} \mapsto \mathrm{T}_k\, w_h(\mathbf{x})$ in closed form.

In order to compute $\mathrm{T}_k\, w_h(\mathbf{x})$ we adhere to the methodology and notation discussed in Section 3.5. For the considered scenario (2.53) yields

$$\mathcal{I}(\mathbf{x}) := \mathrm{T}_k\, w_h(\mathbf{x}) = \int_{\psi_{\mathbf{x}}^{-1}(\Xi(\mathbf{x})\cap\sigma)} k(x,\cdot) \circ |_x\psi_{\mathbf{x}}(\zeta) \frac{|\det \mathrm{D}\,\psi_{\mathbf{x}}\,(\zeta)|}{\sqrt{2}\left\|J_\psi^\top(\zeta)\nu_\sigma\right\|} \mathrm{d}S(\zeta).$$

The panel σ is chosen such that its normal vector is given by $\nu_\sigma = \mathfrak{e}_3 = \begin{pmatrix}0 & 0 & 0 & 1\end{pmatrix}^\top$ and, therefore, $v_\sigma = 0$ holds. In this case, Definition 3.11 dictates the Lorentz transformation $\Lambda = I$ and we set $r_0 := 1$ for simplicity. Application of Proposition 3.15 for $v_\sigma = 0$ yields

$$\mathcal{I}(\mathbf{x}) = \int_{\psi_{\mathbf{x}}^{-1}(\Xi(\mathbf{x})\cap\sigma)} \frac{\rho\sin\theta}{\sqrt{(\cos\theta)^2 + (\rho\sin\theta)^2}} \mathrm{d}S(\zeta).$$

Since the origin is contained in $\overline{\sigma}$ we may set $\mathbf{x}_\sigma := 0$ and observe

$$\mathbf{x} \in \mathcal{T}_\sigma \quad \Leftrightarrow \quad 0 = \left\langle \mathbf{x} - \mathbf{x}_\sigma, \nu \right\rangle = x_3.$$

Choosing $\mathbf{x} \in \mathcal{T}_\sigma$, or equivalently $x_3 = 0$, yields $\rho_0 = 0$ in (3.25). It follows that the height function $h_\theta : \rho \mapsto \pi/2$ is constant-valued and $\mathcal{D}_1 = \varnothing$ as well as $\mathcal{D}_2 = [0,\infty) \times [0, 2\pi)$ hold, see Section 3.5. Exploiting (3.28) yields

$$\mathcal{I}(\mathbf{x}) = \int_U \mathrm{d}(\rho,\varphi), \quad \text{where } U := \{(\rho,\varphi) \in \mathcal{D}_2 : \phi_\sigma \circ \ell_2(\rho,\varphi) < 0\} \tag{3.42}$$

and the parametrization is given by $\ell_2 : (\rho,\varphi) \mapsto \begin{pmatrix}\rho & \varphi & \pi/2\end{pmatrix}^\top$. We observe

$$\psi_{\mathbf{x}} \circ \ell_2 : (\rho,\varphi) \mapsto \mathbf{x} - \rho\begin{pmatrix}1 & \cos\varphi & \sin\varphi & 0\end{pmatrix}^\top$$

because ℓ_2 maps to coordinates with $\theta = \pi/2$. Insertion into (3.26) yields

$$\begin{aligned}\phi_i \circ \ell_2 : (\rho, \varphi) \mapsto &\langle \psi_{\mathbf{x}} \circ \ell_2(\rho, \varphi) - \mathbf{x}_i, \nu_i \rangle \\ &= \langle \mathbf{x} - \mathbf{x}_i, \nu_i \rangle - \rho \left(\langle \mathfrak{e}_0, \nu_i \rangle + \cos\varphi \, \langle \mathfrak{e}_1, \nu_i \rangle + \sin\varphi \, \langle \mathfrak{e}_2, \nu_i \rangle \right)\end{aligned}$$

for $i = 1, \ldots, 4$. Careful inspection yields the conormal vectors of the faces

$$\nu_1 = \begin{pmatrix} -1 \\ 0 \\ 0 \\ 0 \end{pmatrix}, \quad \nu_2 = \begin{pmatrix} 0 \\ 0 \\ -1 \\ 0 \end{pmatrix}, \quad \nu_3 = \begin{pmatrix} 0 \\ -1 \\ 0 \\ 0 \end{pmatrix}, \quad \nu_4 = \frac{1}{\sqrt{3}} \begin{pmatrix} 1 \\ 1 \\ 1 \\ 0 \end{pmatrix}$$

as well as the vertices $\mathbf{x}_1 = \mathbf{x}_2 = \mathbf{x}_3 = 0$, and $\mathbf{x}_4 = h\mathfrak{e}_0 = \begin{pmatrix} h & 0 & 0 & 0 \end{pmatrix}^\top$. We have

$$\begin{aligned}\phi_1 \circ \ell_2 &: (\rho, \varphi) \mapsto \rho - t, \\ \phi_2 \circ \ell_2 &: (\rho, \varphi) \mapsto \rho \sin\varphi - x_2, \\ \phi_3 \circ \ell_2 &: (\rho, \varphi) \mapsto \rho \cos\varphi - x_1,\end{aligned}$$

and

$$\phi_4 \circ \ell_2 : (\rho, \varphi) \mapsto \big(t - h + x_1 + x_2 - \rho \left(1 + \cos\varphi + \sin\varphi\right) \big) / \sqrt{3}.$$

Recall from (3.27) that U in (3.42) is the set in which all four functions are negative

$$U = \{ (\rho, \varphi) \in \mathcal{D}_2 : \phi_i \circ \ell_2(\rho, \varphi) < 0 \quad \forall i = 1, \ldots, 4 \}.$$

We define the set in which only the first three functions are negative

$$U_0 := \{ (\rho, \varphi) \in \mathcal{D}_2 : \rho < t \quad \wedge \quad \rho \sin\varphi < x_2 \quad \wedge \quad \rho \cos\varphi < x_1 \}.$$

Clearly, it holds $U_0 = U$ iff $\phi_4 \circ \ell_2(\rho, \varphi) < 0$ holds for all $(\rho, \varphi) \in U_0$. In the following calculations we shall always choose $\mathbf{x}$ and h such that $U_0 = U$ holds true. In fact, for $(\rho, \varphi) \in U_0$ it holds $0 \le \rho < t$ and $1 + \cos\varphi + \sin\varphi \ge 1 - \sqrt{2}$ yields the bound

$$\phi_4 \circ \ell_2(\rho, \varphi) \le \left(\sqrt{2} t - h + x_1 + x_2 \right) / \sqrt{3}. \tag{3.43}$$

Case 1: Evaluation Point Approaches a Corner

Let $0 < \varepsilon < t$ and set $\mathbf{x} := \begin{pmatrix} t & -\varepsilon\sqrt{2}/2 & -\varepsilon\sqrt{2}/2 & 0 \end{pmatrix}^\top$, satisfying $x_3 = 0$ and, therefore, $\mathbf{x} \in \mathcal{T}_\sigma$. In this case (3.43) becomes

$$\phi_4 \circ \ell_2(\rho, \varphi) \le \left(\sqrt{2} t - h - \sqrt{2} \varepsilon \right) / \sqrt{3}$$

and choosing $h > \sqrt{2}t$ is sufficient for $U_0 = U$. It follows that $(\rho, \varphi) \in \mathcal{D}_2$ is in U iff the three conditions

$$\rho < t \quad \wedge \quad \rho \sin\varphi < -\varepsilon\sqrt{2}/2 \quad \wedge \quad \rho\cos\varphi < -\varepsilon\sqrt{2}/2$$

are satisfied. Since $\rho \geq 0$ and $\varepsilon > 0$ hold, the latter two conditions can both be true only for $\varphi \in (\pi, 3\pi/2)$. Solving these inequalities for ρ yields the parametrizations

$$\rho_1 : \left(\pi, \tfrac{5}{4}\pi\right] \to \mathbb{R},\ \varphi \mapsto -\frac{\sqrt{2}}{2}\frac{\varepsilon}{\sin\varphi}, \quad \rho_2 : \left(\tfrac{5}{4}\pi, \tfrac{3}{2}\pi\right) \to \mathbb{R},\ \varphi \mapsto -\frac{\sqrt{2}}{2}\frac{\varepsilon}{\cos\varphi},$$

where we note the symmetry $\rho_1(5\pi/4 - \varphi) = \rho_2(5\pi/4 + \varphi)$. The angle $\varphi_1 \in (\pi, 5\pi/4]$ such that $\rho_1(\varphi_1) = t$ holds is given by

$$\varphi_1 = \pi + \arcsin\left(\sqrt{2}\varepsilon/(2t)\right).$$

The symmetric counterpart $\varphi_2 \in (5\pi/4, 3\pi/2)$ such that $\rho_2(\varphi_2) = t$ holds follows from $\varphi_2 = 5\pi/2 - \varphi_1$. Figure 3.5a illustrates U as well as the derived parametrizations ρ_1 and ρ_2. Exploiting the symmetry, we obtain from (3.42)

$$\mathcal{I}(t,\varepsilon) = \int_{\varphi_1}^{5\pi/4}\int_{\rho_1(\varphi)}^{t} \mathrm{d}\rho\mathrm{d}\varphi + \int_{5\pi/4}^{\varphi_2}\int_{\rho_2(\varphi)}^{t} \mathrm{d}\rho\mathrm{d}\varphi = 2\int_{\varphi_1}^{5\pi/4}\int_{\rho_1(\varphi)}^{t} \mathrm{d}\rho\mathrm{d}\varphi$$

and a lengthy calculation yields

$$\begin{aligned}\mathcal{I}(t,\varepsilon) &= 2t\left(\pi/4 - \arcsin\left(\sqrt{2}\varepsilon/(2t)\right)\right)\\ &\quad - \sqrt{2}\varepsilon\log\left(\sqrt{2}-1\right) + \sqrt{2}\varepsilon\log\left(\frac{\sqrt{2}-\sqrt{2-\varepsilon^2/t^2}}{\varepsilon/t}\right).\end{aligned}$$

Its partial derivatives read

$$\begin{aligned}\partial_t\mathcal{I}(t,\varepsilon) &= 2\left(\pi/4 - \arcsin\left(\sqrt{2}\varepsilon/(2t)\right)\right),\\ \partial_\varepsilon\mathcal{I}(t,\varepsilon) &= -\sqrt{2}\log\left(\sqrt{2}-1\right) + \sqrt{2}\log\left(\frac{\sqrt{2}-\sqrt{2-\varepsilon^2/t^2}}{\varepsilon/t}\right).\end{aligned}$$

The singularity at $\varepsilon \to 0$ occurs as $\mathbf{x}$ approaches the boundary of σ. The second-order partial derivatives are

$$\partial_t^2\mathcal{I}(t,\varepsilon) = \frac{2\varepsilon}{t^2\sqrt{2-\varepsilon^2/t^2}}, \quad \partial_{t\varepsilon}\mathcal{I}(t,\varepsilon) = -\frac{2}{t\sqrt{2-\varepsilon^2/t^2}}, \quad \partial_\varepsilon^2\mathcal{I}(t,\varepsilon) = \frac{2}{\varepsilon\sqrt{2-\varepsilon^2/t^2}}.$$

The apparent singularity for $\varepsilon \to \sqrt{2}t$ is not relevant because $\varepsilon > t$ implies $U = \varnothing$ and, therefore, $\mathcal{I}(t,\varepsilon) = 0$. Since $t \to 0$ implies $\varepsilon \to 0$ (recall $0 < \varepsilon < t$), it follows that all singularities are confined to the boundary $\partial\sigma$.

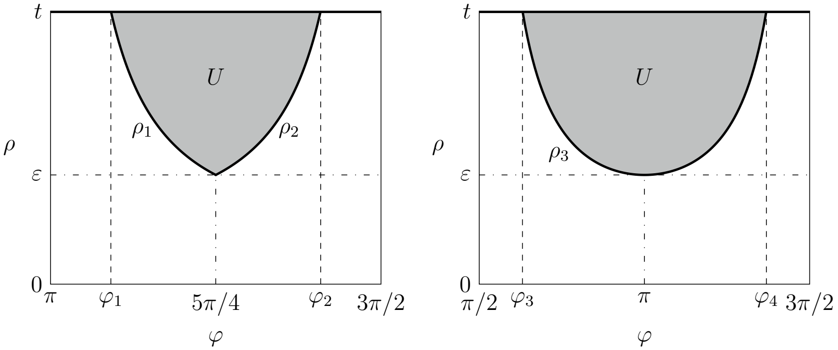

a) case 1: point approaches a corner b) case 2: point approaches an edge

Figure 3.5: Depiction of the set U in (3.42) for $\varepsilon := 2t/5$; the curved lines are parametrized via ρ_1 and ρ_2 (case 1) and ρ_3 (case 2) respectively. Dashed lines indicate the angles $\varphi_i, i = 1, \ldots, 4$, where the curved lines intersect the upper bound $\rho = t$. Appreciate the different scaling of the abscissa as well as the symmetry of U about the central axis, which is exploited in the calculation of (3.42).

Case 2: Evaluation Point Approaches an Edge

Let $0 < \varepsilon < t$ and set $\mathbf{x} := \begin{pmatrix} t & -\varepsilon & h/2 & 0 \end{pmatrix}^\top$, where we note that $x_3 = 0$ implies $\mathbf{x} \in \mathcal{T}_\sigma$. From (3.43) we obtain the bound

$$\phi_4 \circ \ell_2(\rho, \varphi) \leq \left(\sqrt{2}t - h/2 - \varepsilon\right)/\sqrt{3}$$

and the condition $h > 2\sqrt{2}t$ is sufficient for $U_0 = U$. In this case, $(\rho, \varphi) \in \mathcal{D}_2$ is in U iff the three conditions

$$\rho < t \quad \wedge \quad \rho \sin\varphi < h/2 \quad \wedge \quad \rho\cos\varphi < -\varepsilon$$

hold true. The first condition implies the middle one, because h is chosen sufficiently large. To confirm this claim, assume that $\rho < t$ and $h > 2\sqrt{2}t$ hold true, yielding

$$\rho < t < \sqrt{2}h/4 \quad \Rightarrow \quad \rho\sin\varphi \leq \rho < \sqrt{2}h/4 < h/2$$

because $\rho \geq 0$ and $\sin\varphi \leq 1$ hold. Consequently, $(\rho, \varphi) \in \mathcal{D}_2$ is in U iff

$$\rho < t \quad \wedge \quad \rho\cos\varphi < -\varepsilon$$

hold. From $\rho \geq 0$ and $\varepsilon > 0$ it follows that the latter inequality holds only for $\varphi \in (\pi/2, 3\pi/2)$. Solving this inequality for ρ yields the map

$$\rho_3 : \left(\tfrac{1}{2}\pi, \tfrac{3}{2}\pi\right) \to \mathbb{R}, \ \varphi \mapsto -\frac{\varepsilon}{\cos\varphi}.$$

We observe the symmetry $\rho_3(\pi + \varphi) = \rho_3(\pi - \varphi)$, which is similar to the first case. The angle $\varphi_3 \in (\pi/2, \pi)$ such that $\rho_3(\varphi_3) = t$ holds is given by

$$\varphi_3 = \arccos(-\varepsilon/t)$$

and its symmetric counterpart by $\varphi_4 = 2\pi - \varphi_3$, see Figure 3.5b. Again, this symmetry is exploited and an extended calculation of (3.42) yields

$$\mathcal{I}(t, \varepsilon) = 2 \int_{\varphi_3}^{\pi} \int_{\rho_3(\varphi)}^{t} \mathrm{d}\rho \mathrm{d}\varphi = 2t\left(\pi - \arccos(-\varepsilon/t)\right) - 2\varepsilon \log\left(\frac{1 + \sqrt{1 - \varepsilon^2/t^2}}{\varepsilon/t}\right).$$

Its partial derivatives are given by

$$\partial_t \mathcal{I}(t, \varepsilon) = 2\left(\pi - \arccos(-\varepsilon/t)\right), \quad \partial_\varepsilon \mathcal{I}(t, \varepsilon) = -2 \log\left(\frac{1 + \sqrt{1 - \varepsilon^2/t^2}}{\varepsilon/t}\right).$$

In analogy to the first scenario, the singularity at $\varepsilon \to 0$ occurs as $\mathbf{x}$ approaches $\partial\sigma$. The second-order partial derivatives, however, reveal a more intriguing behavior

$$\partial_t^2 \mathcal{I}(t, \varepsilon) = \frac{2\varepsilon}{t^2\sqrt{1 - \varepsilon^2/t^2}}, \quad \partial_{t\varepsilon} \mathcal{I}(t, \varepsilon) = -\frac{2}{t\sqrt{1 - \varepsilon^2/t^2}}, \quad \partial_\varepsilon^2 \mathcal{I}(t, \varepsilon) = \frac{2}{\varepsilon\sqrt{1 - \varepsilon^2/t^2}}.$$

While the singularities at $\varepsilon \to 0$ and $t \to 0$ have already been encountered in the first case, the singularity at $\varepsilon \to t$ occurs exclusively in the second case. It is indeed relevant because $\varepsilon \to t$ describes a scenario in which the light cone grazes an edge of σ. This singular behavior is not limited to $\partial\sigma$: the point $\mathbf{x}$ with $\varepsilon = t$ is given by

$$\begin{pmatrix} 0 & 0 & h/2 & 0 \end{pmatrix}^\top + t \begin{pmatrix} 1 & -1 & 0 & 0 \end{pmatrix}^\top,$$

where the latter vector (which indicates the direction) is lightlike. We are inclined to induce that this singularity is related to forward light cones with apexes at the edges of σ. We conclude these investigations by stating that our findings agree with the ones published in [110] astonishingly well.

Remark 3.21. *While the surveys in the references discussed at the beginning of this section [110, 85, 43] feature great detail, this thesis is not intended to delve any deeper into investigations regarding the regularity of retarded potentials. Such a study exceeds the scope of this work, however, a detailed analysis like in [85] could indeed drive the design of tailored quadrature schemes. Nevertheless, the purpose of this section is to support the claim uttered in Section 3.6: the function* $\mathbf{x} \mapsto \mathrm{T}_k w_h(\mathbf{x})$ *is not smooth and standard Gaussian quadrature schemes fail to converge at exponential rate. More detailed investigations might be worthwhile efforts for further research.*

3.8 Algorithmic and Implementational Aspects

This section gathers comments regarding relevant implementational details. In Section 3.8.1, we exhibit an algorithm for evaluating the retarded layer potential T_k based on (3.28), which is derived in Section 3.5. Since numerical integration plays a central role in this thesis, Section 3.8.2 comments on the employed quadrature rules. Section 3.8.3 discusses an idea for the efficient computation of the intersection of light cone and space-time mesh.

3.8.1 An Algorithm for Evaluating Retarded Layer Potentials

A quadrature scheme for the integral (3.28) is devised. This technique facilitates pointwise evaluations of the retarded potential $\mathrm{T}_k\, w(\mathbf{x})$. The index of the domain $n \in \{1, 2\}$ is fixed and we consider the model integral of (3.28)

$$\int_{\mathcal{B}_n} f(\eta)\mathrm{d}\eta, \quad \mathcal{B}_n := \{\eta \in \mathcal{D}_n : \phi_\sigma \circ \ell_n(\eta) < 0\},$$

with the integrand $f : \mathcal{B}_n \to \mathbb{R}$. As already indicated at the end of Section 3.5, the level set function $\phi_\sigma \circ \ell_n$ is not differentiable and, therefore, $\mathcal{B}_n$ might feature corners. To alleviate this difficulty, we introduce a suitable grid of $\mathcal{D}_n \subset \mathbb{R}^2$. Let $\{\mathcal{R}_i^n\}_i$ be a set of open non-overlapping rectangles covering $\mathcal{D}_n$

$$\overline{\mathcal{D}_n} = \bigcup\nolimits_i \overline{\mathcal{R}_i^n}, \quad \mathcal{R}_i^n \cap \mathcal{R}_j^n = \varnothing \text{ for } i \neq j.$$

These rectangles are chosen such that each corner of $\mathcal{B}_n$ coincides with a corner of at least one rectangle in $\{\mathcal{R}_i^n\}_i$. The calculation of the corners of $\mathcal{B}_n$ is addressed in a separate passage. The proposed scheme approximates the integral via

$$\int_{\mathcal{B}_n} f(\eta)\mathrm{d}\eta = \sum\nolimits_i \int_{\mathcal{B}_n \cap \mathcal{R}_i^n} f(\eta)\mathrm{d}\eta \approx \sum\nolimits_i \texttt{IntegrateRectangleBn}(f, n_G, r_{\max}; \mathcal{R}_i^n, 0),$$

where the procedure `IntegrateRectangleBn` is exhibited in Algorithm 1. The number of quadrature points per direction $n_G \in \mathbb{N}$ and the depth of recursion $r_{\max} \in \mathbb{N}_0$ are explained in the following passage. Algorithm 1 attempts to identify the shape of $\mathcal{B}_n \cap \mathcal{R}_j^n$ among a few predefined scenarios. For these shapes suitable parametrizations $(0, 1)^2 \to \mathcal{B}_n \cap \mathcal{R}_j^n$ can be constructed. If this shape identification fails, the procedure resorts to subdivision and recursion. The basic algorithm is adapted from [37], however, it is tailored to the level set function $\phi_\sigma \circ \ell_n$.

Algorithm 1 is a template, several remarks about technical details are in order:

Algorithm 1 `IntegrateRectangleBn`$(f, n_G, r_{\max}; \mathcal{R}, r)$. Given an integrand $f : \mathcal{B}_n \to \mathbb{R}$, the number of quadrature points $n_G \in \mathbb{N}$, the depth of recursion $r_{\max} \in \mathbb{N}_0$, a rectangle $\mathcal{R} \subset \mathcal{D}_n$, and the level of recursion $r \in \mathbb{N}_0$. Return approximation of the integral $\int_{\mathcal{B}_n \cap \mathcal{R}} f(\eta) \mathrm{d}\eta$.

```
 1: set bounds $\phi_L, \phi_U \in \mathbb{R}$ such that ran $\big(\phi_\sigma \circ \ell_n|_{\mathcal{R}}\big) \subset [\phi_L, \phi_U]$ holds
 2: if $\phi_L > 0$ then
 3:     return 0
 4: else if $\phi_U \leq 0$ then
 5:     return $\int_{\mathcal{R}} f(\eta) \mathrm{d}\eta$ via quadrature ($n_G$ points)
 6: end if
 7: compute $\mathcal{Z} \coloneqq \{\eta \in \partial\mathcal{R} : \phi_\sigma \circ \ell_n(\eta) = 0\}$
 8: if $\mathcal{Z}$ matches a predefined scenario then
 9:     construct parametrization $\varkappa : (0,1)^2 \to \mathcal{B}_n \cap \mathcal{R}$
10:     return $\int_{(0,1)^2} f \circ \varkappa(z) \, |\det \mathrm{D} \varkappa(z)| \, \mathrm{d}z$ via quadrature ($n_G$ points)
11: else if $r \geq r_{\max}$ then
12:     return low-order approximation of $\int_{\mathcal{B}_n \cap \mathcal{R}} f(\eta) \mathrm{d}\eta$
13: else
14:     subdivide $\overline{\mathcal{R}} = \bigcup_i \overline{\mathcal{R}_i}$ into non-overlapping rectangles $\{\mathcal{R}_i\}_i$
15:     return $\sum_i$ IntegrateRectangleBn$(f, n_G, r_{\max}; \mathcal{R}_i, r+1)$
16: end if
```

- In line 1, the values $\phi_L, \phi_U \in \mathbb{R}$ are chosen such that

  $$\phi_L \leq \inf_{\eta \in \mathcal{R}} \phi_\sigma \circ \ell_n(\eta) \leq \sup_{\eta \in \mathcal{R}} \phi_\sigma \circ \ell_n(\eta) \leq \phi_U$$

  holds. We suggest to employ the bounds

  $$\phi_L \coloneqq \max_{i=1,\ldots,4} \inf_{\eta \in \mathcal{R}} \phi_i \circ \ell_n(\eta), \quad \phi_U \coloneqq \max_{i=1,\ldots,4} \sup_{\eta \in \mathcal{R}} \phi_i \circ \ell_n(\eta).$$

  The computation of the minimum/maximum of $\phi_i \circ \ell_n, i = 1, \ldots, 4$ in $\mathcal{R}$ is discussed in one of the following segments. While ϕ_U is the exact maximum of $\phi_\sigma \circ \ell_n$, the max-min inequality suggests that ϕ_L is only a lower bound

  $$\inf_{\eta \in \mathcal{R}} \phi_\sigma(\eta) = \inf_{\eta \in \mathcal{R}} \max_{i=1,\ldots,4} \phi_i(\eta) \geq \max_{i=1,\ldots,4} \inf_{\eta \in \mathcal{R}} \phi_i(\eta) = \phi_L.$$

- Lines 2–6 identify and resolve simple scenarios. From $\phi_L > 0$ it follows that $\phi_\sigma \circ \ell_n$ is strictly positive on $\mathcal{R}$ and, therefore, $\mathcal{B}_n \cap \mathcal{R} = \varnothing$. Conversely, $\phi_U \leq 0$ implies the nonpositivity of $\phi_\sigma \circ \ell_n$ on $\mathcal{R}$, yielding $\mathcal{B}_n \cap \mathcal{R} = \mathcal{R}$.

- The set $\mathcal{Z}$ in line 7 contains all roots of $\phi_\sigma \circ \ell_n$ along the edges of $\mathcal{R}$. It is used to characterize the shape of $\mathcal{B}_n \cap \mathcal{R}$ and its calculation is addressed separately.

- Lines 8–10 are concerned with evaluating the integral if the shape of $\mathcal{B}_n \cap \mathcal{R}$ is deemed admissible. This process is adapted from [37] and discussed below.
- The integrals in lines 5 and 10 are posed on rectangles. Their approximation via tensor-Gauss quadrature is straightforward, see Section 3.8.2. Since $n_G \in \mathbb{N}$ denotes the number of quadrature points per direction, a total of n_G^2 points is used to evaluate the integral.
- In line 8, only few scenarios for $\mathcal{Z}$ are considered admissible. If the shape of $\mathcal{B}_n \cap \mathcal{R}$ is too complicated it might not fit to such a template, even after many recursive calls of `IntegrateRectangleBn`. To ensure that the algorithm terminates correctly, lines 11–12 implement a low-order approximation if the level of recursion exceeds a predefined depth $r_{\max} \in \mathbb{N}_0$. This approach is justified by noting that $|\mathcal{R}|$ is presumed to be small after $r_{\max}$ successive subdivisions. Therefore, the contribution to the overall error is expected to be moderate. In our implementation, we resort to a midpoint rule as suggested in [105]

  $$\int_{\mathcal{B}_n \cap \mathcal{R}} f(\eta) \mathrm{d}\eta \approx \begin{cases} |\mathcal{R}| f(\eta_M) & \text{if } \phi_\sigma \circ \ell_n(\eta_M) \leq 0, \\ 0 & \text{if } \phi_\sigma \circ \ell_n(\eta_M) > 0, \end{cases}$$

  where η_M denotes the centroid of $\mathcal{R}$. Alternatively, one might employ a first-order approximation due to affine interpolation of the values of $\phi_\sigma \circ \ell_n$ at the corners of $\mathcal{R}$. Based on whether these values are positive or nonpositive this yields $2^4 = 16$ cases, see [75, Figure 6]. The first-order approximations of $\mathcal{B}_n \cap \mathcal{R}$ depicted in the cited reference can be decomposed into not more than four triangles. A midpoint rule is employed in each triangle. Both low-order approximations were compared by means of a few numerical experiments. The observed differences between these approaches are insignificant and, therefore, the straightforward midpoint rule is preferred.
- Line 14 prepares the recursive call of `IntegrateRectangleBn` by subdividing $\mathcal{R}$. In our implementation, $\mathcal{R}$ is subdivided into four rectangles of equal size obtained by bisecting the edges of $\mathcal{R}$.

Prior to addressing the details indicated in the list above, we investigate the level set function of the ith face for $i = 1, \dots, 4$ defined in (3.26)

$$\phi_i : \zeta \mapsto \langle \psi_{\mathbf{x}}(\zeta) - \mathbf{x}_i, \nu_i \rangle = \langle \mathbf{x} - \mathbf{x}_i, \nu_i \rangle - r_0 \rho \left\langle \begin{pmatrix} 1 \\ e_{\mathbb{S}}(\varphi, \theta) \end{pmatrix}, \Lambda^\top \nu_i \right\rangle .$$

For $j = 1, \dots, 4$ let $\alpha_{i,j} := \left\langle \Lambda^\top \nu_i, \mathfrak{e}_{(j-1)} \right\rangle$ or in other words $\alpha_{i,j} \in \mathbb{R}$ is the jth coefficient of $\Lambda^\top \nu_i$. Insertion of $e_{\mathbb{S}}$ as in Definition 2.20 yields

$$\phi_i : \zeta \mapsto \langle \mathbf{x} - \mathbf{x}_i, \nu_i \rangle - r_0 \rho \left(\alpha_{i,1} + (\alpha_{i,2} \cos\varphi + \alpha_{i,3} \sin\varphi) \sin\theta + \alpha_{i,4} \cos\theta \right).$$

Define the modified normal distance value

$$d_i := \langle \mathbf{x} - \mathbf{x}_i, \nu_i \rangle - r_0 \rho_0 \alpha_{i,4}$$

and insertion of the parametrization $\rho(\theta) := h_\rho(\theta)$ introduced in Section 3.5 yields

$$\phi_i \circ \ell_1 : (\theta, \varphi) \mapsto d_i - \alpha_{i,1} \frac{r_0 \rho_0}{\cos\theta} - r_0 \rho_0 \tan\theta \left(\alpha_{i,2} \cos\varphi + \alpha_{i,3} \sin\varphi \right), \tag{3.44}$$

while insertion of the map $\theta(\rho) := h_\theta(\rho)$ discussed in Section 3.5 yields (with $\rho \geq 0$)

$$\phi_i \circ \ell_2 : (\rho, \varphi) \mapsto d_i - \alpha_{i,1} r_0 \rho - r_0 \sqrt{\rho^2 - \rho_0^2} \left(\alpha_{i,2} \cos\varphi + \alpha_{i,3} \sin\varphi \right). \tag{3.45}$$

Preliminary Task: Finding the Corners of $\mathcal{B}_n$

The functions $\phi_i \circ \ell_n, i = 1, \ldots, 4$ are smooth and, therefore, $\eta \in \partial\mathcal{B}_n$ is a corner only if at least two of these functions vanish. Consequently, there exist $i \in \{1, \ldots, 4\}$ and $j \in \{1, \ldots, 4\} \setminus \{i\}$ such that η satisfies $\phi_i \circ \ell_n(\eta) = \phi_j \circ \ell_n(\eta) = 0$. In other words, a corner of $\mathcal{B}_n$ corresponds to a point where the ith and the jth face of the tetrahedron σ intersect. Evidently, the corners of $\mathcal{B}_n$ correspond to the intersection of the backward light cone $\Xi(\mathbf{x})$ and the edges of σ.

We suggest to compute these intersections directly in four-dimensional space-time and transport them to $\mathcal{D}_n$ by inversion of the parametrization $\psi_{\mathbf{x}} \circ \ell_n$. Consider an edge of σ given by the end points $\mathbf{y}_A, \mathbf{y}_B \in \mathbb{R}^4$. The employed parametrization of this edge $\chi_{AB} : [0,1] \to \mathbb{R}^4$ is defined by $\chi_{AB} : s \mapsto \mathbf{y}_A + (\mathbf{y}_B - \mathbf{y}_A)\, s$. The intersection of the considered edge and the double light cone with apex at $\mathbf{x} \in \mathbb{R}^4$ satisfies

$$[\mathbf{x} - \chi_{AB}(s), \mathbf{x} - \chi_{AB}(s)] = 0$$

resulting in the quadratic equation for s

$$[\mathbf{y}_B - \mathbf{y}_A, \mathbf{y}_B - \mathbf{y}_A]\, s^2 - 2\, [\mathbf{y}_B - \mathbf{y}_A, \mathbf{x} - \mathbf{y}_A]\, s + [\mathbf{x} - \mathbf{y}_A, \mathbf{x} - \mathbf{y}_A] = 0.$$

Only real solutions $s \in [0,1]$ associated to the backward cone $\Xi(\mathbf{x})$

$$t \geq \tau_A + (\tau_B - \tau_A)\, s$$

are relevant. All relevant parameters s are mapped to points in space-time by virtue of $\mathbf{y} := \chi_{AB}(s)$. Each of these points is transported to $\mathcal{P}$ via $\zeta := \psi_{\mathbf{x}}^{-1}(\mathbf{y})$ and mapped to the correct parameter domain

$$\eta := \begin{cases} \ell_1^{-1}(\zeta) & \text{if } \rho < \rho_{\text{eq}}, \\ \ell_2^{-1}(\zeta) & \text{if } \rho \geq \rho_{\text{eq}}. \end{cases}$$

Note that for $\rho < \rho_{\text{eq}}$ the parameter η is in $\mathcal{D}_1$ while for $\rho \geq \rho_{\text{eq}}$ it lies in $\mathcal{D}_2$. Applying this procedure to all six edges of σ yields the set of corners of $\mathcal{B}_n, n = 1, 2$. Its cardinality does not exceed twelve because each of the six quadratic equations has at most two real solutions.

Line 1 of Algorithm 1: Computing the Extrema of $\phi_i \circ \ell_n$

The simplicity of the functions (3.44) and (3.45) is exploited to evaluate their extrema. For $\alpha, \beta \in \mathbb{R}$ consider the auxiliary function

$$f_\star[\alpha,\beta] : \mathbb{R} \to \mathbb{R}, \quad \varphi \mapsto \alpha \cos\varphi + \beta \sin\varphi. \tag{3.46}$$

Given $\varphi_A, \varphi_B \in \mathbb{R}$ with $\varphi_A < \varphi_B$ we wish to find the extrema of $f_\star[\alpha,\beta]$ in $[\varphi_A, \varphi_B]$. Clearly, φ is a local extremum of $f_\star[\alpha,\beta]$ only if $f_\star'[\alpha,\beta](\varphi) = 0$ holds, leading to

$$0 = f_\star'[\alpha,\beta](\varphi) = f_\star[\beta,-\alpha](\varphi) \quad \Leftrightarrow \quad \alpha \sin\varphi = \beta\cos\varphi. \tag{3.47}$$

Note that if φ solves (3.47), then $\varphi + m\pi$ solves (3.47) also for any $m \in \mathbb{Z}$. With this periodicity in mind we provide two solutions of (3.47)

$$\varphi_1 = 2\arctan2\left(\operatorname{sgn}(\beta)\sqrt{\alpha^2+\beta^2} - \alpha, \beta\right), \quad \varphi_2 = \varphi_1 + \pi,$$

where $\arctan2 : \mathbb{R}\times\mathbb{R} \to (-\pi, \pi]$ is the usual four-quadrant inverse tangent function. The extrema at φ_1 and φ_2 are attained in $[\varphi_A, \varphi_B]$ iff any of their 2π-periodic shifts lies in $[\varphi_A, \varphi_B]$. In particular, for $j = 1, 2$ let $m_j \in \mathbb{Z}$ be such that

$$\frac{\varphi_A - \varphi_j}{2\pi} \le m_j \le \frac{\varphi_B - \varphi_j}{2\pi} \tag{3.48}$$

is satisfied. The minimum/maximum of $f_\star[\alpha,\beta]$ in $[\varphi_A, \varphi_B]$ follows by taking the minimum/maximum of the values $f_\star[\alpha,\beta](\varphi_A)$, $f_\star[\alpha,\beta](\varphi_B)$, and all $f_\star[\alpha,\beta](\varphi_j)$ for which $m_j, j = 1, 2$ in (3.48) exists. This procedure is employed to evaluate

$$\beta_{\min} := \min_{\varphi\in[\varphi_A,\varphi_B]} f_\star[-\alpha_{i,2}, -\alpha_{i,3}](\varphi), \quad \beta_{\max} := \max_{\varphi\in[\varphi_A,\varphi_B]} f_\star[-\alpha_{i,2}, -\alpha_{i,3}](\varphi), \tag{3.49}$$

which are used to compute the extrema of (3.44) and (3.45) in the following paragraphs.

Given a rectangle $[\theta_A, \theta_B] \times [\varphi_A, \varphi_B] \subset \mathcal{D}_1$ we are concerned with (3.44)

$$\phi_i \circ \ell_1 : (\theta, \varphi) \mapsto d_i - \alpha_{i,1}\frac{r_0\rho_0}{\cos\theta} + r_0\rho_0 \tan\theta\, f_\star[-\alpha_{i,2}, -\alpha_{i,3}](\varphi).$$

Since ℓ_1 maps $\mathcal{D}_1$ to solutions of (3.25) it follows that $\operatorname{sgn}\rho_0 = \operatorname{sgn}\cos\theta$ holds (recall $\rho \ge 0$). For $\theta \in [0,\pi]\backslash\{\pi/2\}$ it holds $\operatorname{sgn}\cos\theta = \operatorname{sgn}\tan\theta$, yielding $\operatorname{sgn}\rho_0 = \operatorname{sgn}\tan\theta$. Therefore, $r_0\rho_0\tan\theta \ge 0$ holds true in $\mathcal{D}_1$ and (3.49) leads to

$$\beta_{\min} r_0\rho_0 \tan\theta \le r_0\rho_0\tan\theta\, f_\star[-\alpha_{i,2}, -\alpha_{i,3}](\varphi) \le \beta_{\max} r_0\rho_0\tan\theta.$$

For $* \in \{\min, \max\}$ consider the function $g_{\theta,*} : \mathbb{R} \to \mathbb{R}$ defined by

$$g_{\theta,*} : \theta \mapsto d_i - \alpha_{i,1}\frac{r_0\rho_0}{\cos\theta} + \beta_* r_0\rho_0 \tan\theta.$$

We evaluate the necessary condition for a local extremum of $g_{\theta,*}$

$$0 = g'_{\theta,*}(\theta) = -\alpha_{i,1} r_0 \rho_0 \frac{\sin\theta}{(\cos\theta)^2} + \frac{\beta_* r_0 \rho_0}{(\cos\theta)^2} \quad \Leftrightarrow \quad \alpha_{i,1}\sin\theta = \beta_*,$$

where we used that $\rho_0 \neq 0$ must hold for $\mathcal{D}_1 \neq \varnothing$. Solutions to this equation exist for $|\beta_*/\alpha_{i,1}| \leq 1$ and the two relevant ones are given by

$$\theta_1^* = \arcsin\left(\beta_*/\alpha_{i,1}\right), \quad \theta_2^* = \pi - \theta_1^*.$$

The minimum/maximum of $\phi_i \circ \ell_1$ in $[\theta_A, \theta_B] \times [\varphi_A, \varphi_B]$ is computed as follows: set $* = \min$ or $* = \max$, respectively, and compute the minimum/maximum of the values $g_{\theta,*}(\theta_A)$, $g_{\theta,*}(\theta_B)$, and all $g_{\theta,*}(\theta_j^*)$ for which $\theta_j^*, j = 1, 2$ is in $[\theta_A, \theta_B]$.

The function (3.45) in $[\rho_A, \rho_B] \times [\varphi_A, \varphi_B] \subset \mathcal{D}_2$ can be treated similarly. We observe

$$\phi_i \circ \ell_2 : (\rho, \varphi) \mapsto d_i - \alpha_{i,1} r_0 \rho + r_0\sqrt{\rho^2 - \rho_0^2}\, f_\star[-\alpha_{i,2}, -\alpha_{i,3}](\varphi)$$

and with $\beta_{\min}$ and $\beta_{\max}$ as in (3.49) we obtain (recall $r_0 > 0$)

$$\beta_{\min} r_0\sqrt{\rho^2 - \rho_0^2} \leq r_0\sqrt{\rho^2 - \rho_0^2}\, f_\star[-\alpha_{i,2}, -\alpha_{i,3}](\varphi) \leq \beta_{\max} r_0\sqrt{\rho^2 - \rho_0^2}.$$

For $* \in \{\min, \max\}$ define $g_{\rho,*} : [\rho_0, \infty) \to \mathbb{R}$ by

$$g_{\rho,*} : \rho \mapsto d_i - \alpha_{i,1} r_0 \rho + \beta_* r_0 \sqrt{\rho^2 - \rho_0^2}.$$

It follows

$$0 = g'_{\rho,*}(\rho) = -\alpha_{i,1} r_0 + \frac{\beta_* r_0 \rho}{\sqrt{\rho^2 - \rho_0^2}} \quad \Rightarrow \quad \frac{\beta_*^2 \rho^2}{\rho^2 - \rho_0^2} = \alpha_{i,1}^2.$$

A relevant solution exists iff $|\alpha_{i,1}| > |\beta_*|$ holds and it is given by

$$\rho_1^* = |\rho_0 \alpha_{i,1}| / \sqrt{\alpha_{i,1}^2 - \beta_*^2}.$$

Again, set $* = \min$ or $* = \max$, respectively, and take the minimum/maximum of the values $g_{\rho,*}(\rho_A)$, $g_{\rho,*}(\rho_B)$, and $g_{\rho,*}(\rho_1^*)$ if ρ_1^* exists and is in $[\rho_A, \rho_B]$.

Line 7 of Algorithm 1: Finding Roots Along the Axes

Line 7 of Algorithm 1 requires the computation of roots of $\phi_\sigma \circ \ell_n$ along edges of a given rectangle. As an example, let $\mathcal{R} := (\eta_{1,A}, \eta_{1,B}) \times (\eta_{2,A}, \eta_{2,B})$. In order to determine the roots along the first edge we have to find $\eta_1 \in [\eta_{1,A}, \eta_{1,B}]$ such that $\phi_\sigma \circ \ell_n(\eta_1, \eta_{2,A}) = 0$ holds. We suggest to compute all parameters $\eta_1 \in [\eta_{1,A}, \eta_{1,B}]$ that solve $\phi_i \circ \ell_n(\eta_1, \eta_{2,A}) = 0$ for at least one $i = 1, \ldots, 4$. For all those candidates η_1, the actual level set function ϕ_σ is evaluated and only those values are kept that satisfy $\phi_\sigma \circ \ell_n(\eta_1, \eta_{2,A}) = 0$. This example shows that we have to be capable of treating the following four cases for any $i = 1, \ldots, 4$:

(i) $n=1$, fix φ and find θ such that $\phi_i \circ \ell_1(\theta,\varphi)=0$ holds,

(ii) $n=1$, fix θ and find φ such that $\phi_i \circ \ell_1(\theta,\varphi)=0$ holds,

(iii) $n=2$, fix φ and find ρ such that $\phi_i \circ \ell_2(\rho,\varphi)=0$ holds,

(iv) $n=2$, fix ρ and find φ such that $\phi_i \circ \ell_2(\rho,\varphi)=0$ holds.

Prior to tackling each of these cases, the solution of an auxiliary problem is discussed. For $\alpha,\beta\in\mathbb{R}$ and $c_0\in\mathbb{R}$ consider the problem

$$f_\star[\alpha,\beta](z)=c_0, \tag{3.50}$$

where $f_\star[\alpha,\beta]$ is as in (3.46). Two solutions of (3.50) are given by

$$\begin{aligned}\beta\neq 0: &\quad z_1=\arcsin\left(\frac{c_0}{\operatorname{sgn}\beta\sqrt{\alpha^2+\beta^2}}\right)-\arctan(\alpha/\beta), && z_2=\pi-z_1,\\ \beta=0: &\quad z_1=\arccos(c_0/\alpha), && z_2=2\pi-z_1.\end{aligned} \tag{3.51}$$

Note that these solutions exist iff the absolute values of the arguments of arcsin and arccos are not greater than 1. The provided solutions can be shifted by $m2\pi$ for $m\in\mathbb{Z}$ to transport them to suitable intervals $[z_A,z_B]$.

We discuss (i) and multiply (3.44) by $\cos\theta$ (recall $\cos\theta\neq 0$ in $\mathcal{D}_1$), leading to

$$0=\phi_i\circ\ell_1(\theta,\varphi) \quad\Leftrightarrow\quad 0=d_i\cos\theta-\alpha_{i,1}r_0\rho_0-r_0\rho_0\sin\theta\left(\alpha_{i,2}\cos\varphi+\alpha_{i,3}\sin\varphi\right).$$

Insertion of the fixed value $\beta_\varphi:=(\alpha_{i,2}\cos\varphi+\alpha_{i,3}\sin\varphi)$ yields

$$0=d_i\cos\theta-\alpha_{i,1}r_0\rho_0-\beta_\varphi r_0\rho_0\sin\theta \quad\Leftrightarrow\quad f_\star[d_i,-\beta_\varphi r_0\rho_0](\theta)=\alpha_{i,1}r_0\rho_0,$$

whose solution is due to (3.50) and (3.51). We turn our attention to (ii)

$$0=\phi_i\circ\ell_1(\theta,\varphi) \quad\Leftrightarrow\quad r_0\rho_0\tan\theta\left(\alpha_{i,2}\cos\varphi+\alpha_{i,3}\sin\varphi\right)=d_i-\alpha_{i,1}\frac{r_0\rho_0}{\cos\theta},$$

where we used (3.44). This results in

$$0=\phi_i\circ\ell_1(\theta,\varphi) \quad\Leftrightarrow\quad f_\star\left[r_0\rho_0\alpha_{i,2}\tan\theta,\ r_0\rho_0\alpha_{i,3}\tan\theta\right](\varphi)=d_i-\alpha_{i,1}\frac{r_0\rho_0}{\cos\theta},$$

whose solution is also due to (3.50) and (3.51). For (iii) we obtain from (3.45)

$$\begin{aligned}0=\phi_i\circ\ell_2(\rho,\varphi) \quad&\Leftrightarrow\quad d_i-\alpha_{i,1}r_0\rho=\beta_\varphi r_0\sqrt{\rho^2-\rho_0^2}\\ &\Rightarrow\quad \left(d_i-\alpha_{i,1}r_0\rho\right)^2=\beta_\varphi^2r_0^2\left(\rho^2-\rho_0^2\right)\\ &\Leftrightarrow\quad \left(\alpha_{i,1}^2-\beta_\varphi^2\right)r_0^2\rho^2-2d_i\alpha_{i,1}r_0\rho+d_i^2+r_0^2\rho_0^2\beta_\varphi^2=0,\end{aligned}$$

which is a quadratic equation for ρ. The real solutions of this equation are inserted into $\phi_i \circ \ell_2$ and only those solutions satisfying $\phi_i \circ \ell_2(\rho, \varphi) = 0$ are kept. Finally, we address (iv) and (3.45) yields

$$0 = \phi_i \circ \ell_2(\rho, \varphi) \quad \Leftrightarrow \quad r_0\sqrt{\rho^2 - \rho_0^2}\,(\alpha_{i,2}\cos\varphi + \alpha_{i,3}\sin\varphi) = d_i - \alpha_{i,1} r_0 \rho.$$

This leads to

$$0 = \phi_i \circ \ell_2(\rho, \varphi) \quad \Leftrightarrow \quad f_\star\left[r_0\sqrt{\rho^2 - \rho_0^2}\alpha_{i,2},\, r_0\sqrt{\rho^2 - \rho_0^2}\alpha_{i,3}\right](\varphi) = d_i - \alpha_{i,1} r_0 \rho,$$

whose solution is due to (3.50) and (3.51).

Line 8 of Algorithm 1: Identification of Admissible Scenarios

The algorithm exhibited in this section considers only the admissible cases discussed in [37, Sections 3.2 and 3.3.2]. A necessary condition for admissibility is $|\mathcal{Z}| = 2$, i.e., there are exactly two roots along $\partial\mathcal{R}$. Let $\mathcal{Z} = \{\eta_A, \eta_B\}$, where $\eta_A, \eta_B \in \partial\mathcal{R}$ are the roots. Further assumptions are imposed:

- The points η_A and η_B are not exclusively contained in the same edge.
- A unique face can be assigned to the zero level set of $\phi_\sigma \circ \ell_n$ in $\mathcal{R}$

$$\exists!\; i \in \{1, \ldots, 4\} : \phi_i \circ \ell_n(\eta_A) = \phi_i \circ \ell_n(\eta_B) = 0. \tag{3.52}$$

These conditions lead to three basic scenarios (after rotation and reindexing) which are depicted and discussed in Figure 3.6. These cases are used to classify the shape of $\mathcal{B}_n \cap \mathcal{R}$ and eventually construct the parametrization $\varkappa : (0,1)^2 \to \mathcal{B}_n \cap \mathcal{R}$ employed in Algorithm 1. This parametrization is defined using the list of four nodes provided in Figure 3.6 and the index i of (3.52). The implemented procedure is described in the next segment.

Remark 3.22. *The set of admissible scenarios considered in this passage is not exhaustive. All results exhibited in [37], however, indicate that this set already facilitates a powerful method. Between lines 7 and 8 of Algorithm 1 one might already return zero if $\mathcal{Z} = \varnothing$ holds and all four corners η satisfy $\phi_\sigma \circ \ell_n(\eta) > 0$.*

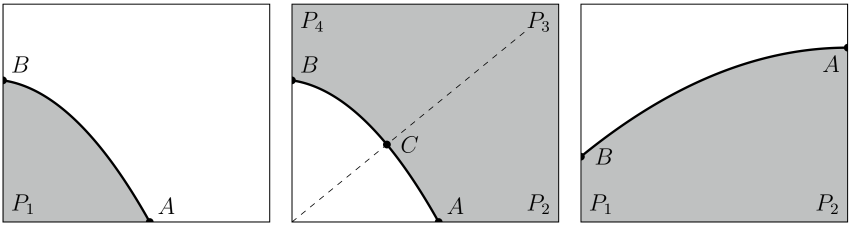

a) nodes (A, B, P_1, P_1) b) two subsets (C, A, P_2, P_3) and (B, C, P_3, P_4) c) nodes (A, B, P_1, P_2)

Figure 3.6: Figures 3.6a and 3.6b display the two scenarios for η_A and η_B lying on adjacent edges. The case when η_A and η_B are on opposing edges is shown in Figure 3.6c. Curved lines depict the zero level set of $\phi_i \circ \ell_n$ for the index i as in (3.52). Gray regions indicate the set $\{\eta \in \mathcal{R} : \phi_\sigma \circ \ell_n(\eta) < 0\}$. The nodes of the parametrization are provided in the captions of the images. In Figure 3.6b the point η_C is found along the diagonal such that $\phi_i \circ \ell_n(\eta_C) = 0$ holds.

Line 9 of Algorithm 1: Construction of the Parametrization

This final technical comment on Algorithm 1 addresses the construction of the parametrization $\varkappa : (0,1)^2 \to \mathcal{B}_n \cap \mathcal{R}$. By virtue of the scenarios discussed in Figure 3.6, line 8 in Algorithm 1 provides four input nodes $\eta_A, \eta_B, \eta_C, \eta_D \in \mathbb{R}^2$ and the index i of (3.52). The zero level set $\{\eta \in \mathcal{R} : \phi_i \circ \ell_n(\eta) = 0\}$ describes a curved path from η_A to η_B. First, a parametrization $[0,1] \to \{\eta \in \mathcal{R} : \phi_i \circ \ell_n(\eta) = 0\}$ is sought. To this end, introduce the affine map $\chi_{AB} : [0,1] \to \mathbb{R}^2$ defined by $s \mapsto \eta_A + (\eta_B - \eta_A)\, s$. This first-order approximation is mapped onto the zero level set via the ideal transformation discussed in [65], which is also used in [39]. It is defined by

$$\Psi : \mathbb{R}^2 \to \mathbb{R}^2, \quad \eta \mapsto \eta + r_\Psi(\eta) s_\Psi(\eta),$$

where $s_\Psi : \mathbb{R}^2 \to \mathbb{R}^2$ is the search direction field and $r_\Psi : \mathbb{R}^2 \to \mathbb{R}$ is the distance function. Given $\eta \in \mathbb{R}^2$, the value $r_\Psi(\eta)$ is the solution (with minimal absolute value) of

$$r_\Psi(\eta) \in \mathbb{R} : \; \phi_i \circ \ell_n \left(\eta + r_\Psi(\eta) s_\Psi(\eta)\right) = 0. \tag{3.53}$$

As in [65, 39] we resort to the search direction field $s_\Psi := \nabla \left(\phi_i \circ \ell_n\right)$. The desired parametrization is given by $\Psi \circ \chi_{AB} : [0,1] \to \{\eta \in \mathcal{R} : \phi_i \circ \ell_n(\eta) = 0\}$. It satisfies the continuity conditions $\Psi \circ \chi_{AB}(0) = \eta_A$ and $\Psi \circ \chi_{AB}(1) = \eta_B$ because $\Psi(\eta) = \eta$ holds for any η that satisfies $\phi_i \circ \ell_n(\eta) = 0$. It is crucial to note that Ψ is well-defined only for arguments sufficiently close to the zero level set, see [65]. Therefore, the first-order approximation induced by χ_{AB} has to be sufficiently close to the zero level set. In our implementation, we employ the Newton-Raphson method to solve the nonlinear equation (3.53) with initial guess $r_\Psi(\eta) = 0$. In the experiments of Chapter 4, the prescribed tolerance $|\phi_i \circ \ell_n (\eta + r_\Psi(\eta) s_\Psi(\eta))| < 1 \times 10^{-12}$ was always achieved in not more than 20 iterations. In most cases, however, the error threshold was reached in fewer than ten iterations.

Eventually, Ψ is the key ingredient for the transformation $\varkappa : (0,1)^2 \to \mathcal{B}_n \cap \mathcal{R}$. The chosen transformation stems from a bilinearly blended interpolation of the boundary parametrizations, see [49, Equation (10a)]. It is tailored to the examined case in which only the path from η_A to η_B is curved, while all other edges remain straight

$$\varkappa : (z_1, z_2) \mapsto (1 - z_2)\, \Psi \circ \chi_{AB}(z_1) + z_2 \eta_D + z_1 z_2 \left(\eta_C - \eta_D\right).$$

In order to evaluate the transformation determinant

$$|\det \mathrm{D}\, \varkappa| : z \mapsto \sqrt{\|\partial_1 \varkappa(z)\|^2 \, \|\partial_2 \varkappa(z)\|^2 - \langle \partial_1 \varkappa(z), \partial_2 \varkappa(z) \rangle^2},$$

the partial derivatives $\partial_1 \varkappa$ and $\partial_2 \varkappa$ are necessary. Clearly, $\partial_1 \varkappa$ involves the derivative of $\Psi \circ \chi_{AB}$. For details on its computation the reader is referred to [39, Section 4].

3.8.2 A Word on Gaussian Quadrature

Let $f : (a,b) \to \mathbb{R}$ be an integrable function on the interval $(a,b) \subset \mathbb{R}$. Define the affine transformation $\chi_{(a,b)} : [0,1] \to [a,b]$ by $\chi_{(a,b)} : x \mapsto a + (b-a)x$. Its functional determinant is constant $\left|\det \mathrm{D}\, \chi_{(a,b)}\right| = b - a$. We are concerned with the integral

$$\int_a^b f(x) \mathrm{d}x = (b-a) \int_0^1 f \circ \chi_{(a,b)}(x) \mathrm{d}x,$$

where substitution via $\chi_{(a,b)}$ transfers the integral to the unit interval $(0,1)$. Consequently, it suffices to consider integrals of the form $\int_0^1 g(x)\mathrm{d}x$ with $g := f \circ \chi_{(a,b)}$. Numerical integration schemes typically find approximations of the form

$$\int_0^1 g(x) \mathrm{d}x \approx \sum\nolimits_{i=1}^{n_G} g(x_i) \omega_i, \tag{3.54}$$

where $\{x_i\}_{i=1}^{n_G}$ and $\{\omega_i\}_{i=1}^{n_G}$ are the sets of $n_G \in \mathbb{N}$ quadrature points and weights respectively. We employ Gauss-Legendre quadrature rules, see, e.g., [90, Section 4.6], which are perhaps the most commonly used rules. They are typically defined in the interval $(-1,1)$ and we map them to $(0,1)$ via $x_i \mapsto \frac{1}{2}(1 + x_i)$ and $\omega_i \mapsto \frac{1}{2}\omega_i$ for $i = 1, \ldots, n_G$. The quadrature points in $(-1,1)$ stem from the roots of the Legendre polynomial $P_{n_G} \in \mathbb{P}_{n_G}(-1,1)$. The weights satisfy [62, Equation (7.2.5)]

$$\omega_i = \frac{2}{(1 - x_i^2)\left(P'_{n_G}(x_i)\right)^2}, \; i = 1, \ldots, n_G.$$

For the sake of completeness, recall that $\{P_n\}_{n\in\mathbb{N}_0}$ is an orthogonal basis of $L^2(-1,1)$

$$(P_n, P_m)_{L^2(-1,1)} = \int_{-1}^{1} P_n(x)P_m(x)\mathrm{d}x = \begin{cases} 0 & \text{if } n \neq m, \\ \frac{2}{2n+1} & \text{if } n = m, \end{cases}$$

as well as the recurrence relation for $n \in \mathbb{N}$

$$(n+1)\,P_{n+1}(x) = (2n+1)\,xP_n(x) - nP_{n-1}(x), \tag{3.55}$$

with $P_0(x) \coloneqq 1$ and $P_1(x) \coloneqq x$.

It can be shown [62, Section 7.1] that a Gauss-Legendre quadrature rule involving $n_G \in \mathbb{N}$ points satisfies (3.54) exactly if $g \in \mathbb{P}_n(-1,1)$ holds with $n \leq 2n_G - 1$. The reader is referred to [62] for further details on Gaussian quadrature. There exist several numerical procedures for computing these quadrature rules. In the code developed for this thesis, two widely used methods are implemented:

- A modified version of `gauleg` [90, Section 4.6.1]: this routine computes the roots of P_n directly using the Newton-Raphson method. Our modification lies, apart from some technical details, in a different initial guess for the roots of P_n. We employ the asymptotic expansion due to [113, Equations (2), (11), and (13)], leading to slightly faster convergence of the root-finding algorithm.

- Golub-Welsch algorithm, see [45] and [90, Section 4.6.2]: the recurrence relation (3.55) is used to reformulate the problem as a symmetric tridiagonal eigenvalue problem. In our code we employ a standard eigenvalue solver, however, significant improvement could be achieved if the tridiagonal structure were exploited.

In the experiments conducted for this thesis we observed little difference in the performance of both methods.

In order to evaluate integrals like (2.2) numerically we require quadrature rules for the n-dimensional simplex (2.1), $n \in \mathbb{N}$. While one could derive Gaussian quadrature rules for certain n-simplices explicitly, we pursue an approach that forgoes efficiency in favor of simplicity (to some extent). This technique is adapted from [100, Section 5.2.5] and eventually only requires one-dimensional Gaussian quadrature rules. For $n \in \mathbb{N}$ define the transformation $\mathrm{G} : (0,1)^n \to \widehat{\sigma}_n$ by

$$\mathrm{G} : \begin{pmatrix} x_1 \\ x_2 \\ \vdots \\ x_{n-1} \\ x_n \end{pmatrix} \mapsto \begin{pmatrix} x_1 \\ x_1x_2 \\ \vdots \\ x_1x_2x_3\ldots x_{n-2}x_{n-1} \\ x_1x_2x_3\ldots x_{n-1}x_n \end{pmatrix}, \quad \mathrm{G}^{-1} : \begin{pmatrix} \xi_1 \\ \xi_2 \\ \vdots \\ \xi_{n-1} \\ \xi_n \end{pmatrix} \mapsto \begin{pmatrix} \xi_1 \\ \xi_2/\xi_1 \\ \vdots \\ \xi_{n-1}/\xi_{n-2} \\ \xi_n/\xi_{n-1} \end{pmatrix}.$$

Denote by $\mathrm{G}_i(x), \mathrm{G}_i^{-1}(\xi) \in \mathbb{R}$ the ith components of $\mathrm{G}(x)$ and $\mathrm{G}^{-1}(\xi)$, respectively

$$\mathrm{G}_i : x \mapsto \prod_{j=1}^{i} x_j, \quad \mathrm{G}_i^{-1} : \xi \mapsto \begin{cases} \xi_1 & \text{if } i = 1, \\ \xi_i/\xi_{i-1} & \text{if } i \geq 2. \end{cases}$$

Proposition 3.23. *For any $x \in (0,1)^n$ it holds $|\det \mathrm{D}\,\mathrm{G}\,(x)| = \prod_{i=1}^{n-1} x_i^{n-i}$.*

Proof. For $x \in (0,1)^n$ it holds $|\det \mathrm{D}\,\mathrm{G}\,(x)| = \det J(x)$, where $J(x) \in \mathbb{R}^{n\times n}$ is the Jacobi matrix defined by its coefficients $J_{ij}(x) := \partial_j \mathrm{G}_i(x)$ for $i, j = 1, \dots, n$. From $\mathrm{G}_i(x) = \prod_{k=1}^{i} x_k$ it follows

$$J_{ij}(x) = \partial_j \mathrm{G}_i(x) = \begin{cases} 0 & \text{if } i < j, \\ \prod_{k=1,k\neq j}^{i} x_k & \text{if } i \geq j. \end{cases}$$

The property $J_{ij}(x) = 0$ for $i < j$ implies that $J(x)$ is lower triangular and the assertion follows

$$\begin{aligned} \det J(x) &= \prod_{i=1}^{n} J_{ii}(x) = \prod_{i=2}^{n} \prod_{k=1}^{i-1} x_k \\ &= (x_1)(x_1x_2)(x_1x_2x_3)\dots(x_1x_2x_3\dots x_{n-2}x_{n-1}) = \prod_{i=1}^{n-1} x_i^{n-i}. \end{aligned}$$ □

Given an integrable function $f_S : \widehat{\sigma}_n \to \mathbb{R}$, the bijection $\mathrm{G} : (0,1)^n \to \widehat{\sigma}_n$ yields

$$\int_{\widehat{\sigma}_n} f_S(\xi)\mathrm{d}\xi = \int_{(0,1)^n} f_S \circ \mathrm{G}(x)\,|\det \mathrm{D}\,\mathrm{G}\,(x)|\,\mathrm{d}x.$$

The transformation G pulls integrals on the simplex back to the n-dimensional unit hypercube. This integral can be approximated by iterated application of one-dimensional Gaussian quadrature rules. For $f_C : (0,1)^n \to \mathbb{R}$, defined by $f_C := f_S \circ \mathrm{G}\,|\det \mathrm{D}\,G|$ for instance, we use tensor-Gauss quadrature, see [100, Section 5.3.1]

$$\begin{aligned} &\int_0^1 \int_0^1 \cdots \int_0^1 f_C(x_1, x_2, \dots, x_n)\mathrm{d}x_1\mathrm{d}x_2\dots\mathrm{d}x_n \\ &\qquad\approx \sum_{i_1=1}^{m_1} \sum_{i_2=1}^{m_2} \cdots \sum_{i_n=1}^{m_n} f_C(x_{i_1}, x_{i_2}, \dots, x_{i_n})\omega_{i_1}\omega_{i_2}\dots\omega_{i_n}, \end{aligned}$$

where $\{x_{i_j}\}_{i=1}^{m_j}$ and $\{\omega_{i_j}\}_{i=1}^{m_j}$ are the $m_j \in \mathbb{N}$ Gauss-Legendre points and weights in the direction $j = 1, \dots, n$. This prompts the following question: given a polynomial $f_p \in \mathbb{P}_p\left(\widehat{\sigma}_n\right), p \in \mathbb{N}_0$, what are the numbers $m_j, j = 1, \dots, n$ necessary such that

$$\int_{\widehat{\sigma}_n} f_p(\xi)\mathrm{d}\xi = \sum_{i_1=1}^{m_1} \cdots \sum_{i_n=1}^{m_n} f_p \circ \mathrm{G}(x_{i_1}, \dots, x_{i_n})\,|\det \mathrm{D}\,G\,(x_{i_1}, \dots, x_{i_n})|\,\omega_{i_1}\dots\omega_{i_n} \quad (3.56)$$

holds, i.e., the quadrature yields the exact result? To answer this question, consider the monomial $g_p : \widehat{\sigma}_n \to \mathbb{R}$ defined by $g_p : \xi \mapsto \prod_{i=1}^n \xi_i^{p_i}$ with orders $p_i \in \mathbb{N}_0$ for each direction $i = 1, \dots, n$ and $p = \sum_{i=1}^n p_i$. We observe

$$\begin{aligned} g_p \circ \mathrm{G} : x \mapsto \prod\nolimits_{i=1}^n \Big(\prod\nolimits_{j=1}^i x_j\Big)^{p_i} &= \prod\nolimits_{i=1}^n \prod\nolimits_{j=1}^i x_j^{p_i} \\ &= (x_1^{p_1})(x_1^{p_2} x_2^{p_2})(x_1^{p_3} x_2^{p_3} x_3^{p_3}) \dots (x_1^{p_n} x_2^{p_n} x_3^{p_n} \dots x_n^{p_n}) = \prod\nolimits_{i=1}^n x_i^{\sum_{j=i}^n p_j} \end{aligned}$$

and with Proposition 3.23 we obtain for the product of $g_p \circ \mathrm{G}$ and $|\det \mathrm{D}\,\mathrm{G}|$

$$g_p \circ \mathrm{G}\, |\det \mathrm{D}\,\mathrm{G}| : x \mapsto \prod\nolimits_{i=1}^n x_i^{\sum_{j=i}^n p_j} \prod\nolimits_{i=1}^{n-1} x_i^{n-i} = \prod\nolimits_{i=1}^n x_i^{n-i+\sum_{j=i}^n p_j}.$$

The worst case, i.e., $\sum_{j=i}^n p_j = p$ for any $i = 1, \dots, n$ is achieved by setting $p_j = 0$ for $j = 1, \dots, n-1$ and $p_n = p$. In this case it holds

$$g_p \circ \mathrm{G}\, |\det \mathrm{D}\,\mathrm{G}| : x \mapsto \prod\nolimits_{i=1}^n x_i^{p+n-i}. \tag{3.57}$$

We achieve (3.56) if the quadrature rules integrate (3.57) exactly in $(0,1)^n$. Therefore, the rule in the ith directions has to be capable of integrating polynomials of degree $p+n-i$ exactly. We obtain m_i via the relation $p + n - i \le 2m_i - 1$, leading to

$$m_i := \left\lceil \frac{p+n+1-i}{2} \right\rceil, \; i = 1, \dots, n. \tag{3.58}$$

The first direction requires $m_1 \approx (p+n)/2$ points, while the nth direction requires $m_n \approx (p+1)/2$ points. When using (3.58) the total number of function evaluations necessary to compute (3.56) is estimated by

$$\prod\nolimits_{i=1}^n m_i = \prod\nolimits_{i=1}^n \left\lceil \frac{p+n+1-i}{2} \right\rceil \le \prod\nolimits_{i=1}^n \frac{p+n+2-i}{2} = \frac{1}{2^n} \prod\nolimits_{i=1}^n p+1+i.$$

This strikingly shows that the outlined approach suffers severely from the curse of dimensionality. Nevertheless, the described procedure can deal with integrals on $\widehat{\sigma}_n$ for any $n \in \mathbb{N}$ using only one-dimensional quadrature rules in the unit interval. That is why we state that this technique is motivated by simplicity rather than efficiency.

Finally, (3.58) is employed to compute entries of the mass and stiffness matrices of Section 3.2 exactly. For the mass matrix M whose ansatz and test spaces are of orders $p_A \in \mathbb{N}_0$ and $p_T \in \mathbb{N}_0$, respectively, we set $p := p_A + p_T$ in (3.58) to determine $m_i, i = 1, \dots, n$. Analogously, for the stiffness matrix H we set $p := p_A + p_T - 2$ due to the occurrence of first-order derivatives in the bilinear form.

3.8.3 Computation of the Intersection of Mesh and Light Cone

Throughout this section $\mathbf{x} \in \mathbb{R}^4$ denotes an arbitrary but fixed evaluation point, $w : \Sigma \to \mathbb{R}$ a sufficiently smooth surface density, and Σ_N a mesh as in Definition 2.4 and Assumption 2.5. We investigate the implementation of the retarded potential $\mathrm{T}_k\, w(\mathbf{x})$ of Definition 2.16. For any $\sigma \in \Sigma_N$ define $w{\restriction_\sigma} \colon \Sigma \to \mathbb{R}$ by

$$w{\restriction_\sigma} \colon \mathbf{x} \mapsto \begin{cases} w(\mathbf{x}) & \text{if } \mathbf{x} \in \sigma, \\ 0 & \text{otherwise.} \end{cases}$$

The linearity of the integral operator T_k yields $\mathrm{T}_k\, w(\mathbf{x}) = \sum_{\sigma \in \Sigma_N} \mathrm{T}_k\, w{\restriction_\sigma}(\mathbf{x})$ and

$$\mathrm{T}_k\, w(\mathbf{x}) = \sum\nolimits_{\sigma \in \Sigma_N^{\Xi}(\mathbf{x})} \mathrm{T}_k\, w{\restriction_\sigma}(\mathbf{x}) + \sum\nolimits_{\sigma \in \Sigma_N \setminus \Sigma_N^{\Xi}(\mathbf{x})} \mathrm{T}_k\, w{\restriction_\sigma}(\mathbf{x}) \,, \tag{3.59}$$

where $\Sigma_N^{\Xi}(\mathbf{x}) \subset \Sigma_N$ is the set of panels lit by the backward light cone

$$\Sigma_N^{\Xi}(\mathbf{x}) := \{\sigma \in \Sigma_N : \Xi(\mathbf{x}) \cap \sigma \neq \varnothing\}.$$

The last term in (3.59) vanishes, see (2.42) and (2.53), yielding

$$\mathrm{T}_k\, w(\mathbf{x}) = \sum\nolimits_{\sigma \in \Sigma_N^{\Xi}(\mathbf{x})} \mathrm{T}_k\, w{\restriction_\sigma}(\mathbf{x}) \,.$$

Since both $\Xi(\mathbf{x})$ and Σ are three-dimensional hypersurfaces, their intersection $\Xi(\mathbf{x}) \cap \Sigma$ is two-dimensional (unless it degenerates). The dimensions of the involved sets suggest that although $|\Sigma_N| = N$ holds, we expect $\left|\Sigma_N^{\Xi}(\mathbf{x})\right| = \mathcal{O}\left(N^{2/3}\right)$ as $N \to \infty$ for a sequence of meshes obeying Definition 3.1. This prompts the question of how to determine the set $\Sigma_N^{\Xi}(\mathbf{x})$. Algorithm 2 serves as a template for computing subsets of lit panels. In general, executing Algorithm 2 involves $\mathcal{O}(|S|)$ operations because the check in line 3 requires a maximum number of operations independent of $|S|$.

Algorithm 2 `ComputeLitPanels`(S). Given a set of panels $S \subseteq \Sigma_N$. Return the set of lit panels $S^{\Xi}(\mathbf{x}) := \{\sigma \in S : \Xi(\mathbf{x}) \cap \sigma \neq \varnothing\}$.

```
1: $S^{\Xi}(\mathbf{x}) := \varnothing$
2: for all $\sigma \in S$ do
3:     if $\exists \mathbf{y} \in \sigma : \phi_{\Xi}(\mathbf{x} - \mathbf{y}) = 0$ then
4:         $S^{\Xi}(\mathbf{x}) \leftarrow S^{\Xi}(\mathbf{x}) \cup \{\sigma\}$
5:     end if
6: end for
7: return $S^{\Xi}(\mathbf{x})$
```

In an approach we are inclined to consider “naive”, one might simply call the routine `ComputeLitPanels`(Σ_N), which yields the correct set $\Sigma_N^{\Xi}(\mathbf{x})$. However, this method involves $\mathcal{O}(N)$ operations, thereby spoiling the $\mathcal{O}\left(N^{2/3}\right)$ behavior dictated by the cardinality of $\Sigma_N^{\Xi}(\mathbf{x})$. In the remainder of this section we exhibit a straightforward approach to construct $\Sigma_N^{\Xi}(\mathbf{x})$ more efficiently. Since $\mathbf{x}$ is fixed, it is omitted as an argument from here on.

Assume we had access to a set $X_N \subset \Sigma_N$ such that $\Sigma_N^{\Xi} \subset X_N$ and $|X_N| \leq C|\Sigma_N^{\Xi}|$ held for some $C > 0$ independent of N. Calling `ComputeLitPanels`(X_N) yields the correct set Σ_N^{Ξ} due to $\Sigma_N^{\Xi} \subset X_N$, however, it requires $\mathcal{O}(|X_N|) = \mathcal{O}\left(|\Sigma_N^{\Xi}|\right)$ operations and we may expect an $\mathcal{O}\left(N^{2/3}\right)$ complexity. In this sense, the sketched approach is optimal, yet we merely deferred the difficulty to computing X_N efficiently. We propose an algorithm for constructing X_N based on a typical hierarchical organization of the panels, see, e.g., [15].

DEFINITION 3.24 (Binary cluster tree). *Let $\mathfrak{I}$ be an index set with $|\mathfrak{I}| = N$. Each index corresponds to a unique panel in Σ_N via the bijection $\mathfrak{I} \to \Sigma_N$, $i \mapsto \sigma_i$. Let $\mathbb{T} := (\mathcal{V}, \mathcal{E})$ be a tree with vertex set $\mathcal{V}$ and edge set $\mathcal{E}$. The vertices are called clusters. For $v \in \mathcal{V}$ define the sets* $\operatorname{successors}(v) := \{v' \in \mathcal{V} : (v, v') \in \mathcal{E}\}$ *and* $\operatorname{leaves}\mathbb{T} := \{v \in \mathcal{V} : \operatorname{successors}(v) = \varnothing\}$*. Let $n_{\min} \in \mathbb{N}$ be the given upper bound for the cardinality of clusters in* $\operatorname{leaves}\mathbb{T}$*. The tree $\mathbb{T}$ is called binary cluster tree if*

(i) $\operatorname{root}\mathbb{T} = \mathfrak{I}$,

(ii) for all $v \in \mathcal{V}$ it holds $v \subset \mathfrak{I}$ and $v \neq \varnothing$,

(iii) $v \in \operatorname{leaves}\mathbb{T} \quad \Rightarrow \quad |v| \leq n_{\min}$,

(iv) for all $v \in \mathcal{V}$ it holds either $\operatorname{successors}(v) = \varnothing$ *or* $\operatorname{successors}(v) = \{v', v''\}$*, where $v = v' \cup v''$ and $v' \cap v'' = \varnothing$ hold, or in other words, any vertex $v \notin$* $\operatorname{leaves}\mathbb{T}$ *has precisely two disjoint successors whose union is v.*

We identify $\mathcal{V}$ with $\mathbb{T}$, i.e., we write $v \in \mathbb{T}$ in lieu of $v \in \mathcal{V}$.

Algorithm 3 `CreateBinaryClusterTree`$(n_{\min}; \mathcal{V}, \mathcal{E}, v)$. Given the maximum size of leaf-level clusters $n_{\min} \in \mathbb{N}$, the current iterates of the vertex set $\mathcal{V}$ and the edge set $\mathcal{E}$, and a cluster $v \in \mathcal{V}$.

```
if $|v| \leq n_{\min}$ then
    return
end if
$\{v', v''\} :=$ SeparateCluster($v$)
$\mathcal{V} \leftarrow \mathcal{V} \cup \{v', v''\}$
$\mathcal{E} \leftarrow \mathcal{E} \cup \{(v, v'), (v, v'')\}$
for all $v^* \in \{v', v''\}$ do
    CreateBinaryClusterTree($n_{\min}; \mathcal{V}, \mathcal{E}, v^*$)
end for
```

Algorithm 4 `SeparateCluster`(v). Given a cluster $v \in \mathbb{T}$. Return the set of successors $\{v', v''\}$.

```
1: for all $i \in v$ do
2:     $m_i := \int_{\sigma_i} \mathrm{d}S$                          ▷ surface measure of panel
3:     $\mathbf{x}_i := \int_{\sigma_i} \mathbf{y}\mathrm{d}S(\mathbf{y})/m_i$          ▷ centroid of panel
4: end for
5: $\mathbf{y} := \sum_{i\in v} m_i\mathbf{x}_i / \sum_{i\in v} m_i$               ▷ centroid of cluster
6: $C := \sum_{i\in v} m_i(\mathbf{x}_i - \mathbf{y}) \otimes (\mathbf{x}_i - \mathbf{y})$     ▷ covariance matrix of cluster
7: $e \in \mathbb{S}^3 : Ce = \lambda_{\max} e$                   ▷ eigenvector of largest eigenvalue
8: $v' := \{i \in v : \langle \mathbf{x}_i - \mathbf{y}, e\rangle \geq 0\}$
9: return $\{v', v \setminus v'\}$
```

The construction of $\mathbb{T}$ is realized via Algorithms 3 and 4, which are adapted from [15, Section 1.4.1.1, Equation (1.21)]. As an initialization set $\mathcal{V} := \{\mathfrak{I}\}$ and $\mathcal{E} := \varnothing$, then call `CreateBinaryClusterTree`$(n_{\min}; \mathcal{V}, \mathcal{E}, \mathfrak{I})$. Once the routine terminates, set $\mathbb{T} := (\mathcal{V}, \mathcal{E})$. Algorithm 4 divides the given cluster into two successors such that the involved panels are close to each other. It is based on the principal component analysis, which is applied to the centroids of the panels. The quantities in line 2 and 3 are to be precomputed and stored appropriately upon calling `CreateBinaryClusterTree` initially.

The sketched construction procedure of $\mathbb{T}$ requires $\mathcal{O}(N \log(N))$ operations for quasiuniform meshes [15, Theorem 1.27]. However, $\mathbb{T}$ depends only on Σ_N and $n_{\min}$, therefore, it is set up once and used for every evaluation point. For each $v \in \mathbb{T}$ a bounding space-time volume $Q_B(v) \subset \mathbb{R}^4$ is constructed such that $\Xi \cap Q_B(v) = \varnothing$ implies that every $\sigma_i, i \in v$ satisfies $\sigma_i \notin \Sigma_N^{\Xi}$. We resort to bounding balls (spheres) due to their simplicity.

THEOREM 3.25. *Let* $\mathbf{x} \in \mathbb{R}^4$ *and* $B_r(\mathbf{y})$ *be the closed ball of radius* $r > 0$ *around* $\mathbf{y} \in \mathbb{R}^4$. *It holds*

$$\min_{\mathbf{z}\in B_r(\mathbf{y})} \phi_\Xi(\mathbf{x} - \mathbf{z}) = \phi_\Xi(\mathbf{x} - \mathbf{y}) - d_r(\|x - y\|),$$

$$\max_{\mathbf{z}\in B_r(\mathbf{y})} \phi_\Xi(\mathbf{x} - \mathbf{z}) = \phi_\Xi(\mathbf{x} - \mathbf{y}) + r\sqrt{2},$$

where $d_r : [0, \infty) \to \left[r, r\sqrt{2}\right]$ *is defined by*

$$d_r : \alpha \mapsto \begin{cases} \alpha + \sqrt{r^2 - \alpha^2} & \text{if } 0 \leq \alpha < r/\sqrt{2}, \\ r\sqrt{2} & \text{if } \alpha \geq r/\sqrt{2}. \end{cases}$$

Proof. We fix the decomposition $\mathbf{z} := (s, z)$ with $s \in \mathbb{R}$, $z \in \mathbb{R}^3$ and observe

$$\mathbf{z} \in B_r(\mathbf{y}) \quad \Leftrightarrow \quad \|\mathbf{z} - \mathbf{y}\|^2 \leq r^2 \quad \Leftrightarrow \quad \|z - y\|^2 \leq r^2 - (s - \tau)^2. \tag{3.60}$$

We expand

$$\phi_\Xi(\mathbf{x}-\mathbf{z}) = \|x-z\| - (t-s) = \|x-y+y-z\| - (t-\tau+\tau-s) \tag{3.61}$$

and the triangle inequality as well as (3.60) lead to

$$\begin{aligned}\phi_\Xi(\mathbf{x}-\mathbf{z}) &\leq \|x-y\| + \|z-y\| - (t-\tau) + (s-\tau)\\ &\leq \phi_\Xi(\mathbf{x}-\mathbf{y}) + \sqrt{r^2-(s-\tau)^2} + (s-\tau).\end{aligned}$$

The maximum in above expression is attained at $s-\tau = r/\sqrt{2}$, yielding the bound $\phi_\Xi(\mathbf{x}-\mathbf{z}) \leq \phi_\Xi(\mathbf{x}-\mathbf{y}) + r\sqrt{2}$. This bound is attained in $B_r(\mathbf{y})$ because we observe

$$\mathbf{z} := \mathbf{y} - \frac{r}{\sqrt{2}}\begin{pmatrix}-1\\(x-y)/\|x-y\|\end{pmatrix} \in B_r(\mathbf{y}) \quad \Rightarrow \quad \phi_\Xi(\mathbf{x}-\mathbf{z}) = \phi_\Xi(\mathbf{x}-\mathbf{y}) + r\sqrt{2}.$$

In order to derive the lower bound, the reverse triangle inequality is applied to (3.61)

$$\begin{aligned}\phi_\Xi(\mathbf{x}-\mathbf{z}) &\geq |\|x-y\| - \|z-y\|| - (t-\tau) + (s-\tau)\\ &\geq |\|x-y\| - \|z-y\|| - (t-\tau) - \sqrt{r^2-\|z-y\|^2},\end{aligned} \tag{3.62}$$

where we used $s-\tau \geq -|s-\tau| \geq -(r^2-\|z-y\|^2)^{1/2}$ due to (3.60). Define the parameter $q := \|z-y\| \in [0,r]$ and the function $f_r : [0,r] \to \mathbb{R}$ by $q \mapsto |\|x-y\|-q| - \sqrt{r^2-q^2}$. We have $\phi_\Xi(\mathbf{x}-\mathbf{z}) \geq f_r(q) - (t-\tau)$ and the weak derivative of f_r reads

$$f_r' : q \mapsto -\operatorname{sgn}(\|x-y\|-q) + q/\sqrt{r^2-q^2}.$$

It holds $f_r'(q) < 0$ iff $q < \|x-y\|$ and $q < r/\sqrt{2}$ hold. We distinguish the two scenarios: $\|x-y\| \geq r/\sqrt{2}$ and $\|x-y\| < r/\sqrt{2}$. Assuming that $\|x-y\| \geq r/\sqrt{2}$ holds we have $f_r'(q) < 0$ iff $q < r/\sqrt{2}$ and f_r is monotonically decreasing in $[0, r/\sqrt{2})$ while it is nondecreasing (almost) everywhere else. As a consequence, f_r attains its minimum at $q = r/\sqrt{2}$ and insertion of $q = \|z-y\| = r/\sqrt{2} \leq \|x-y\|$ in (3.62) yields $\phi_\Xi(\mathbf{x}-\mathbf{z}) \geq \phi_\Xi(\mathbf{x}-\mathbf{y}) - r\sqrt{2}$. The sharpness is confirmed by considering

$$\begin{aligned}&\mathbf{z} := \mathbf{y} + \frac{r}{\sqrt{2}}\begin{pmatrix}-1\\(x-y)/\|x-y\|\end{pmatrix} \in B_r(\mathbf{y})\\ &\qquad\qquad \Rightarrow \quad \phi_\Xi(\mathbf{x}-\mathbf{z}) = \left\|x-y-\frac{r}{\sqrt{2}}\frac{x-y}{\|x-y\|}\right\| - \left(t-\tau+r/\sqrt{2}\right)\end{aligned}$$

and, therefore, $\phi_\Xi(\mathbf{x}-\mathbf{z}) = \phi_\Xi(\mathbf{x}-\mathbf{y}) - r\sqrt{2}$ for $\|x-y\| \geq r/\sqrt{2}$. We turn our attention to the case $\|x-y\| < r/\sqrt{2}$. The minimum of f_r is located at $q = \|x-y\|$ because $f_r'(q) < 0$ holds iff $q < \|x-y\|$. Setting $q = \|z-y\| = \|x-y\|$ in (3.62) leads to

$$\phi_\Xi(\mathbf{x}-\mathbf{z}) \geq -(t-\tau) - \sqrt{r^2-\|x-y\|^2} = \phi_\Xi(\mathbf{x}-\mathbf{y}) - \|x-y\| - \sqrt{r^2-\|x-y\|^2}.$$

Finally

$$\mathbf{z} := \begin{pmatrix} \tau - \sqrt{r^2 - \|x-y\|^2} \\ x \end{pmatrix} \in B_r(\mathbf{y}) \quad \Rightarrow \quad \phi_\Xi\left(\mathbf{x} - \mathbf{z}\right) = -(t-\tau) - \sqrt{r^2 - \|x-y\|^2}$$

confirms that the lower bound is attained for $\|x-y\| < r/\sqrt{2}$. ☐

Algorithm 5 exhibits the proposed approach for computing the proxy set X_N. As an initialization, set $L := \varnothing$, then call `ApproximateLitLeaves`$(L, \operatorname{root} \mathbb{T})$. Once the algorithm terminates, set $X_N := \bigcup_{v \in L} \bigcup_{i \in v} \sigma_i$. We exploit Theorem 3.25 in line 2 of Algorithm 5. There is no root of $\mathbf{z} \mapsto \phi_\Xi\left(\mathbf{x}-\mathbf{z}\right)$ in $B_r(\mathbf{y})$, or equivalently, the bounding sphere of $v \in \mathbb{T}$ does not intersect $\Xi\left(\mathbf{x}\right)$, iff either its maximum value is negative or its minimum value is positive. The routine `GetBoundingSphere`(v) in line 1 returns a precomputed bounding sphere that contains every panel $\sigma_i, i \in v$. In our implementation, we use a slightly modified version of the algorithm proposed in [92], which computes a non-minimal bounding sphere. Although the cited source exhibits the algorithm explicitly for $\mathbb{R}^3$, its extension to $\mathbb{R}^n, n \in \mathbb{N}$ is immediate.

Algorithm 5 `ApproximateLitLeaves`(L, v). Given the current iterate of the set $L \subset \operatorname{leaves} \mathbb{T}$ and a cluster $v \in \mathbb{T}$.

```
 1: $B_r(\mathbf{y}) :=$ GetBoundingSphere($v$)
 2: if $\phi_\Xi(\mathbf{x}-\mathbf{y}) < -r\sqrt{2}$ or $\phi_\Xi(\mathbf{x}-\mathbf{y}) > d_r(\|x-y\|)$ then
 3:     return
 4: end if
 5: if $v \in \operatorname{leaves} \mathbb{T}$ then
 6:     $L \leftarrow L \cup \{v\}$
 7: else
 8:     for all $v' \in \operatorname{successors}(v)$ do
 9:         ApproximateLitLeaves($L, v'$)
10:     end for
11: end if
```

Remark 3.26. *Although the approach proposed in this section is based on concepts encountered in so-called fast BEMs, it does not constitute a fast method in the usual sense. The discussed procedure aims at efficient evaluation procedures of exact retarded potential integral operators (apart from quadrature). The necessity for such implementational tricks arises even outside the realm of fast methods due to the strong Huygens principle: retarded potentials are not classically global integral operators, because their integrals are supported on (subsets of) the hypersurface* $\Xi\left(\mathbf{x}\right)$.

The performance of the proposed method is investigated at the end of Section 4.1 by means of numerical experiments.

4 In Silico Experiments

The methods proposed in Chapter 3 are implemented in an experimental research code. This chapter exhibits numerical experiments intended to verify the implementation and to demonstrate the potential of the devised procedures. Section 4.1 provides code verification of the space-time boundary elements introduced in Section 3.1 as well as the computation of the intersection of mesh and light cone proposed in Section 3.8.3. In Sections 4.2 and 4.3, we investigate the numerical integration schemes discussed in Sections 3.5, 3.6 and 3.8.1. Finally, Section 4.4 presents numerical experiments on the space-time BEMs of Section 3.3.

4.1 Verification of the Space-Time Technology

In order to conduct numerical experiments, the space-time boundary elements discussed in Section 3.1 are implemented. A research code is written from scratch, solely for the purposes of this thesis. We deem it necessary to verify the basic technology prior to addressing the verification of BEMs. This machinery includes the construction of the tetrahedral hypersurface meshes, the implementation of the Lagrange bases of the boundary element spaces, and Gaussian quadrature. As already indicated in Section 3.2, we suggest a verification procedure based on orthogonal projections, which are considered ordinary in numerical analysis. In the performed tests, a smooth function is approximated using the trial spaces of Definition 3.2. The approximations are based on $L^2(\Sigma)$-orthogonal and $H^1_{0,\cdot}(\Sigma)$-orthogonal projections, respectively. The convergence rates observed in the numerical experiments are compared to the theoretical predictions (3.4) and (3.5) in order to verify the implementation. The second part of this section investigates the algorithm for computing the set of lit panels discussed in Section 3.8.3. We compare the observed orders of complexity to the conjectured ones in order to support the viability of the method.

Given a domain $\Omega^- \subset \mathbb{R}^3$ and a simulation end time $T > 0$, consider the function $u : \mathbb{R}^4 \to \mathbb{R}$ defined by

$$u : \mathbf{x} \mapsto \sin\left(\pi \frac{t}{T}\right) \prod_{i=1}^{3} \sin\left(\pi \frac{x_i}{\operatorname{diam} \Omega^-}\right)$$

and abbreviate its trace by $w := \gamma_0^+ u = \gamma_0^- u$. Clearly, $w \in H^1_{0,\cdot}(\Sigma)$ holds true for any Σ obeying Assumption 2.5. We examine two simple choices for the domain Ω^-, namely the unit cube $\Omega^- := \left(-\frac{1}{2}, \frac{1}{2}\right)^3$ and the unit ball $\Omega^- := \{x \in \mathbb{R}^3 : \|x\| < 1\}$. For the unit cube $T := 1$ is chosen, while the unit ball is equipped with $T := 2$. Note that the space-time boundary of the unit ball $\Sigma = (0, T) \times \mathbb{S}^2$ is not represented exactly by the simplex mesh Σ_N. This, however, is of no practical significance because the manufactured solution w is defined as the trace of u to the boundary described by the mesh Σ_N.

Let $w_h \in S_p^*(\Sigma_N)$ be the $L^2(\Sigma)$-orthogonal projection of w onto $S_p^*(\Sigma_N)$, where $* \in \{\mathrm{d}, \mathrm{c}\}$ indicates either the discontinuous or the continuous trial spaces of Definition 3.2. In other words, w_h is the unique solution of (3.2) with $W = S_p^*(\Sigma_N)$. We consider polynomial degrees $p \in \{0, 1, 2\}$ for $* = \mathrm{d}$ and $p \in \{1, 2\}$ for $* = \mathrm{c}$. Furthermore, let $v_h \in S_p^{\mathrm{c}}(\Sigma_N) \cap H_{0,\cdot}^1(\Sigma)$ be the $H_{0,\cdot}^1(\Sigma)$-orthogonal projection of w onto $S_p^{\mathrm{c}}(\Sigma_N) \cap H_{0,\cdot}^1(\Sigma)$ for $p \in \{1, 2\}$. The function v_h is the unique solution of (3.3) with $V = S_p^{\mathrm{c}}(\Sigma_N) \cap H_{0,\cdot}^1(\Sigma)$ and $v = w$. Remarks about the discrete systems are provided in Section 3.2. The employed quadrature orders for the matrices M and H of Section 3.2 are computed via (3.58) for $n = 3$. For a trial space of polynomial degree $p \in \mathbb{N}_0$ the coefficients of M integrate polynomials of degree $2p$. Therefore, we replace p in (3.58) with $2p$ and obtain the numbers of points in the three directions $m_i = \lceil p + 2 - i/2 \rceil$, $i = 1, 2, 3$. Evaluating this formula for $p = 0$ yields the numbers of Gaussian quadrature points $(m_1, m_2, m_3) = (2, 1, 1)$. Furthermore, this procedure suggests the quadrature orders $(3, 2, 2)$ for $p = 1$ and $(4, 3, 3)$ for $p = 2$, respectively. Since the matrix H involves only first-order derivatives, the necessary numbers of points coincide with the numbers provided for M of one lower degree, i.e., $p - 1$.

Convergence studies are conducted for both projections and both domains. The experimental results of the $L^2(\Sigma)$- and $H_{0,\cdot}^1(\Sigma)$-projection are depicted in Figures 4.1 and 4.2, respectively. The initial mesh of the space-time boundary of the unit cube features 72 panels. Execution of five successive refinement steps yields a final mesh composed of roughly 2.36×10^6 panels. The initial mesh of the space-time boundary of the unit sphere involves 1464 panels. Four steps of refinement result in a final mesh of approximately 5.99×10^6 panels. The sequences of meshes are shape regular and quasiuniform in the sense of Definition 3.1. As a consequence, we may apply the (conjectured) a priori error estimates (3.4) and (3.5). The expected order of convergence $p + 1$ for the $L^2(\Sigma)$-orthogonal projection is matched quite well in Figure 4.1. Furthermore, the estimated convergence rate p for the $H_{0,\cdot}^1(\Sigma)$-orthogonal projection can be observed in Figure 4.2. The convergence rates predicted by theory are matched by experimental results, which provides strong evidence about the correctness of the implementation. Figure 4.1 illustrates that the errors for projections onto $S_p^{\mathrm{d}}(\Sigma_N)$ are smaller than for projections onto $S_p^{\mathrm{c}}(\Sigma_N)$ for equal p and Σ_N. This observation is due to the inclusion $S_p^{\mathrm{c}}(\Sigma_N) \subset S_p^{\mathrm{d}}(\Sigma_N)$, implying

$$\min_{w_h \in S_p^{\mathrm{d}}(\Sigma_N)} \|w - w_h\|_{L^2(\Sigma)} \leq \min_{w_h \in S_p^{\mathrm{c}}(\Sigma_N)} \|w - w_h\|_{L^2(\Sigma)}.$$

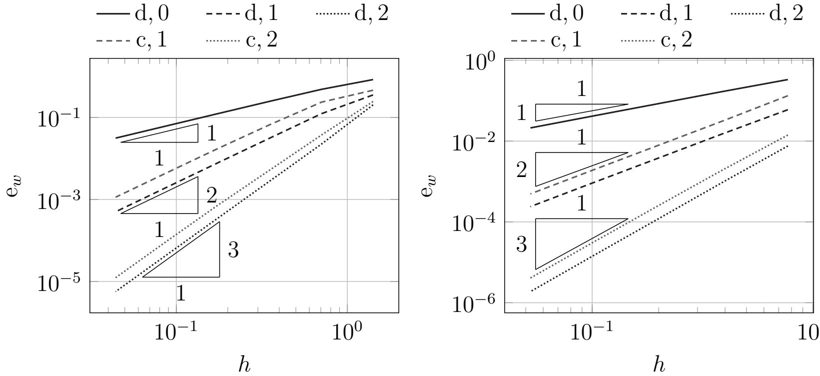

a) $L^2(\Sigma)$-projection, unit cube b) $L^2(\Sigma)$-projection, unit sphere

Figure 4.1: Convergence study of the $L^2(\Sigma)$-orthogonal projection; the reported error measure is defined by $e_w := \|w - w_h\|_{L^2(\Sigma)} / \|w\|_{L^2(\Sigma)}$. In the legends, the letters d and c represent the trial spaces $S_p^{\mathrm{d}}(\Sigma_N)$ and $S_p^{\mathrm{c}}(\Sigma_N)$, respectively. The numbers 0, 1, and 2 indicate the degree p.

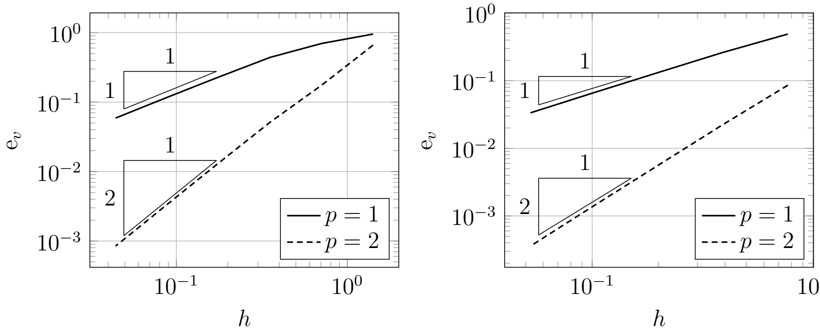

a) $H^1_{0,\cdot}(\Sigma)$-projection, unit cube b) $H^1_{0,\cdot}(\Sigma)$-projection, unit sphere

Figure 4.2: Convergence study of the $H^1_{0,\cdot}(\Sigma)$-orthogonal projection; the reported error measure is defined by $e_v := \|\nabla_\Sigma (w - v_h)\|_{L^2(\Sigma)} / \|\nabla_\Sigma w\|_{L^2(\Sigma)}$.

In the remainder of this section, the performance of the algorithm discussed in Section 3.8.3 is investigated. Recall that this procedure is intended to compute the set of lit panels $\Sigma_N^{\Xi}(\mathbf{x})$ for a given evaluation point $\mathbf{x} \in \mathbb{R}^4$ efficiently. In the following examples, three different domains are considered. We examine the unit cube $\Omega^- := \left(-\frac{1}{2}, \frac{1}{2}\right)^3$ with $T := 1$ and the unit ball $\Omega^- := \{x \in \mathbb{R}^3 : \|x\| < 1\}$ with $T := 5$. The third domain is a distorted torus, which is illustrated in Figure 4.3, with $T := 2$. Furthermore, three evaluation points $\mathbf{x}_A, \mathbf{x}_B, \mathbf{x}_C \in \mathbb{R}^4$ are employed. They are given by $\mathbf{x}_* := (T, x_*), * \in \{A, B, C\}$ with the spatial components $x_A, x_B, x_C \in \mathbb{R}^3$

$$x_A := \begin{pmatrix} 0 & 0 & 0 \end{pmatrix}^\top, \quad x_B := \tfrac{1}{\sqrt{3}} \begin{pmatrix} 1 & 1 & 1 \end{pmatrix}^\top, \quad x_C := \begin{pmatrix} -1 & -\frac{1}{\sqrt{2}} & -\frac{1}{\pi} \end{pmatrix}^\top.$$

All execution times (provided in ordinary time, seconds) reported in the remainder of this section are minimum values of five consecutive runs of the stated procedures.

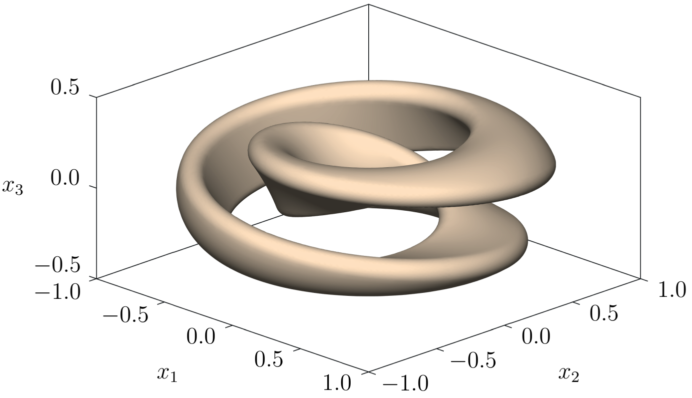

Figure 4.3: Depiction of the distorted torus domain used in Section 4.1; this image of the spatial boundary Γ is based on a mesh of 40960 triangular panels.

In a preliminary experiment, the computational time of the construction of the binary cluster tree $\mathbb{T}$ is studied. For $n := n_{\min} \in \{1, 5, 50\}$ we report the time t_n required to execute the procedure `CreateBinaryClusterTree`$(n; \{\mathfrak{I}\}, \varnothing, \mathfrak{I})$ and compute the bounding spheres of all clusters in $\mathbb{T}$. For the sake of comparison, the time t_N is provided, which is the execution time of `ComputeLitPanels`(Σ_N) with $\mathbf{x} := \mathbf{x}_A$. In other words, t_N is the time it takes to compute $\Sigma_N^{\Xi}(\mathbf{x}_A)$ in a naive fashion. Figure 4.4 displays results of this investigation for all three considered domains. The $\mathcal{O}(N)$ behavior of t_N as well as the $\mathcal{O}(N \log(N))$ behavior of the construction time of $\mathbb{T}$ can be observed clearly. In all examined scenarios the construction time of $\mathbb{T}$ falls below t_N, even for $n_{\min} = 1$. In Figure 4.4b, the black and gray lines overlap. This suggests that the shape of Γ (sphere or distorted torus) has hardly any influence on the construction time of $\mathbb{T}$, only the number of panels N matters. The finest considered mesh of the sphere is composed of $N \approx 1.11 \times 10^7$ panels. For this mesh, the binary cluster tree is composed of $|\mathbb{T}| \approx 6.09 \times 10^5$ clusters for $n_{\min} = 50$, while $|\mathbb{T}| = 2N - 1 \approx 2.23 \times 10^7$ is observed for $n_{\min} = 1$.

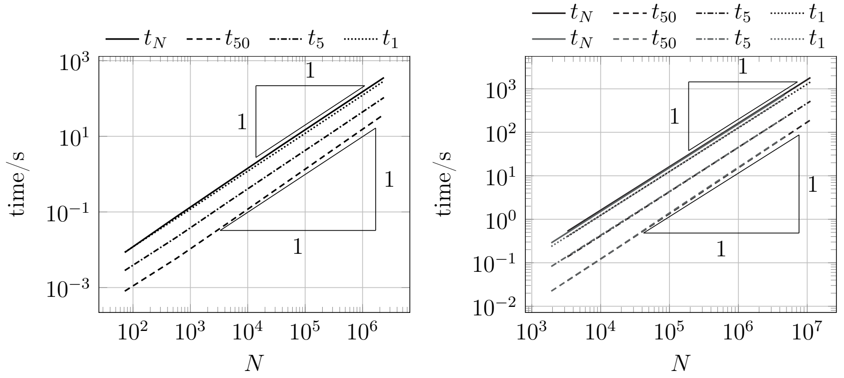

a) construction time of $\mathbb{T}$, unit cube

b) construction time of $\mathbb{T}$, unit sphere (black) and distorted torus (gray)

Figure 4.4: Construction time of the binary cluster tree $\mathbb{T}$; the ordinates depict the elapsed time in seconds. The subscript $n := n_{\min} \in \{1, 5, 50\}$ of t_n indicates the maximum size of leaf-level clusters. The reference value t_N is the execution time of `ComputeLitPanels`(Σ_N) for $\mathbf{x} := \mathbf{x}_A$.

In the second experiment regarding the geometric clustering technique, we investigate the numbers of lit panels $|\Sigma_N^{\Xi}|$ and panels in the proxy set $|X_N|$ of Section 3.8.3. Only the evaluation point $\mathbf{x}_C$ is considered, however, three upper bounds for the size of leaf-level clusters $n_{\min} \in \{1, 5, 50\}$ are examined. Results of this study are exhibited in Figure 4.5. On the one hand, the conjectured $\mathcal{O}\left(N^{2/3}\right)$ behavior of $|\Sigma_N^{\Xi}|$ can be observed. On the other hand, the results indicate that the cardinality of the proxy set $|X_N|$ shares the asymptotic behavior of $|\Sigma_N^{\Xi}|$. The existence of $C > 0$, independent of N, such that $|X_N| < C|\Sigma_N^{\Xi}|$ holds is a key assumption in Section 3.8.3 in order to compute Σ_N^{Ξ} efficiently via `ComputeLitPanels`(X_N). The experimental observation of this property provides evidence about the capacity of the proposed approach. Furthermore, it is easy to see that $|\Sigma_N^{\Xi}| < |X_N|$ holds in all examined scenarios, even for $n_{\min} = 1$. For $n_{\min} = 1$, each leaf-level cluster contains only a single panel. Consequently, the bounding sphere of a leaf-level cluster matches the one of its panel. We are lead to the conclusion that there exists a significant portion of panels whose bounding sphere intersects the light cone although the panel itself is not lit. Still, the algorithm discussed in Section 3.8.3 yields a set $X_N \supset \Sigma_N^{\Xi}$ sufficiently small for our purposes.

Finally, a numerical experiment is presented which aims at demonstrating the increase in performance achieved by the proposed technique. The naive approach $\Sigma_N^{\Xi}(\mathbf{x}) := \texttt{ComputeLitPanels}(\Sigma_N)$ is compared to the following procedure outlined in Section 3.8.3:

1. $L := \varnothing$, $\texttt{ApproximateLitLeaves}(L, \operatorname{root} \mathbb{T})$,
2. $X_N := \bigcup_{v \in L} \bigcup_{i \in v} \sigma_i$,
3. $\Sigma_N^{\Xi}(\mathbf{x}) := \texttt{ComputeLitPanels}(X_N)$.

Both approaches yield the identical set $\Sigma_N^{\Xi}(\mathbf{x})$, however, the time required to execute these procedures is of interest. Let t_N be the execution time of the naive approach based on $\texttt{ComputeLitPanels}(\Sigma_N)$ and t_n be the time required to execute the list of the three steps above. Again the subscript $n := n_{\min} \in \{1, 50\}$ indicates the maximum size of leaf-level clusters. Figure 4.6 exhibits results of this survey, suggesting that the construction of Σ_N^{Ξ} by means of the proposed procedure involves the optimal $\mathcal{O}\left(N^{2/3}\right)$ operations. The three solid lines overlap, indicating that t_N depends little on the actual position of the evaluation point $\mathbf{x}$. In contrast, t_{50} and t_1 depend heavily on $\mathbf{x}$, at least for the unit cube. This is a desirable property because it enables large reductions of the execution time for points $\mathbf{x}$ such that $\Sigma_N^{\Xi}(\mathbf{x})$ is relatively small. The difference between t_{50} and t_1 is noteworthy. This observation suggests that the extreme choice $n_{\min} = 1$ is optimal if $\Sigma_N^{\Xi}(\mathbf{x})$ is computed for sufficiently many evaluation points $\mathbf{x}$.

REMARK 4.1. *All results of this section are obtained on an* Intel® Core™ *i7-8700 desktop machine with a clock speed of* 3.2 GHz. *The absolute values of the elapsed times in Figures 4.4 and 4.6 are of little significance, because the implementation is both single-threaded as well as immature. Sophisticated implementations of the proposed procedures might yield execution times several orders of magnitude smaller than the exhibited ones. However, the presented results reveal the improvement of the asymptotic behavior achieved by means of the technique discussed in Section 3.8.3.*

4.2 Verification of the “Inner Quadrature”

The experiments of this section aim at verifying the numerical integration procedure proposed in Sections 3.5 and 3.8.1. The experimental setup is adapted from our earlier

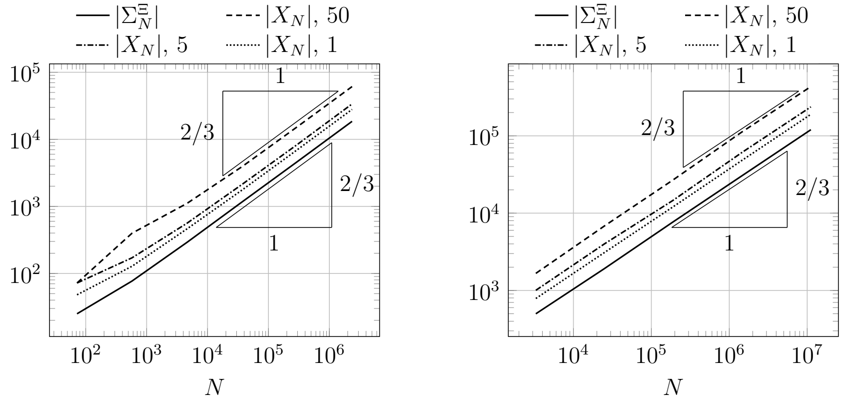

a) cardinalities of sets, unit cube

b) cardinalities of sets, unit sphere

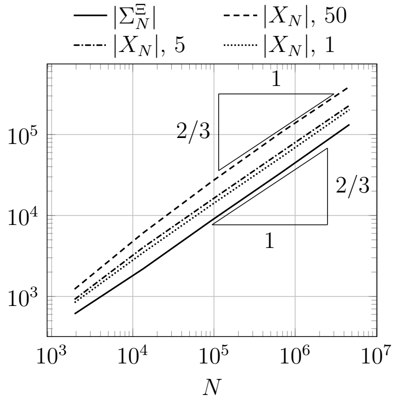

c) cardinalities of sets, distorted torus

Figure 4.5: Cardinalities of the set of lit panels Σ_N^Ξ and the proxy set X_N for the evaluation point $\mathbf{x}_C$; in the legends, the numbers next to $|X_N|$ indicate the corresponding maximum sizes of leaf-level clusters $n_{\min} \in \{1, 5, 50\}$.

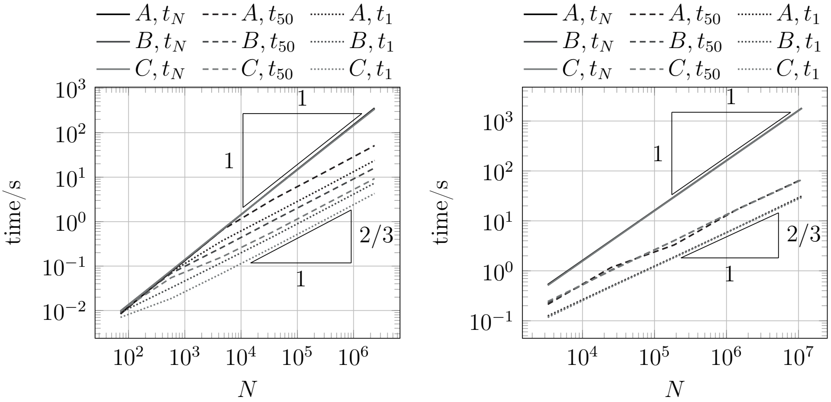

a) construction time of Σ_N^{Ξ}, unit cube b) construction time of Σ_N^{Ξ}, unit sphere

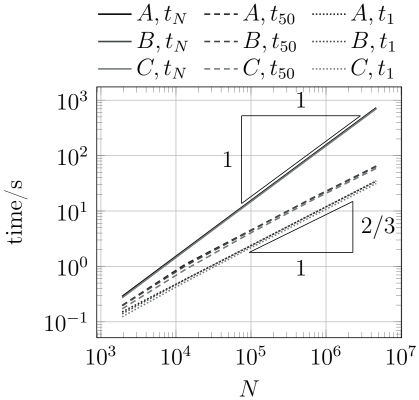

c) construction time of Σ_N^{Ξ}, distorted torus

Figure 4.6: Construction time of the set of lit panels $\Sigma_N^{\Xi}(\mathbf{x}_*)$; the ordinates depict the elapsed time in seconds. In the legends, the letters represent the evaluation points $\mathbf{x}_*$ for $* \in \{A, B, C\}$. The subscript $n := n_{\min} \in \{1, 50\}$ of t_n indicates the corresponding maximum size of leaf-level clusters. The value t_N is the execution time of `ComputeLitPanels`(Σ_N). In all three images, the lines of t_N overlap for all points $\mathbf{x}_A$, $\mathbf{x}_B$, and $\mathbf{x}_C$.

work [89, Section 4.1] and hinges on evaluations of the function $\widetilde{u} : Q^+ \cup \Sigma \to \mathbb{R}$

$$\widetilde{u} : \mathbf{x} \mapsto \begin{cases} \mathrm{D}\,\gamma_0^+ u(\mathbf{x}) - \mathrm{S}\,\gamma_1^+ u(\mathbf{x}) & \text{if } \mathbf{x} \in Q^+, \\ \mathrm{K}\,\gamma_0^+ u(\mathbf{x}) - \mathrm{V}\,\gamma_1^+ u(\mathbf{x}) + \mathcal{J}(x)\gamma_0^+ u(\mathbf{x}) & \text{if } \mathbf{x} \in \Sigma, \end{cases} \tag{4.1}$$

by means of quadrature. The function $\mathcal{J} : \Gamma \to [0, 1]$ in (4.1) is known as solid angle or jump term, see [108, Equation (6.11)] or [100, Equation (3.36)]. It holds $\mathcal{J}(x) = 1/2$ if the tangent space of Γ exists at $x \in \Gamma$. Clearly, (4.1) corresponds to Kirchhoff's formula (2.14) for $\mathbf{x} \in Q^+$ and the weakly singular BIE (2.15) for $\mathbf{x} \in \Sigma$ in case of $\mathfrak{d} = +$. If a sufficiently smooth $u : Q^+ \to \mathbb{R}$ satisfies (2.7) it follows that $u(\mathbf{x}) = \widetilde{u}(\mathbf{x})$ holds for any $\mathbf{x} \in Q^+ \cup \Sigma$. In the subsequent experiments, all integral operators in (4.1) are approximated by the quadrature technique introduced in Section 3.8.1. This approximation is the only relevant source of the error $u - \widetilde{u}$ because the exact Cauchy data of u are used in (4.1). As a consequence, $u - \widetilde{u}$ is a viable measure for the error induced by quadrature. The quadrature scheme based on Algorithm 1 features two primary options, namely the number of quadrature points per direction $n_G \in \mathbb{N}$ and the depth of recursion $r_{\max} \in \mathbb{N}_0$. In the following experiments, we consider a few different values for $r_{\max}$ and examine the convergence of the method with respect to n_G. The employed manufactured solution u of (2.7) is specified in the following paragraph.

Let $y_S \in \Omega^-$ be a fixed source point and $\mu \in C^2(\mathbb{R})$ satisfy $\mu(t) = 0$ for all $t \in (-\infty, 0]$. The spherical wave function $f : \mathbb{R} \times (\mathbb{R}^3 \setminus \{y_S\}) \to \mathbb{R}$ is defined by

$$f : (t, x) \mapsto \frac{\mu(t - \|x - y_S\|)}{\|x - y_S\|}. \tag{4.2}$$

A direct computation verifies that $f(0, \cdot) = 0$ and $\partial_t f(0, \cdot) = 0$ hold in $\mathbb{R}^3 \setminus \{y_S\}$, while $\Box f = 0$ holds everywhere in its domain. It follows that $u := f|_{Q^+}$ is a solution of (2.7) for $\mathfrak{d} = +$. The continuity of u implies $\gamma_0^+ u = u|_\Sigma$ and the corresponding Neumann trace is given by $\gamma_1^+ u : \mathbf{x} \mapsto \langle \nu_\Gamma(x), \nabla_x u(\mathbf{x}) \rangle$. In this section, the causal signal

$$\mu : t \mapsto \begin{cases} \exp\left(\left(\frac{t^2}{4} - t \right)^{-1} \right) & \text{if } t \in (0, 4), \\ 0 & \text{otherwise}, \end{cases}$$

is employed. It holds $\mu \in C_0^\infty(\mathbb{R})$ and, therefore, the field u is smooth. The considered source point is fixed to $y_S := -\frac{1}{10} \begin{pmatrix} 1 & 2 & 3 \end{pmatrix}^\top$.

In the first test, the considered computational domain is the unit cube $\Omega^- := \left(-\frac{1}{2}, \frac{1}{2}\right)^3$ with $T := 5$. The mesh Σ_N of the lateral boundary is composed of $N = 180$ panels. Both u and $\widetilde{u}$ are evaluated at the point $\mathbf{x}_d := (T, x_d)$, where $x_d \in \mathbb{R}^3$ is defined by

$$x_d := \begin{pmatrix} \frac{1}{2} & \frac{1}{2} & \frac{1}{2} \end{pmatrix}^\top + d \begin{pmatrix} 1 & 0 & 0 \end{pmatrix}^\top$$

with $0 \leq d = \mathrm{dist}_\Gamma(x_d)$. The error measure

$$\mathrm{e}_d := \frac{|u(\mathbf{x}_d) - \widetilde{u}(\mathbf{x}_d)|}{|u(\mathbf{x}_d)|} \tag{4.3}$$

is evaluated for the distances $d \in \{0, \frac{1}{10}, 1, 3\}$ considered in [89, Figure 3(a)].

Results of this experiment are exhibited in Figure 4.7 for depths of recursion $r_{\max} \in \{7, 10, 14, 20\}$. On the one hand, it can be observed that the error decays rapidly as n_G is increased. On the other hand, convergence with respect to n_G ceases once the error falls below a certain magnitude, which depends on $r_{\max}$. The existence of such a threshold indicates that the set of admissible scenarios in Algorithm 1 is not immaculate. It seems that non-admissible scenarios are encountered even after $r_{\max} = 20$ steps of recursion. They are treated by low-order approximations, thereby capping the convergence of the overall scheme. Nevertheless, the proposed method enables highly accurate evaluations: for $r_{\max} = 20$ the achievable error is roughly $\mathrm{e}_d \approx 1 \times 10^{-12}$, which is rather close to the employed machine precision. Furthermore, we observe little dependence on the actual position of the evaluation point. The case $d = 0$, which involves weakly singular kernel functions, is approximated with the same accuracy as the cases with $d > 0$. This behavior is due to the employed transformations, which regularize the integrand and enable rapid convergence of standard Gaussian quadrature rules, see Lemma 3.16. Finally, we emphasize that the results for $r_{\max} = 20$ are quite comparable to numerical results provided in our earlier work [89, Figure 3(a)].

A further example is considered in order to support the capacity of the proposed quadrature approach. Still, the aim is to evaluate (4.1), however, only points $\mathbf{x} \in \Sigma$ are examined. Considering evaluation points exclusively on Σ lays focus on numerical integration of the weakly singular kernel functions (2.32). Given a set of $m \in \mathbb{N}$ evaluation points $\{\mathbf{x}_i\}_{i=1}^{m}$, the error

$$\mathrm{e}_\Sigma := \frac{\sum_{i=1}^{m} |u(\mathbf{x}_i) - \widetilde{u}(\mathbf{x}_i)|}{\sum_{i=1}^{m} |u(\mathbf{x}_i)|} \tag{4.4}$$

is computed for increasing numbers of quadrature points per direction $n_G \in \mathbb{N}$. The simulation end time is set to $T := 5$ and two cases are considered:

- Let Γ be the boundary of the unit cube and Σ_N be a mesh of $N = 288$ panels. The error e_Σ is evaluated at the $m = N$ centroids of the panels.
- Let Γ be a polyhedral approximation of the unit sphere and Σ_N be a mesh of $N = 5490$ panels. The error e_Σ is evaluated at the $m = 244$ centroids of the panels whose time coordinates t satisfy $t > T - h/3$. This condition is established in order to achieve a number of points m similar to the cube. Note that (4.1) uses the Cauchy data on the true polyhedral boundary. Therefore, the fact that Σ_N merely approximates a sphere introduces no error.

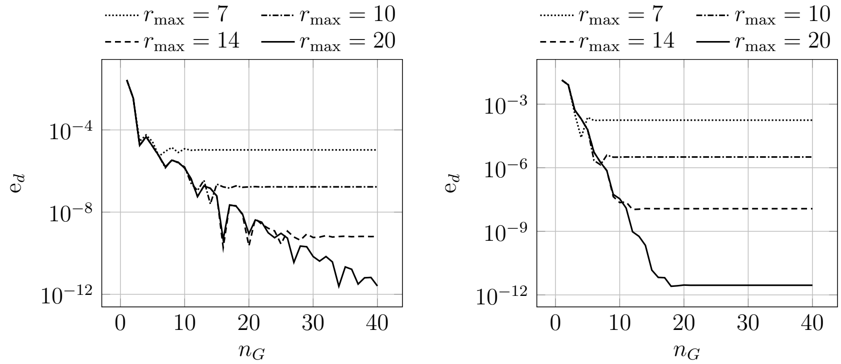

a) distance to boundary $d = 3.0$

b) distance to boundary $d = 1.0$

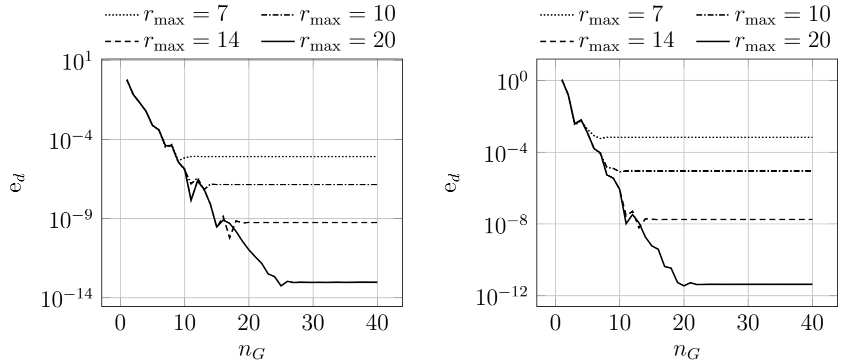

c) distance to boundary $d = 0.1$

d) distance to boundary $d = 0.0$

Figure 4.7: Convergence study of the quadrature method discussed in Section 3.8.1; the ordinates depict the relative error measure (4.3). The parameters $r_{\max}$ and n_G denote the depth of recursion and the number of quadrature points per direction in Algorithm 1. Note that the total number of quadrature points behaves like $\mathcal{O}\left({n_G}^2\right)$.

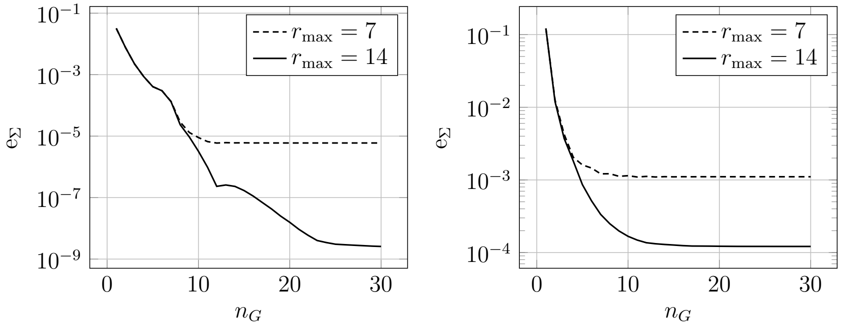

a) error (4.4) for the unit cube ($m = 288$) b) error (4.4) for the unit sphere ($m = 244$)

Figure 4.8: Convergence study of the quadrature method discussed in Section 3.8.1 for weakly singular integrands; the ordinates depict the relative error measure (4.4). The parameters $r_{\max}$ and n_G denote the depth of recursion and the number of quadrature points per direction in Algorithm 1. Note that the total number of quadrature points behaves like $\mathcal{O}\left({n_G}^2\right)$.

Figure 4.8 displays results of both cases for depths of recursion $r_{\max} \in \{7, 14\}$. It can be observed that the error decays rapidly for sufficiently small n_G. The smallest achievable error depends on $r_{\max}$, similar to the data depicted in Figure 4.7. For $r_{\max} = 14$, the minimum error is approximately 1×10^{-9} for the unit cube, however, it is merely 1×10^{-4} for the unit sphere. This observation suggests that Algorithm 1 encounters substantially more non-admissible scenarios in the latter configuration. These scenarios occur due to the lack of smoothness of the level set function and the entailed corners of $\mathcal{B}_n$, see Section 3.8.1. Nevertheless, the results depicted in Figure 4.8a are quite comparable to the data displayed in [89, Figure 3(b)]. This indicates that Algorithm 1 is, albeit immature, indeed capable of achieving highly accurate pointwise evaluations of retarded layer potentials.

The experimental results of this section support the conclusion that the quadrature scheme proposed in Sections 3.5 and 3.8.1 is a competitive alternative to the method discussed in [89].

4.3 An Experiment on the "Outer Quadrature"

This numerical experiment is intended to investigate the performance of the quadrature procedure for the bilinear form b_{T_k} discussed in Section 3.6. The basic idea of the experiment is discussed in the following passage. Let a domain $\Omega^- \subset \mathbb{R}^3$ and a solution $u : Q^- \to \mathbb{R}$ of (2.7) be given. Consider the weakly singular BIE (2.15) for the interior problem $\mathrm{V}\,\gamma_1^- u = \frac{1}{2}\gamma_0^- u + \mathrm{K}\,\gamma_0^- u$. It is assumed that the Cauchy data $\big(\gamma_0^- u, \gamma_1^- u\big)$ are contained in the boundary element space $V_h \times U_h$, where V_h and U_h are as in Section 3.3 for a given mesh Σ_N. This requirement is critical for the experimental setup. Since $\gamma_0^- u \in V_h$ and $\gamma_1^- u \in U_h$ hold, the coefficient vectors $\mathsf{u} := \mathrm{R}_{V_h}(\gamma_0^- u)$ and $\mathsf{p} := \mathrm{R}_{U_h}(\gamma_1^- u)$ may be defined, where R is the Ritz isomorphism of Section 3.2. The discretization of the weakly singular BIE (3.10) is equivalent to the linear system

$$\mathsf{V}\mathsf{p} = \frac{1}{2}\mathsf{A}\mathsf{u} + \mathsf{K}\mathsf{u},$$

which is discussed in Section 3.3. The entries of the matrices V and K are computed via the quadrature methods of Sections 3.5 and 3.6. Let V_m and K_m be the matrices computed by means of a quadrature rule for the "outer integral" (3.41) with $m := m_Q \in \mathbb{N}$ points per direction as in Figure 3.4. In terms of the quadrature for the "inner integral" discussed in Section 3.8.1 we shall compare the two scenarios $(r_{\max}, n_G) = (10, 11)$ and $(r_{\max}, n_G) = (16, 21)$. For $m = 1, \dots, 8$ the relative error is computed

$$\mathrm{e}_m := \frac{\left\|\mathsf{V}_m\mathsf{p} - \mathsf{K}_m\mathsf{u} - \frac{1}{2}\mathsf{A}\mathsf{u}\right\|_2}{\left\|\mathsf{A}\mathsf{u}\right\|_2}, \tag{4.5}$$

which is solely induced by numerical integration of the entries of V_m and K_m. Note that the entries of A are computed exactly by Gaussian quadrature of sufficiently high order. Furthermore, let $\mathsf{V}_{\mathrm{ref}}$ and $\mathsf{K}_{\mathrm{ref}}$ be reference matrices computed by $m = 16$ outer quadrature points per direction. The parameters of the inner quadrature are fixed to $(r_{\max}, n_G) = (16, 21)$ for the reference matrices. We compute the estimates for the errors of the matrices V_m and K_m

$$\mathrm{e}_m^{\mathsf{V}} := \frac{\left\|\mathsf{V}_{\mathrm{ref}} - \mathsf{V}_m\right\|_2}{\left\|\mathsf{V}_{\mathrm{ref}}\right\|_2}, \quad \mathrm{e}_m^{\mathsf{K}} := \frac{\left\|\mathsf{K}_{\mathrm{ref}} - \mathsf{K}_m\right\|_2}{\left\|\mathsf{K}_{\mathrm{ref}}\right\|_2} \tag{4.6}$$

for $m = 1, \dots, 8$. The matrix 2-norm $\|\cdot\|_2$ in (4.6) denotes the spectral norm, which equals the largest singular value of the input matrix.

In the following paragraph, the employed solution $u : Q^- \to \mathbb{R}$ is specified, which is adapted from [61, Appendix A.4]. This solution corresponds to a linearly elastic rod which is fixed on one end and a constant force is applied on the other end. Let $\Omega^- := (0,1) \times \left(-\frac{1}{2}, \frac{1}{2}\right)^2$ and $T := 2$. For $n \in \mathbb{N}_0$ define the affine function $s_n : \mathbb{R} \times \mathbb{R} \to \mathbb{R}$ by

$$s_n : (t, r) \mapsto t - r - (2n+1).$$

The examined solution $u : \mathbb{R}^4 \to \mathbb{R}$ reads

$$u : \mathbf{x} \mapsto \sum_{n=0}^{\infty} (-1)^n \big[s_n(t, -x_1)\theta \circ s_n(t, -x_1) - s_n(t, x_1)\theta \circ s_n(t, x_1)\big], \tag{4.7}$$

where $\theta : \mathbb{R} \to \{0,1\}$ is the Heaviside step function. It holds $\gamma_0^- u = u|_\Sigma$ because u is continuous. The corresponding Neumann trace reads

$$\gamma_1^- u : \mathbf{x} \mapsto \sum_{n=0}^{\infty} (-1)^n \big[\theta \circ s_n(t, -x_1) + \theta \circ s_n(t, x_1)\big] \nu_{\Gamma,1}(x),$$

where $\nu_{\Gamma,1}(x)$ denotes the x_1-component of the unit outward normal vector at $x \in \Gamma$. For $\mathbf{x} \in \overline{Q^-}$ the series in (4.7) is in fact a sum in disguise. It holds

$$\theta \circ s_n(t, \pm x_1) = 0 \quad \Leftrightarrow \quad s_n(t, \pm x_1) \leq 0 \quad \Leftrightarrow \quad 2n \geq t - 1 \mp x_1.$$

For $\mathbf{x} \in \overline{Q^-}$ we have $t \leq T$ and $x_1 \in [0,1]$, implying that $n \geq T/2$ is sufficient for $s_n(t, \pm x_1) \leq 0$ for all $\mathbf{x} \in \overline{Q^-}$. As a consequence, all contributions in (4.7) with $n \geq 1$ vanish for the considered case $T = 2$. The mesh Σ_N is set such that the zero level sets of s_0

$$\{\mathbf{x} \in \Sigma : t = 1 - x_1\}, \quad \{\mathbf{x} \in \Sigma : t = 1 + x_1\} \tag{4.8}$$

are aligned with faces of the mesh, see Figure 4.9. This appropriate meshing enables the properties $\gamma_0^- u \in V_h$ and $\gamma_1^- u \in U_h$, which are crucial for this numerical experiment. The employed mesh is composed of $N = 72$ panels.

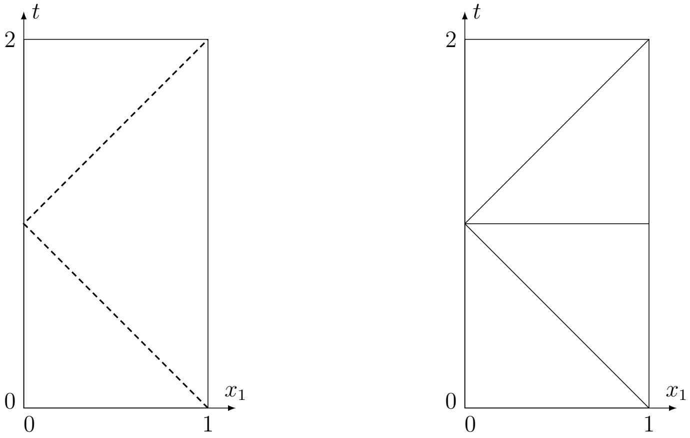

a) zero level sets of s_0 b) aligned simplex mesh

Figure 4.9: Figure 4.9a depicts the zero level sets of s_0 (4.8) as dashed lines in the plane $(t, x_1) \in [0,2] \times [0,1]$. The solution (4.7) is not classically differentiable at these sets of points. Figure 4.9b illustrates the employed simplex mesh whose faces (edges) are aligned with the zero level sets of s_0.

Remark 4.2. *The functions* $s_n, n \in \mathbb{N}_0$ *cannot be represented as the product of a function in time and a function in the spatial component. In other words, there are no* $f_t, f_x : \mathbb{R} \to \mathbb{R}$ *such that* $s_n(t,r) = f_t(t)f_x(r)$ *holds for all* $(t,r) \in \mathbb{R} \times \mathbb{R}$*. As a consequence, the solution* u *defined in (4.7) cannot be represented as such a product either. Classical approximation methods based on semi-discretization are incapable of supplying the exact solution. In contrast, the space-time scheme discussed in this thesis offers sufficient flexibility to capture the features of the considered wave field exactly, provided a suitable mesh* Σ_N *is available. This reasoning suggests that discretization methods based on unstructured space-time meshes are capable of approximating typical solutions of the d'Alembertian with greater accuracy. A similar train of thought leads Frangi to the development of his "causal" shape functions [34].*

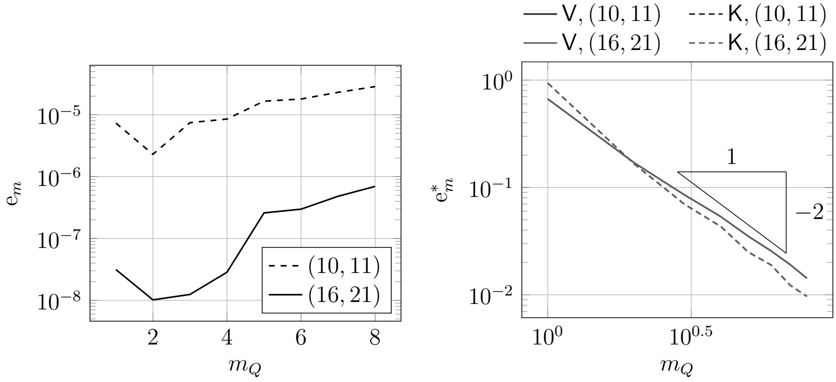

a) error of algebraic BIE (4.5) b) approximate errors of matrices (4.6)

Figure 4.10: Convergence study of the quadrature scheme for the bilinear form b_{T_k}; the number of quadrature points per triangular face is m_Q^2, see Figure 3.4. The 2-tuple $(r_{\max}, n_G) \in \{(10,11),(16,21)\}$ indicates the parameters employed in Algorithm 1. Figure 4.10a depicts the error measure (4.5) and Figure 4.10b shows the error e_m^*, $* \in \{\mathsf{V},\mathsf{K}\}$, which is defined in (4.6). The lines for $(r_{\max}, n_G) = (10,11)$ and $(r_{\max}, n_G) = (16,21)$ overlap because their difference falls below 4×10^{-6}.

Figure 4.10 presents results of this experiment. We observe in Figure 4.10a that the error (4.5) grows as m_Q is increased. However, the error is reduced drastically by augmenting the parameters of the inner quadrature $(r_{\max}, n_G)$ from $(10,11)$ to $(16,21)$. Increasing m_Q seems to accumulate more and more errors induced by the inner quadrature. In order to explain this behavior, note that the BIE $\mathrm{V}\,\gamma_1^- u(\mathbf{x}) = \frac{1}{2}\gamma_0^- u(\mathbf{x}) + \mathrm{K}\,\gamma_0^- u(\mathbf{x})$ is satisfied for almost any $\mathbf{x} \in \Sigma$ if the inner quadrature were exact. Consequently, the outer quadrature contributes nothing to the reduction of (4.5) but stacks up errors due to the inner quadrature for $\mathcal{O}\left(m_Q^2\right)$ points. Still, the magnitude of e_m indicates that the method discussed in Section 3.6 yields faithful approximations of the matrices V and K. In contrast to these findings, Figure 4.10b shows roughly second-order convergence of the errors (4.6) with respect to m_Q. This rate is optimal for the employed composite midpoint rules. Evidently, the considered parameters for the inner quadrature have little impact on the errors of the matrices as operators. This suggests that (4.6) is dominated by the accuracy of the outer quadrature, which behaves as expected. These findings lead us to the conclusion that the approach proposed in Section 3.6 enables moderately accurate evaluations of the energetic bilinear form b_{T_k}.

4.4 Experiments on Space-Time Boundary Element Methods

The final numerical experiments investigate the performance of the space-time BEMs discussed in Section 3.3. Three tests are considered, one for each of the discretized variational formulations (3.10), (3.12), and (3.14). Throughout this section, the parameters for the inner quadrature are set to $(r_{\max}, n_G) := (7, 8)$, while the outer quadrature employs $m_Q := 3$ points per direction. The arising sparse linear systems are solved via the biconjugate gradient stabilized method, see [115] or [99, Section 7.4.2]. Although we forgo any form of preconditioning, such iterative methods are advantageous: all matrices have to be available in the code only as a matrix-vector product.

In the first example, a convergence study for the direct BEM (3.10) is conducted. The considered manufactured solution is based on the spherical wave function f as in (4.2) with the causal signal

$$\mu : t \mapsto \begin{cases} t^3 \exp(-t) & \text{if } t > 0, \\ 0 & \text{if } t \leq 0. \end{cases}$$

A straightforward calculation shows that $\mu \in C^2(\mathbb{R})$ holds, however, μ'' is not classically differentiable at the origin. The manufactured solution $u := f|_{Q^+}$ and the source point $y_S := -\frac{1}{10}\begin{pmatrix} 1 & 2 & 3 \end{pmatrix}^\top$ are defined analogously to Section 4.2. In terms of computational domain the unit cube is chosen with $T \in \{\frac{5}{2}, 5\}$. The variational RPBIE (3.10) is solved for the approximate Neumann unknown $w_h \approx \gamma_1^+ u$ on a sequence of meshes obeying Definition 3.1. The examined error measures are

$$\mathrm{e}_{\mathrm{BEM}} := \frac{\left\|\gamma_1^+ u - w_h\right\|_{L^2(\Sigma)}}{\left\|\gamma_1^+ u\right\|_{L^2(\Sigma)}}, \quad \mathrm{e}_{\mathrm{opt}} := \frac{\min\limits_{z_h \in U_h} \left\|\gamma_1^+ u - z_h\right\|_{L^2(\Sigma)}}{\left\|\gamma_1^+ u\right\|_{L^2(\Sigma)}}. \tag{4.9}$$

As discussed in Section 3.1, $\mathrm{e}_{\mathrm{opt}}$ is achieved by the $L^2(\Sigma)$-projection of $\gamma_1^+ u$ onto U_h. In addition, the discretized version of Kirchhoff's formula (3.11) is evaluated at points $\mathbf{x} \in Q^+$ in order to investigate the error of the wave field. In particular, a set of 26 points $\{x_i\}_{i=1}^{26}$ is considered, where each $x_i \in \mathbb{R}^3, i = 1, \dots, 26$ is located on the boundary of the cube $\left(-\frac{3}{5}, \frac{3}{5}\right)^3$. The evaluation points are defined by $\mathbf{x}_i := (T, x_i), i = 1, \dots, 26$ and the arithmetic mean of the relative pointwise errors is computed

$$\mathrm{e}_Q := \frac{1}{26} \sum_{i=1}^{26} \frac{|u(\mathbf{x}_i) - u_h(\mathbf{x}_i)|}{|u(\mathbf{x}_i)|}, \tag{4.10}$$

where u_h is given by (3.11) with $\mathfrak{d} = +$.

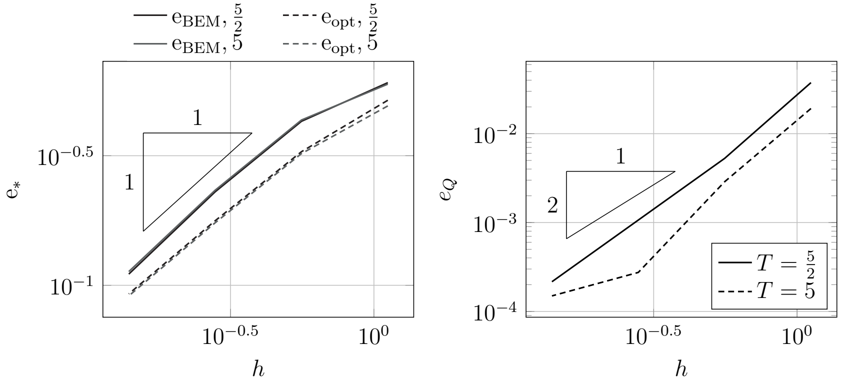

a) error of Neumann unknown (4.9)

b) error of wave field in Q^+ (4.10)

Figure 4.11: Convergence study of the direct BEM (3.10) on the unit cube; the ordinate in Figure 4.11a depicts the relative $L^2(\Sigma)$-norm of the error of the Neumann unknown (4.9). The numbers in the legends indicate the simulation end time $T \in \{\frac{5}{2}, 5\}$. In Figure 4.11b, the ordinate represents the arithmetic mean of the relative pointwise errors of the solution in Q^+ at 26 points (4.10).

Results of this experiment are displayed in Figure 4.11. In Figure 4.11a, we observe that the errors of the Neumann unknown (4.9) converge linearly with respect to h in the asymptotic regime. This conforms to the theoretical prediction (3.4) for $p = 0$. It seems that the lines of $\mathrm{e}_{\mathrm{BEM}}$ and $\mathrm{e}_{\mathrm{opt}}$ are parallel, at least in the asymptotic regime. This suggests that the error of the boundary element approximation satisfies a quasioptimality principle in $L^2(\Sigma)$, see Remark 4.3. Both considered simulation end times $T \in \{\frac{5}{2}, 5\}$ yield similar results. Figure 4.11b exhibits the error (4.10) of pointwise evaluations of the wave field. Apparently, the considered mesh sizes still lie in the preasymptotic regime. Nevertheless, the experimental order of convergence with respect to h is two on average. If the theory of BIEs for elliptic problems indeed carried over to hyperbolic RPBIEs, we would expect cubic convergence with respect to h, see [108, Theorem 12.7, Equation (12.22)] or [100, Example 4.2.15, Remark 4.2.16]. However, the proof of this estimate relies on an Aubin-Nitsche duality argument which imposes restrictive assumptions on the mapping properties of V and K. Under more moderate assumptions, quadratic convergence with respect to h can be proven [108, Equation (12.21)], matching the results displayed in Figure 4.11b. We observe little impact of the considered values of T on the convergence of the method. This behavior, however, is investigated more thoroughly in the following tests.

REMARK 4.3. *Consider the d'Alembertian in one spatial dimension posed in the interval* $\Omega^- := (0, L)$ *for* $L > 0$*. In this case, the bilinear form* $b_T^{\mathcal{Z}} : L^2(\Sigma) \times L^2(\Sigma) \to \mathbb{R}$ *discussed in Section 2.5 is bounded and coercive. There exists a* $c_1 > 0$ *such that*

$$b_T^{\mathcal{Z}}(w, w) \geq c_1 \|w\|^2_{L^2(\Sigma)}, \quad b_T^{\mathcal{Z}}(w, v) \leq \|w\|_{L^2(\Sigma)} \|v\|_{L^2(\Sigma)}$$

hold for all $w, v \in L^2(\Sigma)$*, where* c_1 *satisfies the lower bound*

$$c_1 \geq \left(\sin\left(\frac{\pi}{2\lceil T/L\rceil + 2}\right)\right)^2,$$

see [6, Proposition 2.1, Theorem 2.1]. Given a functional $\ell : L^2(\Sigma) \to \mathbb{R}$ *let* $w \in L^2(\Sigma)$ *be the solution of*

$$b_T^{\mathcal{Z}}(w, v) = \ell(v) \quad \forall v \in L^2(\Sigma). \tag{4.11}$$

Let $S \subset L^2(\Sigma)$ *be a finite-dimensional subspace and let* $w_h \in S$ *be the solution of*

$$b_T^{\mathcal{Z}}(w_h, v_h) = \ell(v_h) \quad \forall v_h \in S. \tag{4.12}$$

As discussed in Remark 2.13, the Lax-Milgram lemma implies the unique solvability of both (4.11) *and* (4.12)*. Furthermore, Cea's lemma yields the quasioptimal error estimate*

$$\|w - w_h\|_{L^2(\Sigma)} \leq \frac{1}{c_1} \min_{v_h \in S} \|w - v_h\|_{L^2(\Sigma)},$$

see, e.g., [108, Theorem 8.1]. For a fixed domain Ω^-*, the lower bound for* c_1 *behaves like* T^{-2} *as* $T \to \infty$*. Therefore, we expect for* $w \notin S$

$$\frac{\|w - w_h\|_{L^2(\Sigma)}}{\min\limits_{v_h \in S} \|w - v_h\|_{L^2(\Sigma)}} \leq \frac{1}{c_1} \sim \mathcal{O}\left(T^2\right)$$

as $T \to \infty$*. If* w *is sufficiently smooth and* $S = U_h$ *is chosen, we predict the behavior* $\|w - w_h\|_{L^2(\Sigma)} \sim \mathcal{O}(h)$ *as* $h \to 0$ *due to* (3.4) *for* $p = 0$*. Finally, note that the extension of these considerations to the d'Alembertian in more than one spatial dimension demands utmost caution, see the discussions in Section 2.5 and Remark 4.4.*

The remaining two numerical experiments aim at the indirect BEMs (3.12) and (3.14). Since the solutions of (2.20) and (2.22) are not directly related to the Cauchy data of solutions of (2.7), the construction of manufactured solutions is not straightforward. For the unit sphere $\Gamma = \mathbb{S}^2$, however, such solutions are derived in [102] and [117, Chapter 2]. A brief outline of the cited solutions is provided in the following paragraph for the sake of completeness.

Denote by $Y_n^m : \mathbb{S}^2 \to \mathbb{C}$ the spherical harmonic function of degree $n \in \mathbb{N}_0$ and order $m \in \mathbb{Z}$ subject to $-n \leq m \leq n$. It holds

$$Y_n^m \circ e_{\mathbb{S}} : (\varphi, \theta) \mapsto \beta_{nm} P_n^m(\cos\theta) \exp(\imath m \varphi),$$

where $P_n^m : \mathbb{R} \to \mathbb{R}$ are the associated Legendre polynomials, $\imath$ denotes the imaginary unit, β_{nm} is the normalization factor

$$\beta_{nm} := \sqrt{\frac{(2n+1)}{4\pi} \frac{(n-m)!}{(n+m)!}},$$

and $e_{\mathbb{S}} : [0, 2\pi) \times [0, \pi] \to \mathbb{S}^2$ is the map from angular coordinates to the unit sphere provided in Definition 2.20. These functions satisfy the orthogonality relation

$$\begin{aligned} \left(Y_n^m, Y_{n'}^{m'} \right)_{L^2(\mathbb{S}^2)} &= \int_0^{2\pi} \int_0^{\pi} Y_n^m \circ e_{\mathbb{S}}(\varphi, \theta) \overline{Y_{n'}^{m'} \circ e_{\mathbb{S}}(\varphi, \theta)} \sin\theta \, \mathrm{d}\theta \mathrm{d}\varphi \\ &= \begin{cases} 1 & \text{if } n = n' \wedge m = m', \\ 0 & \text{otherwise}, \end{cases} \end{aligned}$$

where the overline indicates complex conjugation. The set of spherical harmonics constitutes an orthonormal basis of (complex-valued) $L^2(\mathbb{S}^2)$. Consider the BIEs (2.20) and (2.22) posed on the lateral space-time boundary $\Sigma := (0, T) \times \mathbb{S}^2$. Assume that $g_D, g_N : \Sigma \to \mathbb{C}$ are of the form

$$g_D : \mathbf{x} \mapsto g_0(t) Y_n^m(x), \quad g_N : \mathbf{x} \mapsto g_0(t) Y_n^m(x),$$

where $g_0 : \mathbb{R} \to \mathbb{R}$ satisfies $g_0(t) = 0$ for all $t \in (-\infty, 0]$ as well as $\partial_t g_0(0) = 0$. It follows that w solving (2.20) and v solving (2.22) are of the form

$$w : \mathbf{x} \mapsto w_0(t) Y_n^m(x), \quad v : \mathbf{x} \mapsto v_0(t) Y_n^m(x),$$

where formulas for $w_0, v_0 : \mathbb{R} \to \mathbb{R}$ are provided in [102, Theorem 4] or [117, Theorem 2.1.3]. Numerical evaluations of the time responses w_0 and v_0 are performed by means of the script described in [117, Chapter 2]. All subsequent convergence studies are conducted on polyhedral mesh approximations of Σ. The surface measure of the hypersurfaces defined by the family of meshes $\{\Sigma_N\}_{N \in \mathbb{N}}$

$$\textstyle\sum_{\sigma \in \Sigma_N} |\sigma| = \sum_{\sigma \in \Sigma_N} \int_\sigma \mathrm{d}S$$

approaches the exact value $|\Sigma| = \int_\Sigma \mathrm{d}S = 4\pi T$ from below. Various simulation end times are examined, in particular the five values $T \in \{1, 2, 4, 8, 16\}$ are considered.

In the following example, the single layer BIE (2.20) is investigated with Dirichlet data of the form

$$g_D : \mathbf{x} \mapsto g_0(t) \Re \left(Y_1^0(x) \right), \tag{4.13}$$

where $\Re$ denotes the real part and g_0 is defined by

$$g_0 : t \mapsto \begin{cases} t^4 \exp(-2t) & \text{if } t > 0 \\ 0 & \text{if } t \le 0. \end{cases} \tag{4.14}$$

The solution $w : \mathbf{x} \mapsto w_0(t) \Re \left(Y_1^0(x) \right)$ of (2.20) follows from [102, Equation (4.18)]. It is illustrated in Figure 4.12a. The discretized variational BIE (3.12) is solved for $w_h \in U_h$ and the error measures are evaluated

$$\mathrm{e}_{\text{abs}} := \left\| w - w_h \right\|_{L^2(\Sigma)}, \quad \mathrm{e}_{\text{BEM}} := \frac{\left\| w - w_h \right\|_{L^2(\Sigma)}}{\left\| w \right\|_{L^2(\Sigma)}}, \quad \mathrm{e}_{\text{opt}} := \frac{\min\limits_{z_h \in U_h} \left\| w - z_h \right\|_{L^2(\Sigma)}}{\left\| w \right\|_{L^2(\Sigma)}}. \tag{4.15}$$

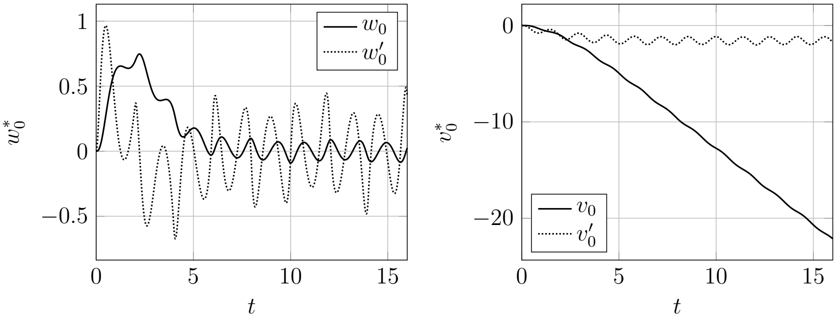

a) solution w_0 for g_0 as in (4.13) and (4.14) b) solution v_0 for g_0 as in (4.16) and (4.17)

Figure 4.12: Functions w_0 and v_0 of the examined solutions of (2.20) and (2.22) on the unit sphere.

Results of this test are exhibited in Figure 4.13. On the one hand, we observe that both the $L^2(\Sigma)$-projection and the solution of (3.12) converge linearly with respect to h. On the other hand, the error clearly increases as T is raised. By virtue of Remark 4.3 such a behavior is plausible. However, the behavior with respect to T is more modest than the conjectured worst case $\mathrm{e}_{\text{BEM}}/\mathrm{e}_{\text{opt}} \sim \mathcal{O}(T^2)$. Nevertheless, we observe first-order convergence with respect to h across all considered values of T, which conforms to the prediction (3.4) for $p = 0$. The experimental convergence

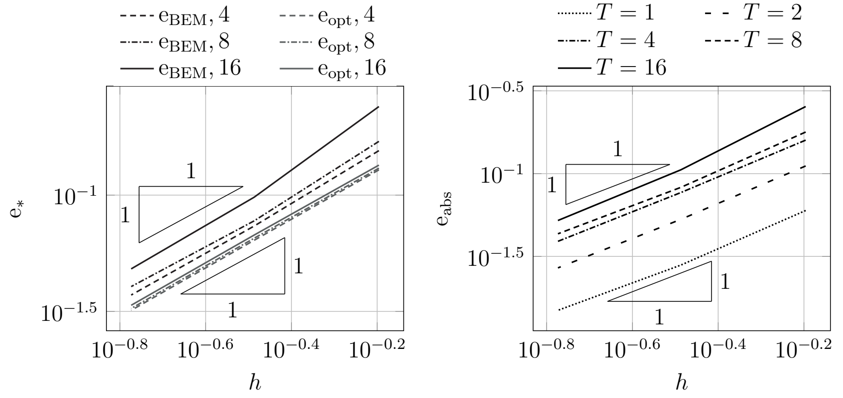

a) relative error measures of (4.15) b) absolute error measure of (4.15)

Figure 4.13: Convergence study of the single layer operator problem (3.12) on the unit sphere; the ordinates depict differently scaled $L^2(\Sigma)$-norms of the errors of the proxy densities (4.15). The numbers in the legends represent the simulation end times $T \in \{1, 2, 4, 8, 16\}$.

rates slightly exceed one, which might be accredited to Σ_N becoming an increasingly better approximation of the exact hypersurface Σ.

In the final example, the hypersingular BIE (2.22) is considered with Neumann data

$$g_N : \mathbf{x} \mapsto g_0(t) Y_0^0(x), \tag{4.16}$$

where g_0 is given by

$$g_0 : t \mapsto \begin{cases} (\sin(2t))^2 \, t \exp(-t) & \text{if } t > 0 \\ 0 & \text{if } t \leq 0. \end{cases} \tag{4.17}$$

Note that Y_0^0 is constant-valued $Y_0^0 : x \mapsto (4\pi)^{-1/2}$. The solution $v : \mathbf{x} \mapsto v_0(t) Y_0^0(x)$ of (2.22) can be found in [117, Section 2.6.1] and is visualized in Figure 4.12b. The discretized problem (3.14) is solved for $v_h \in V_h$ and the error measures are evaluated

$$\mathrm{e}_{\mathrm{abs}} := \|v - v_h\|_{L^2(\Sigma)}, \quad \mathrm{e}_{\mathrm{BEM}} := \frac{\|v - v_h\|_{L^2(\Sigma)}}{\|v\|_{L^2(\Sigma)}}, \quad \mathrm{e}_{\mathrm{opt}} := \frac{\min_{z_h \in V_h} \|v - z_h\|_{L^2(\Sigma)}}{\|v\|_{L^2(\Sigma)}}. \tag{4.18}$$

Figure 4.14 presents results of this test. The data displayed in Figure 4.14a indicates that both the $L^2(\Sigma)$-projection and the solution of (3.14) enjoy second-order convergence with respect to h. The behavior of the error with respect to T is different

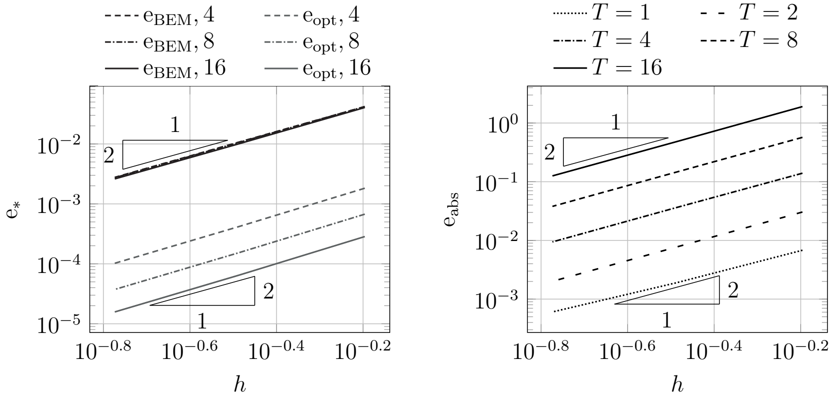

a) relative error measures of (4.18) b) absolute error measure of (4.18)

Figure 4.14: Convergence study of the hypersingular operator problem (3.14) on the unit sphere; the ordinates depict differently scaled $L^2(\Sigma)$-norms of the errors of the proxy densities (4.18). The numbers in the legends represent the simulation end times $T \in \{1, 2, 4, 8, 16\}$. In Figure 4.14a, the lines representing e_{BEM} (almost) overlap for all considered values of T; their differences fall below 2×10^{-3}.

from the observations of the previous example. While e_{BEM} remains roughly the same for all considered values of T, the relative distance e_{opt} decreases greatly as T is increased. In order to explain this behavior consider the illustration of the solution v_0 in Figure 4.12b. While the absolute value of v_0 grows almost linearly in time, we observe that v_0' is bounded and behaves like a periodic function for large times. Therefore, v_0 at earlier times can be approximated as easily as v_0 at larger times. Consequently, the $L^2(\Sigma)$-norm of v grows much faster with T than the $L^2(\Sigma)$-norm of the error $v - v_h^*$. This leads us to the conclusion that the relative error measure e_{opt} is reduced significantly as T is increased. Evidently, the ratio e_{BEM}/e_{opt} increases heavily with T, however, it grows slower than the worst case behavior $\mathcal{O}(T^2)$ conjectured in Remark 4.3. Figure 4.14b shows that the boundary element solution converges quadratically with respect to h across all considered values of T. This conforms to the optimum (3.5) for $p = 1$.

Indeed, the theoretical convergence rates of (3.4) and (3.5) are measured in all conducted experiments. These rates agree with results provided in the literature, see, e.g., [43, Section 4.3.3]. This provides strong evidence about the correctness of the implementation and the potential of the proposed space-time BEMs. Furthermore, the obtained results confirm that the quadrature technique proposed in Section 3.6 is capable of computing sufficiently accurate evaluations of the space-time bilinear forms: even for few quadrature points ($m_Q = 3$), the quadrature errors seem to be sufficiently small such that the overall convergence of the method is not spoiled.

REMARK 4.4. *The errors of the solutions of* (3.10), (3.12), *and* (3.14) *are computed exclusively in the norm* $\|\cdot\|_{L^2(\Sigma)}$. *This norm is chosen because it can be evaluated by means of numerical integration in a straightforward as well as accurate fashion. As indicated in Remark 2.13, the mathematical analysis of the variational problems discussed in Section 2.5 is incomplete. Nevertheless, the investigations in [10, 51, 6, 58] show that significantly more intricate norms than* $\|\cdot\|_{L^2(\Sigma)}$ *are necessary to achieve appropriate functional settings of variational RPBIEs. However, in certain mesh-dependent subspaces of* $L^2(\Sigma)$ *the bilinear forms* $b_T^{\mathcal{Z}}$ *and* b_{W} *are coercive with respect to* $\|\cdot\|_{L^2(\Sigma)}$, *at least for flat* Γ *in two spatial dimensions, see [6, Theorem 3.2, Proposition 3.3] and [7, Theorem 2.1, Remark 1].*

5 CONCLUSION AND OUTLOOK

This monograph presents an innovative space-time discretization scheme for retarded potential boundary integral equations (RPBIEs). Its novelty lies in the decomposition of the lateral boundary of the space-time cylinder into possibly unstructured simplex meshes. These meshes accommodate piecewise polynomial trial spaces, which treat time and space variables uniformly. The discretization of boundary integral equations by means of these eponymous space-time boundary elements furnishes a novel class of boundary element methods (BEMs).

The strong Huygens principle bestows an extraordinary structure upon RPBIEs. A key result of this work is that the proposed space-time discretization method conforms to the nature of RPBIEs in a genuine fashion. The space-time integral representations derived in Sections 2.6.1 and 2.6.2 show vividly that retarded layer potentials integrate along the intersection of the space-time boundary and the backward light cone. The latter is the set of points (events) which can emit perceivable signals. The discussed formulas hold naturally for moving boundaries and enjoy clear parallels to well-known results in the field of electrodynamics.

While the provided representations of retarded potentials are favorable in terms of physical interpretation, their actual computation is complicated. From a practical point of view, major contributions of this thesis are the quadrature techniques for retarded layer potentials exhibited in Sections 3.5, 3.6 and 3.8.1. For simplex panels, the integrals are posed on zero level sets of quadratic functions. These functions and the entailed quadric hypersurfaces are investigated in Sections 3.4 and 3.6, revealing a clear-cut behavior with respect to the geometric alignment of the involved panels. The presented quadrature methods enable highly accurate pointwise evaluations of retarded layer potentials and moderately accurate evaluations of energetic space-time bilinear forms.

These quadrature algorithms require only the panels lit by the backward light cone. In Section 3.8.3, a nimble application of existing geometric clustering techniques furnishes an algorithm for computing the set of lit panels efficiently. The procedure is based on an exact and computationally inexpensive criterion for checking whether the bounding sphere of a cluster is lit.

This thesis presents a relatively unexplored discretization method for RPBIEs. Naturally, many topics for future research present themselves:

- The quadrature technique for RPBIEs in the context of space-time meshes could be extended. The inner (retarded potential) and outer (Galerkin testing) integral could be treated as a single high-dimensional integral, as hinted in Section 3.6. While this approach might outperform the method employed in this work, its design is intricate. An immediate extension of the quadrature scheme presented in this thesis could be based on graded quadrature rules for the outer integral (3.41). Such procedures are based on the explicit knowledge of the relevant singularities of retarded layer potentials unveiled by thorough analysis.

- A well-known drawback of BEMs is the nonlocality of the involved integral operators. Retarded potential integral operators feature an extraordinary structure, which is a core theme of this monograph. Due to their distinguished properties, retarded potentials are neither classically global nor local operators. Efficient approximations of these operators in the sense of fast BEMs might enable the approximate solution of RPBIEs on unstructured space-time meshes with (nigh) optimal complexity. This step of development seems necessary in order to achieve truly competitive methods.

- The investigations of this thesis are restricted to stationary domains, with the exception of several theoretical observations. In physics, the concept of space-time was conceived in order to study the effects of motion. It is of no surprise that space-time discretization schemes handle problems posed on moving domains exceptionally well. The development of space-time methods for RPBIEs posed on moving boundaries is an interesting and unexplored topic from both a theoretical as well as a practical point of view.

- In this work, the lateral boundary of the space-time cylinder Σ is described by a mesh of simplex panels. It might be a worthwhile effort to abandon this first-order approximation and explore high-order parametrizations. For polynomial parametrizations of degree $p \in \mathbb{N}$ the intersection of panel and light cone studied in Section 3.4 is the zero level set of a polynomial of degree $2p$ in three dimensions. Furthermore, one might abandon polynomial parametrizations and investigate isogeometric approaches. These methods are based on parametrizations involving non-uniform rational basis splines (NURBS) used in computer aided design and computer graphics.

- The perhaps greatest and most pivotal challenge is not touched in this thesis: the mathematical analysis of RPBIEs. A functional setting built around computable bilinear forms which are bounded and coercive in the same Sobolev space norm would pave the path for conforming discretization methods. Such a highly desirable result would serve as a starting point for many theoretical investigations like sharp a priori error estimates and preconditioning.

Above list is far from being exhaustive and hints the richness of the field of research. It also indicates that the road to competitive space-time methods for RPBIEs is still a long one. Nevertheless, the findings of this thesis show that genuine space-time approximation schemes for RPBIEs are technically feasible and can furnish deep theoretical insight as well as great numerical results.

REFERENCES

[1] B. ABBOTT AND OTHERS (LIGO SCIENTIFIC COLLABORATION AND VIRGO COLLABORATION), *Observation of gravitational waves from a binary black hole merger*, Phys. Rev. Lett., 116 (2016), p. 061102, `https://doi.org/10.1103/PhysRevLett.116.061102`.

[2] T. ABBOUD, P. JOLY, J. RODRÍGUEZ, AND I. TERRASSE, *Coupling discontinuous Galerkin methods and retarded potentials for transient wave propagation on unbounded domains*, J. Comput. Phys., 230 (2011), pp. 5877–5907, `https://doi.org/10.1016/j.jcp.2011.03.062`.

[3] A. AIMI AND M. DILIGENTI, *A new space-time energetic formulation for wave propagation analysis in layered media by BEMs*, Internat. J. Numer. Methods Engrg., 75 (2008), pp. 1102–1132, `https://doi.org/10.1002/nme.2290`.

[4] A. AIMI, M. DILIGENTI, A. FRANGI, AND C. GUARDASONI, *A stable 3d energetic Galerkin BEM approach for wave propagation interior problems*, Eng. Anal. Bound. Elem., 36 (2012), pp. 1756–1765, `https://doi.org/10.1016/j.enganabound.2012.06.003`.

[5] A. AIMI, M. DILIGENTI, A. FRANGI, AND C. GUARDASONI, *Neumann exterior wave propagation problems: computational aspects of 3d energetic Galerkin BEM*, Comput. Mech., 51 (2013), pp. 475–493, `https://doi.org/10.1007/s00466-012-0796-5`.

[6] A. AIMI, M. DILIGENTI, C. GUARDASONI, I. MAZZIERI, AND S. PANIZZI, *An energy approach to space-time Galerkin BEM for wave propagation problems*, Internat. J. Numer. Methods Engrg., 80 (2009), pp. 1196–1240, `https://doi.org/10.1002/nme.2660`.

[7] A. AIMI, M. DILIGENTI, AND S. PANIZZI, *Energetic Galerkin BEM for wave propagation Neumann exterior problems*, CMES-Comp. Model. Eng., 58 (2010), pp. 185–219, `https://doi.org/doi:10.3970/cmes.2010.058.185`.

[8] K. AKIYAMA AND OTHERS (EVENT HORIZON TELESCOPE COLLABORATION), *First M87 event horizon telescope results. I. the shadow of the supermassive black hole*, Astrophys. J. Lett., 875 (2019), `https://doi.org/10.3847/2041-8213/ab0ec7`.

[9] J. Ballani, L. Banjai, S. Sauter, and A. Veit, *Numerical solution of exterior Maxwell problems by Galerkin BEM and Runge-Kutta convolution quadrature*, Numer. Math., 123 (2013), pp. 643–670, `https://doi.org/10.1007/s00211-012-0503-7`.

[10] A. Bamberger and T. Ha Duong, *Formulation variationnelle espace-temps pour le calcul par potentiel retardé de la diffraction d'une onde acoustique (I)*, Math. Methods Appl. Sci., 8 (1986), pp. 405–435, `https://doi.org/doi:10.1002/mma.1670080127`.

[11] A. Bamberger and T. Ha Duong, *Formulation variationnelle pour le calcul de la diffraction d'une onde acoustique par une surface rigide*, Math. Methods Appl. Sci., 8 (1986), pp. 598–608, `https://doi.org/10.1002/mma.1670080139`.

[12] L. Banjai and S. Sauter, *Rapid solution of the wave equation in unbounded domains*, SIAM J. Numer. Anal., 47 (2009), pp. 227–249, `https://doi.org/10.1137/070690754`.

[13] L. Banjai and M. Schanz, *Wave propagation problems treated with convolution quadrature and BEM*, in Fast Boundary Element Methods in Engineering and Industrial Applications, U. Langer, M. Schanz, O. Steinbach, and W. Wendland, eds., Springer Berlin Heidelberg, 2012, pp. 145–184, `https://doi.org/10.1007/978-3-642-25670-7_5`.

[14] L. Banz, H. Gimperlein, Z. Nezhi, and E. Stephan, *Time domain BEM for sound radiation of tires*, Comput. Mech., 58 (2016), pp. 45–57, `https://doi.org/10.1007/s00466-016-1281-3`.

[15] M. Bebendorf, *Hierarchical Matrices*, Springer, 2008.

[16] M. Behr, *Simplex space-time meshes in finite element simulations*, Internat. J. Numer. Methods Fluids, 57 (2008), pp. 1421–1434, `https://doi.org/10.1002/fld.1796`.

[17] B. Birgisson, E. Siebrits, and A. Peirce, *Elastodynamic direct boundary element methods with enhanced numerical stability properties*, Internat. J. Numer. Methods Engrg., 46 (1999), pp. 871–888, `https://doi.org/10.1002/(SICI)1097-0207(19991030)46:6<871::AID-NME698>3.0.CO;2-6`.

[18] M. Bluck and S. Walker, *Analysis of three-dimensional transient acoustic wave propagation using the boundary integral equation method*, Internat. J. Numer. Methods Engrg., 39 (1996), pp. 1419–1431, `https://doi.org/10.1002/(SICI)1097-0207(19960430)39:8<1419::AID-NME911>3.0.CO;2-C`.

[19] D. Boffi, F. Brezzi, and M. Fortin, *Mixed Finite Element Methods and Applications*, vol. 44 of Springer Series in Computational Mathematics, Springer, Berlin, 2013, `https://doi.org/10.1007/978-3-642-36519-5`.

[20] P. Ciarlet, *The Finite Element Method for Elliptic Problems*, vol. 40 of Classics in Applied Mathematics, SIAM, Philadelphia, 2002, `https://doi.org/10.1137/1.9780898719208`.

[21] M. Costabel and F.-J. Sayas, *Time-dependent problems with the boundary integral equation method*, Encycl. Comput. Mech. Second Ed., 2 (2017), pp. 1–24, `https://doi.org/10.1002/9781119176817.ecm2022`.

[22] P. Davies, *A stability analysis of a time marching scheme for the general surface electric field integral equation*, Appl. Numer. Math., 27 (1998), pp. 33–57, `https://doi.org/10.1016/S0168-9274(97)00107-4`.

[23] P. Davies and D. Duncan, *Averaging techniques for time-marching schemes for retarded potential integral equations*, Appl. Numer. Math., 23 (1997), pp. 291–310, `https://doi.org/10.1016/S0168-9274(96)00069-4`.

[24] P. Davies and D. Duncan, *Stability and convergence of collocation schemes for retarded potential integral equations*, SIAM J. Numer. Anal., 42 (2004), pp. 1167–1188, `https://doi.org/10.1137/S0036142901395321`.

[25] M. Delfour and J. Zolésio, *Shape analysis via oriented distance functions*, J. Funct. Anal., 123 (1994), pp. 129–201, `https://doi.org/10.1006/jfan.1994.1086`.

[26] L. Demkowicz, J. Gopalakrishnan, S. Nagaraj, and P. Sepúlveda, *A spacetime DPG method for the Schrödinger equation*, SIAM J. Numer. Anal., 55 (2017), pp. 1740–1759, `https://doi.org/10.1137/16M1099765`.

[27] W. Dörfler, S. Findeisen, and C. Wieners, *Space-time discontinuous Galerkin discretizations for linear first-order hyperbolic evolution systems*, Comput. Methods Appl. Math., 16 (2016), pp. 409–428, `https://doi.org/10.1515/cmam-2016-0015`.

[28] G. Dziuk and C. Elliott, *Finite element methods for surface PDEs*, Acta Numer., 22 (2013), pp. 289–396, `https://doi.org/10.1017/S0962492913000056`.

[29] A. Einstein, *Näherungsweise Integration der Feldgleichungen der Gravitation*, Sitzungsber. Königl. Preuss. Akad. Wiss. Berlin, (1916), pp. 688–696.

[30] S. Erichsen and S. Sauter, *Efficient automatic quadrature in 3-d Galerkin BEM*, Comput. Methods Appl. Mech. Engrg., 157 (1998), pp. 215–224, `https://doi.org/10.1016/S0045-7825(97)00236-3`.

[31] L. Evans, *Partial Differential Equations*, vol. 19 of Graduate Series in Mathematics, American Mathematical Society, Providence, Rhode Island, 2nd ed., 2010.

[32] H. Federer, *Geometric Measure Theory*, Springer Berlin Heidelberg, 1996.

[33] P. Foteinos and N. Chrisochoides, *4d space-time Delaunay meshing for medical images*, Eng. Comput., 31 (2015), pp. 499–511, `https://doi.org/10.1007/s00366-014-0380-z`.

[34] A. Frangi, *"Causal" shape functions in the time domain boundary element method*, Comput. Mech., 25 (2000), pp. 533–541, `https://doi.org/10.1007/s004660050501`.

[35] M. Friedman and R. Shaw, *Diffraction of pulses by cylindrical obstacles of arbitrary cross section*, J. Appl. Mech., 29 (1962), pp. 40–46, `https://doi.org/10.1115/1.3636495`.

[36] T. Fries, S. Omerović, D. Schöllhammer, and J. Steidl, *Higher-order meshing of implicit geometries-part I: Integration and interpolation in cut elements*, Comput. Methods Appl. Mech. Engrg., 313 (2017), pp. 759–784, `https://doi.org/10.1016/j.cma.2016.10.019`.

[37] T.-P. Fries and S. Omerović, *Higher-order accurate integration of implicit geometries*, Internat. J. Numer. Methods Engrg., 106 (2016), pp. 323–371, `https://doi.org/10.1002/nme.5121`.

[38] M. Gander and M. Neumüller, *Analysis of a new space-time parallel multigrid algorithm for parabolic problems*, SIAM J. Sci. Comput., 38 (2016), pp. A2173–A2208, `https://doi.org/10.1137/15M1046605`.

[39] M. Gfrerer and M. Schanz, *A high-order FEM with exact geometry description for the Laplacian on implicitly defined surfaces*, Internat. J. Numer. Methods Engrg., 114 (2018), pp. 1163–1178, `https://doi.org/10.1002/nme.5779`.

[40] H. Gimperlein, M. Maischak, and E. Stephan, *Adaptive time domain boundary element methods with engineering applications*, J. Integral Equations Appl., 29 (2017), pp. 75–105, `https://doi.org/10.1216/JIE-2017-29-1-75`.

[41] H. Gimperlein, F. Meyer, C. Özdemir, D. Stark, and E. Stephan, *Boundary elements with mesh refinements for the wave equation*, Numer. Math., 139 (2018), pp. 867–912, `https://doi.org/10.1007/s00211-018-0954-6`.

[42] H. Gimperlein and D. Stark, *Algorithmic aspects of enriched time domain boundary element methods*, Eng. Anal. Bound. Elem., 100 (2019), pp. 118–124, `https://doi.org/10.1016/j.enganabound.2018.02.010`.

[43] M. Gläfke, *Adaptive Methods for Time Domain Boundary Integral Equations*, PhD thesis, Brunel University London, 2012.

[44] G. Golub, *Some modified matrix eigenvalue problems*, SIAM Rev., 15 (1973), pp. 318–334, `https://doi.org/10.1137/1015032`.

[45] G. Golub and J. Welsch, *Calculation of Gauss quadrature rules*, Math. Comp., 23 (1969), pp. 221–230.

[46] J. Gopalakrishnan, P. Monk, and P. Sepúlveda, *A tent pitching scheme motivated by Friedrichs theory*, Comput. Math. Appl., 70 (2015), pp. 1114–1135, `https://doi.org/10.1016/j.camwa.2015.07.001`.

[47] J. Gopalakrishnan, J. Schöberl, and C. Wintersteiger, *Mapped tent pitching schemes for hyperbolic systems*, SIAM J. Sci. Comput., 39 (2017), pp. B1043–B1063, `https://doi.org/10.1137/16M1101374`.

[48] J. Gopalakrishnan and P. Sepúlveda, *A space-time DPG method for the wave equation in multiple dimensions*, in Space-Time Methods, U. Langer and O. Steinbach, eds., vol. 25 of Radon Series on Computational and Applied Mathematics, De Gruyter, Berlin, Boston, 2019, ch. 4, pp. 117–140, `https://doi.org/10.1515/9783110548488-004`.

[49] W. Gordon and C. Hall, *Construction of curvilinear co-ordinate systems and applications to mesh generation*, Internat. J. Numer. Methods Engrg., 7 (1973), pp. 461–477, `https://doi.org/10.1002/nme.1620070405`.

[50] D. Griffiths, *Introduction to Electrodynamics*, Cambridge University Press, 4th ed., 2017.

[51] T. Ha-Duong, *On retarded potential boundary integral equations and their discretisation*, in Topics in Computational Wave Propagation, M. Ainsworth, P. Davies, D. Duncan, B. Rynne, and P. Martin, eds., vol. 31, Springer Berlin Heidelberg, 2003, pp. 301–336, `https://doi.org/10.1007/978-3-642-55483-4_8`.

[52] T. Ha-Duong, B. Ludwig, and I. Terrasse, *A Galerkin BEM for transient acoustic scattering by an absorbing obstacle*, Internat. J. Numer. Methods Engrg., 57 (2003), pp. 1845–1882, `https://doi.org/10.1002/nme.745`.

[53] M. Hassell, T. Qiu, T. Sánchez-Vizuet, and F.-J. Sayas, *A new and improved analysis of the time domain boundary integral operators for the acoustic wave equation*, J. Integral Equations Appl., 29 (2017), pp. 107–136, `https://doi.org/10.1216/JIE-2017-29-1-107`.

[54] M. Hestenes and E. Stiefel, *Methods of conjugate gradients for solving linear systems*, J. Res. Nat. Bur. Stand., 49 (1952), pp. 409–436, `https://doi.org/10.6028/jres.049.044`.

[55] L. Hörmander, *The Analysis of Linear Partial Differential Operators I: Distribution Theory and Fourier Analysis*, Springer Berlin Heidelberg, 2003.

[56] S. Hubrich, P. Di Stolfo, L. Kudela, S. Kollmannsberger, E. Rank, A. Schröder, and A. Düster, *Numerical integration of discontinuous functions: moment fitting and smart octree*, Comput. Mech., 60 (2017), pp. 863–881, `https://doi.org/10.1007/s00466-017-1441-0`.

[57] G. Hulbert and T. Hughes, *Space-time finite element methods for second-order hyperbolic equations*, Comput. Methods Appl. Mech. Engrg., 84 (1990), pp. 327–348, `https://doi.org/10.1016/0045-7825(90)90082-W`.

[58] P. Joly and J. Rodríguez, *Mathematical aspects of variational boundary integral equations for time dependent wave propagation*, J. Integral Equations Appl., 29 (2017), pp. 137–187, `https://doi.org/10.1216/JIE-2017-29-1-137`.

[59] R. Jonsson, E. Martín-Martínez, and A. Kempf, *Information transmission without energy exchange*, Phys. Rev. Lett., 114 (2015), p. 110505, `https://doi.org/10.1103/PhysRevLett.114.110505`.

[60] E. Karabelas and M. Neumüller, *Generating admissible space-time meshes for moving domains in $d + 1$-dimensions*, 2015, `https://arxiv.org/abs/1505.03973v1`.

[61] L. Kielhorn, *A Time-Domain Symmetric Galerkin BEM for Viscoelastodynamics*, vol. 5 of Monographic Series TU Graz: Computation in Engineering and Science, Verlag der Technischen Universität Graz, 2009.

[62] V. Krylov and A. Stroud, *Approximate Calculation of Integrals*, Dover, 2006.

[63] L. Kudela, N. Zander, T. Bog, S. Kollmannsberger, and E. Rank, *Efficient and accurate numerical quadrature for immersed boundary methods*, Adv. Model. and Simul. in Eng. Sci., 2 (2015), `https://doi.org/10.1186/s40323-015-0031-y`.

[64] U. Langer, S. Moore, and M. Neumüller, *Space-time isogeometric analysis of parabolic evolution problems*, Comput. Methods Appl. Mech. Engrg., 306 (2016), pp. 342–363, `https://doi.org/10.1016/j.cma.2016.03.042`.

[65] C. Lehrenfeld, *High order unfitted finite element methods on level set domains using isoparametric mappings*, Comput. Methods Appl. Mech. Engrg., 300 (2016), pp. 716–733, `https://doi.org/10.1016/j.cma.2015.12.005`.

[66] M. Lopez-Fernandez and S. Sauter, *Generalized convolution quadrature with variable time stepping*, IMA J. Numer. Anal., 33 (2013), pp. 1156–1175, `https://doi.org/10.1093/imanum/drs034`.

[67] M. Lopez-Fernandez and S. Sauter, *Generalized convolution quadrature with variable time stepping. part II: Algorithm and numerical results*, Appl. Numer. Math., 94 (2015), pp. 88–105, `https://doi.org/10.1016/j.apnum.2015.03.004`.

[68] M. Lopez-Fernandez and S. Sauter, *Generalized convolution quadrature based on Runge-Kutta methods*, Numer. Math., 133 (2016), pp. 743–779, `https://doi.org/10.1007/s00211-015-0761-2`.

[69] C. Lubich, *Convolution quadrature and discretized operational calculus. I*, Numer. Math., 52 (1988), pp. 129–145, `https://doi.org/10.1007/BF01398686`.

[70] C. Lubich, *Convolution quadrature and discretized operational calculus. II*, Numer. Math., 52 (1988), pp. 413–425, `https://doi.org/10.1007/BF01462237`.

[71] C. Lubich, *On the multistep time discretization of linear initial-boundary value problems and their boundary integral equations*, Numer. Math., 67 (1994), pp. 365–389, `https://doi.org/10.1007/s002110050033`.

[72] N. Manson and J. Tausch, *Quadrature for parabolic Galerkin BEM with moving surfaces*, Comput. Math. Appl., 77 (2019), pp. 1–14, `https://doi.org/10.1016/j.camwa.2018.09.004`.

[73] W. Mansur, *A time-stepping technique to solve wave propagation problems using the boundary element method*, PhD thesis, University of Southampton, 1983.

[74] W. Mansur and C. Brebbia, *Numerical implementation of the boundary element method for two dimensional transient scalar wave propagation problems*, Appl. Math. Model., 6 (1982), pp. 299–306, `https://doi.org/10.1016/S0307-904X(82)80038-3`.

[75] H. Mantz, K. Jacobs, and K. Mecke, *Utilizing Minkowski functionals for image analysis: a marching square algorithm*, J. Stat. Mech: Theory Exp., (2008), p. P12015, `https://doi.org/10.1088/1742-5468/2008/12/p12015`.

[76] W. McLean, *Strongly Elliptic Systems and Boundary Integral Equations*, Cambridge University Press, 2000.

[77] H. Minkowski, *Raum und Zeit*, Phys. Z., 10 (1909), pp. 104–115.

[78] C. Misner, K. Thorne, and J. Wheeler, *Gravitation*, Macmillan, San Francisco, 1973.

[79] B. Müller, F. Kummer, and M. Oberlack, *Highly accurate surface and volume integration on implicit domains by means of moment-fitting*, Internat. J. Numer. Methods Engrg., 96 (2013), pp. 512–528, `https://doi.org/10.1002/nme.4569`.

[80] G. Naber, *The Geometry of Minkowski Spacetime: An Introduction to the Mathematics of the Special Theory of Relativity*, vol. 92 of Applied Mathematical Sciences, Springer Science & Business Media, 2012.

[81] J.-C. Nédélec, *Acoustic and Electromagnetic Equations*, vol. 144 of Applied Mathematical Sciences, Springer, New York, 2001, `https://doi.org/10.1007/978-1-4757-4393-7`.

[82] M. Neumüller, *Space-Time Methods: Fast Solvers and Applications*, vol. 20 of Monographic Series TU Graz: Computation in Engineering and Science, Verlag der Technischen Universität Graz, 2013.

[83] N. Ortner, *Regularisierte Faltung von Distributionen. Teil 2: Eine Tabelle von Fundamentallösungen*, Z. Angew. Math. Phys., 31 (1980), pp. 155–173, `https://doi.org/10.1007/BF01601710`.

[84] N. Ortner and P. Wagner, *Fundamental Solutions of Linear Partial Differential Operators: Theory and Practice*, Springer, Cham, 2015, `https://doi.org/10.1007/978-3-319-20140-5`.

[85] E. Ostermann, *Numerical Methods for Space-Time Variational Formulations of Retarded Potential Boundary Integral Equations*, PhD thesis, Gottfried Wilhelm Leibniz Universität Hannover, 2010.

[86] C. Pechstein, *Finite and Boundary Element Tearing and Interconnecting Solvers for Multiscale Problems*, vol. 90 of Lecture Notes in Computational Science and Engineering, Springer, Berlin, 2013, `https://doi.org/10.1007/978-3-642-23588-7`.

[87] I. Perugia, J. Schöberl, P. Stocker, and C. Wintersteiger, *Tent pitching and Trefftz-DG method for the acoustic wave equation*, Comput. Math. Appl., 79 (2020), pp. 2987–3000, `https://doi.org/10.1016/j.camwa.2020.01.006`.

[88] D. Pölz, M. Gfrerer, and M. Schanz, *Wave propagation in elastic trusses: An approach via retarded potentials*, Wave Motion, 87 (2019), pp. 37–57, `https://doi.org/10.1016/j.wavemoti.2018.06.002`.

[89] D. Pölz and M. Schanz, *Space-time discretized retarded potential boundary integral operators: Quadrature for collocation methods*, SIAM J. Sci. Comput., 41 (2019), pp. A3860–A3886, `https://doi.org/10.1137/19M1245633`.

[90] W. Press, S. Teukolsky, W. Vetterling, and B. Flannery, *Numerical Recipes: The Art of Scientific Computing*, Cambridge University Press, 3rd ed., 2007.

[91] T. Qiu and F.-J. Sayas, *New mapping properties of the time domain electric field integral equation*, ESAIM Math. Model. Numer. Anal., 51 (2017), pp. 1–15, `https://doi.org/10.1051/m2an/2016021`.

[92] J. Ritter, *An efficient bounding sphere*, in Graphics Gems, A. Glassner, ed., Academic Press Inc., San Diego, CA, 1990, pp. 301–303.

[93] S. Rjasanow and O. Steinbach, *The Fast Solution of Boundary Integral Equations*, Springer Science & Business Media, 2007.

[94] E. Rothe, *Zweidimensionale parabolische Randwertaufgaben als Grenzfall eindimensionaler Randwertaufgaben*, Math. Ann., 102 (1930), pp. 650–670, `https://doi.org/10.1007/BF01782368`.

[95] B. Rynne, *Instabilities in time marching methods for scattering problems*, Electromagnetics, 6 (1986), pp. 129–144, `https://doi.org/10.1080/02726348608915207`.

[96] B. Rynne, *Time domain scattering from arbitrary surfaces using the electric field integral equation*, J. Electromagn. Waves Appl., 5 (1991), pp. 93–112, `https://doi.org/10.1163/156939391X00491`.

[97] B. Rynne, *The well-posedness of the electric field integral equation for transient scattering from a perfectly conducting body*, Math. Methods Appl. Sci., 22 (1999), pp. 619–631, `https://doi.org/10.1002/(SICI)1099-1476(19990510)22:7<619::AID-MMA59>3.0.CO;2-E`.

[98] B. Rynne and P. Smith, *Stability of time marching algorithms for the electric field integral equation*, J. Electromagn. Waves Appl., 4 (1990), pp. 1181–1205, `https://doi.org/10.1163/156939390X00762`.

[99] Y. Saad, *Iterative Methods for Sparse Linear Systems*, SIAM, Philadelphia, 2nd ed., 2003.

[100] S. Sauter and C. Schwab, *Boundary Element Methods*, vol. 39 of Springer Series in Computational Mathematics, Springer Berlin Heidelberg, 2011, `https://doi.org/10.1007/978-3-540-68093-2`.

[101] S. Sauter and A. Veit, *A Galerkin method for retarded boundary integral equations with smooth and compactly supported temporal basis functions*, Numer. Math., 123 (2013), pp. 145–176, `https://doi.org/10.1007/s00211-012-0483-7`.

[102] S. Sauter and A. Veit, *Retarded boundary integral equations on the sphere: exact and numerical solution*, IMA J. Numer. Anal., 34 (2014), pp. 675–699, `https://doi.org/10.1093/imanum/drs059`.

[103] F.-J. Sayas, *Energy estimates for Galerkin semidiscretizations of time domain boundary integral equations*, Numer. Math., 124 (2013), pp. 121–149, `https://doi.org/10.1007/s00211-012-0506-4`.

[104] F.-J. Sayas, *Retarded Potentials and Time Domain Boundary Integral Equations: A Road Map*, vol. 50 of Springer Series in Computational Mathematics, Springer, Cham, 2016, `https://doi.org/10.1007/978-3-319-26645-9`.

[105] R. Saye, *High-order quadrature methods for implicitly defined surfaces and volumes in hyperrectangles*, SIAM J. Sci. Comput., 37 (2015), pp. A993–A1019, `https://doi.org/10.1137/140966290`.

[106] M. Schanz, *Wave Propagation in Viscoelastic and Poroelastic Continua: A Boundary Element Approach*, vol. 2 of Lecture Notes in Applied and Computational Mechanics, Springer Berlin Heidelberg, 2001, `https://doi.org/10.1007/978-3-540-44575-3`.

[107] K. Schwarzschild, *Über das Gravitationsfeld eines Massenpunktes nach der Einsteinschen Theorie*, Sitzungsber. Königl. Preuss. Akad. Wiss. Berlin, (1916), pp. 189–196.

[108] O. Steinbach, *Numerical Approximation Methods for Elliptic Boundary Value Problems: Finite and Boundary Elements*, Springer Science & Business Media, 2008.

[109] O. Steinbach, *Space-time finite element methods for parabolic problems*, Comput. Methods Appl. Math., 15 (2015), pp. 551–566, `https://doi.org/10.1515/cmam-2015-0026`.

[110] E. Stephan, M. Maischak, and E. Ostermann, *Transient boundary element method and numerical evaluation of retarded potentials*, in Computational Science - ICCS 2008, M. Bubak, G. van Albada, J. Dongarra, and P. Sloot, eds., Springer Berlin Heidelberg, 2008, pp. 321–330, `https://doi.org/10.1007/978-3-540-69387-1_35`.

[111] J. Tausch, *Nyström method for BEM of the heat equation with moving boundaries*, Adv. Comput. Math., 45 (2019), pp. 2953–2968, `https://doi.org/10.1007/s10444-019-09720-x`.

[112] A. Toda, *Radii of the inscribed and escribed spheres of a simplex*, Int. J. Geom., 3 (2014), pp. 5–13.

[113] F. Tricomi, *Sugli zeri dei polinomi sferici ed ultrasferici*, Ann. Mat. Pura Appl. (4), 31 (1950), pp. 93–97.

[114] A. Üngör and A. Sheffer, *Pitching tents in space-time: Mesh generation for discontinuous Galerkin method*, Internat. J. Found. Comput. Sci., 13 (2002), pp. 201–221, `https://doi.org/10.1142/S0129054102001059`.

[115] H. van der Vorst, *Bi-CGSTAB: A fast and smoothly converging variant of Bi-CG for the solution of nonsymmetric linear systems*, SIAM J. Sci. Stat. Comput., 13 (1992), pp. 631–644, `https://doi.org/10.1137/0913035`.

[116] E. van't Wout, D. van der Heul, H. van der Ven, and C. Vuik, *Stability analysis of the marching-on-in-time boundary element method for electromagnetics*, J. Comput. Appl. Math., 294 (2016), pp. 358–371, `https://doi.org/10.1016/j.cam.2015.09.002`.

[117] A. Veit, *Numerical Methods for Time-Domain Boundary Integral Equations*, PhD thesis, Universität Zürich, 2012.

[118] A. Veit, M. Merta, J. Zapletal, and D. Lukáš, *Efficient solution of time-domain boundary integral equations arising in sound-hard scattering*, Internat. J. Numer. Methods Engrg., 107 (2016), pp. 430–449, `https://doi.org/10.1002/nme.5187`.

[119] K. Voronin, C. Lee, M. Neumüller, P. Sepulveda, and P. Vassilevski, *Space-time discretizations using constrained first-order system least squares (CFOSLS)*, J. Comput. Phys., 373 (2018), pp. 863–876, `https://doi.org/10.1016/j.jcp.2018.07.024`.

[120] S. Walter, *Hermann Minkowski's approach to physics*, Math. Semesterber., 55 (2008), `https://doi.org/10.1007/s00591-008-0044-4`.

[121] L. Wang and P.-O. Persson, *A high-order discontinuous Galerkin method with unstructured space-time meshes for two-dimensional compressible flows on domains with large deformations*, Comput. & Fluids, 118 (2015), pp. 53–68, `https://doi.org/10.1016/j.compfluid.2015.05.026`.

[122] K. Yosida, *Functional Analysis*, Springer, Berlin Heidelberg, 6th ed., 1980.

[123] M. Zank and O. Steinbach, *Adaptive space-time boundary element methods for the wave equation*, PAMM. Proc. Appl. Math. Mech., 16 (2016), pp. 777–778, `https://doi.org/10.1002/pamm.201610377`.

Monographic Series TU Graz

Computation in Engineering and Science

Vol. 1 Steffen Alvermann
Effective Viscoelastic Behavior of Cellular Auxetic Materials
2008
ISBN 978-3-902465-92-4

Vol. 2 Sendy Fransiscus Tantono
The Mechanical Behaviour of a Soilbag under Vertical Compression
2008
ISBN 978-3-902465-97-9

Vol. 3 Thomas Rüberg
Non-conforming FEM/BEM Coupling in Time Domain
2008
ISBN 978-3-902465-98-6

Vol. 4 Dimitrios E. Kiousis
Biomechanical and Computational Modeling of Atherosclerotic Arteries
2008
ISBN 978-3-85125-023-7

Vol. 5 Lars Kielhorn
A Time-Domain Symmetric Galerkin BEM for Viscoelastodynamics
2009
ISBN 978-3-85125-042-8

Vol. 6 Gerhard Unger
Analysis of Boundary Element Methods for Laplacian Eigenvalue Problems
2009
ISBN 978-3-85125-081-7

Monographic Series TU Graz

Computation in Engineering and Science

Vol. 7 Gerhard Sommer
Mechanical Properties of Healthy and Diseased Human Arteries
2010
ISBN 978-3-85125-111-1

Vol. 8 Mathias Nenning
Infinite Elements for Elasto- and Poroelastodynamics
2010
ISBN 978-3-85125-130-2

Vol. 9 Thanh Xuan Phan
Boundary Element Methods for Boundary Control Problems
2011
ISBN 978-3-85125-149-4

Vol. 10 Loris Nagler
Simulation of Sound Transmission through Poroelastic Plate-like Structures
2011
ISBN 978-3-85125-153-1

Vol. 11 Markus Windisch
Boundary Element Tearing and Interconnecting Methods for Acoustic and Electromagnetic Scattering
2011
ISBN 978-3-85125-152-4

Vol. 12 Christian Walchshofer
Analysis of the Dynamics at the Base of a Lifted Strongly Buoyant Jet Flame Using Direct Numerical Simulation
2011
ISBN 978-3-85125-185-2

Monographic Series TU Graz

Computation in Engineering and Science

Vol. 13 Matthias Messner
Fast Boundary Element Methods in Acoustics
2012
ISBN 978-3-85125-202-6

Vol. 14 Peter Urthaler
Analysis of Boundary Element Methods for Wave Propagation in Porous Media
2012
ISBN 978-3-85125-216-3

Vol. 15 Peng Li
Boundary Element Method for Wave Propagation in Partially Saturated Poroelastic Continua
2012
ISBN 978-3-85125-236-1

Vol. 16 Andreas Jörg Schriefl
Quantification of Collagen Fiber Morphologies in Human Arterial Walls
2013
ISBN 978-3-85125-238-5

Vol. 17 Thomas S. E. Eriksson
Cardiovascular Mechanics
2013
ISBN 978-3-85125-277-4

Vol. 18 Jianhua Tong

Biomechanics of Abdominal Aortic Aneurysms
2013
ISBN 978-3-85125-279-8

Monographic Series TU Graz

Computation in Engineering and Science

Vol. 19 Jonathan Rohleder
Titchmarsh–Weyl Theory and Inverse Problems for Elliptic Differential Operators
2013
ISBN 978-3-85125-283-5

Vol. 20 Martin Neumüller
Space-Time Methods
2013
ISBN 978-3-85125-290-3

Vol. 21 Michael J. Unterberger
Microstructurally-Motivated Constitutive Modeling of Cross-Linked Filamentous Actin Networks
2013
ISBN 978-3-85125-303-0

Vol. 22 Vladimir Lotoreichik
Singular Values and Trace Formulae for Resolvent Power Differences of Self-Adjoint Elliptic Operators
2013
ISBN 978-3-85125-304-7

Vol. 23 Michael Meßner
A Fast Multipole Galerkin Boundary Element Method for the Transient Heat Equation
2014
ISBN 978-3-85125-350-4

Vol. 24 Lorenz Johannes John
Optimal Boundary Control in Energy Spaces
2014
ISBN 978-3-85125-373-3

Monographic Series TU Graz

Computation in Engineering and Science

Vol. 25 Hannah Weisbecker
Softening and Damage Behavior of Human Arteries
2014
ISBN 978-3-85125-370-2

Vol. 26 Bernhard Kager
Efficient Convolution Quadrature based Boundary Element Formulation for Time-Domain Elastodynamics
2015
ISBN 978-3-85125-382-5

Vol. 27 Christoph M. Augustin
Classical and All-floating FETI Methods with Applications to Biomechanical Models
2015
ISBN 978-3-85125-418-1

Vol. 28 Elias Karabelas
Space-Time Discontinuous Galerkin Methods for Cardiac Electromechanics
2016
ISBN 978-3-85125-461-7

Vol. 29 Thomas Traub
A Kernel Interpolation Based Fast Multipole Method for Elastodynamic Problems
2016
ISBN 978-3-85125-465-5

Vol. 30 Matthias Gsell
Mortar Domain Decomposition Methods for Quasilinear Problems and Applications
2017
ISBN 978-3-85125-522-5

Monographic Series TU Graz

Computation in Engineering and Science

Vol. 31 Christian Kühn

Schrödinger operators and singular infinite rank perturbations
2017
ISBN 978-3-85125-551-5

Vol. 32 Michael H. Gfrerer

Vibro-Acoustic Simulation of Poroelastic Shell Structures
2018
ISBN 978-3-85125-573-7

Vol. 33 Markus Holzmann

Spectral Analysis of Transmission and Boundary Value Problems for Dirac Operators
2018
ISBN 978-3-85125-642-0

Vol. 34 Osman Gültekin

Computational Inelasticity of Fibrous Biological Tissues with a Focus on Viscoelasticity, Damage and Rupture
2019
ISBN 978-3-85125-655-0

Vol. 35 Justyna Anna Niestrawska

Experimental and Computational Analyses of Pathological Soft Tissues – Towards a Better Understanding of the Pathogenesis of AAA
2019
ISBN 978-3-85125-678-9

Monographic Series TU Graz

Computation in Engineering and Science

Vol. 36 Marco Zank
Inf-Sup Stable Space-Time Methods for Time-Dependent Partial Differential Equations
2020
ISBN 978-3-85125-721-2

Vol. 37 Christoph Irrenfried
Convective turbulent near wall heat transfer at high Prandtl numbers
2020
ISBN 978-3-85125-724-3

Vol. 38 Christopher Albert
Hamiltonian Theory of Resonant Transport Regimes in Tokamaks with Perturbed Axisymmetry
2020
ISBN 978-3-85125-746-5

Vol. 39 Daniel Christopher Haspinger
Material Modeling and Simulation of Phenomena at the Nano, Micro and Macro Levels in Fibrous Soft Tissues of the Cardiovascular System
2021
ISBN 978-3-85125-802-8

Vol. 40 Markus Alfons Geith
Percutaneous Coronary Intervention
2021
ISBN 978-3-85125-801-1

Monographic Series TU Graz

Computation in Engineering and Science

Vol. 41 Dominik Pölz

Space-Time Boundary Elements for Retarded Potential Integral Equations
2021
ISBN 978-3-85125-811-0